Thesis Manuscript

PhD defense scheduled on 03/10/2023 at the University of Lille

Submitted by **Sandy AL Bacha**

To obtain the **Grade of Doctor** of the University of Lille
Chemistry of Materials

And the **Grade of Doctor** of the University of Kent
Physical Sciences

Towards the design of oxychalcogenide materials as candidates for solar water-splitting photocatalysis

Committee

Mr. Simon Clarke	Reviewer	Professor Oxford University
Mr. Manuel Gaudon	Reviewer	Professor ICMCB - Bordeaux
Mr. David Portehault	President of the jury	Research director CNRS, LCMCP - Sorbonne University
Miss. Donna Arnold	Co-supervisor	Reader Kent University
Miss. Emma McCabe	Co-supervisor	Associate Professor Durham University
Miss. Houria Kabbour	Supervisor	Researcher CNRS, UCCS - Lille University
Mr. Pascal Roussel	Invited	Research director CNRS, UCCS - Lille University
Mr. Sébastien Saitzek	Invited	Professor UCCS – Artois University

Thèse

Présenté et soutenue le 03 Octobre 2023 à l'Université de Lille

par **Sandy AL Bacha**

En vue d'obtenir le **Grade de Docteur** de l'University de Lille
Discipline : Chimie des Matériaux

Et le **Grade de Docteur** de l'Université de Kent
Discipline : Sciences Physique

Vers le design de matériaux oxychalcogénures pour la photocatalyse solaire du craquage de l'eau

Jury composé de :

M. Simon Clarke	Rapporteur	Professor Université d'Oxford
M. Manuel Gaudon	Rapporteur	Professeur des universités ICMCB - Bordeaux
M. David Portehault	Président du jury	Directeur de recherche CNRS, LCMCP – Paris
Mme Donna Arnold	Co-directrice de thèse	Reader Université de Kent
Mme Emma McCabe	Co-encadrante de thèse	Associate Professor Université de Durham
Mme Houria Kabbour	Directrice de thèse	Chargée de recherche CNRS, UCCS – Université de Lille
M. Pascal Roussel	Invité	Directeur de recherche CNRS, UCCS – Université de Lille
M. Sébastien Saitzek	Invité	Professeur des universités UCCS – Université d'Artois

Acknowledgments

I would like to thank the I-site organization for funding this cotutelle project between the University of Lille (France) and the University of Kent (United Kingdom), as well as the ‘Centre Nationale de recherche scientifique’ CNRS. I had the pleasure of being a part of the Unit of Catalysis and Solid-State Chemistry (UCCS) laboratory, UMR CNRS 8181, more precisely within the axis of "Solid State Chemistry", in the "Inorganic Materials, Structures, Systems and Properties" (MISSP) group; and of the School of physical sciences, in the "Materials for Energy and Electronics" (MEE) group in Kent.

I address all my respectful thanks to my thesis jury members, Mr. Simon Clarke, Professor of Chemistry at Oxford University; Mr. Manuel Gaudon, Professor at the ‘Institut de Chimie de la Matière Condensée’ ICMCB in Bordeaux and Mr. David Portehault, Research director at the ‘Laboratory of Chemistry of Condensed Matter of Paris’ (LCMCP) hosted by Sorbonne University for doing me the honor of reporting and examining this work.

I would like to express my profound gratitude to the people without whom this work could never have been carried out: my thesis supervisors, Mrs. Houria Kabbour and Mrs. Emma McCabe, your knowledge, skills and foresight allowed me to learn a lot and have been an invaluable help to me during this thesis. I know I have been a difficult student sometimes, but you have always been able to advise me and support me in a good mood during these three years, and for all this I can never tell you enough, Thank you!

I address my warmest thanks to Mrs. Donna Arnold, for the useful discussions and for her help in managing the administrative matters. I would like to thank all the members of the UCCS lab: the transmission electron microscopy platform as well as the X-ray diffraction platform of the Chevreul Institute and more particularly, Mrs. Marielle Huvé, Professor of the University of Lille for TEM images, Mr. Pascal Roussel, Research director and Mr. Frédéric Capet. I would also like to thank Mrs. Nora Djelal and Mr. Victor Duffort for the thermal analysis, Laurence for XRD analysis, Philippe for the UV-visible spectroscopy, Maxence for the MEB and EDS analysis and Myriam for her efficiency and kindness.

I would like to thank the UCCS lab in Lens, specifically the "Thin Films and Nanomaterials" (CMNM) group in the University of Artois for allowing me to do the photoelectrochemical

measurements. My profound gratitude goes to Mr. Sébastien Saitzek, Professor at the University of Artois for your welcome, your help as well as the many interesting discussions that we had during my visits to Lens.

As a cotutelle student, I got to visit four different laboratories. I did have the pleasure of moving around France and the UK which was difficult sometimes but still exciting. I got to meet a lot of people and explore various working environment. Therefore, I want to thank the Physics department in Durham University and the 'Jean Rouxel Institute of Materials' in Nantes for hosting me as a visiting student and allowing me to continue my research.

Far away from home yet I got the chance to meet quiet of few extraordinary people that made me feel safe and secure and we got to make unforgettable wonderful memories. Starting with my colleagues from Lille, I want to first thank Batoul, for sharing your knowledge with me and for showing me Lille for the first time! Maxime, even though we drive each other crazy but you've become a close friend and I will always appreciate our jokes and laughs in and outside the office. Mathilde, my fellow female colleague in the office, I probably annoyed you with my questions most of the time but I really appreciated your help and I'm glad that we've become friends. Hicham, my dear friend, we've been through a lot, never give up and keep up your high spirit.

To my Lebanese friends, Bertha, thank you for always being there for me, I will always cherish our conversations, trips and our shopping sprees! I'm forever grateful for you. Mohammad, our shawarma outings and funny moments will never be forgotten, thank you for being there whenever I needed you. Ibrahim, I will never forget our little coffee breaks in SH1 and for always opening the C3 door for me, thank you for being a good friend. To my French family, Soukaina, I am so thankful for you, for being there through my internship and my thesis, for all the advice, all the pep talk, I could've not made without you by my side! Nicolas and Teddy, your humor, our conversations and hangouts will always be one of my favourite memories.

Last but not least, my English family, Glen thank you for making my transition to Durham so easy, I will always appreciate our Starbucks coffees and conversations. Areesha, thank you for being the funniest person in the office and for always missing the bus with me! Jay for keeping up with me and for matching my weirdness level.

I will end by thanking my family, although I'm not usually the type to say it, but I love you. My father Joseph, my mother Jamilé and my brothers Charbel and Anthony; all words are not enough to express my appreciation and respect for you, thank you for always believing in me and supporting me through my ups and downs during these three years. Your love and trust are the reason I am where I am today.

It is with many emotions that I would like to thank all those who contributed directly or indirectly to this work. It was difficult to describe my feelings and I hope I knew how to say things at best and have not forgotten anyone.

Thank you, everyone!

Abstract

Photocatalysts, capable of splitting water for clean hydrogen production, are needed if we are to realize the potential of fuel cells (which combine hydrogen and oxygen to give electrical energy) to help meet the world's energy demands. The use of solar energy is promising and the search for photocatalysts that are active under solar irradiation is growing. Whilst numerous materials have been found to be effective for water splitting, many oxide materials have band gaps too large for excitation by visible light, and many sulfides have smaller band gaps or lower stability. On the other hand, the electronic structure (including band gap nature and magnitude) can be optimized by tuning the chemical composition, including substitutions on the anion sublattice (e.g. with H^-, N^{3-} or S^{2-}) to give mixed-anion materials. By appropriate anion-substitution, this can raise the valence band maximum which will decrease the band gap, moving it to the visible range. This substitution can also promote polarity which can lead to a better charge carrier's (e^-/h^+) separation. In particular, having heteroleptic environments around an active site may lead to enhanced polarity. This innovative strategy has been applied to give optically active materials and has been highlighted by theory work to give improved photocatalytic performance. Thus, the aim of this thesis is to test these hypotheses by combined experimental and computational studies on known oxychalcogenide materials.

In this context, a series of iron-based oxychalcogenides was investigated in which the roles of polar structure, the connectivity and transition metal coordination are highlighted. Polar CaFeOSe demonstrated its activity as photocathode with fast e^-/h^+ separation compared to the non-polar $La_2O_2Fe_2OQ_2$ (Q = S, Se), but on the other hand, these transition metals could suffer from an oxidation reaction which was seen with CaFeOS. Then, investigations of the polar oxysulfide $Sr_6Cd_2Sb_6S_{10}O_7$ indicate its potential for photocatalytic applications with efficient electron-hole separation. This work demonstrates the importance of lone pairs in designing photocatalytic materials, and the balance between the cation site polarity and energies of cation valence states that can be tuned by anion substitution. Lastly, the study of $Sr_2Sb_2O_2Q_3$ (Q = S, Se) phases revealed exceptionally low effective masses for both electrons and holes: this is attributed to the presence of a stereochemically active lone pair and a 1D building block of $SbOS_4$ with ~180° bond angles. Experimentally, this was observed in the photocurrent measurements of $Sr_2Sb_2O_2Se_3$ with even lower effective masses. These studies gave us insight into the structure-property relationships for those families and suggest a potential design strategy for functional oxychalcogenide photocatalysts in the visible light.

Keywords : Hydrogen, mixed-anion, oxychalcogenide, photocatalysis, photodegradation, photoconduction.

Résumé

Les photocatalyseurs, capables de fractionner l'eau pour la production d'hydrogène, sont nécessaires si nous voulons réaliser le potentiel des piles à combustible (qui combinent l'hydrogène et l'oxygène pour fournir de l'énergie électrique) pour aider à répondre à la demande énergétique mondiale. L'utilisation de l'énergie solaire est prometteuse et la recherche de photocatalyseurs actifs sous irradiation solaire se développe. Alors que de nombreux matériaux se sont révélés efficaces pour le fractionnement de l'eau, de nombreux matériaux oxydés ont des bandes interdites trop grandes pour être excitées par la lumière visible, et de nombreux sulfures ont des bandes interdites plus petites ou une moins bonne stabilité. D'autre part, la structure électronique (y compris la nature et la magnitude de la bande interdite) peut être optimisée en ajustant la composition chimique, y compris des substitutions sur le réseau anionique (par exemple avec H^-, N^{3-} ou S^{2-}) pour donner des matériaux à anions mixtes. Par substitution d'anions appropriée, cela peut augmenter le maximum de la bande de valence, ce qui diminuera la bande interdite, la déplaçant vers la plage visible. Cette substitution peut également favoriser la polarité, ce qui peut conduire à une meilleure séparation du porteur de charge (e^-/h^+). En particulier, le fait d'avoir des environnements hétéroleptiques autour d'un site actif peut entraîner une polarité accrue. Cette stratégie innovante a été appliquée pour donner des matériaux optiquement actifs et a été mise en évidence par des travaux théoriques pour améliorer les performances photocatalytiques. Ainsi, le but de cette thèse est de tester ces hypothèses par des études expérimentales et théoriques combinées sur des matériaux oxychalcogénures connus.

Dans ce contexte, une série d'oxychalcogénures à base de fer a été étudiée dans laquelle les rôles de la structure polaire, de la connectivité et de la coordination des métaux de transition sont mis en évidence. CaFeOSe polaire a démontré son activité en tant que photocathode avec séparation rapide des e^-/h^+ par rapport au $La_2O_2Fe_2OQ_2$ non polaire (Q = S, Se) ; mais d'autre part, ces métaux de transition pourraient souffrir d'une réaction d'oxydation qui a été observée avec CaFeOS. Ensuite, les études de l'oxysulfure polaire $Sr_6Cd_2Sb_6S_{10}O_7$ indiquent son potentiel pour des applications photocatalytiques avec une séparation efficace des e^-/h^+. Ce travail démontre l'importance des paires libres dans la conception de matériaux photocatalytiques, et l'équilibre entre la polarité du site cationique et les énergies des états de valence cationique qui peuvent être ajustés par substitution d'anions. Enfin, l'étude des phases $Sr_2Sb_2O_2Q_3$ (Q = S, Se) a révélé des masses effectives faibles pour les e^- et les h^+ : ceci est attribué à la présence d'une paire isolée stéréochimiquement active et d'un bloc de construction 1D de $SbOS_4$ avec des angles de liaison de ~180°. Expérimentalement, cela a été observé dans les mesures de photocourant de $Sr_2Sb_2O_2Se_3$ avec des masses effectives encore plus faibles. Ces études nous ont donné un aperçu des relations structure-propriété pour ces familles et suggèrent une stratégie de conception potentielle pour les photocatalyseurs oxychalcogénures fonctionnels dans la lumière visible.

Mots Clé : Hydrogène, anion mixte, oxychalcogénure, photocatalyse, photo-dégradation, photo-conduction.

Table of Contents

General Introduction

While the world's energy demand is growing, the move towards renewable sources (e.g. solar, wind, tidal) is increasingly urgent to minimize fuel shortages and worldwide climate disruption caused by fossil fuels. As shown in **Figure 1**, it is predicted that more than 50% of global power generation will come from renewable sources by 2035, with solar energy making a significant contribution to this. Whilst these sources are sustainable, they are somewhat intermittent and energy storage remains a key challenge. The most two common storage solutions include batteries and fuel cells. Fuel cells combine hydrogen and oxygen to give electrical energy and water as the waste product. Oxygen is readily available in the earth's atmosphere, but the challenge is to obtain hydrogen safely and efficiently. Photocatalytic water splitting is one solution to this challenge. The concept of this method is to simply split water to give hydrogen and oxygen while using a functional material that facilitates (or catalyses) the reaction when irradiated with light (UV or solar). A range of materials were found to be active under UV irradiation but the current challenge is to develop and optimise materials that are active in visible light. To carry out this reaction in the visible region requires appropriate band gap and band edge positions of the photocatalysts; this is why it is essential to explore functional materials with optimized band gaps, which can be tuned by chemical adjustments.

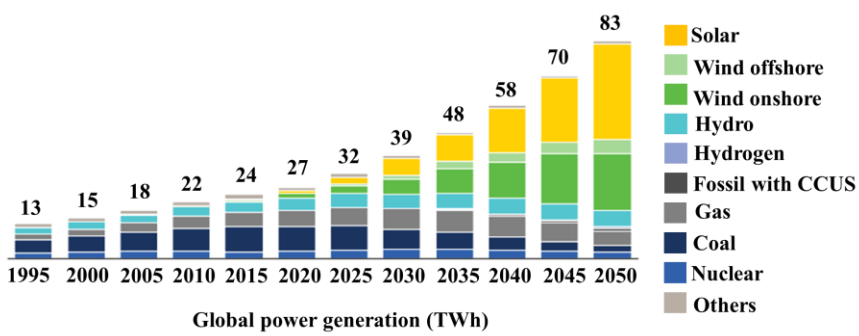

Figure 1 : Global energy perspective from McKinsey and Company in 2022.[1]

Anionic substitution is an effective strategy to tune the band gap, allowing the design of promising photocatalysts under visible light with appropriate electronic structures.[2] Single anion materials, (e.g. oxides) are widely used, whereas the exploration of mixed anions is promising but still developing (**Figure 2**). For example, oxynitrides such as $LaTi(O,N)_3$ are active photocatalysts under solar irradiation.[3] However, oxychalcogenides appear to be a more promising family to explore due to the alternation of both ionic oxide layer and covalent chalcogenide layer, which

allow easier chemical substitution.[4] The presence of a chalcogenide offers narrow band gap suitable for photocatalysis under visible-light irradiation (e.g. $CuInS_2$[5]), but sulfides don't show the same stability as oxides: they suffer from self-oxidation of sulfur anions which competes with the oxidation reaction of water to produce O_2 resulting in non-stoichiometric water-splitting reactions. This effect may be overcome with oxysulfides because they are often more stable due to the presence of oxygen states in the valence band while they can exhibit suitable band gaps. This was highlighted for the oxysulfide $Y_2Ti_2O_5S_2$ photocatalyst with its outstanding stability and efficient production of stoichiometric hydrogen and oxygen.[6]

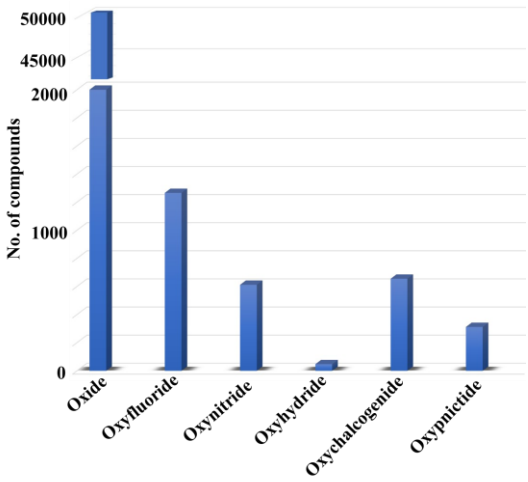

Figure 2 : Graph showing the number of studied single and mixed-anions compounds.[2]

Another crucial feature in designing photocatalysts is the dynamics of charge carriers. Introducing heteroleptic environments (i.e. coordination by different anions) around an active site, can give an acentric coordination environment and enhance polarity. The associated local field or built-in electrical field if the global structure crystallizes in a polar space group could help minimizing the recombination of the separated charge carriers.[7] This strategy was highlighted by theoretical work on oxynitrides[8,9] and on oxysulfides.[9,10]

With these considerations, numerous oxysulfides are potential candidates for photocatalysis: several have strongly polar structures and suitable electronic structures (band gap sizes and band edge positions) but minimal systematic studies on their photocatalytic properties has been carried

out. Thus, by combining both experimental and computational study, we will explore the photocatalytic properties of several oxychalcogenides with the aims of understanding:

i. The effects of the cation's choice and the anion coordination environment (e.g. *Q*:O ratio) on the photocatalytic properties in terms of the band gap size and the band edge positions

ii. The influence of the connectivity of the active units MQ_n (*M* = photoactive cation; *Q* = O, S, Se anion) on the properties

iii. The impact of the polarity on the electronic and photocatalytic properties (e.g. the presence of a polar unit *vs.* polar structure)

Therefore, after picking out known transition metal and p-block oxychalcogenides in terms of band gap size and predicting their band edge positions[11,12], we proceeded to the synthesis of the promising candidates and assessing their photocatalytic activity by photocurrent and photocatalytic experiments, band gap measurements; and carrying out electronic structure calculations to give insight into structure-composition-properties relationship.

This thesis work was developped within the MISSP (Inorganic Materials, Structures, Systems and Properties) group of the Solid-State Chemistry department of the UCCS laboratory in Lille, France; and the MEE (Materials for Energy and Electronics) group, of the school of Physical sciences in Kent University, United Kingdom. The focus of the MISSP group is to develop new inorganic compounds for various applications including for energy, in particular new phases with remarkable magnetic, optical and conduction properties and the understanding of their structure-properties relationship using both experimental and computational methods. The MEE group deals with the synthesis of new materials, the investigation of their physical properties and understanding of their atomic, magnetic and electronic structures.

Numerous systems were investigated during this thesis work, where they differentiate with their composition, structural types and properties. Some important features were unlocked, which can be used for the development of a promising strategy to design new functional visible light driven photocatalysts in the future. Therefore, this thesis consists of five chapters:

To start, **Chapter 1** is a bibliographic review to introduce some oxychalcogenide materials for photocatalytic water splitting. Generalities on photocatalysis reaction, specifically solar water-splitting and its requirements are presented. The context of mixed anion is introduced, in particular

oxychalcogenides, which is the family of material investigated during this work. Likewise, we will present some reported oxysulfides photocatalysts for water splitting and develop our design strategy for this thesis work.

In **Chapter 2**, the various experimental and computational techniques used during these three years are described. In the first part, the standard characterization techniques are briefly presented, with a focus on the photoconduction measurements. For the photodegradation measurements, the protocol and the Langmuir Hinshelwood model are discussed. In the second part, the basis of density functional theory (DFT) is discussed, with an emphasis on some of the important analysis tools used for the electronic structure, *i.e.* the charge carriers effective mass calculation, the electron localization function (ELF) and the COHPs.

Chapter 3 is allocated to study the photocurrent responses and electronic properties in layered iron based oxychalcogenides. The structure-properties relationship of Ca-Fe-O-*Q* and La-Fe-O-*Q* (*Q* = S, Se) systems are investigated. Using both experiences and DFT computed electronic structure, including charge carrier's effective masses, the role of transition metals and of the connectivity is explored.

We dedicated **Chapter 4** to study a different system that was reported with a high electrical polarization and high SHG response. The basis of the study is to investigate the origin of the polarity in this material and its effect on the photocurrent response and photocatalytic behaviour and their link with the calculated charge carriers' transport properties. Its complex structure and the presence of a lone pair cation were two essential aspects we focused on.

Finally, the Sr-Sb-O-*Q* (*Q* = S, Se) oxychalcogenides are discussed in **Chapter 5**. By combining both experimental and computational approaches, some key characteristics in the reported oxyselenide $Sr_2Sb_2O_2Se_3$ and the newly discovered $Sr_2Sb_2O_2S_3$ oxysulfide are unlocked which allowed the understanding of their activity in photodegradation under solar irradiation and the exceptionally low effective masses for both electrons and holes. Specifically, the role of the building blocks in these phases in lowering the effective masses is highlighted.

REFERENCES

(1) McKinsey & Company. Global Energy Perspective 2022. https://www.mckinsey.com/~/media/McKinsey/Industries/Oil%20and%20Gas/Our%20Insights/Global%20Energy%20Perspective%202022/Global-Energy-Perspective-2022-Executive-Summary.pdf.

(2) Kageyama, H.; Hayashi, K.; Maeda, K.; Attfield, J. P.; Hiroi, Z.; Rondinelli, J. M.; Poeppelmeier, K. R. Expanding Frontiers in Materials Chemistry and Physics with Multiple Anions. *Nature communications* **2018**, *9* (1), 1–15.

(3) Aguiar, R.; Kalytta, A.; Reller, A.; Weidenkaff, A.; Ebbinghaus, S. G. Photocatalytic Decomposition of Acetone Using LaTi (O, N) 3 Nanoparticles under Visible Light Irradiation. *Journal of Materials Chemistry* **2008**, *18* (36), 4260–4265.

(4) Clarke, S. J.; Adamson, P.; Herkelrath, S. J.; Rutt, O. J.; Parker, D. R.; Pitcher, M. J.; Smura, C. F. Structures, Physical Properties, and Chemistry of Layered Oxychalcogenides and Oxypnictides. *Inorganic chemistry* **2008**, *47* (19), 8473–8486.

(5) Liu, Z.; Lu, X.; Chen, D. Photoelectrochemical Water Splitting of CuInS2 Photocathode Collaborative Modified with Separated Catalysts Based on Efficient Photogenerated Electron–Hole Separation. *ACS Sustainable Chemistry & Engineering* **2018**, *6* (8), 10289–10294.

(6) Wang, Q.; Nakabayashi, M.; Hisatomi, T.; Sun, S.; Akiyama, S.; Wang, Z.; Pan, Z.; Xiao, X.; Watanabe, T.; Yamada, T. Oxysulfide Photocatalyst for Visible-Light-Driven Overall Water Splitting. *Nature materials* **2019**, *18* (8), 827–832.

(7) Vonrüti, N.; Aschauer, U. Band-Gap Engineering in AB (O x S 1− x) 3 Perovskite Oxysulfides: A Route to Strongly Polar Materials for Photocatalytic Water Splitting. *Journal of Materials Chemistry A* **2019**, *7* (26), 15741–15748.

(8) Vonrüti, N.; Aschauer, U. Epitaxial Strain Dependence of Band Gaps in Perovskite Oxynitrides Compared to Perovskite Oxides. *Physical review materials* **2018**, *2* (10), 105401.

(9) Almoussawi, B.; Huvé, M.; Dupray, V.; Clevers, S.; Duffort, V.; Mentré, O.; Roussel, P.; Arevalo-Lopez, A. M.; Kabbour, H. Oxysulfide Ba5 (VO2S2) 2 (S2) 2 Combining Disulfide Channels and Mixed-Anion Tetrahedra and Its Third-Harmonic-Generation Properties. *Inorganic Chemistry* **2020**, *59* (9), 5907–5917.

(10) Park, H.; Alharbi, F. H.; Sanvito, S.; Tabet, N.; El-Mellouhi, F. Supporting Information for: Searching for Photoactive Polymorphs of CsNbQ 3 (Q= O, S, Se, Te) with Enhanced Optical Properties and Intrinsic Thermodynamic Stabilities.

(11) Butler, M.; Ginley, D. Prediction of Flatband Potentials at Semiconductor-electrolyte Interfaces from Atomic Electronegativities. *Journal of the Electrochemical Society* **1978**, *125* (2), 228.

(12) Xu, Y.; Schoonen, M. A. The Absolute Energy Positions of Conduction and Valence Bands of Selected Semiconducting Minerals. *American mineralogist* **2000**, *85* (3–4), 543–556.

Chapter 1

Introduction to Oxychalcogenide materials for photocatalytic water splitting

Chapter 1: Introduction to oxychalcogenide materials for photocatalytic water splitting

1.1. Introduction

This chapter is a bibliographic review and it will be divided into three distinct parts. The first section focuses mainly on the photocatalysis and solar water splitting process, and some materials well-known for their photocatalytic activity. The second part of this chapter introduces mixed-anion materials, in particular, oxychalcogenides which are the focus of this thesis. The final section builds on these ideas by presenting possible design strategies for oxychalcogenide photocatalysts which are explored in this thesis.

1.2. Generalities on photocatalytic water splitting

1.2.1. Introduction to photocatalysis

Solar energy, the most abundant energy source[1,2,3,4] can be converted into chemical energy, for instance in the case of water-splitting photocatalysis[5,6] or photoelectrochemistry[7]; and into electrical energy by means of photovoltaics. Photocatalysis has been developping for a long time, first in plants and later with oxides like ZnO that introduced the concept of photo-reduction.[8] The observation that TiO_2 could catalyse the decomposition of organic materials (under UV light),[9] and then catalyse water splitting to give O_2 and H_2[10] has motivated research into new and efficient photocatalysts.[11,12,13] A schematic illustration of the photocatalytic reaction process indicating factors that may affect the photocatalytic activity is presented in **Figure 1.1**.

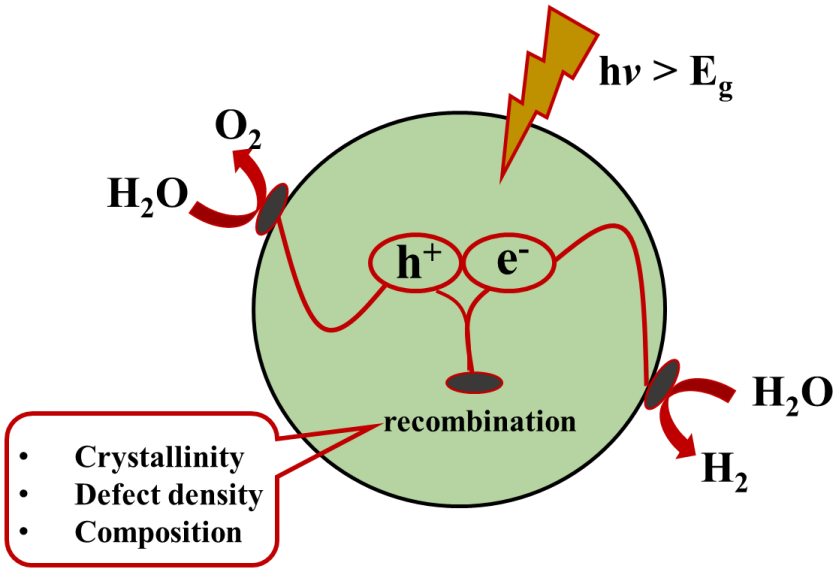

Figure 1.1 : Schematic illustration of the entire photocatalytic reaction process, indicating factors that may affect photocatalytic activity.[14]

For photocatalysis, first the semiconductor has to be irradiated by an incident light of energy greater than or equal to the band gap energy of the material. The absorption of photons will cause the excitation of electrons (e^-) from the valence band (VB) to the conduction band (CB) leaving then a positive hole (h^+) in the valence band. The e^-/h^+ pairs will separate and migrate to the reaction sites on the surface of the material or recombine. In an ideal photocatalytic reaction, after the adsorption of the phase to be catalyzed and the migration of the electron-hole pairs to the reaction sites, a transfer of electrons and holes will occur towards an oxidizing or reducing agent, respectively.

In addition to the desired photocatalytic redox reactions, the e^-/h^+ pairs could recombine a short time after their separation which is detrimental to the photocatalytic activity.[15,16] This recombination can result from various features, especially:

- Defects that can adsorb electrons and holes
- Low crystallinity: charge transfers (conduction) within the materials is more limited in lower crystallinity material.

1.2.2. Concept and requirements of water splitting photocatalysis

It is important to develop new and more sustainable strategies that can anticipate the future energetical transition and maintain the technological progress. In this context, fuel cells are one such example, as they use renewable sources (oxygen and hydrogen) to give electrical energy.[17] Since oxygen is readily available, the challenge is to produce the required hydrogen. To this purpose, solar photocatalytic water splitting is very attractive due to its simplicity: using only sunlight and water, the photocatalyst can efficiently produce renewable hydrogen. **Figure 1.2** illustrates the process of the water splitting reaction in a typical semiconductor material on the conduction and the valence band level, with a suitable band gap for the solar spectrum.[18,16]

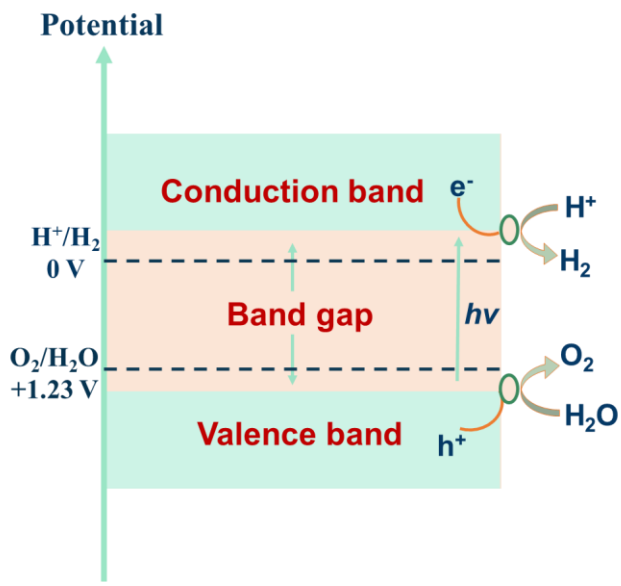

Figure 1.2 : Concept of water-splitting in a semiconductor photocatalyst.

Carrying out solar photocatalytic water splitting imposes constraints on the semiconductor, such as the magnitude of the band gap (between 1.23 and 3.10 eV, where 1.23 eV is the theoretical minimum band gap and 3.10 eV corresponds to the wavelength of the visible light ranging from 400 nm to 700 nm). Secondly, the conduction band potential must be more negative than the reduction potential of H_2O/H_2 (0V) and the valence band potential must be more positive potential than the oxidation potential of O_2/H_2O (1.23V)[19], in a way to satisfy relations (1) and (2):

$$\text{Oxidation: } H_2O + 2h^+ \rightarrow 2H^+ + \frac{1}{2}O_2 \quad (1)$$

$$\text{Reduction: } 2H^+ + 2e^- \rightarrow H_2 \quad (2)$$

Therefore, after identifying compounds with suitable optical band gaps for the solar spectrum, the band edge positions can be estimated using the empirical method based on the Mulliken electronegativities proposed by Butler and Ginley[20] and was further described by Xu and Schoonen;[21] which is explained thoroughly in **Chapter 2**, **Section 2.1.2.4**. An example of the simplicity of this method is shown by Castelli *et al.*[22] (**Figure 1.3**); it compares the band edge positions for a series of oxides, oxynitrides and oxyfluorides materials, showing the potential of mixed anion materials for photocatalysts.

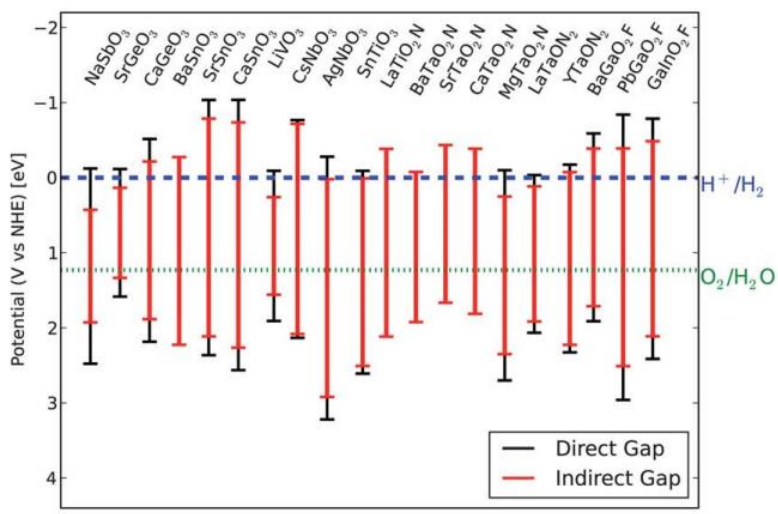

Figure 1.3 : Band gap energies and band edges positions of various semiconductor photocatalysts. Taken from ref.[22]

1.3. Generalities on photoconduction

Photoconduction, defined as the movement of electrons and holes in the conduction and valence bands, respectively, is important for the photocatalytic process. As such, photoconduction measurements can give important insights into materials e.g. the semiconductor type, charge carriers' behaviour, absorption range. It is one form of solar - chemical energy conversion and it was first reported in the 80's for $Ln_2Ti_2O_7$ pyrochlore and $Ln_{2/3}TiO_3$ perovskite (*Ln* = La, Pr, Nd).[23]

The electronic band structure of semiconductors is defined by valence and conduction bands separated by a band gap (E_{gap}); with the Fermi level energy (E_F) representing the highest energy level that an electron can occupy.[24] In the case of an intrinsic semiconductor, the Fermi level is situated in the middle of the gap; whilst in the case of a n-type or p-type semiconductor, the Fermi level is near the conduction band minimum or valence band maximum, respectively.[25] In this context, in order to observe a photoconduction mechanism for a semiconductor, we should submit the material to an incident energy equal or higher than its band gap energy, this is called photoexcitation and it allows the excitation of the charge carriers, i.e. the transfer of an electron from the valence to the conduction band.

During photocurrent measurements, the semiconductor is in contact with an electrolyte of choice and two electrodes (reference and auxiliary), the electrochemical device is then submitted to different ignition and extinction cycles (see **Chapter 2**, **Section 2.1.3**). When a semiconductor is in contact with an electrolyte, an electrochemical potential is generated at the interface and the valence/conduction bands of the semiconductor bend (i.e. the fermi levels of both the electrolyte and the semiconductor are not aligned). Having this shift in the bands will cause the transfer of the charge carriers towards the interface.[26,27] Depending on the flat band potential V_{fb} position (i.e. the potential at which there is no depletion layer and the VB/CB bands are at an equilibrium state), in relation to the applied potential (V_{bias}), the semiconduction type can be determined.[28]

Throughout the dark cycle, for a n-type semiconductor, electrons dominate and a cathodic current is favoured; whilst for a p-type semiconductor, holes are the majority and an anodic current is observed.[29] The redox reactions at the interface are described using the Butler and Volmer model[30] in which the intensity depends only on the charge transfer within the semiconductor (and not the charge transfer towards the interface) and is defined as follow:

$$i = i_0(e^{\frac{\alpha nF\eta}{RT}} - e^{\frac{\beta nF\eta}{RT}}) \qquad (1.1)$$

where i_0 is the exchange current, α and β are the anodic and cathodic transfer coefficients, respectively, F is the Faraday constant (F = 96485 C.mol^{-1}), n is the number of exchanged electrons, R is the gas constant (R = 8.31 J.K^{-1}.mol^{-1}), T is the temperature (Kelvin), η is the overvoltage which is the difference between the equilibrium potential (E_{eq}) and the applied potential (E).

Upon illumination, charge carriers are excited and electron-hole pairs are created (**Figure 1.4**). When applying a bias voltage these pairs will separate in a way that the majority is transfered inside the semiconductor and the minority of the charge carriers move to the interface (depending on the semiconduction type) generating a photocurrent:

- n-type semiconductor: holes are directed towards the interface and electrons towards the semiconductor core (anodic photocurrent).
- p-type semiconductor: electrons are directed towards the interface and holes towards the semiconductor core (cathodic photocurrent).

In this case, by adding the generated photocurrent term, equation (1.1) is now transformed to this relation[31]:

$$i = i_0 \left(e^{\frac{\alpha n F \eta}{RT}} - e^{\frac{\beta n F \eta}{RT}} \right) + i_{ph} \qquad (1.2)$$

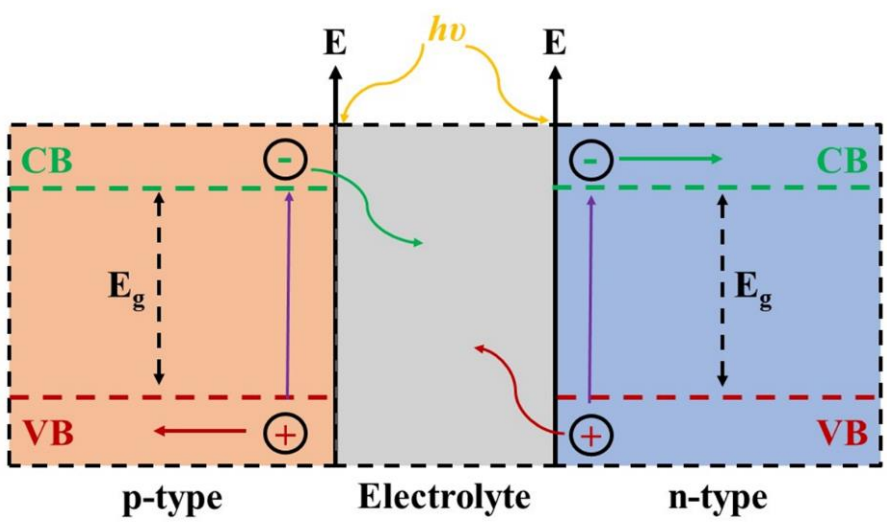

Figure 1.4 : Principal of the photocurrent generation in n-type and p-type semiconductors.

1.4. Generalities on single-anion photocatalysts

A number of oxides and sulfides are efficient photocatalysts for water splitting reactions under solar or UV irradiation. Several recent reviews give an overview on the history and recent developments of these materials.[16,32]

Many oxide photocatalysts are stable and have relatively easy synthetic routes (solid-state reactions), but unfortunately they typically have band gaps too large for excitation by the visible part of the electromagnetic spectrum, such that they are only photocatalytically active for half reactions in the visible region.[33,34,35] TiO_2 (**Figure 1.5a**), an n-type semiconductor (E_g ~ 3.2 eV),[36] was the first to show capacity to degradate organic dyes when illuminated by UV light during the 50s,[37] water photolysis later on in the early 70s,[38] and water vapor split in the 80s.[39] $SrTiO_3$ (**Figure 1.5b**) is another widely used oxide photocatalyst (E_g ~ 3.2 eV), that demonstrated its efficiency for water splitting in 1980 when loaded with NiO on its surface and irradiated; the catalyst succeeded in photochemically decomposing water vapor into hydrogen and oxygen.[40,41] It was found that coating the cocatalyst/catalyst, with NaOH for example, is beneficial in the case of these oxides and favours the stochiometric evolution of H_2 and/or O_2;[42] due to the effect of NaOH in suppressing $H_2 – O_2$ recombination (reverse reaction) on Pt and to hold water molecules near the catalyst surface.[32]

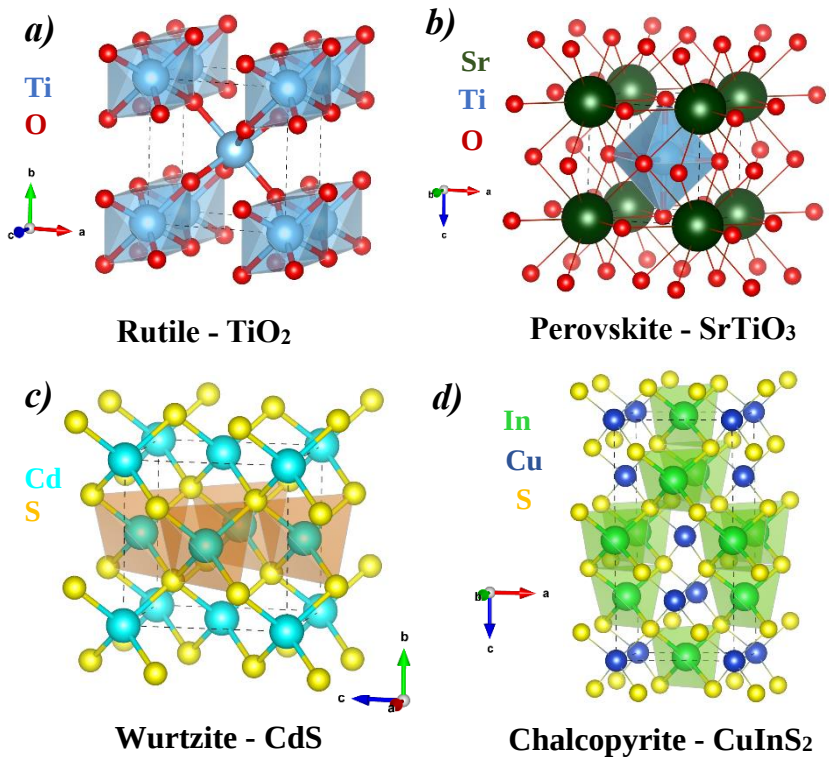

Figure 1.5 : Structural presentation of (a) TiO_2, (b) $SrTiO_3$, (c) CdS and (d) $CuInS_2$.

Alternately, sulfides have sufficiently small band gaps to allow absorption in the visible range, resulting in appropriate conduction and valence band edge positions with respect to the redox potential of water, making them potential photocatalysts for solar water splitting. For instance, CdS (E_g ~ 2.4 eV) (**Figure 1.5c**) can photocatalytically oxidize methanol, formaldehyde, and formic acid when platinized.[43] CdS can also produce hydrogen with the sacrificial oxidation of EDTA and cystein[44]or ethanol.[45] It has also been used for hydrogen production from an aqueous solution of sulfite.[46,47] The ternary metal sulfide $CuInS_2$ (E_g ~ 1.5 eV) (**Figure 1.5d**), has been widely explored as a photocatalyst for efficient hydrogen evolution.[48] $CuInS_2$-based photocatalysts exhibit large absorption coefficient (approximately 10^5 cm^{-1}) and good band alignment.[49,50,51] But these chalcogenides do not always show the same stability as oxides in the water oxidation reaction to form O_2 because the S^{2-} anions are more susceptible to oxidation than water and thus they may suffer from sulfur self-oxidation and degradation.[52,53] As a result, research has turned towards mixed-anion materials in the search for stable and efficient visible light photocatalysts.[54,55]

1.5. Generalities on mixed-anion compounds

A mixed-anion compound is a material containing more than one anion in a single phase such as oxychalcogenides and oxypnictides,[56] oxyhydrides[57] and oxyhalides.[58] The coexistence of more than one anion type in the material is a promising strategy to control various properties, giving them a range of applications (photocatalysis[59,60,61,62] superconductivity,[63,64,65] magnetism,[66,67,68] non-linear optical (NLO),[69] battery material,[70] thermoelectricity[71] and photoluminescence[72]).

Kageyama et *al.*[73] reviewed the huge progress and achievements in mixed-anion materials, which unbolted some important factors in designing new materials. The different anionic characteristics, such as charge, ionic radii, electronegativity and bonding character, result in anions ordering/disordering; giving access to new structural types (**Figure 1.6**).[74] For example, oxynitrides often exhibit correlated disorder instead of a long-range one;[75] oxyarsenides show a long-range order of O^{2-} and Ar^{3-} anions (e.g. iron-based superconductors with insulating oxide layers and more delocalized (even superconducting) iron arsenide layers).[76,77]

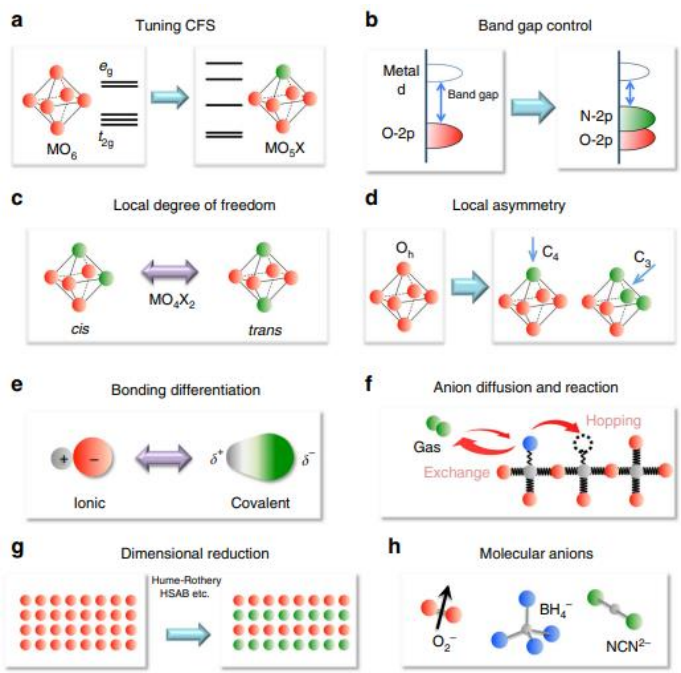

Figure 1.6 : What mixed-anion compounds can do. Taken from ref.[73]

Among mixed-anion materials, layered oxychalcogenides are a promising family that gained a lot more attention recently. Oxychalcogenides contain an oxide as well as a chalcogenide (sulfide/selenide/telluride) anion. These materials adopt a diversity of structure types and show a range of properties related to the ordering of the small oxide and the larger chalcogenide, likely due to their different sizes and bonding characters.[78] **Figure 1.7** shows a typical layered structure of LaCuOS[79] where we can distinguish the ionic $(La_2O_2)^{2+}$ layer and the covalent $(Cu_2S_2)^{2-}$ layer.

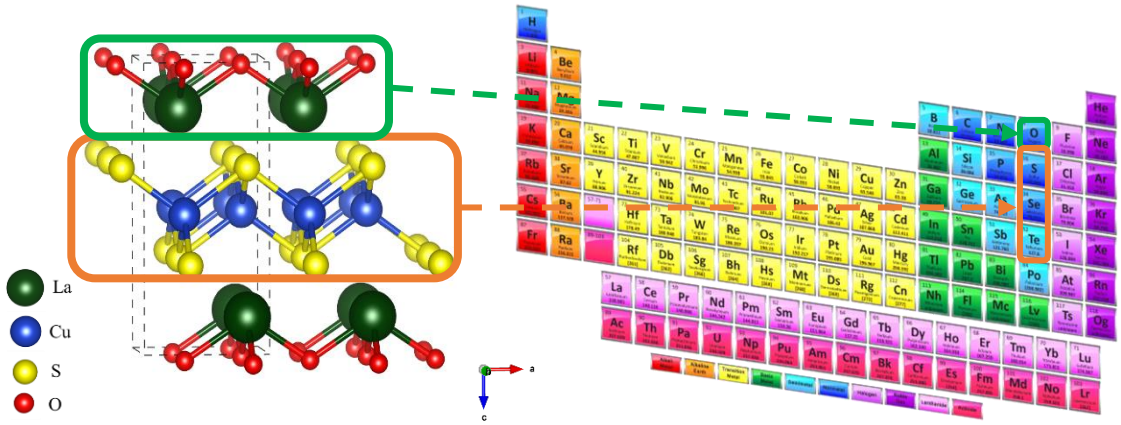

Figure 1.7 : Crystal structures of typical layered oxychalcogenides LaCuOS.

1.5.1. Structures of oxychalcogenide materials

Oxychalcogenides, with the presence of larger and softer chalcogenide anion, tend to stabilize lower transition metal oxidation states and lower coordination numbers, compared with oxides. As mentioned before, this family of materials present different structural types, but they often express layered structures due to a certain anion order that can lead to their segregation into different layers.[56]

This layered arrangement of anions can depend on the relative electronegativities of the accompanying cations.[80] For instance, in the case of a big difference in hardness/softness of cations, stronger bonds can be formed with either hard oxide or soft chalcogenide anions and so layered structures with a greater proportion of homoleptic (single anion) coordinations are favoured[81]; whilst in the case of a less difference, heteroleptic coordinations (mixed anion) can be more likely promoted.[82]

These oxychalcogenides present some common structural features such as the building blocks that they contain (**Figure 1.8**). For example, OLn_4 units in fluorite-like sheets, ribbons or chains (consisting of edge-linked units);[83,84] MQ_4 tetrahedra edge-linked into chains or antifluorite-like sheets[85] or square-based pyramid MQ_5 or MOQ_4 units for Bi, Sb with their $6s^2$ or $5s^2$ inert pairs.[86]

Having this layered aspect in most oxychalcogenides can give rise to a wide range of promising properties, due to the easy chemical substitutions that can be done in both layers; such as highly anisotropic electronic structure and properties and high mobility semiconduction favoured by the covalent aspect of the chalcogenide.[87] For example, layered LaOCuS[79] and BiCuOSe[88] are known as important thermoelectrics, due to the presence of the insulating oxide layers and the semiconducting copper chalcogenide layers. As another example, $Ln_2O_2M_2OQ_2$, with M cations coordinated by both O^{2-} and Q^{2-} anions with long-range magnetic order, but electronically quite separated by the insulating $[La_2O_2]^{2+}$ layers.[89,90] These oxychalcogenide materials are used in numerous other applications such as magnetism;[91,92,93] thermoelectricity;[94,95] IR-nonlinear optical materials;[96,97,98,99,100] second harmonic generation (SHG);[101,102,103] semiconductivity;[104,105,106] photocatalysis[107] and piezoelectricity.[108]

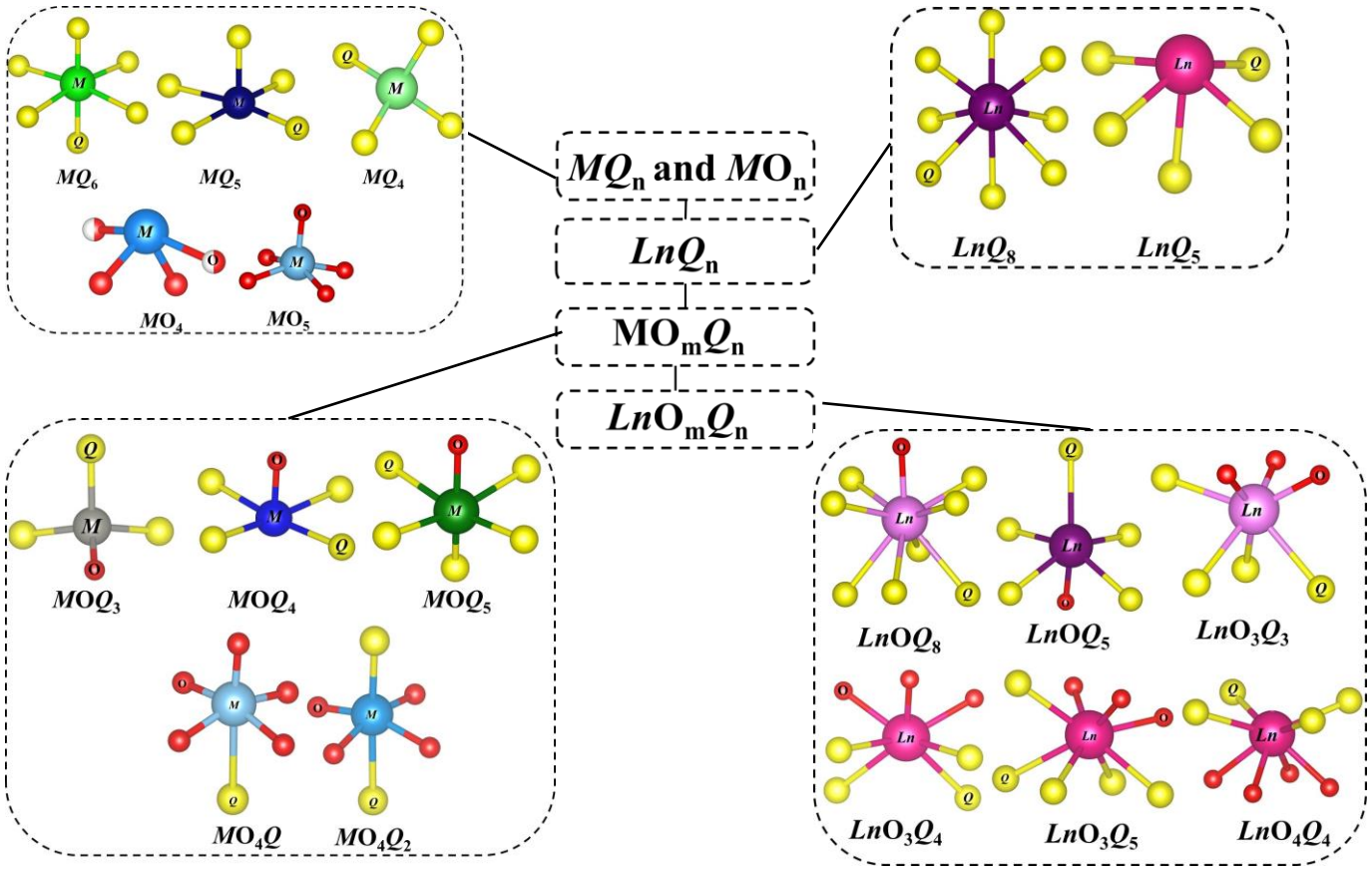

Figure 1.8 : Schematic summarizing some coordination environments in oxychalcogenides.

1.5.2. Key features of oxychalcogenides for photocatalysis

1.5.2.1. Optimized band gap

Mixed-anion materials allow some tuning of the band gap by choice of anion, particularly relevant for solar photocatalysis. For example, introducing softer anions (chalcogenides) in an oxide sublattice to give mixed-anion oxychalcogenides (**Figure 1.9**) can introduce higher energy states at the top of the valence band, reducing the band gap. This strategy is effective to tune the band gap and meet the requirements of water splitting under visible light and give effective photocatalysis.[109,110] For example, antimony oxides such as α-Sb_2O_3 present large band gaps (3.38 eV),[111] whilst antimony chalcogenides such as Sb_2S_3 and Sb_2Se_3 present narrower band gaps (2.16 and 1.66 eV for S and Se, respectively).[112] Therefore, a mix of both oxide and chalcogenide can give a moderate band gap, suitable for the solar spectrum such as $Sr_6Cd_2Sb_6O_7S_{10}$ and $Sr_6Cd_2Sb_6O_7Se_{10}$ (1.89 and 1.55 eV for S and Se, respectively).[101,103]

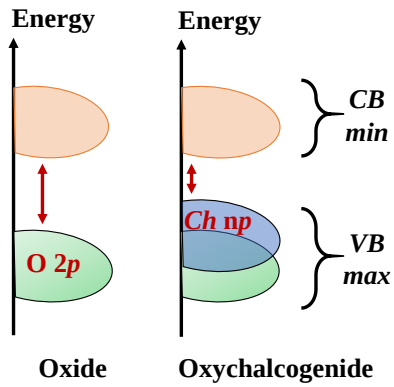

Figure 1.9 : Difference in the band gap energy and band edges positions between oxides and oxychalcogenides.

1.5.2.2. Cation choice

Cation choice for photocatalysts can be a key feature. Lone pair cations for example (Bi^{3+}, Sb^{3+}, Sn^{2+}) can induce oriented dipoles[113] which favour lower-symmetry coordination environments.[114] The relative energy of the ns^2 lone pair electrons to the anion *p* orbitals can determine the energy of states at the top of the valence band which are key to explaining the optical response of these materials.[115,116] This key feature was found to be effective in designing photocatalytic and photovoltaic materials.[117,118,119]

Metal cations in their oxidation states are not always compatible with the oxychalcogenide chemistry; for instance, it can be hard to get higher oxidation state cations because it'll likely reduce the metal to a lower oxidation state and partly oxidize the chalcogenide, not very effective for the photocatalytic activity. Then again, cations with the presence of slightly localized *nf* orbitals can increase the recombination rates[120] and cations with the presence of n*d* orbitals or highly hybridizing *ns* - *np* orbitals can increment the dispersion of the valence and conduction bands, respectively, very efficient for better charge carriers' transport properties.[121,122]

1.5.2.3. Connectivity

The impact of the structure dimensionality (1D *vs*. 2D *vs*. 3D) on the photocatalytic outcome is still under investigated. But it is certain that having a layered structure is advantageous, especially for the transport properties of the photoexcited charges. The connectivity of the different building

blocks within the structure can result in having different pathway for the electrons and the holes which can diminish their recombination during the photocatalytic reaction.

The presence of this feature in most oxychalcogenides promotes the fast mobility which favours the charge migration to the surface of the photocatalyst to participate in the reaction; whilst slow mobility is more prone to result in charge recombination. Consequently, having a large mobility difference could be useful for the separation of e^- and h^+, reduction of the recombination rate, and improvement of the photocatalytic activity.[123,124,125,126]

1.5.2.4. Stability

For successful photocatalytic applications, the materials' stability in water/aqueous solution needs to be adequate. As mentioned earlier, oxides have proven their good stability as photocatalysts; but on the other hand, chalcogenides haven't, where they can suffer from sulfur oxidation, in the case of sulfide for example. Oxychalcogenides offers a moderate stability (better than the sulfide/selenides), whereas the introduction of the O 2*p* ortbitals gives more stability to the system.[127]

1.5.2.5. Polarity

Polarity in heterogeneous photocatalysts was shown to enhance charge-carrier separation, resulting in superior efficiency for example for photocatalytic water splitting.[128] Having polar distortions can also increase the band gaps; although this increase is minimal in the case of oxides ($SrTiO_3$ for example[129]), it is much larger in the case of oxysulfides because of the lower electronegativity of the sulfide.[130]

This hypothesis was further investigated by Vonruti and Aschauer[131] using DFT to study the suitability of polar $AB(O_xS_{1-x})_3$ perovskites for photocatalytic water splitting. It was found that the presence of polar distortions, induced by epitaxial strain (for oxynitrides[132]) or substitution of sulfur by oxygen (for oxysulfides) can be a promising route to suppress the recombination phenomena of the charge carriers. This is due to the out-of-plane spontaneous polarization that has risen from the epitaxial strain on the anion order within the structure. Therefore, this can indeed be a promising route to adopt for increasing the band gap and design new materials with efficient photocatalytic properties.

1.5.2.6. Heteroleptic units

A heteroleptic unit is when the cation is coordinated by two types of anions, O^{2-} and S^{2-}/Se^{2-}. These are often polar, and materials with polar, heteroleptic coordination environments may exhibit enhanced electron-hole separation, crucial for an improved photocatalytic activity.[133]

1.5.3. Examples of photocatalytic oxychalcogenides

Little research has been done on oxychalcogenides in terms of water splitting photocatalysis. A survey of the literature helped gather different oxychalcogenides with their important characteristics (band gap, semiconduction type, cation choice, coordination environment, anion ratio and polarity); the band edge positions has also been estimated, which allowed the identification of some potential candidates for possible future characterizations (see **Appendix 1**). In the following section, the top materials with proved capacity to evolve H_2 and/or O_2 are discussed. Very few oxyselenides have been reported for this kind of measurements.

1.5.3.1. $Ln_2Ti_2S_2O_5$ (*Ln* = Y, Nd, Sm, Gd, Tb, Dy, Ho and Er) series

The series of $Ln_2Ti_2S_2O_5$ (*Ln* = Y, lanthanide) adopt a tetragonal Ruddlesden-Popper crystal structure.[134,135] It is built from double-layers of corner-linked TiO_5 square-based pyramids separated by $[Ln_2S_2]^{2+}$ rocksalt slabs (**Figure 1.10**); where this separation between the covalency of the sulfides and the ionicity of oxides resulted in an intermediate situation of strong interlayer connections. Optical band gaps of these phases were found to be matching the solar spectrum,[136] and under visible-light (λ = 440 - 650 nm) irradiation they demonstrated their capacity to evolve both O_2 and H_2 (**Appendix 1**, **Section 1.5**).[137] Studies on $Sm_2Ti_2S_2O_5$ highlights the importance of the pH and the surface modification on the photocatalytic activity;[138] and the influence of the synthetic route with lower temperatures and reduced heating time to increase the photocatalytic activity.[139] In addition, the n-type $Y_2Ti_2O_5S_2$ was the first to demonstrate a capacity to evolve both hydrogen and oxygen in a stoichiometric ratio, under visible irradiation.[140,141,142]

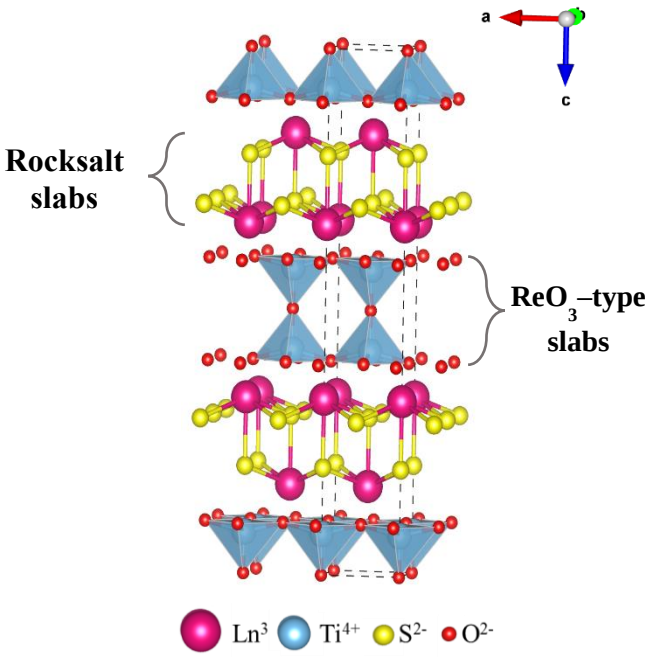

Figure 1.10 : Structural representation of the Ruddlesden-Popper structure of the $Ln_2Ti_2S_2O_5$ series of *I*4/*mmm* symmetry.

The fact of having suitable band gaps as well as layered structure definitely contributed to the good activity demonstrated by this series. Another common factor is the presence of Ti 3*d* orbitals in the CBM; whilst for the VBM the lanthanide based phases have partially filled, highly localized, *Ln* 4*f* orbitals which are less effective in photoconductivity or photocatalysis and are usually ignored.[138] $Y_2Ti_2O_5S_2$ had the extra contribution of the Y 3*d* orbitals to its VBM which could be an explanation for the interesting activity that this material showed. Finally some of these phases exhibited lower activities compared to other which could be related to the larger amounts of sulfur defects or the thermodynamically less favourable VB position.[137]

1.5.3.2. $SrZn_2S_2O$

The Zn-based oxysulfide $SrZn_2S_2O$ adopts a wurtzite-derived crystal structure consisting of double layers of corner-shared ZnS_3O tetrahedra separated by Sr^{2+} ions (**Figure 1.11**).[143,144] $SrZn_2S_2O$ is an n-type semiconductor with a 3.86 eV direct band gap; a CB composed of Zn 4*s* and 4*p* orbitals hybridizing with Sr 4*d* orbitals, and a VB mainly composed of O 2*p* and S 3*p* orbitals

hybridizing. $SrZn_2S_2O$ was capable on reducing and oxidizing water under UV-light irradiation, with a certain photocorrosive resistance.[145]

Compared to the $Ln_2Ti_2S_2O_5$ series discussed above, the O_2 rate is similar but the H_2 evolution is slightly higher for $SrZn_2S_2O$ (**Appendix 1**, **Section 1.5**). This indicates the advantage of having the Zn orbitals contributing to the CB compared to the Ti orbitals. $SrZn_2S_2O$ exhibit a 3D structure with the presence of heteroleptic coordination environment (ZnS_3O) unlike the layered $Ln_2Ti_2S_2O_5$, which could also have an impact on the transport properties of the charge carriers.

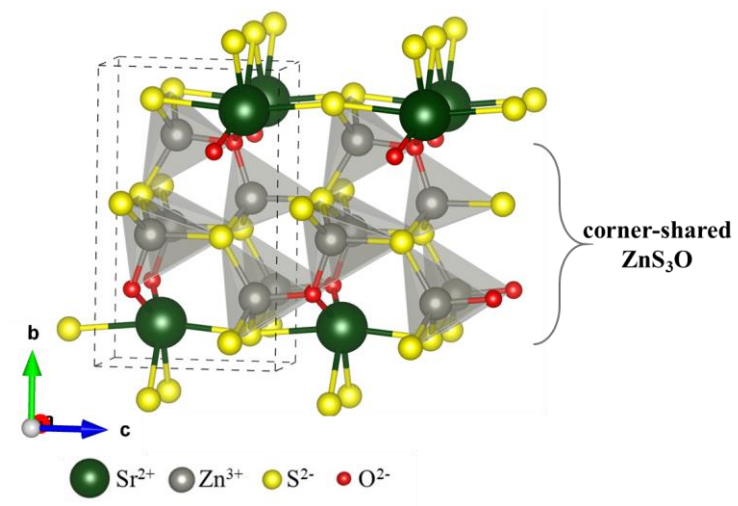

Figure 1.11 : Structural representation of $SrZn_2S_2O$ oxysulfide of $Pmn2_1$ symmetry.

1.5.3.3. *Ln*OInS$_2$ (*Ln* = La, Ce, Pr)

Yellow $LaOInS_2$ has a band gap of 2.73 eV and is a p-type semiconductor that adopts an orthorhombic structure.[146] Its crystal structure is composed of [InS_2] NaCl-type slabs made of InS_4 tetrahedra and InS_6, InS_5O octahedra and $[LaO]^+$ fluorite-type ribbons alternating in different directions (**Figure 1.12a**).[147] Under Xe lamp irradiation, the sample exhibited a reproducible photocatalytic activity, and showed H_2 evolution. On the other hand, using metathesis reaction, the metastable layered polymorph of $LaOInS_2$ (also predicted in ref 146), was synthesized. It has a direct band gap of ~2.64 eV, and it adopts a monoclinic structure consisting of alternately stacked [InS_2] layers (rock-salt type) composed of InS_6 octahedra and oxide $[LaO]^+$ layers (PbO-type), with a split in the In sites (**Figure 1.12b**). This polymorph was capable on evolving higher rates of H_2 and O_2 under visible light ($420 < \lambda < 800$ nm).[148]

Then again, $CeOInS_2$ and $PrOInS_2$ phases were found to be isostructural to the monoclinic layered $LaOInS_2$,[148] except that the indium in these phases is on-center unlike the one in $LaOInS_2$, which is off-center. They revealed direct band gaps of 2.41 and 2.43 eV, respectively. Compared to $LaOInS_2$, these phases demonstrated an H_2 evolution 10% less under visible light.[120]

The CBM in the La-based phases is mainly composed of In 5*s*/5*p* orbitals, whilst O 2*p* and S 3*p* contributes to the VBM. It looks as if the presence of the In element is beneficial and is contributing to the higher dispersion of the CBM, thus the capacity to evolve H_2. But the layered polymorph exhibited higher rates, probably related to the structure's connectivity (compared to the α- $LaOInS_2$) which can increase orbital overlap in the CB, beneficial for the reduction reaction.

As for $CeOInS_2$ and $PrOInS_2$ phases, the presence of the on-center indium decreased the hybridization of the In 5*p* – S 3*p* orbitals, which resulted in an increase in the energy difference of these hybridized orbitals; slightly shifting the optical absorption edge of these phases.[120] Even though the 4*f* orbitals of *Ln* are negligible when highly localized (**Section 1.5.3.1**), it seems that their presence can sometimes increase the electron–hole recombination rates.[149,150]

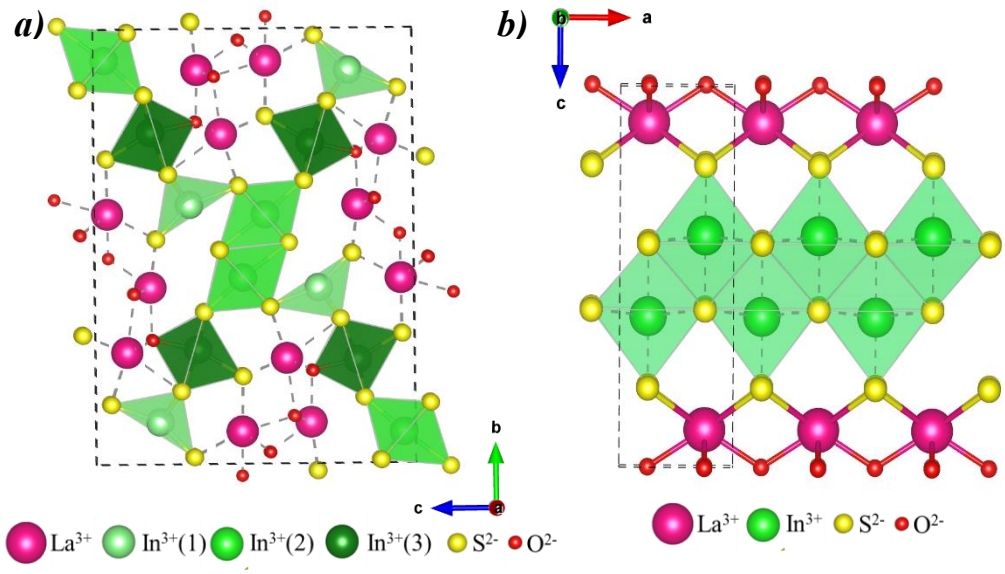

Figure 1.12 : Structural representation of $LaOInS_2$ material with (a) alpha model of *Pbcm* symmetry and (b) metastable layered model of $P2_1/m$ symmetry.

1.5.3.4. $La_5In_3S_9O_3$

The structure of $La_5In_3S_9O_3$ consists of fluorite-type ribbons of lanthanide ions alternating with rocksalt InS layers to form 2D $La_5In_3S_6O_3$ layers in a zigzag pattern (**Figure 1.13**).[146] In^{3+} cations are only coordinated by sulfur, while La^{3+} ions are coordinated by both oxide and sulfide ions (similar to other La-In based compounds[151]). The optical band gap of the yellow powder was 2.60 eV, slightly smaller than that of $LaInS_2O$ (2.73 eV), probably due to the increased sulfur coordination in $La_5In_3S_9O_3$ decreasing the band gap.[146] Even though a pure polycrystalline phase was not obtained for the p-type semiconductor $La_5In_3S_9O_3$, it was able to reduce and oxidize water under visible irradiation.[121] A stable H_2 evolution occurred, unlike the O_2 evolution where it decreased over time (deposition of metallic silver).

Similar to the *Ln*OInS$_2$ (*Ln* = La, Ce, Pr) series, the presence of the In 5*s*-5*p* orbitals are contributing to the higher H_2 efficiency.[138] This result can also be comparable to $SrZn_2S_2O$, with the presence of the Zn 4*s*-4*p* orbitals contributing to the enhanced H_2 evolution.

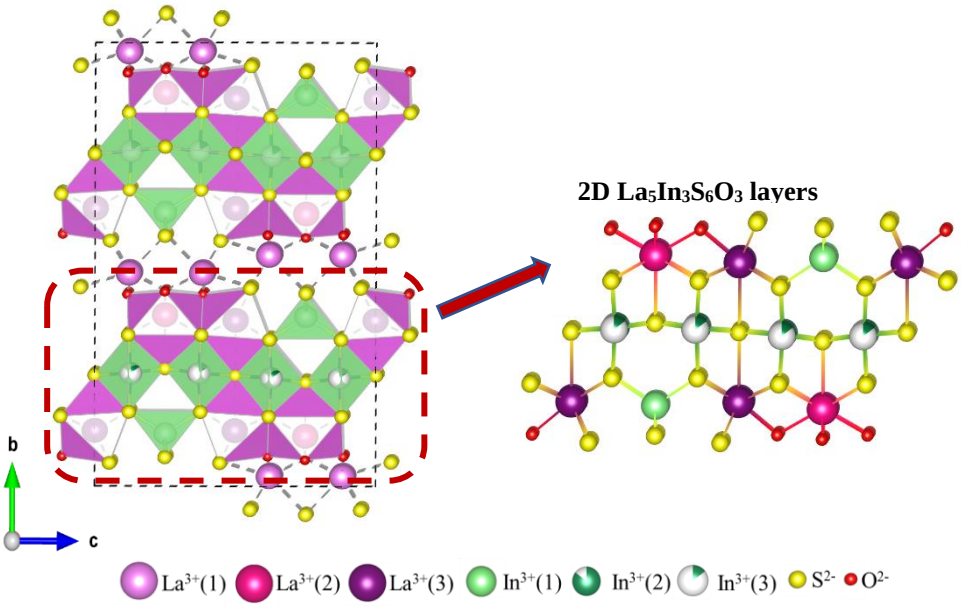

Figure 1.13 : Structural representation of $La_5In_3S_9O_3$ oxysulfide (*Pbcm* symmetry) with the 2D $La_5In_3S_6O_3$ layers consisting of two building blocks: rock-salt layers formed by both indium and lanthanum and fluorite-type ribbons formed by lanthanum atoms; alternating regularly along *b*.

1.5.3.5. La-Ga based oxysulfides ($LaGaS_2O$ and La_3GaS_5O)

$LaGaS_2O$ adopts an orthorhombic KVO3-type structure consisting of layers of corner-shared distorted GaO_2S_2 tetrahedra sharing oxygen with La^{3+} cations (**Figure 1.14a**).[152] La_3GaS_5O adopts an orthorhombic shear type structure consisting of corner-shared GaS_4 tetrahedra layers and a second layer of $(La_2O)_n$ formed by edge sharing LaS_2, LaS_2O and $LaSO_2$, both parallel to the *b* direction (**Figure 1.14b**).[153]

$LaGaS_2O$ demonstrated a n-type semiconduction with an indirect band gap of 3 eV whilst La_3GaS_5O exhibited a n-type semiconduction with a direct band gap of 2.3 eV. The CBM level is similar in both phases, whereas the VBM in La_3GaS_5O is higher than $LaGaS_2O$, due to the higher sulfur content. Both phases were found to be potential photocatalyst but only La_3GaS_5O was tested for water reduction and oxidation reactions under visible light, whilst $LaGaS_2O$ produced anodic photocurrent under ultraviolet light.[154] The comparison of these phases highlights the importance of the chalcogen ratio in narrowing the band gaps.

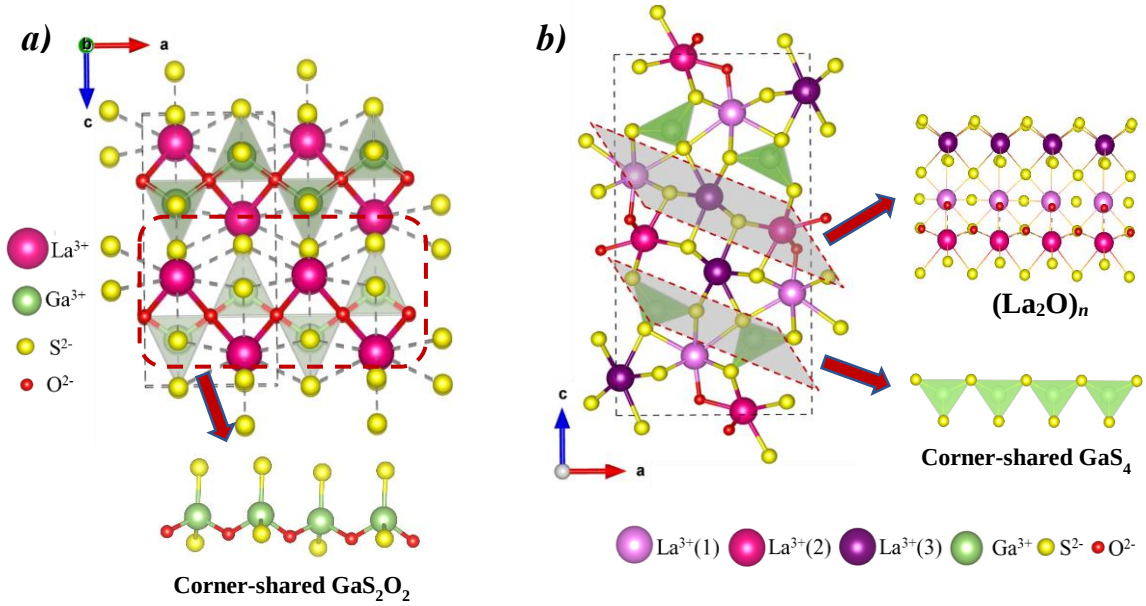

Figure 1.14 : Structural representation of (a) $LaGaS_2O$ (*Pmca* symmetry) and (b) La_3GaS_5O (*Pnma* symmetry), highlighting the different layers between the two compounds.

1.5.3.6. $La_5Ti_2MS_5O_7$ (*M* = Cu, Ag) systems

$La_5Ti_2MS_5O_7$ (*M* = Cu, Ag) oxysulfides adopt an orthorhombic structure that is not layered but rather present condensed fragments of layers that forms a building unit repeating periodically along the *b* direction (**Figure 1.15**). It consists of: i) rock-salt-type fragment containing CuS_4 tetrahedra, ii) perovskite building block made of double chains of corner-sharing Ti-centered octahedra (TiO_4S_2 or TiO_5S). The orange-yellow powder revealed an optical band gap of 2.02 and 2.17 eV for Cu and Ag, respectively.[155] Preliminary photoelectrochemical measurements revealed p-type semiconduction and a photocatalytic activity under visible light;[156] with higher rates occurring when loaded with convenient amount of cocatalysts.[157]

$La_5Ti_2CuS_5O_7$ photocathode was investigated further more trying different synthetic methods for the enhancement of its photocatalytic outcome.[158,159] The electronic band structures of these phases were found to be suitable for charge separation and revealed a CBM consisting of Ti 3*d* orbitals whilst the VBM was formed by hybridized Cu 3*d* and S 3*p* orbitals in $La_5Ti_2CuS_5O_7$, rather than just S 3*p* orbitals in $La_5Ti_2AgS_5O_7$, responsible for the longer absorption edge wavelength.[157] The study of these materials highlights the importance of having disassociated paths for accelerating the charge separation while inhibiting the recombination process.[160]

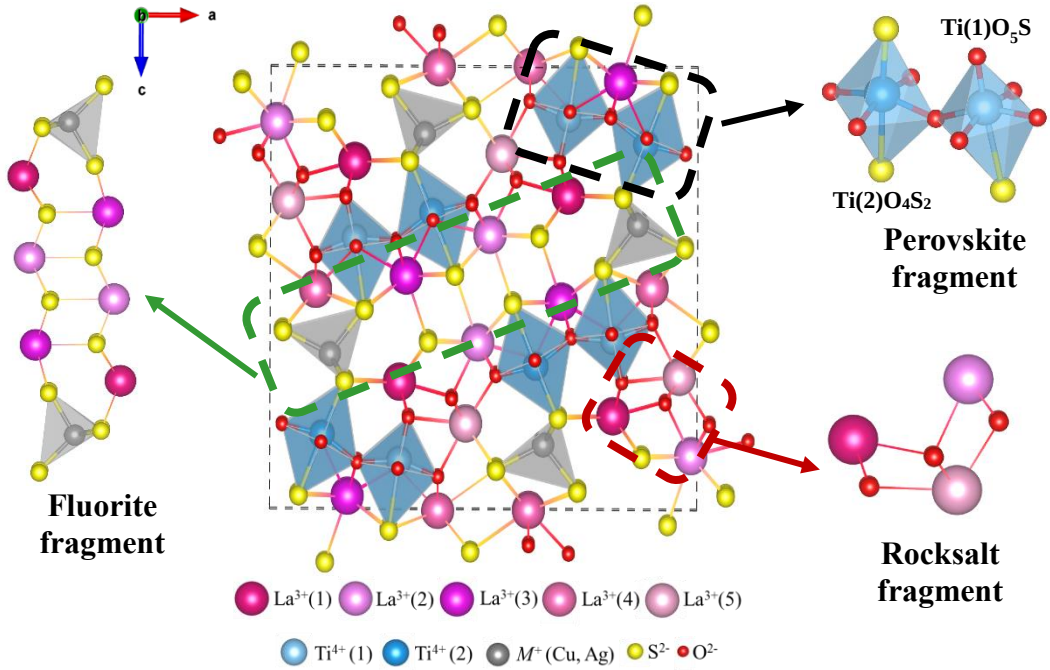

Figure 1.15 : Structural representation of (a) $La_5Ti_2MS_5O_7$, (*M* = Cu, Ag) oxysulfides (*Pnma* symmetry) highlighting the different building blocks within the structure.

Numerous factors can influence the outcome of the overall water splitting photocatalytic reaction: i) morphology and microstructure such as defects and crystallinity (intrinsic features) and ii) pH, temperature, concentration of the catalyst, type and amount of cocatalyst loading, incident light intensity (extrinsic features). But the focus of this survey is to compare the structural (connectivity, polarity) and electronic (band gap magnitude and nature, density of states, charge carriers behaviour) properties, which allowed us to take some key points contributing to the good activity of these materials (discussed in **Section 1.6**).

1.6. Design strategies for photocatalysts

Looking at the characteristics of these materials, we noticed that the nature of the band gap (direct or indirect), the semiconduction type (n or p-type) were not of great influence as both types were revealed and exhibited by the studied materials. Regarding the polarity, all the materials contained one or two cations with polar coordination environments; even when this aspect was not discussed in the reports of the materials discussed above, we think that it can be of importance and this will be the basis of our thesis work.

But on the other hand, we were able to pick few common structural features, some are regarding the composition, cation choice, different orbital contribution and structure connectivity, which can be of important influence on the photocatalytic activity. We therefore summarized these points as follow:

- Higher sulfur content can increase the VBM position, more suitable for the oxidation evolution but this can create larger amounts of defects within the structure which can be a disadvantageous for the photocatalytic activity result (i.e. $LaInOS_2$ *vs*. $La_5In_3S_9O_3$).
- The charge carriers' behaviour is a very important factor and having a structure that enables disassociated paths for the photoexcited electrons and holes enhances their separation and decreases the rate of their recombination (i.e. $La_5Ti_2MS_5O_7$).
- The size of the *Ln* cations doesn't seem to impact the band gaps but the presence of a cation with highly localized 4*f* orbitals, such as Sm, are less effective in photocatalysis and their contribution is usually ignored. Whilst the cations with less localized 4*f* orbitals, such as Ce

or Pr, can potentially increase the recombination rate of the photoexcited charges therefore decrease the photocatalytic activity (i.e. $Sm_2Ti_2S_2O_5$ *vs*. Ce/$PrInOS_2$).

- Highly dispersed conduction and valence bands is definitely an asset for a better H_2 and O_2 evolution, respectively. Such as the presence of *ns-np* orbitals (for example, In or Zn cations) highly hybridizing in the CBM, or the additional presence of 3*d* orbitals (for example Y or Cu cations) strongly hybridizing with the S 3*p* and O 2*p* orbitals in the VBM (i.e. $La_5In_3S_9O_3$, $SrZn_2S_2O$ $La_5Ti_2CuS_5O_7$ and $Y_2Ti_2O_5S_2$).
- An increase in the energy difference of the corresponding orbitals can decrease their hybridization which can also be an origin of witnessing a decrease in the photocatalytic activity. For once this can be attributed to a structural factor, such as the cation displacement (on or off center) (i.e. layered-$LaInOS_2$ *vs*. Ce/$PrInOS_2$).

Having surveyed the literature on oxysulfide photocatalysts, it's clear that numerous factors can influence the photocatalytic behaviour. Firstly, the band gaps of oxysulfides can be tuned to match the solar spectrum. The structure and its connectivity are important for the transport properties of the photoexcited charges. The band structure gives insight to the electronic properties of the material, in particular the effective masses of the charge carriers which describes their mobilities; where higher bands dispersity around Fermi level (E_F) are favoured, resulting in low effective masses, and hence, high mobility carriers, therefore enhanced transfer process.

Cation choice is another important feature, regarding the contributions of their corresponding orbitals to the band edges; this can tune the band gap as well as the charge carriers' transport properties. Lastly, the polarity, is not widely studied as a design feature in photocatalysis, but it could enhance a catalyst's performance by improving charge carrier separation, as seen in ferroelectrics such as $AB(O_xS_{1-x})_3$.[131] A schematic diagram of a potential design strategy for efficient oxychalcogenide materials is presented in **Figure 1.16**.

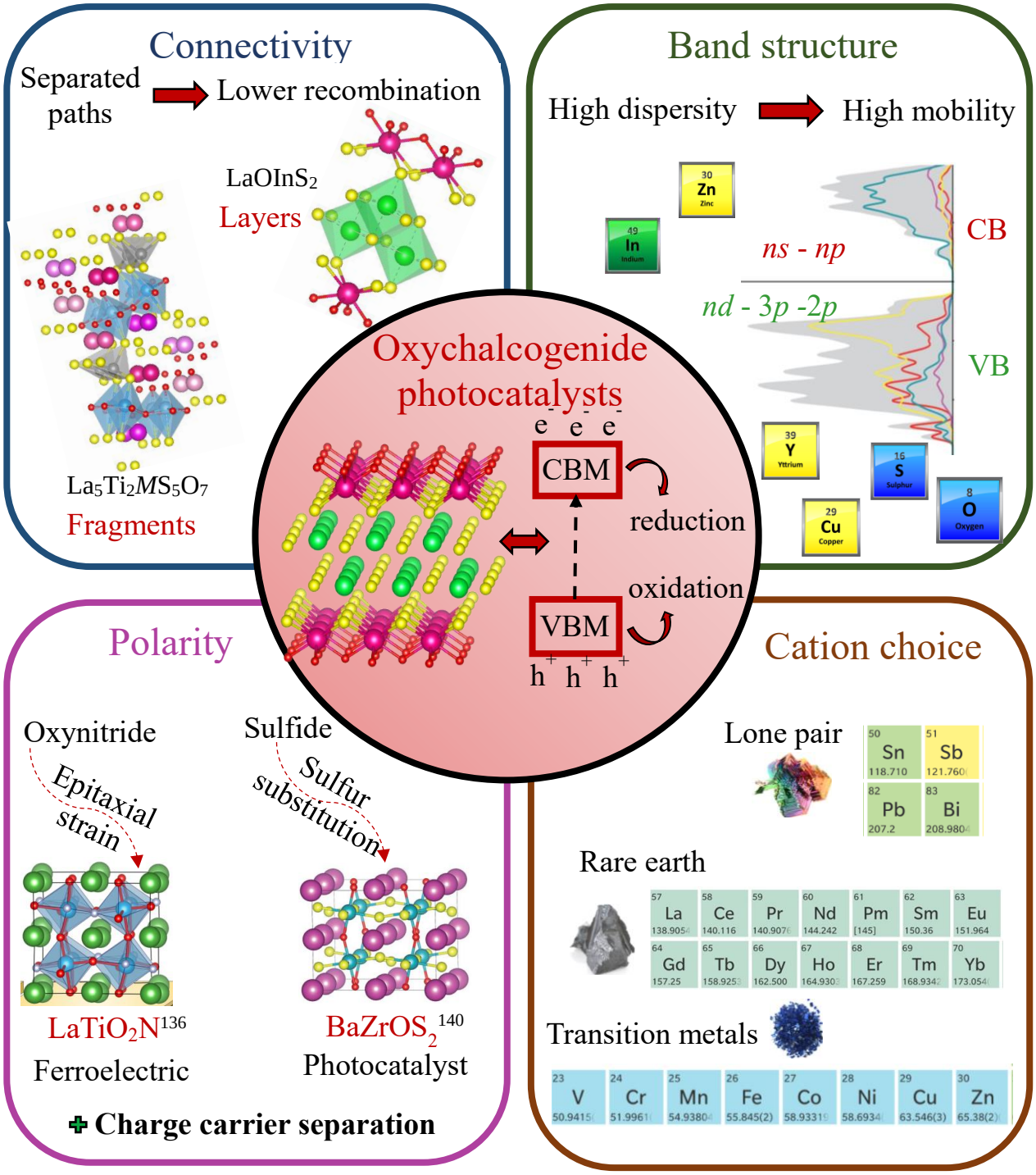

Figure 1.16 : Schematic diagram of a potential design strategy for oxysulfide photocatalysts.

1.7. Aims and Objectives

Having discussed some key points for the design of efficient oxychalcogenide materials for water splitting photocatalysis, the focus of this thesis will be to investigate the following aspects:

- Optimization of the band gaps to match the solar spectrum, by studying the impact of the chalcogenide choice (sulfide *vs.* selenide).
- Structural features (connectivity and dimensionality) and their impact on the transport phenomena (promoting e^-/h^+ separation and repressing their recombination).
- Polarity, specifically whether having polar units or a polar structure is more important for enhancing the charge carriers' transfer properties.
- Cation choice (transition metals, lone pairs cations) and its effect on the band gaps (orbital contribution to the band edges) and promoting some interesting structural features beneficial for the photocatalytic activity.

REFERENCES

(1) Nzihou, A.; Flamant, G.; Stanmore, B. Synthetic Fuels from Biomass Using Concentrated Solar Energy–a Review. *Energy* **2012**, *42* (1), 121–131.

(2) Yang, Y.; Zhao, R.; Zhang, T.; Zhao, K.; Xiao, P.; Ma, Y.; Ajayan, P. M.; Shi, G.; Chen, Y. Graphene-Based Standalone Solar Energy Converter for Water Desalination and Purification. *ACS Nano* **2018**, *12* (1), 829–835.

(3) Mekhilef, S.; Saidur, R.; Safari, A. A Review on Solar Energy Use in Industries. *Renew. Sustain. Energy Rev.* **2011**, *15* (4), 1777–1790.

(4) Martinez, B.; Roig, A.; Obradors, X.; Molins, E.; Rouanet, A.; Monty, C. Magnetic Properties of Γ-Fe2O3 Nanoparticles Obtained by Vaporization Condensation in a Solar Furnace. *J. Appl. Phys.* **1996**, *79* (5), 2580–2586.

(5) Qi, J.; Zhang, W.; Cao, R. Solar-to-hydrogen Energy Conversion Based on Water Splitting. *Adv. Energy Mater.* **2018**, *8* (5), 1701620.

(6) Zhang, P.; Lou, X. W. Design of Heterostructured Hollow Photocatalysts for Solar-to-chemical Energy Conversion. *Adv. Mater.* **2019**, *31* (29), 1900281.

(7) Shiyani, T.; Agrawal, S.; Banerjee, I. Natural-Dye-Sensitized Photoelectrochemical Cells for Solar Energy Conversion. *Nanomater. Energy* **2020**, *9* (2), 215–226.

(8) Goodeve, C. F.; Kitchener, J. A. Photosensitisation by Titanium Dioxide. *Trans. Faraday Soc.* **1938**, *34*, 570–579.

(9) Hashimoto, K.; Irie, H.; Fujishima, A. TiO2 Photocatalysis: A Historical Overview and Future Prospects. *Jpn. J. Appl. Phys.* **2005**, *44* (12R), 8269.

(10) Fujishima, A.; Honda, K. Electrochemical Photolysis of Water at a Semiconductor Electrode. *nature* **1972**, *238* (5358), 37–38.

(11) Fujishima, A.; Rao, T. N.; Tryk, D. A. Titanium Dioxide Photocatalysis. *J. Photochem. Photobiol. C Photochem. Rev.* **2000**, *1* (1), 1–21.

(12) Fujishima, A.; Zhang, X.; Tryk, D. A. TiO2 Photocatalysis and Related Surface Phenomena. *Surf. Sci. Rep.* **2008**, *63* (12), 515–582.

(13) Hashimoto, K.; Irie, H.; Fujishima, A. TiO2 Photocatalysis: A Historical Overview and Future Prospects. *Jpn. J. Appl. Phys.* **2005**, *44* (12R), 8269.

(14) Miyoshi, A.; Maeda, K. Recent Progress in Mixed-Anion Materials for Solar Fuel Production. *Sol. RRL* **2021**, *5* (6), 2000521.

(15) LEROY, S. Etude Des Propriétés Photocatalytiques et Photoélectriques Du Dititanate de Lanthane (La2Ti2O7) à Structure Pérovskite En Feuillets et Son Utilisation Dans Des Hétérojonctions Tout Oxyde Pour La Conversion d'énergie.

(16) Jafari, T.; Moharreri, E.; Amin, A. S.; Miao, R.; Song, W.; Suib, S. L. Photocatalytic Water Splitting—the Untamed Dream: A Review of Recent Advances. *Molecules* **2016**, *21* (7), 900.

(17) Wachsman, E. D.; Lee, K. T. Lowering the Temperature of Solid Oxide Fuel Cells. *Science* **2011**, *334* (6058), 935–939. https://doi.org/10.1126/science.1204090.

(18) Staykov, A.; Lyth, S. M.; Watanabe, M. Photocatalytic Water Splitting. In *Hydrogen Energy Engineering*; Springer, 2016; pp 159–174.

(19) Kong, D.; Zheng, Y.; Kobielusz, M.; Wang, Y.; Bai, Z.; Macyk, W.; Wang, X.; Tang, J. Recent Advances in Visible Light-Driven Water Oxidation and Reduction in Suspension Systems. *Mater. Today* **2018**, *21* (8), 897–924.

(20) Butler, M.; Ginley, D. Prediction of Flatband Potentials at Semiconductor-electrolyte Interfaces from Atomic Electronegativities. *J. Electrochem. Soc.* **1978**, *125* (2), 228.

(21) Xu, Y.; Schoonen, M. A. The Absolute Energy Positions of Conduction and Valence Bands of Selected Semiconducting Minerals. *Am. Mineral.* **2000**, *85* (3–4), 543–556.

(22) Castelli, I. E.; Landis, D. D.; Thygesen, K. S.; Dahl, S.; Chorkendorff, I.; Jaramillo, T. F.; Jacobsen, K. W. New Cubic Perovskites for One-and Two-Photon Water Splitting Using the Computational Materials Repository. *Energy Environ. Sci.* **2012**, *5* (10), 9034–9043.

(23) Campet, G.; Jakani, M.; Doumerc, J. P.; Claverie, J.; Hagenmuller, P. Photoconduction Mechanisms in Titanium and Rare Earth N-Type Semiconducting Electrodes with Pyrochlore and Perovskite Structures. *Solid State Commun.* **1982**, *42* (2), 93–96.

(24) Khan, M. N.; Panigrahi, S. *Principles of Engineering Physics 2*; Cambridge University Press, 2017; Vol. 2.

(25) Cardona, M.; Peter, Y. Y. *Fundamentals of Semiconductors*; Springer, 2005; Vol. 619.

(26) Schmickler, W.; Santos, E. *Interfacial Electrochemistry*; Springer Science & Business Media, 2010.

(27) Finklea, H. O. *Photoelectrochemistry: Introductory Concepts*; ACS Publications, 1983.

(28) Rajeshwar, . K. *Fundamentals of Semiconductor Electrochemistry and Photoelectrochemistry*; Encyclopedia of Electrochemistry, 2007.

(29) Memming, R. *Semiconductor Electrochemistry*; John Wiley & Sons, 2015.

(30) Bard, A. J.; Faulkner, L. R. Fundamentals and Applications. *Electrochem. Methods* **2001**, *2* (482), 580–632.

(31) Newman, J.; Balsara, N. P. *Electrochemical Systems*; John Wiley & Sons, 2021.

(32) Maeda, K. Photocatalytic Water Splitting Using Semiconductor Particles: History and Recent Developments. *J. Photochem. Photobiol. C Photochem. Rev.* **2011**, *12* (4), 237–268.

(33) Maruska, H. P.; Ghosh, A. K. Photocatalytic Decomposition of Water at Semiconductor Electrodes. *Sol. Energy* **1978**, *20* (6), 443–458.

(34) Van Benthem, K.; Elsässer, C.; French, R. Bulk Electronic Structure of SrTiO 3: Experiment and Theory. *J. Appl. Phys.* **2001**, *90* (12), 6156–6164.

(35) Ji, S. M.; Choi, S. H.; Jang, J. S.; Kim, E. S.; Lee, J. S. Band Gap Tailored Zn (Nb1− x V x) 2O6 Solid Solutions as Visible Light Photocatalysts. *J. Phys. Chem. C* **2009**, *113* (41), 17824–17830.

(36) Hashimoto, K.; Irie, H.; Fujishima, A. TiO2 Photocatalysis: A Historical Overview and Future Prospects. *Jpn. J. Appl. Phys.* **2005**, *44* (12R), 8269.

(37) Kato, S.; Mashio, F. Autooxidation by TiO2 as a Photocatalyst. *Abtr Book Annu Meet Chem. Soc. Jpn.* **1956**, *223*.

(38) Fujishima, A.; Honda, K. Electrochemical Photolysis of Water at a Semiconductor Electrode. *nature* **1972**, *238* (5358), 37–38.

(39) Sato, S.; White, J. M. *Photodecomposition of Water over Pt/TiO2 Catalysts.*; TEXAS UNIV AT AUSTIN DEPT OF CHEMISTRY, 1980.

(40) Lehn, J. M.; JP, S. Photochemical Water Splitting Continuous Generation of Hydrogen and Oxygen by Irradiation of Aqueous Suspensions of Metal Loaded Strontium Titanate. **1980**.

(41) Domen, K.; Naito, S.; Soma, M.; Onishi, T.; Tamaru, K. Photocatalytic Decomposition of Water Vapour on an NiO–SrTiO 3 Catalyst. *J. Chem. Soc. Chem. Commun.* **1980**, No. 12, 543–544.

(42) Yamaguti, K.; Sato, S. Photolysis of Water over Metallized Powdered Titanium Dioxide. *J. Chem. Soc. Faraday Trans. 1 Phys. Chem. Condens. Phases* **1985**, *81* (5), 1237–1246.

(43) Matsumura, M.; Hiramoto, M.; Iehara, T.; Tsubomura, H. Photocatalytic and Photoelectrochemical Reactions of Aqueous Solutions of Formic Acid, Formaldehyde, and Methanol on Platinized Cadmium Sulfide Powder and at a Cadmium Sulfide Electrode. *J. Phys. Chem.* **1984**, *88* (2), 248–250.

(44) Darwent, J. R. H 2 Production Photosensitized by Aqueous Semiconductor Dispersions. *J. Chem. Soc. Faraday Trans. 2 Mol. Chem. Phys.* **1981**, *77* (9), 1703–1709.

(45) SAKATA, T.; KAWAI, T. Photodecomposition of Water by Using Organic Compounds Hydrogen Evolution by Powdered Semiconductor Photocatalysts. *J. Synth. Org. Chem. Jpn.* **1981**, *39* (7), 589–602.

(46) Matsumura, M.; Saho, Y.; Tsubomura, H. Photocatalytic Hydrogen Production from Solutions of Sulfite Using Platinized Cadmium Sulfide Powder. *J. Phys. Chem.* **1983**, *87* (20), 3807–3808.

(47) Reber, J. F.; Rusek, M. Photochemical Hydrogen Production with Platinized Suspensions of Cadmium Sulfide and Cadmium Zinc Sulfide Modified by Silver Sulfide. *J. Phys. Chem.* **1986**, *90* (5), 824–834.

(48) Fan, X.-B.; Yu, S.; Zhan, F.; Li, Z.-J.; Gao, Y.-J.; Li, X.-B.; Zhang, L.-P.; Tao, Y.; Tung, C.-H.; Wu, L.-Z. Nonstoichiometric CuxInyS Quantum Dots for Efficient Photocatalytic Hydrogen Evolution. *ChemSusChem* **2017**, *10* (24), 4833–4838.

(49) Nie, C.; Ni, W.; Gong, L.; Jiang, J.; Wang, J.; Wang, M. Charge Transfer Dynamics and Catalytic Performance of a Covalently Linked Hybrid Assembly Comprising a Functionalized Cobalt Tetraazamacrocyclic Catalyst and CuInS 2/ZnS Quantum Dots for Photochemical Hydrogen Production. *J. Mater. Chem. A* **2019**, *7* (48), 27432–27440.

(50) Chumha, N.; Pudkon, W.; Chachvalvutikul, A.; Luangwanta, T.; Randorn, C.; Inceesungvorn, B.; Ngamjarurojana, A.; Kaowphong, S. Photocatalytic Activity of CuInS2 Nanoparticles Synthesized via a Simple and Rapid Microwave Heating Process. *Mater. Res. Express* **2020**, *7* (1), 015074.

(51) Cheng, Z.; Wang, Z.; Shifa, T. A.; Wang, F.; Zhan, X.; Xu, K.; Liu, Q.; He, J. Au Plasmonics in a WS2-Au-CuInS2 Photocatalyst for Significantly Enhanced Hydrogen Generation. *Appl. Phys. Lett.* **2015**, *107* (22), 223902.

(52) Williams, R. Becquerel Photovoltaic Effect in Binary Compounds. *J. Chem. Phys.* **1960**, *32* (5), 1505–1514.

(53) Ellis, A. B.; Kaiser, S. W.; Bolts, J. M.; Wrighton, M. S. Study of N-Type Semiconducting Cadmium Chalcogenide-Based Photoelectrochemical Cells Employing Polychalcogenide Electrolytes. *J. Am. Chem. Soc.* **1977**, *99* (9), 2839–2848.

(54) Subramanian, Y.; Dhanasekaran, A.; Omeiza, L. A.; Somalu, M. R.; Azad, A. K. A Review on Heteroanionic-Based Materials for Photocatalysis Applications. *Catalysts* **2023**, *13* (1), 173.

(55) Yadav, G.; Ahmaruzzaman, M. Multi Anion-Based Materials: Synthesis and Catalytic Applications. *Mater. Res. Bull.* **2022**, *152*, 111836.

(56) Clarke, S. J.; Adamson, P.; Herkelrath, S. J.; Rutt, O. J.; Parker, D. R.; Pitcher, M. J.; Smura, C. F. Structures, Physical Properties, and Chemistry of Layered Oxychalcogenides and Oxypnictides. *Inorg. Chem.* **2008**, *47* (19), 8473–8486.

(57) Kobayashi, Y.; Hernandez, O.; Tassel, C.; Kageyama, H. New Chemistry of Transition Metal Oxyhydrides. *Sci. Technol. Adv. Mater.* **2017**, *18* (1), 905–918.

(58) Wang, L.; Wang, L.; Du, Y.; Xu, X.; Dou, S. X. Progress and Perspectives of Bismuth Oxyhalides in Catalytic Applications. *Mater. Today Phys.* **2021**, *16*, 100294.

(59) Nakada, A.; Kato, D.; Nelson, R.; Takahira, H.; Yabuuchi, M.; Higashi, M.; Suzuki, H.; Kirsanova, M.; Kakudou, N.; Tassel, C. Conduction Band Control of Oxyhalides with a Triple-Fluorite Layer for Visible Light Photocatalysis. *J. Am. Chem. Soc.* **2021**, *143* (6), 2491–2499.

(60) Li, Y.; Jiang, H.; Wang, X.; Hong, X.; Liang, B. Recent Advances in Bismuth Oxyhalide Photocatalysts for Degradation of Organic Pollutants in Wastewater. *RSC Adv.* **2021**, *11* (43), 26855–26875.

(61) Cho, E. J.; Oh, S.-J.; Jo, H.; Lee, J.; You, T.-S.; Ok, K. M. Layered Bismuth Oxyfluoride Nitrates Revealing Large Second-Harmonic Generation and Photocatalytic Properties. *Inorg. Chem.* **2019**, *58* (3), 2183–2190.

(62) Kobayashi, Y.; Tang, Y.; Kageyama, T.; Yamashita, H.; Masuda, N.; Hosokawa, S.; Kageyama, H. Titanium-Based Hydrides as Heterogeneous Catalysts for Ammonia Synthesis. *J. Am. Chem. Soc.* **2017**, *139* (50), 18240–18246.

(63) Ai-Mamouri, M.; Edwards, P. P.; Greaves, C.; Slaski, M. Synthesis and Superconducting Properties of the Strontium Copper Oxy-Fluoride Sr2CuO2F2+ δ. *Nature* **1994**, *369* (6479), 382–384.

(64) Kamihara, Y.; Hiramatsu, H.; Hirano, M.; Kawamura, R.; Yanagi, H.; Kamiya, T.; Hosono, H. Iron-Based Layered Superconductor: LaOFeP. *J. Am. Chem. Soc.* **2006**, *128* (31), 10012–10013.

(65) Kamihara, Y.; Watanabe, T.; Hirano, M.; Hosono, H. Iron-Based Layered Superconductor La [O1-x F x] FeAs (X= 0.05− 0.12) with T C= 26 K. *J. Am. Chem. Soc.* **2008**, *130* (11), 3296–3297.

(66) Oogarah, R. K.; Suard, E.; McCabe, E. E. Magnetic Order and Phase Transition in the Iron Oxysulfide La2O2Fe2OS2. *J. Magn. Magn. Mater.* **2018**, *446*, 101–107.

(67) Okada, S.; Matoba, M.; Fukumoto, S.; Soyano, S.; Kamihara, Y.; Takeuchi, T.; Yoshida, H.; Ohoyama, K.; Yamaguchi, Y. Magnetic Properties of Layered Oxysulfide Sr 2 Cu 2 (Co, Cu) O 2 S 2 with Cu-Doped CoO 2 Square Planes. *J. Appl. Phys.* **2002**, *91* (10), 8861–8863.

(68) Ryan, F. M.; Pugh, E. W.; Smoluchowski, R. Superparamagnetism, Nonrandomness, and Irradiation Effects in Cu-Ni Alloys. *Phys. Rev.* **1959**, *116* (5), 1106.

(69) Li, Y.-Y.; Wang, W.-J.; Wang, H.; Lin, H.; Wu, L.-M. Mixed-Anion Inorganic Compounds: A Favorable Candidate for Infrared Nonlinear Optical Materials. *Cryst. Growth Des.* **2019**, *19* (7), 4172–4192.

(70) Sauvage, F.; Bodenez, V.; Vezin, H.; Albrecht, T. A.; Tarascon, J.-M.; Poeppelmeier, K. R. Ag4V2O6F2 (SVOF): A High Silver Density Phase and Potential New Cathode Material for Implantable Cardioverter Defibrillators. *Inorg. Chem.* **2008**, *47* (19), 8464–8472.

(71) Li, J.; Zhai, W.; Zhang, C.; Yan, Y.; Liu, P.-F.; Yang, G. Anharmonicity and Ultralow Thermal Conductivity in Layered Oxychalcogenides BiAgOCh (Ch= S, Se, and Te). *Mater. Adv.* **2021**, *2* (14), 4876–4882.

(72) Hirosaki, N.; Xie, R.-J.; Kimoto, K.; Sekiguchi, T.; Yamamoto, Y.; Suehiro, T.; Mitomo, M. Characterization and Properties of Green-Emitting β-SiAlON: Eu 2+ Powder Phosphors for White Light-Emitting Diodes. *Appl. Phys. Lett.* **2005**, *86* (21), 211905.

(73) Kageyama, H.; Hayashi, K.; Maeda, K.; Attfield, J. P.; Hiroi, Z.; Rondinelli, J. M.; Poeppelmeier, K. R. Expanding Frontiers in Materials Chemistry and Physics with Multiple Anions. *Nat. Commun.* **2018**, *9* (1), 1–15.

(74) Sheath, B. C.; Cassidy, S. J.; Clarke, S. J. Cation Site Preferences in Layered Oxide Chalcogenides, Synthesis, Structures and Magnetic Ordering in Sr3-XCaxFe2O5Cu2Ch2 (Ch= S, Se; X= 1, 2). *J. Solid State Chem.* **2021**, *293*, 121761.

(75) Attfield, J. P. Principles and Applications of Anion Order in Solid Oxynitrides. *Cryst. Growth Des.* **2013**, *13* (10), 4623–4629.

(76) G. Shi, Y.; Yu, S.; A. Belik, A.; Matsushita, Y.; Tanaka, M.; Katsuya, Y.; Kobayashi, K.; Yamaura, K.; Takayama-Muromachi, E. Synthesis and Superconducting Properties of the Iron Oxyarsenide TbFeAsO0. 85. *J. Phys. Soc. Jpn.* **2008**, *77* (Suppl. C), 155–157.

(77) Chong, S. V.; Mochiji, T.; Kadowaki, K. Superconductivity in Yttrium Iron Oxyarsenide System. In *Journal of Physics: Conference Series*; IOP Publishing, 2009; Vol. 150, p 052036.

(78) Luu, S. D.; Vaqueiro, P. Layered Oxychalcogenides: Structural Chemistry and Thermoelectric Properties. *J. Materiomics* **2016**, *2* (2), 131–140.

(79) Palazzi, M.; Carcaly, C.; Laruelle, P.; Flahaut, J. Crystal Structure and Properties of (LaO) CuS and (LaO) AgS. In *The Rare Earths in Modern Science and Technology*; Springer, 1982; pp 347–350.

(80) Orr, M.; Hebberd, G. R.; McCabe, E. E.; Macaluso, R. T. Structural Diversity of Rare-Earth Oxychalcogenides. *ACS Omega* **2022**.

(81) Sathiya, M.; Rousse, G.; Ramesha, K.; Laisa, C. P.; Vezin, H.; Sougrati, M. T.; Doublet, M.-L.; Foix, D.; Gonbeau, D.; Walker, W. Reversible Anionic Redox Chemistry in High-Capacity Layered-Oxide Electrodes. *Nat. Mater.* **2013**, *12* (9), 827–835.

(82) Salter, E. J.; Blandy, J. N.; Clarke, S. J. Crystal and Magnetic Structures of the Oxide Sulfides CaCoSO and BaCoSO. *Inorg. Chem.* **2016**, *55* (4), 1697–1701.

(83) Shah, K.; Ćirić, A.; Murthy, K. V. R.; Chakrabarty, B. S. Investigation of a New Way of Synthesis for Nano Crystallites of La2O2S & 1% Ln3+ (Ln= Pr, Eu, Tb, Dy, Er) Doped La2O2S and Study Their Structural and Optical Properties. *J. Alloys Compd.* **2021**, *851*, 156725.

(84) Strobel, S.; Choudhury, A.; Dorhout, P. K.; Lipp, C.; Schleid, T. Rare-Earth Metal (III) Oxide Selenides M4O4Se [Se2](M= La, Ce, Pr, Nd, Sm) with Discrete Diselenide Units: Crystal Structures, Magnetic Frustration, and Other Properties. *Inorg. Chem.* **2008**, *47* (11), 4936–4944.

(85) Johnson, V.; Jeitschko, W. ZrCuSiAs: A “Filled” PbFCl Type. *J. Solid State Chem.* **1974**, *11* (2), 161–166.

(86) Phelan, W. A.; Wallace, D. C.; Arpino, K. E.; Neilson, J. R.; Livi, K. J.; Seabourne, C. R.; Scott, A. J.; McQueen, T. M. Stacking Variants and Superconductivity in the Bi–O–S System. *J. Am. Chem. Soc.* **2013**, *135* (14), 5372–5374.

(87) Ueda, K.; Hiramatsu, H.; Hirano, M.; Kamiya, T.; Hosono, H. Wide-Gap Layered Oxychalcogenide Semiconductors: Materials, Electronic Structures and Optoelectronic Properties. *Thin Solid Films* **2006**, *496* (1), 8–15.

(88) Zhao, L.-D.; He, J.; Berardan, D.; Lin, Y.; Li, J.-F.; Nan, C.-W.; Dragoe, N. BiCuSeO Oxyselenides: New Promising Thermoelectric Materials. *Energy Environ. Sci.* **2014**, *7* (9), 2900–2924.

(89) McCabe, E. E.; Free, D. G.; Mendis, B. G.; Higgins, J. S.; Evans, J. S. Preparation, Characterization, and Structural Phase Transitions in a New Family of Semiconducting Transition Metal Oxychalcogenides β-La2O2 M Se2 (M= Mn, Fe). *Chem. Mater.* **2010**, *22* (22), 6171–6182.

(90) Peschke, S.; Johrendt, D. Flux Synthesis, Crystal Structures, and Magnetism of the Series La2 N+ 2MnSe N+ 2O2 N+ 2 (N= 0–2). *Inorganics* **2017**, *5* (1), 9.

(91) Lü, M.; Mentré, O.; Gordon, E. E.; Whangbo, M.-H.; Wattiaux, A.; Duttine, M.; Tiercelin, N.; Kabbour, H. A Comprehensive Study of Magnetic Exchanges in the Layered Oxychalcogenides Sr3Fe2O5Cu2Q2 (Q=S, Se). *J. Magn. Magn. Mater.* **2017**, *444*, 147–153. https://doi.org/10.1016/j.jmmm.2017.07.026.

(92) McCabe, E. E.; Free, D. G.; Mendis, B. G.; Higgins, J. S.; Evans, J. S. Preparation, Characterization, and Structural Phase Transitions in a New Family of Semiconducting Transition Metal Oxychalcogenides β-La2O2 M Se2 (M= Mn, Fe). *Chem. Mater.* **2010**, *22* (22), 6171–6182.

(93) Gál, Z. A.; Rutt, O. J.; Smura, C. F.; Overton, T. P.; Barrier, N.; Clarke, S. J.; Hadermann, J. Structural Chemistry and Metamagnetism of an Homologous Series of Layered Manganese Oxysulfides. *J. Am. Chem. Soc.* **2006**, *128* (26), 8530–8540.

(94) Parida, A.; Senapati, S.; Naik, R. Recent Developments on Bi-Based Oxychalcogenide Materials with Thermoelectric and Optoelectronic Applications: An Overview. *Mater. Today Chem.* **2022**, *26*, 101149.

(95) Reshak, A. H. CaCoSO Diluted Magnetic Antiferromagnet Semiconductor as Efficient Thermoelectric Materials. *Mater. Res. Bull.* **2017**, *94*, 22–30.

(96) Shi, Y.-F.; Wei, W.-B.; Wu, X.-T.; Lin, H.; Zhu, Q.-L. Recent Progress in Oxychalcogenides as IR Nonlinear Optical Materials. *Dalton Trans.* **2021**, *50* (12), 4112–4118.

(97) Shi, Y.-F.; Wei, W.-B.; Wu, X.-T.; Lin, H.; Zhu, Q.-L. Recent Progress in Oxychalcogenides as IR Nonlinear Optical Materials. *Dalton Trans.* **2021**, *50* (12), 4112–4118.

(98) Liu, B.-W.; Jiang, X.-M.; Wang, G.-E.; Zeng, H.-Y.; Zhang, M.-J.; Li, S.-F.; Guo, W.-H.; Guo, G.-C. Oxychalcogenide BaGeOSe2: Highly Distorted Mixed-Anion Building Units Leading to a Large Second-Harmonic Generation Response. *Chem. Mater.* **2015**, *27* (24), 8189–8192.

(99) Xing, W.; Fang, P.; Wang, N.; Li, Z.; Lin, Z.; Yao, J.; Yin, W.; Kang, B. Two Mixed-Anion Units of [GeOSe3] and [GeO3S] Originating from Partial Isovalent Anion Substitution and Inducing Moderate Second Harmonic Generation Response and Large Birefringence. *Inorg. Chem.* **2020**, *59* (22), 16716–16724.

(100) Liu, B.-W.; Jiang, X.-M.; Wang, G.-E.; Zeng, H.-Y.; Zhang, M.-J.; Li, S.-F.; Guo, W.-H.; Guo, G.-C. Oxychalcogenide BaGeOSe2: Highly Distorted Mixed-Anion Building Units Leading to a Large Second-Harmonic Generation Response. *Chem. Mater.* **2015**, *27* (24), 8189–8192.

(101) Wang, R.; Liang, F.; Wang, F.; Guo, Y.; Zhang, X.; Xiao, Y.; Bu, K.; Lin, Z.; Yao, J.; Zhai, T. Sr6Cd2Sb6O7S10: Strong SHG Response Activated by Highly Polarizable Sb/O/S Groups. *Angew. Chem. Int. Ed.* **2019**, *58* (24), 8078–8081.

(102) Wang, Y.; Luo, M.; Zhao, P.; Che, X.; Cao, Y.; Huang, F. Sr 4 Pb 1.5 Sb 5 O 5 Se 8: A New Mid-Infrared Nonlinear Optical Material with a Moderate SHG Response. *CrystEngComm* **2020**, *22* (20), 3526–3530.

(103) Wang, R.; Wang, F.; Zhang, X.; Feng, X.; Zhao, C.; Bu, K.; Zhang, Z.; Zhai, T.; Huang, F. Improved Polarization in the Sr6Cd2Sb6O7Se10 Oxyselenide through Design of Lateral Sublattices for Efficient Photoelectric Conversion. *Angew. Chem.* **2022**.

(104) Zhu, W. J.; Hor, P. H. Unusual Layered Transition-Metal Oxysulfides: Sr2Cu2MO2S2 (M= Mn, Zn). *J. Solid State Chem.* **1997**, *130* (2), 319–321.

(105) Zhu, W. J.; Hor, P. H. Sr2CuGaO3S, a Rare Example of Square Pyramidal Gallium. *Inorg. Chem.* **1997**, *36* (17), 3576–3577.

(106) Guittard, M.; Benazeth, S.; Dugue, J.; Jaulmes, S.; Palazzi, M.; Laruelle, P.; Flahaut, J. Oxysulfides and Oxyselenides in Sheets, Formed by a Rare Earth Element and a Second Metal. *J. Solid State Chem.* **1984**, *51* (2), 227–238.

(107) Subramanian, Y.; Dhanasekaran, A.; Omeiza, L. A.; Somalu, M. R.; Azad, A. K. A Review on Heteroanionic-Based Materials for Photocatalysis Applications. *Catalysts* **2023**, *13* (1), 173.

(108) Sambrook, T.; Smura, C. F.; Clarke, S. J.; Ok, K. M.; Halasyamani, P. S. Structure and Physical Properties of the Polar Oxysulfide CaZnOS. *Inorg. Chem.* **2007**, *46* (7), 2571–2574.

(109) Cui, J.; Li, C.; Zhang, F. Development of Mixed-Anion Photocatalysts with Wide Visible-Light Absorption Bands for Solar Water Splitting. *ChemSusChem* **2019**, *12* (9), 1872–1888.

(110) Goto, Y.; Seo, J.; Kumamoto, K.; Hisatomi, T.; Mizuguchi, Y.; Kamihara, Y.; Katayama, M.; Minegishi, T.; Domen, K. Crystal Structure, Electronic Structure, and Photocatalytic Activity of Oxysulfides: La2Ta2ZrS2O8, La2Ta2TiS2O8, and La2Nb2TiS2O8. *Inorg. Chem.* **2016**, *55* (7), 3674–3679.

(111) Allen, J. P.; Carey, J. J.; Walsh, A.; Scanlon, D. O.; Watson, G. W. Electronic Structures of Antimony Oxides. *J. Phys. Chem. C* **2013**, *117* (28), 14759–14769.

(112) Vadapoo, R.; Krishnan, S.; Yilmaz, H.; Marin, C. Self-Standing Nanoribbons of Antimony Selenide and Antimony Sulfide with Well-Defined Size and Band Gap. *Nanotechnology* **2011**, *22* (17), 175705.

(113) Liang, F.; Kang, L.; Lin, Z.; Wu, Y. Mid-Infrared Nonlinear Optical Materials Based on Metal Chalcogenides: Structure–Property Relationship. *Cryst. Growth Des.* **2017**, *17* (4), 2254–2289.

(114) Sayama, K.; Nomura, A.; Zou, Z.; Abe, R.; Abe, Y.; Arakawa, H. Photoelectrochemical Decomposition of Water on Nanocrystalline BiVO 4 Film Electrodes under Visible Light. *Chem. Commun.* **2003**, No. 23, 2908–2909.

(115) Kavanagh, S. R.; Savory, C. N.; Scanlon, D. O.; Walsh, A. Hidden Spontaneous Polarisation in the Chalcohalide Photovoltaic Absorber Sn 2 SbS 2 I 3. *Mater. Horiz.* **2021**, *8* (10), 2709–2716.

(116) Wang, X.; Li, Z.; Kavanagh, S. R.; Ganose, A. M.; Walsh, A. Lone Pair Driven Anisotropy in Antimony Chalcogenide Semiconductors. *Phys. Chem. Chem. Phys.* **2022**, *24* (12), 7195–7202.

(117) Ok, K. M. Functional Layered Materials with Heavy Metal Lone Pair Cations, Pb 2+, Bi 3+, and Te 4+. *Chem. Commun.* **2019**, *55* (85), 12737–12748.

(118) Handy, J. V.; Zaheer, W.; Rothfuss, A. R.; McGranahan, C. R.; Agbeworvi, G.; Andrews, J. L.; García-Pedraza, K. E.; Ponis, J. D.; Ayala, J. R.; Ding, Y. Lone but Not Alone: Precise Positioning of Lone Pairs for the Design of Photocatalytic Architectures. *Chem. Mater.* **2022**.

(119) Suzuki, H.; Kunioku, H.; Higashi, M.; Tomita, O.; Kato, D.; Kageyama, H.; Abe, R. Lead Bismuth Oxyhalides PbBiO2X (X= Cl, Br) as Visible-Light-Responsive Photocatalysts for Water Oxidation: Role of Lone-Pair Electrons in Valence Band Engineering. *Chem. Mater.* **2018**, *30* (17), 5862–5869.

(120) Ito, H.; Miura, A.; Goto, Y.; Mizuguchi, Y.; Moriyoshi, C.; Kuroiwa, Y.; Azuma, M.; Liu, J.; Wen, X.-D.; Nishioka, S. An Electronic Structure Governed by the Displacement of the Indium Site in In–S 6 Octahedra: LnOInS 2 (Ln= La, Ce, and Pr). *Dalton Trans.* **2019**, *48* (32), 12272–12278.

(121) Ogisu, K.; Ishikawa, A.; Teramura, K.; Toda, K.; Hara, M.; Domen, K. Lanthanum–Indium Oxysulfide as a Visible Light Driven Photocatalyst for Water Splitting. *Chem. Lett.* **2007**, *36* (7), 854–855.

(122) Hisatomi, T.; Okamura, S.; Liu, J.; Shinohara, Y.; Ueda, K.; Higashi, T.; Katayama, M.; Minegishi, T.; Domen, K. La 5 Ti 2 Cu 1− x Ag x S 5 O 7 Photocathodes Operating at Positive Potentials during Photoelectrochemical Hydrogen Evolution under Irradiation of up to 710 Nm. *Energy Environ. Sci.* **2015**, *8* (11), 3354–3362.

(123) Zhang, H.; Liu, L.; Zhou, Z. Towards Better Photocatalysts: First-Principles Studies of the Alloying Effects on the Photocatalytic Activities of Bismuth Oxyhalides under Visible Light. *Phys. Chem. Chem. Phys.* **2012**, *14* (3), 1286–1292.

(124) Zhang, J.; Zhou, P.; Liu, J.; Yu, J. New Understanding of the Difference of Photocatalytic Activity among Anatase, Rutile and Brookite TiO2. *Phys. Chem. Chem. Phys.* **2014**, *16* (38), 20382–20386.

(125) Zhang, J.; Yu, W.; Liu, J.; Liu, B. Illustration of High-Active Ag2CrO4 Photocatalyst from the First-Principle Calculation of Electronic Structures and Carrier Effective Mass. *Appl. Surf. Sci.* **2015**, *358*, 457–462.

(126) Yang, J.; Jiang, P.; Yue, M.; Yang, D.; Cong, R.; Gao, W.; Yang, T. Bi2Ga4O9: An Undoped Single-Phase Photocatalyst for Overall Water Splitting under Visible Light. *J. Catal.* **2017**, *345*, 236–244.

(127) Vonrüti, N. Ferroelectricity and Metastability in (Mixed-Anion) Perovskite Oxides for Improved Solar Water Splitting, 2019.

(128) Vonrüti, N.; Aschauer, U. Catalysis on Oxidized Ferroelectric Surfaces—Epitaxially Strained LaTiO2N and BaTiO3 for Photocatalytic Water Splitting. *J. Chem. Phys.* **2020**, *152* (2), 024701.

(129) Berger, R. F.; Fennie, C. J.; Neaton, J. B. Band Gap and Edge Engineering via Ferroic Distortion and Anisotropic Strain: The Case of SrTiO 3. *Phys. Rev. Lett.* **2011**, *107* (14), 146804.

(130) Vonrüti, N.; Aschauer, U. Epitaxial Strain Dependence of Band Gaps in Perovskite Oxynitrides Compared to Perovskite Oxides. *Phys. Rev. Mater.* **2018**, *2* (10), 105401.

(131) Vonrüti, N.; Aschauer, U. Band-Gap Engineering in AB (O x S 1− x) 3 Perovskite Oxysulfides: A Route to Strongly Polar Materials for Photocatalytic Water Splitting. *J. Mater. Chem. A* **2019**, *7* (26), 15741–15748.

(132) Vonrüti, N.; Aschauer, U. Anion Order and Spontaneous Polarization in LaTiO 2 N Oxynitride Thin Films. *Phys. Rev. Lett.* **2018**, *120* (4), 046001.

(133) Vonrüti, N.; Aschauer, U. Band-Gap Engineering in AB (O x S 1− x) 3 Perovskite Oxysulfides: A Route to Strongly Polar Materials for Photocatalytic Water Splitting. *J. Mater. Chem. A* **2019**, *7* (26), 15741–15748.

(134) Boyer, C.; Deudon, C.; Meerschaut, A. Synthesis and Structure Determination of the New Sm2Ti2O5S2 Compound. *Comptes Rendus Académie Sci. - Ser. IIC - Chem.* **1999**, *2* (2), 93–99. https://doi.org/10.1016/S1387-1609(99)80007-3.

(135) Goga, M.; Seshadri, R.; Ksenofontov, V.; Gütlich, P.; Tremel, W. Ln 2 Ti 2 S 2 O 5 (Ln= Nd, Pr, Sm): A Novel Series of Defective Ruddlesden–Popper Phases. *Chem. Commun.* **1999**, No. 11, 979–980.

(136) Boyer-Candalen, C.; Derouet, J.; Porcher, P.; Moëlo, Y.; Meerschaut, A. The Family of Ln2Ti2S2O5 Compounds (Ln= Nd, Sm, Gd, Tb, Dy, Ho, Er, and Y): Optical Properties. *J. Solid State Chem.* **2002**, *165* (2), 228–237.

(137) Ishikawa, A.; Takata, T.; Matsumura, T.; Kondo, J. N.; Hara, M.; Kobayashi, H.; Domen, K. Oxysulfides Ln2Ti2S2O5 as Stable Photocatalysts for Water Oxidation and Reduction under Visible-Light Irradiation. *J. Phys. Chem. B* **2004**, *108* (8), 2637–2642.

(138) Ishikawa, A.; Takata, T.; Kondo, J. N.; Hara, M.; Kobayashi, H.; Domen, K. Oxysulfide Sm2Ti2S2O5 as a Stable Photocatalyst for Water Oxidation and Reduction under Visible Light Irradiation (Λ≤ 650 Nm). *J. Am. Chem. Soc.* **2002**, *124* (45), 13547–13553.

(139) Ishikawa, A.; Yamada, Y.; Takata, T.; Kondo, J. N.; Hara, M.; Kobayashi, H.; Domen, K. Novel Synthesis and Photocatalytic Activity of Oxysulfide Sm2Ti2S2O5. *Chem. Mater.* **2003**, *15* (23), 4442–4446.

(140) Denis, S. G.; Clarke, S. J. Two Alternative Products from the Intercalation of Alkali Metals into Cation-Defective Ruddlesden–Popper Oxysulfides. *Chem. Commun.* **2001**, No. 22, 2356–2357.

(141) Hyett, G.; Rutt, O. J.; Gál, Z. A.; Denis, S. G.; Hayward, M. A.; Clarke, S. J. Electronically Driven Structural Distortions in Lithium Intercalates of the N= 2 Ruddlesden− Popper-Type Host Y2Ti2O5S2: Synthesis, Structure, and Properties of Li x Y2Ti2O5S2 (0< X< 2). *J. Am. Chem. Soc.* **2004**, *126* (7), 1980–1991.

(142) Wang, Q.; Nakabayashi, M.; Hisatomi, T.; Sun, S.; Akiyama, S.; Wang, Z.; Pan, Z.; Xiao, X.; Watanabe, T.; Yamada, T. Oxysulfide Photocatalyst for Visible-Light-Driven Overall Water Splitting. *Nat. Mater.* **2019**, *18* (8), 827–832.

(143) Tsujimoto, Y.; Juillerat, C. A.; Zhang, W.; Fujii, K.; Yashima, M.; Halasyamani, P. S.; zur Loye, H.-C. Function of Tetrahedral ZnS3O Building Blocks in the Formation of SrZn2S2O: A Phase Matchable Polar Oxysulfide with a Large Second Harmonic Generation Response. *Chem. Mater.* **2018**, *30* (18), 6486–6493.

(144) Reshak, A. H. Sulfide Oxide XZnSO (X= Ca or Sr) as Novel Active Photocatalytic Water Splitting Solar-to-Hydrogen Energy Conversion. *Appl. Catal. B Environ.* **2018**, *225*, 273–283.

(145) Nishioka, S.; Kanazawa, T.; Shibata, K.; Tsujimoto, Y.; Zur Loye, H.-C.; Maeda, K. A Zinc-Based Oxysulfide Photocatalyst SrZn 2 S 2 O Capable of Reducing and Oxidizing Water. *Dalton Trans.* **2019**, *48* (42), 15778–15781.

(146) Kabbour, H.; Cario, L.; Moëlo, Y.; Meerschaut, A. Synthesis, X-Ray and Optical Characterizations of Two New Oxysulfides: LaInS2O and La5In3S9O3. *J. Solid State Chem.* **2004**, *177* (4–5), 1053–1059.

(147) Kabbour, H.; Sayede, A.; Saitzek, S.; Lefevre, G.; Cario, L.; Trentesaux, M.; Roussel, P. Structure of the Water-Splitting Photocatalyst Oxysulfide α-LaOInS 2 and Ab Initio Prediction of New Polymorphs. *Chem. Commun.* **2020**, *56* (11), 1645–1648.

(148) Miura, A.; Oshima, T.; Maeda, K.; Mizuguchi, Y.; Moriyoshi, C.; Kuroiwa, Y.; Meng, Y.; Wen, X.-D.; Nagao, M.; Higuchi, M. Synthesis, Structure and Photocatalytic Activity of Layered LaOInS 2. *J. Mater. Chem. A* **2017**, *5* (27), 14270–14277.

(149) Machida, M.; Murakami, S.; Kijima, T.; Matsushima, S.; Arai, M. Photocatalytic Property and Electronic Structure of Lanthanide Tantalates, LnTaO4 (Ln= La, Ce, Pr, Nd, and Sm). *J. Phys. Chem. B* **2001**, *105* (16), 3289–3294.

(150) Wakayama, H.; Hibino, K.; Fujii, K.; Oshima, T.; Yanagisawa, K.; Kobayashi, Y.; Kimoto, K.; Yashima, M.; Maeda, K. Synthesis of a Layered Niobium Oxynitride, Rb2NdNb2O6N· H2O, Showing Visible-Light Photocatalytic Activity for H2 Evolution. *Inorg. Chem.* **2019**, *58* (9), 6161–6166.

(151) Gastaldi, L.; Carre, D.; Pardo, M. P. Structure de l'oxysulfure d'indium et de Lanthane In6La10O6S17. *Acta Crystallogr. B* **1982**, *38* (9), 2365–2367.

(152) Jaulmes, S. Oxysulfure de Gallium et de Lanthane LaGaOS2. *Acta Crystallogr. B* **1978**, *34* (8), 2610–2612.

(153) Jaulmes, S.; Mazurier, A.; Guittard, M. Structure de l'oxypentasulfure de Gallium et de Trilanthane, GaLa3OS5. *Acta Crystallogr. C* **1983**, *39* (12), 1594–1597.

(154) Ogisu, K.; Ishikawa, A.; Shimodaira, Y.; Takata, T.; Kobayashi, H.; Domen, K. Electronic Band Structures and Photochemical Properties of La− Ga-Based Oxysulfides. *J. Phys. Chem. C* **2008**, *112* (31), 11978–11984.

(155) Meignen, V.; Cario, L.; Lafond, A.; Moëlo, Y.; Guillot-Deudon, C.; Meerschaut, A. Crystal Structures of Two New Oxysulfides La5Ti2MS5O7 (M= Cu, Ag): Evidence of Anionic Segregation. *J. Solid State Chem.* **2004**, *177* (8), 2810–2817.

(156) Katayama, M.; Yokoyama, D.; Maeda, Y.; Ozaki, Y.; Tabata, M.; Matsumoto, Y.; Ishikawa, A.; Kubota, J.; Domen, K. Fabrication and Photoelectrochemical Properties of La5Ti2MS5O7 (M= Ag, Cu) Electrodes. *Mater. Sci. Eng. B* **2010**, *173* (1–3), 275–278.

(157) Suzuki, T.; Hisatomi, T.; Teramura, K.; Shimodaira, Y.; Kobayashi, H.; Domen, K. A Titanium-Based Oxysulfide Photocatalyst: La 5 Ti 2 MS 5 O 7 (M= Ag, Cu) for Water Reduction and Oxidation. *Phys. Chem. Chem. Phys.* **2012**, *14* (44), 15475–15481.

(158) Liu, J.; Hisatomi, T.; Ma, G.; Iwanaga, A.; Minegishi, T.; Moriya, Y.; Katayama, M.; Kubota, J.; Domen, K. Improving the Photoelectrochemical Activity of La5Ti2CuS5O7 for Hydrogen Evolution by Particle Transfer and Doping. *Energy Environ. Sci.* **2014**, *7* (7), 2239–2242.

(159) Ma, G.; Suzuki, Y.; Singh, R. B.; Iwanaga, A.; Moriya, Y.; Minegishi, T.; Liu, J.; Hisatomi, T.; Nishiyama, H.; Katayama, M. Photoanodic and Photocathodic Behaviour of La 5 Ti 2 CuS 5 O 7 Electrodes in the Water Splitting Reaction. *Chem. Sci.* **2015**, *6* (8), 4513–4518.

(160) Hirose, H.; Ueda, K.; Kawazoe, H.; Hosono, H. Electronic Structure of Sr2Cu2ZnO2S2 Layered Oxysulfide with CuS Layers. *Chem. Mater.* **2002**, *14* (3), 1037–1041.

Appendix 1

1.1. Oxysulfide materials

Compounds	Band gap magnitude & Nature	Semiconduction type	Cation choice	Coordination environment & Anion ratio	Polar units?	Polar Structure?	H_2 or O_2 production?	Reference
$Sr_6Cd_2Sb_6S_{10}O_7$	Indirect (1.89 eV)	n-type	Sb^{3+}	SbS_5 $SbOS_4$ SbO_3	Yes	Yes (*Cm*)	H_2 & O_2 (theory)	DOI: 10.1021/acs.inorgchem.2c03040
$Sm_2Ti_2S_2O_5$	Indirect (2 eV)	n-type	Ti^{4+}	TiO_5	Yes	No (*I4/mmm*)	H_2 & O_2 (measured)	DOI: 10.1021/ja0269643
$Y_2Ti_2O_5S_2$	- (1.9 eV)	n-type	Ti^{4+}	TiO_5	Yes	No (*I4/mmm*)	H_2 & O_2 (measured)	DOI: 10.1038/s41563-019-0399-z
Layered - $LaOInS_2$	Direct (~2.64 eV)	-	In^{3+}	InS_6	Yes	$P2_1/m$	H_2 & O_2 (measured)	DOI :10.1039/c7ta04440b DOI :10.1246/cl.2007.854
α - $LaOInS_2$	- (~2.7 eV)	p-type	In^{3+}	InS_5O InS_4 InS_6	Yes	*Pmcn*	H_2 & O_2 (theory)	DOI: 10.1039/C9CC09797J
$La_5In_3S_9O_3$	- (2.60 eV)	p-type	In^{3+}	InS_4	Yes	*Pbcm*	H_2 & O_2 (measured)	DOI : 10.1016/j.jssc.2003.10.012 DOI : 10.1246/cl.2007.854
LaCuOS	Direct (3.2 eV)	p-type	Cu^{2+}	CuS_4	No	*P4/nmm*	-	DOI: 10.1063/1.1319507
PrCuOS	Direct (3.03 eV)	p-type	Cu^{2+}	CuS_4	No	*P4/nmm*	-	DOI: 10.1021/cm030175i
NdCuOS	Direct (2.98 eV)	p-type	Cu^{2+}	CuS_4	No	*P4/nmm*	-	DOI: 10.1021/cm030175i
LaAgOS	Direct (2.50 eV)	p-type	Ag^{+}	AgS_4	No	*P4/nmm*	-	DOI: 10.1002/smtd.202201368

$LaGaS_2O$	Indirect (3 eV)	n-type	Ga^{3+}	GaS_2O_2	No	*Pmca*	Anodic photocurrent under UV light	DOI :10.1021/jp802153t
La_3GaS_5O	Direct (2.3 eV)	n-type	Ga^{3+}	GaS_4	No	No (*Pnma*)	H_2 or O_2 Under visible light (measured)	DOI :10.1021/jp802153t
$CeInOS_2$	Direct (2.41 eV)	-	In^{3+}	InS_6	Yes	$P2_1/m$	H_2 (measured)	DOI: 10.1039/c9dt01562k
$PrInOS_2$	Direct (2.43 eV)	-	In^{3+}	InS_6	Yes	$P2_1/m$	H_2 (measured)	DOI: 10.1039/c9dt01562k
$La_2O_2Fe_2OS_2$	Direct (0.19 eV)	-	Fe^{2+}	FeO_2S_4	No	No (*I4/mmm*)	-	DOI: 10.1103/PhysRevLett.104.216405 DOI: 10.1103/PhysRevB.86.125122
SrZnSO	Direct (3.1 eV)	p-type	Zn^{2+}	ZnS_3O	Yes	Yes ($P6_3mc$)	H_2 (theory)	DOI: 10.1016/j.apcatb.2017.12.006
$SrZn_2S_2O$	Direct (3.86 eV)	n-type	Zn^{2+}	ZnS_3O	Yes	Yes ($Pmn2_1$)	H_2 & O_2 (measured)	DOI: 10.1039/C9DT03699G
CaCoSO	Indirect (0.4 eV)	p-type	Co^{2+}	CoS_3O	Yes	Yes ($P6_3mc$)	-	DOI: 10.1016/j.materresbull.2017.05.041
CaZnSO	Direct (3.7 eV)	p-type	Zn^{2+}	ZnS_3O	Yes	Yes ($P6_3mc$)	H_2 (theory)	DOI: 10.1016/j.apcatb.2017.12.006
BaCoSO	- (1.3 eV)	-	Co^{2+}	CoS_2O_2	No	(*Cmcm*)	-	DOI :10.1103/PhysRevB.100.205130
CaFeSO	Indirect (1.6 eV)	-	Fe^{2+}	FeS_3O	Yes	Yes ($P6_3mc$)	-	DOI: 10.1103/PhysRevMaterials.1.034406
BaZnSO	Direct (3.9 eV)	-	Zn^{2+}	ZnS_2O_2	No	(*Cmcm*)	-	DOI :10.1021/ic051240o
BiCuOS	Indirect (1.1 eV)	p-type	Cu^{2+}	CuS_4	No	*P4/nmm*	Decomposition of pollutant (CR) aqueous under visible light: 55 % in 70 mins	DOI :10.3390/ma8031043 DOI: 10.3390/ma11030447
BiAgOS	Indirect (1.5 eV)	p-type	Ag^{+}	AgS_4	No	*P4/nmm*	-	DOI: 10.1021/acs.chemmater.7b02664
$Ln_2Ti_2S_2O_5$ (Ln = Sm, Gd, Tb, Dy, Ho and Er)	Indirect (2.13-1.94 eV)	-	Ti^{4+}	$TiSO_5$	Yes	No (*I4/mmm*)	H_2 & O_2 under visible light (measured)	DOI :10.1021/jp036890x

$La_5Ti_2CuS_5O_7$	Indirect (2.02 eV)	p-type	Ti^{4+} Cu^{+}	TiO_4S_2 TiO_5S CuS_4	Yes	No (*Pnma*)	H_2 & O_2 (measured)	DOI: 10.1039/c2cp43132g
$La_5Ti_2AgS_5O_7$	Indirect (2.17 eV)	p-type	Ti^{4+} Ag^{+}	TiO_4S_2 TiO_5S AgS_4	Yes	No (*Pnma*)	H_2 & O_2 (measured)	DOI: 10.1039/c2cp43132g
$Sr_2Cu_2ZnO_2S_2$	- (2.7 eV)	p-type	Cu^{2+} Zn^{2+}	CuS_4 ZnO_4	No	No (*I4/nmm*)	-	DOI :10.1021/cm0105864
Sr_2CuGaO_3S	- (2.6 eV)	p-type	Cu^{2+} Ga^{3+}	CuS_4 GaO_5	No Yes	*P4/nmm*	-	DOI: 10.1021/cm0007813
Sr_2CuInO_3S	- (2.3 eV)	p-type	Cu^{2+} In^{3+}	CuS_4 InO_5	No Yes	*P4/nmm*	-	DOI: 10.1021/cm0007813
$Sr_3Cu_2Sc_2O_5S_2$	Direct (3.1 eV)	p-type	Cu^{2+} Sc^{3+}	CuS_4 ScO_5	No Yes	No (*I4/nmm*)	-	DOI: 10.1063/1.2817643
$La_2SnO_2S_3$	- (3 eV)	n-type	Sn^{4+}	SnS_4	Yes	(*Pbnm*)	-	DOI: 10.1107/S0108270185004978
$RE_2M_2S_3O_4$ (RE = Y, Tm; M = Zr, Hf)	Direct (2.95 – 2.80 – 2.93 eV)	-	M^{4+}	MS_3O_4	No	No (*Pbam*)	-	DOI: 10.1039/D1CC00351H
$Sm_3NbS_3O_4$	Direct (2.68 eV)	-	Sm^{3+} Nb^{5+}	$[NbS_2O_4]^{7-}$	Yes	Yes ($Pna2_1$)	-	DOI: 10.1021/acs.inorgchem.1c01634
$Gd_3NbS_3O_4$	Direct (2.74 eV)	-	Gd^{3+} Nb^{5+}	$[NbS_2O_4]^{7-}$	Yes	Yes ($Pna2_1$)	-	DOI: 10.1021/acs.inorgchem.1c01634
$Dy_3NbS_3O_4$	Direct (2.72 eV)	-	Dy^{3+} Nb^{5+}	$[NbS_3O_4]^{9-}$	No	No (*Pnma*)	-	DOI: 10.1021/acs.inorgchem.1c01634
$A_2GeGa_2OS_6$ (A = Ca, Sr)	Indirect (3.15 eV)	-	Ga^{3+}	GaS_4 GaS_3O	No Yes	($P\bar{4}2_1m$)	-	DOI: 10.1021/acsami.2c04422
$Sr_2CdGe_2OS_6$	Indirect (3.62 eV)	-	Cd^{2+}	CdS_4 GeS_3O	No Yes	($P\bar{4}2_1m$)	-	DOI : 10.1021/acsami.2c04422 DOI : 10.1021/acs.chemmater.2c00385
$Sr_2ZnGe_2OS_6$	Indirect (3.73 eV)	-	Zn^{2+}	ZnS_4 GeS_3O	No Yes	($P\bar{4}2_1m$)	-	DOI : 10.1021/acsami.2c04422 DOI : 10.1021/acs.chemmater.2c00385
$Sr_2MnGe_2OS_6$	Indirect (3.51 eV)	-	Mn^{2+}	MnS_4 GeS_3O	No Yes	($P\bar{4}2_1m$)	-	DOI : 10.1021/acsami.2c04422 DOI : 10.1021/acs.chemmater.2c00385

$LnMGa_3S_6O$ (Ln = La, Pr, and Nd; M = Ca and Sr)	Direct (3.21-3.27 eV)	-	Ln^{3+} M^{2+} Ga^{3+}	$(Ln/M)S_7O$ GaS_3O GaS_4	Yes	($P\bar{4}2_1m$)	-	DOI: 10.1021/acsami.2c11199
$Sr_2CoGe_2OS_6$	Indirect (2.77 eV)	-	Co^{2+}	CoS_4 Ge_2OS_6	No Yes	($P\bar{4}2_1m$)	-	DOI: 10.1021/acs.inorgchem.2c03283
$Ba_5Ga_2SiO_4S_6$	Direct (4.03 eV)	-	Ba^{2+} Ga^{3+}	$[Ga_2SiO_4S_6]$ clusters made of corner-sharing $[SiO_4]$ and $[GaOS_3]$ tetrahedra	No Yes	(*Cc*)	-	DOI: 10.1021/acs.inorgchem.2c03577
$Ba_2SnSSi_2O_7$ Fresnoite - type	- (> 4.00 eV)	-	Sn^{4+}	SnO_4S	Yes	(*P4bm*)	-	DOI: 10.1039/d2qm00621a
$[Sr_3VO_4][GaS_3]$ 0D	Direct (2.23 eV-DFT)	-	Ga^{3+} V^{5+}	GaS_4 VO_4	Yes Yes	No ($P2_1/c$)	-	DOI: 10.1039/d2qi01160c
$[Sr_3VO_4][InS_3]$ 1D	Indirect (2.13 eV-DFT)	-	In^{3+} V^{5+}	InS_4 VO_4	Yes Yes	Yes ($Pmc2_1$)	-	DOI: 10.1039/d2qi01160c
$Ae_3S[GeOS_3]$(*Ae*=Ba, Sr) Antiperovskite structure	Direct (3.63 eV Ba) (4.10 eV Sr)	-	Ae^{2+} Ge^{4+}	$[GeOS_3]$ $[SAe_6]$	Yes	Yes ($Pca2_1$)	-	DOI: 10.1002/advs.202204755

1.2. Oxyselenide materials

Compounds	Band gap magnitude & Nature	Semiconduction type	Cation choice	Coordination environment & Anion ratio	Polar units?	Polar Structure?	H_2 or O_2 production?	Reference
LaCuOSe	Direct (2.8 eV)	p-type	Cu^{2+}	$CuSe_4$	No	*P4/nmm*	-	DOI: 10.1021/acsaem.2c00590
LaAgOSe	Direct (2.50 eV)	p-type	Ag^{+}	$AgSe_4$	No	*P4/nmm*	-	DOI: 10.1002/smtd.202201368
BiCuOSe	Indirect (0.8 eV)	p-type	Cu^{2+}	$CuSe_4$	No	*P4/nmm*	Degradation of organic contaminants in solar light	DOI: 10.3390/ma8031043 DOI: 10.3390/ma11030447
CaFeSeO	Indirect (1.8 eV)	n-type	Fe^{2+}	$FeSe_2O_2$	Yes	(*Cmc*2_1 *Pmcn*)	-	DOI : 10.1021/acs.chemmater.5b02164 DOI: 10.1021/acs.inorgchem.6b01951
$La_2CdO_2Se_2$	Direct (3.3 eV)	n-type	La^{3+} Cd^{2+}	La_4O $CdSe_4$	No	*P*4_2*/nmc*	-	DOI :10.1021/jp048722q
$La_2O_2Fe_2OSe_2$	Direct (0.17 eV)	-	Fe^{2+}	FeO_2Se_4	No	No (*I4/mmm*)	-	DOI: 10.1103/PhysRevLett.104.216405 DOI: 10.1103/PhysRevB.86.125122
$Sr_6Cd_2Sb_6Se_{10}O_6$	Indirect (1.55 eV)	p-type	Sb^{3+}	$SbSe_5$ $SbOSe_4$ SbO_3	Yes	Yes (*Cm*)	-	DOI: 10.1002/anie.202206816
$Sr_2Sb_2Se_3O_2$	Direct (1.7 eV)	-	Sb^{3+}	SbOSe4	Yes	*P*2_1*/mc*	-	DOI: 10.1021/acs.chemmater.5b04536
[Sr_3VO_4][$GaSe_3$] **0D**	Indirect (2.51 eV)	-	Ga^{3+} V^{5+}	$GaSe_4$ VO_4	Yes Yes	No (*P*2_1*/c*)	-	DOI: 10.1039/d2qi01160c
[Sr_3VO_4][$InSe_3$] **1D**	Indirect (2.62 eV)	-	In^{3+} V^{5+}	$InSe_4$ VO_4	Yes Yes	Yes (*Pmc*2_1)	-	DOI: 10.1039/d2qi01160c
[Ae_3Se[$GeOSe_3$](Ae=Ba, Sr) **Antiperovskite structure**	Direct (3.52 eV Ba) (3.50 eV Sr)	-	Ae^{2+} Ge^{4+}	[$GeOSe_3$] [SAe_6]	Yes	Yes (*Pca*2_1)	-	DOI: 10.1002/advs.202204755

1.3. Oxytelluride materials

Compounds	Band gap magnitude & Nature	Semiconduction type	Cation choice	Coordination environment & Anion ratio	Polar units?	Polar Structure?	H_2 or O_2 production?	Reference
BiCuOTe	Indirect (0.5 eV)	p-type	Cu^{2+}	$CuTe_4$	No	*P4/nmm*	-	DOI: 10.1016/j.solidstatesciences.2016.05.012
$Ba_3Yb_2O_5Te$	Direct (2.2 eV)	-	Yb^{3+}	YbO_5	Yes	*P4/mmm*	-	DOI: 10.1016/j.jssc.2013.04.030
La_2O_2Te	Indirect (2.7 eV)	-	La^{3+}	La_4O	Yes	No (*I4/mmm*)	-	DOI: 10.1021/acs.inorgchem.2c02287
Pr_2O_2Te	Indirect (2.6 eV)	-	Pr^{3+}	Pr_4O	Yes	No (*I4/mmm*)	-	DOI: 10.1021/acs.inorgchem.2c02287
Ce_2O_2Te	Indirect (2.1 eV)	-	Ce^{3+}	Ce_4O	Yes	No (*I4/mmm*)	-	DOI: 10.1021/acs.inorgchem.2c02287
LaCuOTe	Direct (2.4 eV)	p-type	Cu^{2+}	$CuTe_4$	No	*P4/nmm*	-	DOI: 10.1021/acsaem.2c00590

1.4. Band edges positions

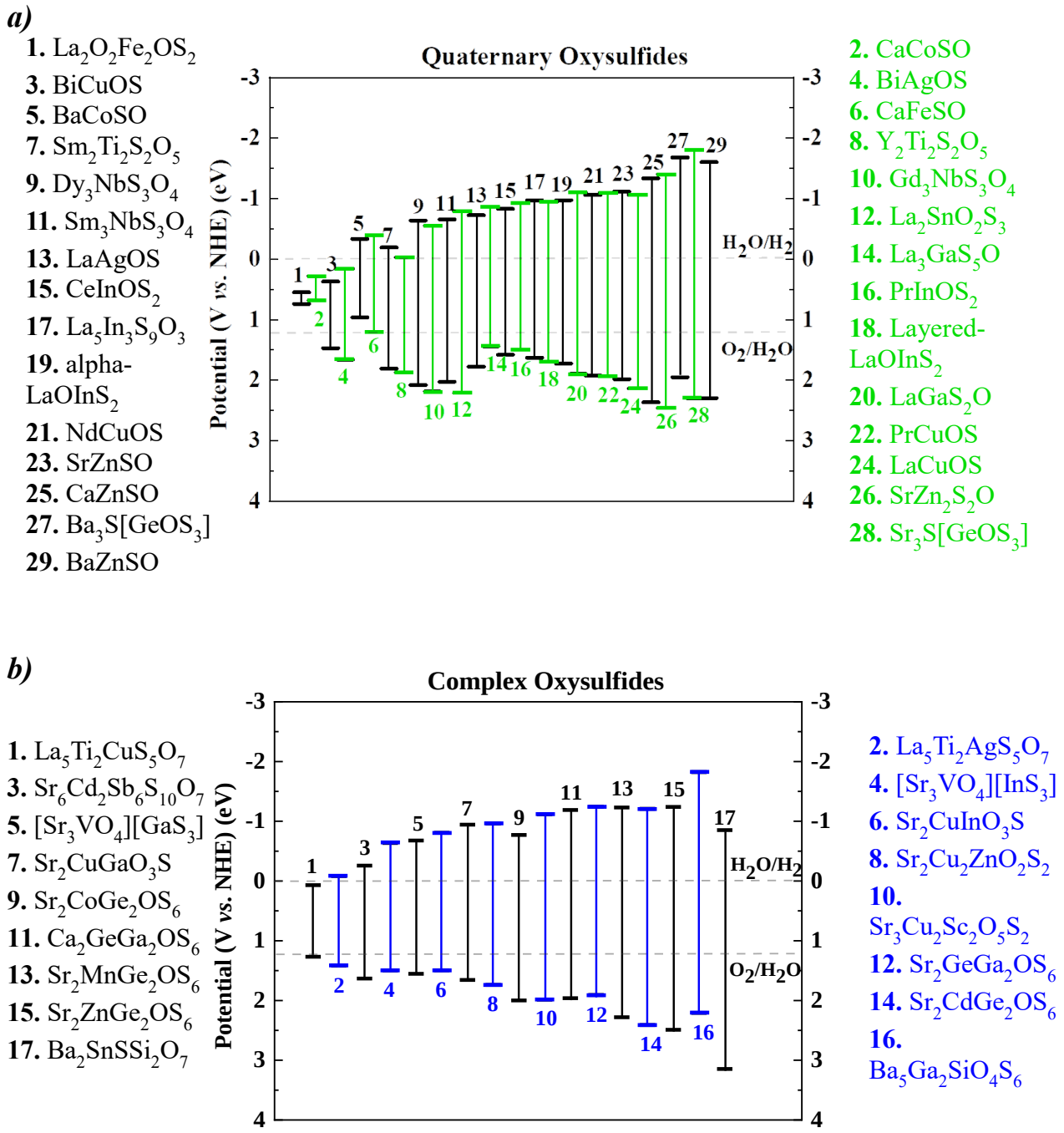

Figure 1.1 : Estimated band edge positions using the empirical method of (a) Quaternary Oxysulfides and (b) Complex Oxysulfides.

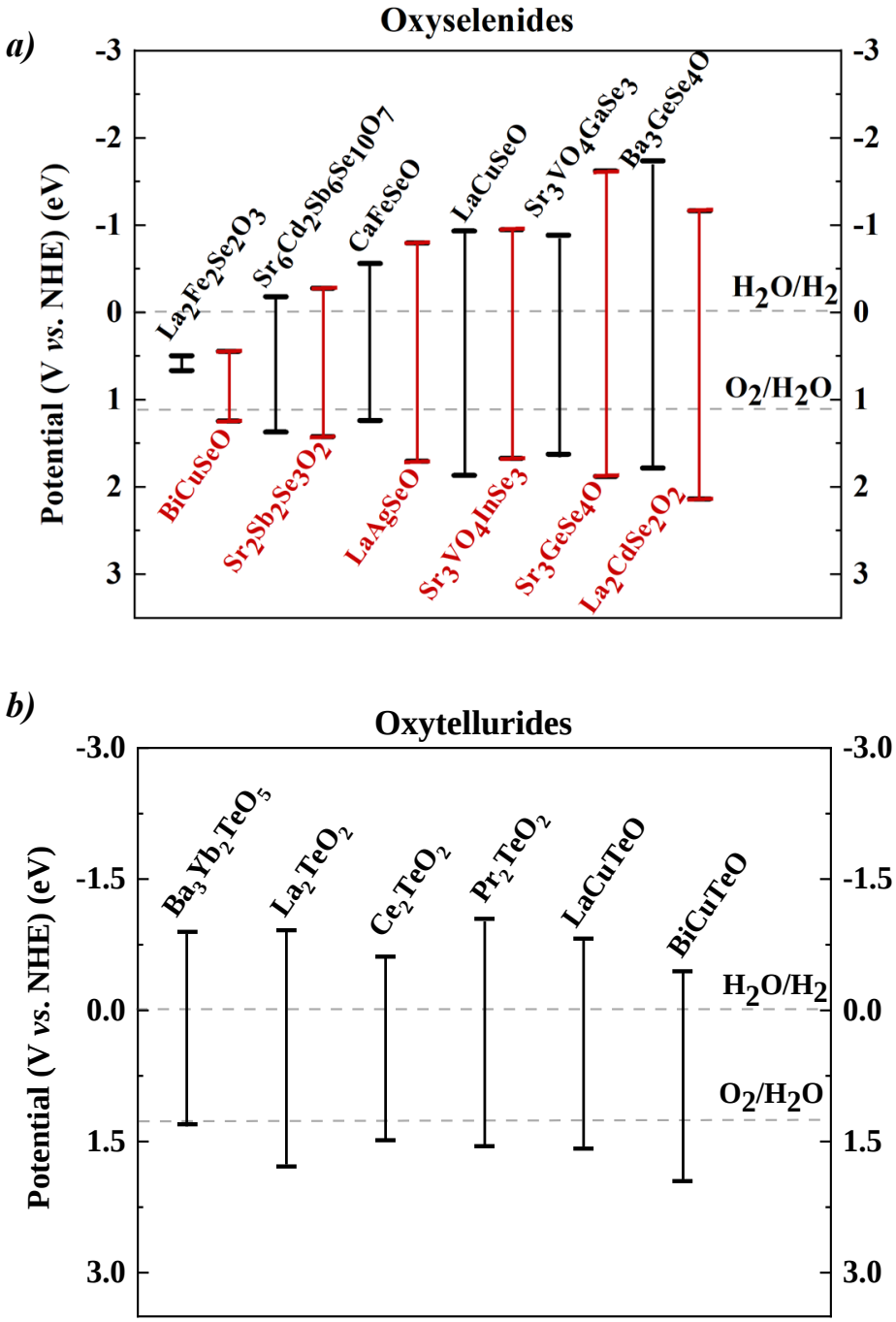

Figure 1.2 : Estimated band edge positions using the empirical method of (a) Oxyselenides and (b) Oxytellurides.

1.5. List of the photocatalytic activity of the reported oxysulfides

Compounds		Cocatalysts		Rate of gas evolution (μmol/h)	
		H_2 promotor	O_2 promotor	H_2	O_2
Ln$_2$Ti$_2$S$_2$O$_5$[1]	$Pr_2Ti_2S_2O_5$	Pt	-	0	0
	$Nd_2Ti_2S_2O_5$			4	3
	$Gd_2Ti_2S_2O_5$			24	21
	$Tb_2Ti_2S_2O_5$			19	20
	$Dy_2Ti_2S_2O_5$			10	9
	$Ho_2Ti_2S_2O_5$			22	5
	$Er_2Ti_2S_2O_5$			21	1
$Y_2Ti_2S_2O_5$[2]		Cr_2O_3/Rh/IrO_2		~50	~25
$Sm_2Ti_2S_2O_5$[3,4]		Pt	IrO_2	22	22
$SrZn_2S_2O$[5]		Pt	IrO_2	67.8	26.9
$LaInOS_2$	α-$LaInOS_2$[6]	Pt	-	5.1	-
	Layered-$LaInOS_2$[7]	Pt	IrO_2	~25	~6
A$InOS_2$[8]	$CeInOS_2$	Pt	-	< 2.5	-
	$PrInOS_2$	Pt	-	< 2.5	-
$La_5In_3S_9O_3$[9]		Pt	IrO_2	~50	~12
La_3GaS_5O[10]		$RuCl_3.3H_2O$	IrO_2	80.7	~12
$La_5Ti_2MS_5O_7$[11,12]	$La_5Ti_2CuS_5O_7$	Pt	IrO_2	110	24
	$La_5Ti_2AgS_5O_7$	Pt	IrO_2	220	12
$La_5Ti_2Cu_{1-x}Ag_xS_5O_7$[13]		Pt	-	~32	-

REFERENCES

(1) Ishikawa, A.; Takata, T.; Matsumura, T.; Kondo, J. N.; Hara, M.; Kobayashi, H.; Domen, K. Oxysulfides Ln2Ti2S2O5 as Stable Photocatalysts for Water Oxidation and Reduction under Visible-Light Irradiation. *The Journal of Physical Chemistry B* **2004**, *108* (8), 2637–2642.

(2) Wang, Q.; Nakabayashi, M.; Hisatomi, T.; Sun, S.; Akiyama, S.; Wang, Z.; Pan, Z.; Xiao, X.; Watanabe, T.; Yamada, T. Oxysulfide Photocatalyst for Visible-Light-Driven Overall Water Splitting. *Nature materials* **2019**, *18* (8), 827–832.

(3) Ishikawa, A.; Takata, T.; Kondo, J. N.; Hara, M.; Kobayashi, H.; Domen, K. Oxysulfide Sm2Ti2S2O5 as a Stable Photocatalyst for Water Oxidation and Reduction under Visible Light Irradiation (Λ≤ 650 Nm). *Journal of the American Chemical Society* **2002**, *124* (45), 13547–13553.

(4) Ishikawa, A.; Yamada, Y.; Takata, T.; Kondo, J. N.; Hara, M.; Kobayashi, H.; Domen, K. Novel Synthesis and Photocatalytic Activity of Oxysulfide Sm2Ti2S2O5. *Chemistry of materials* **2003**, *15* (23), 4442–4446.

(5) Nishioka, S.; Kanazawa, T.; Shibata, K.; Tsujimoto, Y.; Zur Loye, H.-C.; Maeda, K. A Zinc-Based Oxysulfide Photocatalyst SrZn 2 S 2 O Capable of Reducing and Oxidizing Water. *Dalton Transactions* **2019**, *48* (42), 15778–15781.

(6) Kabbour, H.; Sayede, A.; Saitzek, S.; Lefevre, G.; Cario, L.; Trentesaux, M.; Roussel, P. Structure of the Water-Splitting Photocatalyst Oxysulfide α-LaOInS 2 and Ab Initio Prediction of New Polymorphs. *Chemical Communications* **2020**, *56* (11), 1645–1648.

(7) Miura, A.; Oshima, T.; Maeda, K.; Mizuguchi, Y.; Moriyoshi, C.; Kuroiwa, Y.; Meng, Y.; Wen, X.-D.; Nagao, M.; Higuchi, M. Synthesis, Structure and Photocatalytic Activity of Layered LaOInS 2. *Journal of Materials Chemistry A* **2017**, *5* (27), 14270–14277.

(8) Ito, H.; Miura, A.; Goto, Y.; Mizuguchi, Y.; Moriyoshi, C.; Kuroiwa, Y.; Azuma, M.; Liu, J.; Wen, X.-D.; Nishioka, S. An Electronic Structure Governed by the Displacement of the Indium Site in In–S 6 Octahedra: LnOInS 2 (Ln= La, Ce, and Pr). *Dalton transactions* **2019**, *48* (32), 12272–12278.

(9) Ogisu, K.; Ishikawa, A.; Teramura, K.; Toda, K.; Hara, M.; Domen, K. Lanthanum–Indium Oxysulfide as a Visible Light Driven Photocatalyst for Water Splitting. *Chemistry letters* **2007**, *36* (7), 854–855.

(10) Ogisu, K.; Ishikawa, A.; Shimodaira, Y.; Takata, T.; Kobayashi, H.; Domen, K. Electronic Band Structures and Photochemical Properties of La− Ga-Based Oxysulfides. *The Journal of Physical Chemistry C* **2008**, *112* (31), 11978–11984.

(11) Katayama, M.; Yokoyama, D.; Maeda, Y.; Ozaki, Y.; Tabata, M.; Matsumoto, Y.; Ishikawa, A.; Kubota, J.; Domen, K. Fabrication and Photoelectrochemical Properties of La5Ti2MS5O7 (M= Ag, Cu) Electrodes. *Materials Science and Engineering: B* **2010**, *173* (1–3), 275–278.

(12) Suzuki, T.; Hisatomi, T.; Teramura, K.; Shimodaira, Y.; Kobayashi, H.; Domen, K. A Titanium-Based Oxysulfide Photocatalyst: La 5 Ti 2 MS 5 O 7 (M= Ag, Cu) for Water Reduction and Oxidation. *Physical Chemistry Chemical Physics* **2012**, *14* (44), 15475–15481.

(13) Hisatomi, T.; Okamura, S.; Liu, J.; Shinohara, Y.; Ueda, K.; Higashi, T.; Katayama, M.; Minegishi, T.; Domen, K. La 5 Ti 2 Cu 1− x Ag x S 5 O 7 Photocathodes Operating at Positive Potentials during Photoelectrochemical Hydrogen Evolution under Irradiation of up to 710 Nm. *Energy & Environmental Science* **2015**, *8* (11), 3354–3362.

Chapter 2

Experimental & Computational methods

Chapter 2: Experimental & Computational methods

2.1. Experimental methods

2.1.1. Synthesis methods

The solid-state reaction is one of the most common routes, adapted to the synthesis of numerous materials of different families, such as oxides,[1,2,3] sulfides[4] and oxychalcogenides.[5,6,7] It is a simple method that consists on heating a mixture of reagents in a stochiometric ratio, which allows the inter-diffusion of the different precursors to form a homogenous powder. This method has many advantages, especially in its simple realization, and the use of not so expensive reagents. On the other hand, this method requires good mixing of reagents which takes long time compared with other synthesis routes and needs high temperatures (up to 1100°C for some perovskites)[8] as it requires diffusion of ions to reaction points. It can also result in big grain sizes (µm or higher) compared to other synthesis such as citrate or co-precipitation.

The reagents used in this project are air sensitive. Therefore, the reagents were all stored in an argon filled glovebox, where the mixing and grinding took place. To ensure better contact, mixtures were pelletized and then loaded into quartz tubes. Depending on the reactivity of the precursors with the quartz tubes, pellets were placed in alumina crucibles or the tubes were carbon coated to avoid contact. Thermal treatments varied for each family of materials.

2.1.2. Characterization techniques

2.1.2.1. Single Crystal and Powder X-ray Diffraction (SCXRD/ PXRD)

Crystalline materials have two major characteristics: (i) the periodic arrangement of atoms resulting in defined planes within the structure differentiated with the Miller indices (hkl); (ii) the interarticular distances (d_{hkl}) between the different planes, varying between 0.1 to 15 Å. One way to characterize these materials is by X-ray diffraction, which is a nondestructive and very effective method. It consists of directing X-rays at a sample, which will be diffracted by the different planes in the structure, and then detected as a function of scattering angle.

For powder analysis, X-ray powder diffraction (XRPD) is used for phase identification and can provide information on unit cell dimensions.[9,10] The sample is usually scanned through a range of

2θ angles in all possible directions (crystallites in powder samples are randomly oriented) and diffracted rays are detected (**Figure 2.1a**) when conditions satisfy Bragg's law:

$$n\lambda = 2d_{hkl}sin\theta \qquad (2.1)$$

where λ is the wavelength of the X-ray, *n* is the diffraction order, d_{hkl} is the interplanar distance and *θ* is the Bragg angle. Using equation (2.1), the interplanar distances (d_{hkl}) can be determined. A Bruker D8 A25 diffractometer equipped with a Lynxeye XET linear detector (Cu Kα) in Bragg−Brentano geometry at room temperature was used to collect the X-ray diffraction patterns presented in this work. Regarding the profile of the obtained peaks, other structural parameters can be determined, such as the crystallites size using the Scherrer method[11] or the micro-constraints using Williamson et Hall method.[12,13]

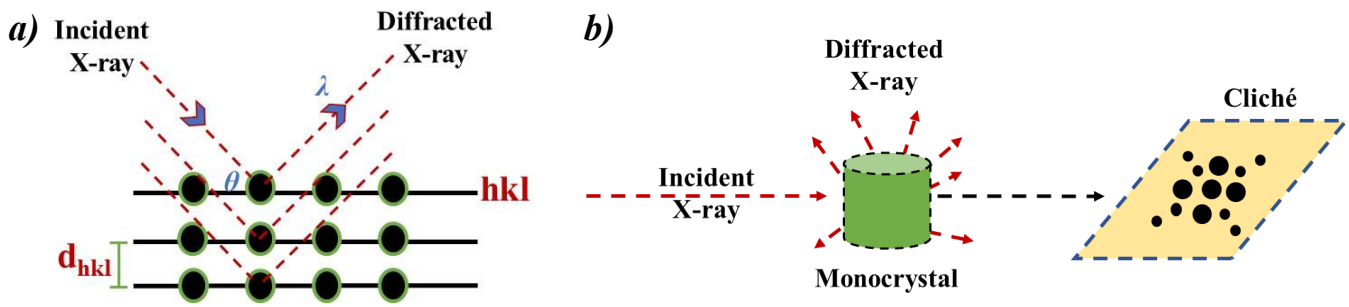

Figure 2.1 : (a) Bragg-Brentano geometry. (b) Single crystal diffraction principle.

Single crystal X-ray diffraction (SCXRD) (**Figure 2.1b**) works based on the same principle as powder X-ray diffraction and is very powerful for crystal structure solution. In a SCXRD experiment, the geometry of the incident rays, the orientation of the centered crystal and the detector can be changed, which allows all possible diffraction directions of the lattice. The data generated by the X-ray analysis can later be interpreted and refined to determine the crystal structure. A Bruker DUO diffractometer equipped with a two-dimensional (2D) CDD detector and a Mo Kα source was used to perform the single crystal X-ray diffraction (SCXRD) experiment presented in this manuscript.

2.1.2.2. Rietveld refinement

The Rietveld method is valuable for structure analyses of nearly all classes of crystalline materials; it consists on carrying out least-square method to refine crystal structures to fit experimental XRPD data. A good starting model is required then structural, instrumental features and specimen effects (displacement, transparency) are refined to fit the whole pattern until the best fit is reached.[14] To judge the proceeding of the refinement, fitting statistics are reported at each refinement cycle such as χ^2 that determines how well the calculated pattern fits, R_{wp} that indicates if the residual is minimized and describes how closely the calculated data fits the observed pattern and R_p based on the deduced Bragg intensities. Rietveld refinements presented in this work were carried out using Fullprof[15] software. The background, sample height, lattice parameters, peak profiles (pseudo-Voight), atomic positions and atomic displacement parameters were refined.

With powder X-ray diffraction data, we have the problem of peak or profile overlapping which makes it hard to use for structure solution, thus single crystal data is used for structure solution. Therefore, Jana2006 suite[16] allows structure solutions using the charge flipping procedure of the SUPERFLIP program[17] implemented in it. Using X-ray, neutron, synchrotron or electron diffraction data, this software allows the solution of periodic and aperiodic crystal structures. For processing the data, two routes can be used: (i) using predefined diffractometer outputs (cell parameters, wavelength…) imported automatically, (ii) use the reflection file and enter manually the necessary information. The next step is the symmetry wizard, where the highest possible lattice symmetry is searched (regarding the provided unit cell parameters). This is followed by the determination of the Laue symmetry for comparison of the internal *R* values and the redundancies. Depending on the figure of merit values, the space group can be chosen. SUPERFLIP[18] or SIRWARE[19] can be used for structure solution; refinements combined with Fourier difference maps analysis can be conducted in order to reach the final structural model.

2.1.2.3. Electron Microscopy (TEM/SEM) and energy-dispersive X-ray (EDX)

One technique widely used to observe and chemically characterize materials is electron microscopy, in which a beam of electrons bombards a sample. The two common types are: transmission (TEM) and scanning (SEM) electron microscopy. Electron microscopy relies on the strong interaction between accelerated electrons and the sample which can result in many phenomena including transmitted or scattered electrons and photons (**Figure 2.2**).

In transmission electron microscopy (TEM), a beam of accelerated electrons is transmitted through the sample which are then investigated to characterize the material. The electron beam is focused using a set of condenser lenses. Samples must be thin (100 nm) and the applied voltage is high enough for the electron beam to pass through the sample without being fully absorbed. Experiments can be conducted in two modes: image or diffraction depending on the required information. The advantage of this technique is that the obtained images are very high resolution (~ 0.04 nm) which allows atomic resolution; crystallographic information (crystal lattice defects and faults) can be determined as well in crystalline materials.

In a scanning electron microscope (SEM), unlike TEM, the electron beam is scanned on the surface and not transmitted through the sample. SEM uses secondary and backscattered electrons to give an image. In the backscattered mode, the image is more sensitive to the atomic number.[20]

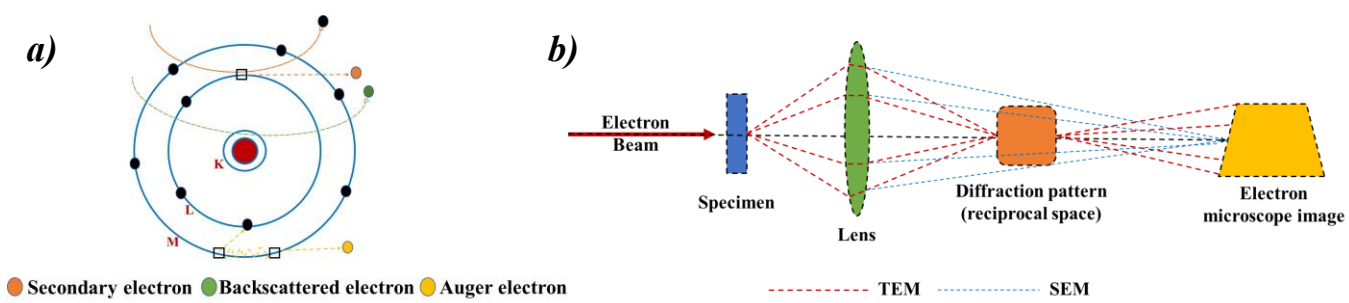

Figure 2.2 : (a) Different electrons-nucleus interactions. (b) Concept of the diffraction function of electron microscopy.

Another widely used spectroscopic technique is energy-dispersive X-ray (EDX) spectroscopy. It is for elemental analysis and chemical characterizations. Similar to the other spectroscopic techniques, EDX depends on the interaction between the incident electrons and the sample and gives characteristic X-rays. When the specimen is stimulated with the electron beam, an electron from the inner shell of the atom is ejected, creating then a hole and an electron from the outer shell (higher energy) fills it. The X-rays released have energy corresponding to the energy difference of the two electron levels. These X-rays, characteristic of the elements present, are detected.

Professor Marielle Huvé performed the TEM experiments presented in **Chapter 5** on a FEI Technai G2-20 twin microscope; the powder was crushed and dropped in the form of an alcohol suspension on carbon-supported copper grids, followed by evaporation under ambient conditions. EDX is usually coupled with SEM and the measurements can be done simultaneously. A Hitachi

S3400N microscope was used and the powder specimens were deposited on Platine plots. A carbon coat (done by cathodic pulverization) was sometimes added, depending on the nature of the elements in the tested powder to avoid surface charging.

2.1.2.4. UV-Visible spectroscopy and band edge position calculations

The optical band gaps of the compounds presented in this work were determined using UV-visible spectroscopy. Its principle consists of exciting the outermost electrons of the atoms using a source of photons, the absorbance is the absorbed part of the photon spectrum by the sample whilst the reflectance is the reflected part of the photon flux by the samples' surface. Usually the observed signals are recorded against a reference material (borate of sodium in our case). Depending on the measured variable, the other one can be determined according to equation (2.2):

$$A = -logR \qquad (2.2)$$

where A is the absorbance and R is the reflectance.

A PerkinElmer Lambda 650 spectrophotometer was used for our measurements; both absorbance and reflectance could be measured from 200 to 900 nm with a 1 nm resolution. The corresponding plot is of the reflectance/absorbance against the wavelength. The Kubelka-Munk transformation[21] $F(R)=(1-R)^{(1/n)}/2R$ was applied to the reflectance and the magnitude of the optical band gap E_g was determined using the Tauc plot method[22,23] by drawing $[F(R)h\upsilon]^{1/n}$ vs. $[h\upsilon]$ (where $h\upsilon$ is the photon energy), n is a constant that depends on the gap transition nature (n = 1/2 for a direct band gap and n = 2 for an indirect band gap). The intersection between the linear part of the plot with the x axis (wavelengths) is the value of the optical band gap we are looking for, which can help calculate the band edges positions, discussed in the next section.

One requirement in semiconductors for water splitting photocatalysis under solar light is having band edge positions compatible with the redox potential of water: CBM < 0 V (reduction potential of H_2O/H_2) and a VBM > 1.23 V (oxidation potential of O_2/H_2O) (**Chapter 1**, **Section 1.2.2**). Butler and Ginley[24] proposed an empirical model that allows the calculation of both valence and conduction band edge positions, which is based on the Mulliken electronegativities and the band gap of the compound. This method was further described by Xu and Schoonen,[25] using equation (2.3) to do the calculations:

$$E_{VB,CB} = E_0 + \prod_{M=1}^{n} \chi_M^{j\,1/n} \pm E_{gap}/2 \tag{2.3}$$

where $E_{VB,CB}$ corresponds to the positions of the valence and conduction band edges; E_0 to the difference between the normal hydrogen electrode (NHE) and the vacuum (E_0 = -4.5 eV); χ_M is the electronegativity of the atom M in the Mulliken scale with n the number of atoms and j the stochiometric ratio calculated using the equation (2.4):

$$\chi_M = \frac{Electron\ Affinity + Ionization\ Potential}{2} \tag{2.4}$$

where the electron affinity (*EA*) is the tendency of the atoms to capture an electron whilst the ionization potential (*E*) is the necessary energy to extract an electron (in electronvolt (eV)). Such calculations for the band edge positions were previously reported in a study by Castelli *et al.*[26]

Our strategy consisted of calculating the band edge positions for different reported materials depending on their band gaps (measured or calculated), which allowed us to narrow the number of compounds to go forward in synthesizing and characterizing. Thus, after measuring the optical band gaps, we calculated the VB and CB band edge positions which allowed us to check their compatibility with the redox potential of water, confirming then their potential candidature as visible light water splitting photocatalysts. **Figure 2.3** presents an example of the band edge positioning towards the redox potential of water.

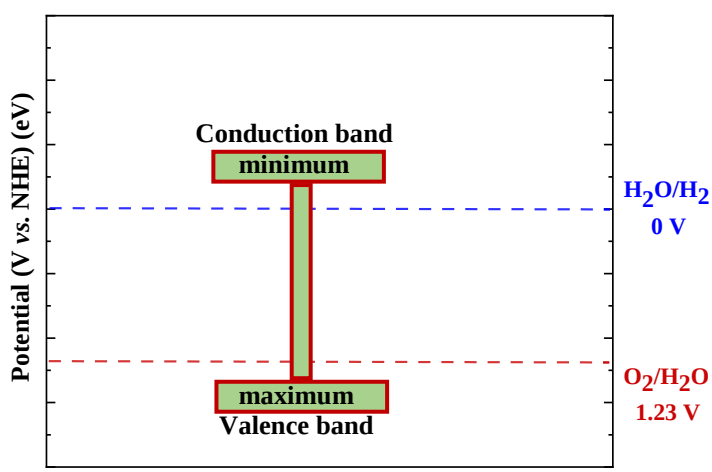

Figure 2.3 : Example of an ideal band edge positions encompassing the redox potential of water.

2.1.2.5. Thermal Analysis

The thermal stability of our compounds was investigated by means of thermogravimetric analysis (TGA), thermal dilatometric analysis (TDA) and mass spectrometry (MS). Using these techniques gave us insight into the temperature limit required for the synthesis of some compounds, an helped investigate phase transitions and identifying its nature.

Thermogravimetric analysis (TGA) consists of measuring the variation of the samples mass as a function of an applied thermal treatment with or without a controlled atmosphere (argon, nitrogen, air). It is a plot of the percentage of mass variation against the temperature or the time, and then the derivative of the curve allows the determination of the temperature values where the mass varies significantly. As mentioned before, the temperature limit of materials can be identified and depending on the observed mass losses, oxidation and degradation can be detected. On the other hand, thermal dilatometric analysis (TDA) is a complementary method that can be coupled with TGA and that helps identify other sorts of transitions that are not accompanied with certain mass loss, such as phase transitions including fusion and crystallization. As for the thermogravimetric analysis, TDA can be performed under controlled atmosphere and in this case, the enthalpy variation is measured as a function of temperature. The plot is the variation of the heat flow against the temperature or the time, where exothermic and endothermic peaks can be observed. Depending on the nature of the observed peaks, different transition types can be identified (e.g. a peak with no weight loss associated can be a phase transition).

In the case of phase degradation (peaks associated with a weight loss), mass spectrometry (MS) is a very effective technique that gives insight to the nature of the evolved gases from the sample by measuring the mass-to-charge ratio (m/z) of charged particles. This proved to be useful in determining the elemental composition of evolved gases. Its principle consists of ionizing the tested compounds which then will result in molecular fragments (charged molecules) of which the m/z ratios can be measured.

TGA and TDA signals are measured simultaneously using the a TGA-92 thermobalance, and the atmosphere was controlled by evacuating and then filling the thermobalance with the carrier gas before heating the sample. The evolved gases of the MS signal were monitored by an Omnistar quadrupole mass spectrometer (Pfeiffer). The experiments presented in this work were performed under pure argon at a rate of 5 °C/min.

2.1.3. Electrochemical measurements

2.1.3.1. Film preparation and photocurrent setup description

For electrochemical measurements, the studied material is considered to be the working electrode. As our sample is a powder, it had to be transformed into a thick film for measurements and this was done using the drop casting method.[27] **Figure 2.4** presents the principle of this method, it consists first of dispersing the photocatalyst powder in water and an organic solvent (Polyvinylidene fluoride PVDF), acting as binder until an homogeneous paste is obtained. Depending on the desired thickness of the film, drops of the prepared paste are deposited on an ITO/glass substrate (DeltaTechnologies®). Finally, the electrode is heated at high temperatures (300 °C) for a certain time to eliminate any organic residue and enhance the adherence.

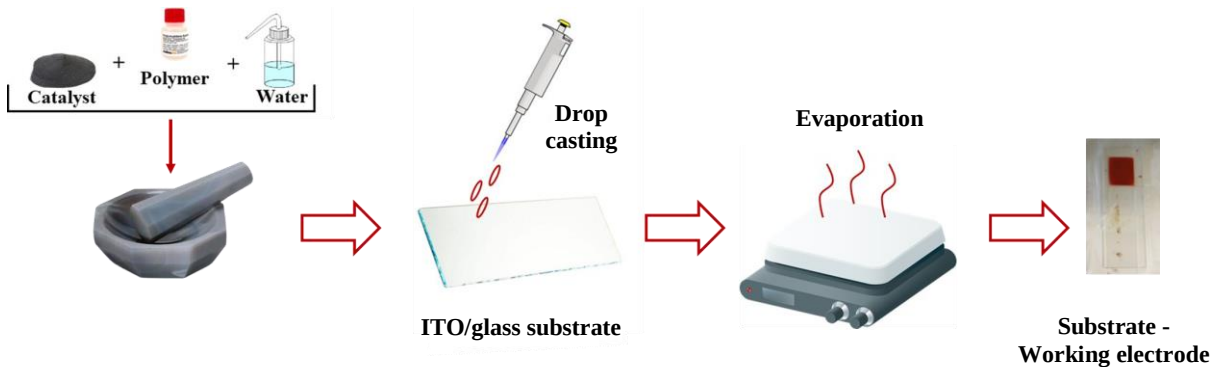

Figure 2.4 : Explanatory diagram of the ''Drop-casting'' method.

The electrochemical device (Autolab PGSTAT204, Metrohm) coupled to a LED module (LED driver kit, Metrohm) was used to collect the photocurrents. The measurements were performed in standard three-electrode cell (Magnetic mount photo-electrochemical cell (Redox.me®) (**Figure 2.5**). Ag/AgCl and Pt wire acted as reference electrode and counter electrode, respectively. This cell allows standardized illumination over 1 cm² by the backside of the working electrode. The electrolyte employed is an aqueous 0.1 M sodium sulfate (Na_2SO_4) solution.

The LEDs (450, 470, 505, 530, 590 and 627 nm with low spectral dispersion) were calibrated using a photodiode to determine the density of the luminous flux received by the sample. This procedure requires placing a photodiode at a certain distance from the source and exposing it to various intensities controlled by the current passing in the LED device. The density of the luminous flux (P_{LED}) is calculated depending on the current measured by the photodiode (i_p).

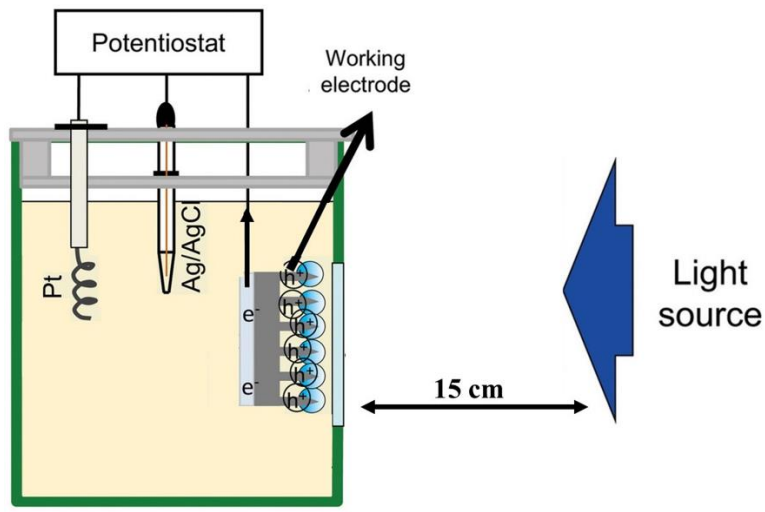

Figure 2.5 : Photo-electrochemical measurements device.

Several factors can affect the intensity, such as the distance source/photodiode (*d*), intensity of the current of the LED (I_{LED}) even the nature of the LED (each LED has a different flux regarding the wavelengths). Based on previous results, we chose a 15 cm distance and a 450 nm wavelength excitation to do the calibration (**Figure 2.6**).

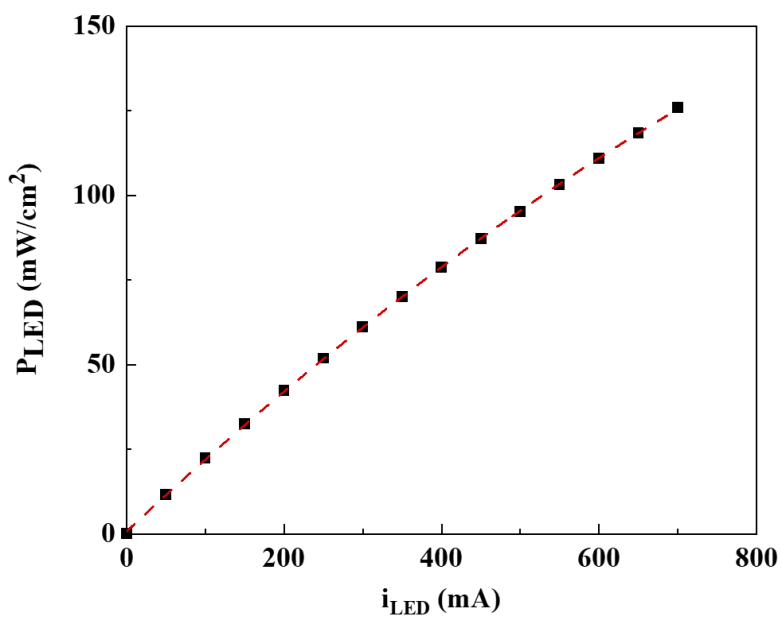

Figure 2.6 : Evolution of the density of the luminous flux received by the sample in function of the distance between the source and the photodiode.

2.1.3.2. Photocurrent measurements description

During the electrochemical measurements, the device (semiconductor/electrolyte) is illuminated with incident light (*hυ*) with higher energy than the band gap, resulting in electron – hole pairs. Then by applying an external bias voltage, these pairs can separate and migrate either towards the inside of the semiconductor or the semiconductor/electrolyte interface. In the second case, the corresponding charge carriers can be transferred to the electrolyte generating then the photocurrent.[28] Depending on the semiconduction type, an anodic or cathodic photocurrent can be seen for p or n type semiconductor, respectively. Linear sweep is another test that confirms the presence or not of a photocurrent, and gives insight to the semiconduction type. **Figure 2.7** represents the current-potential (j-V) plots characteristics for both semiconductors.[29]

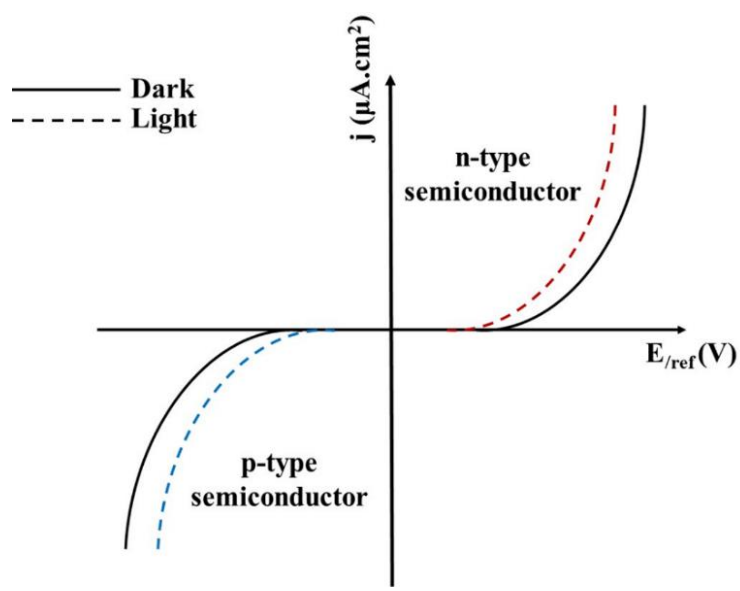

Figure 2.7 : Linear sweep plots characteristics for an n-type and p-type semiconductors.

The photocurrent was defined by Gärtner and Butler[30,31] using equation (2.5):

$$i_{ph} = \Phi_0 (1 - \frac{e^{-\alpha_{abs} W}}{1 + \alpha_{abs} L_c}) \qquad (2.5)$$

where i_{ph} is the photocurrent, Φ_0 is the incident luminous flux, α_{abs} is the semiconductor absorption coefficient, W is the depletion layer thickness and L_c is the diffusion length. The absorption is a function of the semiconductor band gap (E_g) and transition nature (direct/indirect), which means that the absorbance is significant for an incident light energy higher than the band gap; resulting in higher photocurrent values.

Following the Gärtner & Butler theory,[30,31] it is clear that the photocurrent varies linearly with the intensity of the luminous flux. **Figure 2.8** show its evolution as a function of the intensity of the luminous flux. During this evolution, two phenomena can be detected: i) Linear, following the Gärtner & Butler model ($\Delta j = a\Phi_0$, in green) and ii) non-linear, according to a classical power law[32] ($\Delta j = a\Phi_0^n$, in red). The fitting of this non-linear evolution gives a curve that goes through the origin and that allows the value of the exponent *n* to be determined. This exponent is dependent on the thickness of the film and gives insight to the traps number within the material. It can vary between 0.5 (suggesting a complex process of electron-hole generation, recombination and trapping within the sample) and 1 (ideal trap-free system).[33] For high light intensities, the photocurrent becomes independent of the light intensity received, due to a saturation of photo-generated electron-hole pairs and/or a limitation of mobility in the layer.[34] This observation was further investigated by B. Ullrich,[35] and helped calculate the generated photoelectrons:

$$G_{pe} = B_c n_{pe}(n_{pe} + M) \infty \, \Phi_0 \qquad (2.6)$$

where G_{pe} is the generated photoelectrons, B_c is the capture coefficient, n_{pe} is density of the photoelectrons, M is the impurity and Φ_0 is the intensity of the luminous flux.

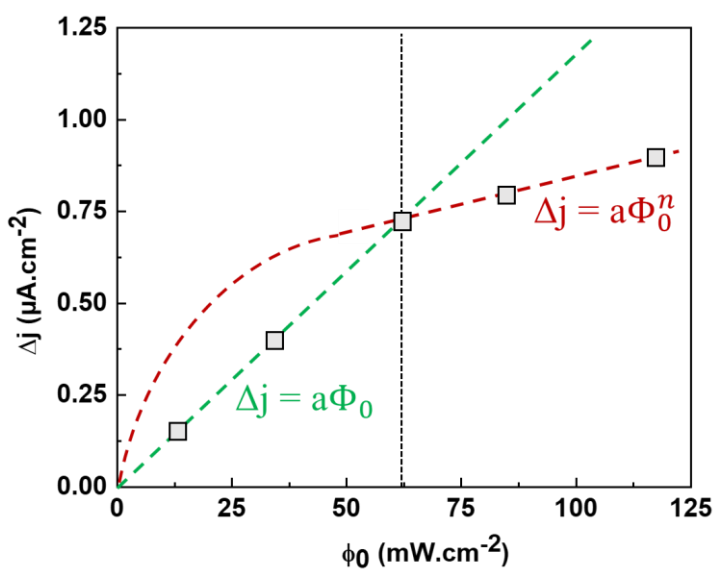

Figure 2.8 : Evolution of the photocurrent density in function of the intensity of the luminous flux.

According to the Gärtner-Butler model discussed above, they only considered the transferred charge carriers' phenomena for the photocurrent generation. But other phenomena can occur where these separated pairs can recombine and therefore can also influence the generated photocurrent.

The competition between these two phenomena can be seen in the photocurrent plots characterized with a spikey peak shape. Upon illumination the electron/hole pairs separate rapidly, loading then the semiconductor/electrolyte intersurface which results in the spike; then the establishment of an equilibrium state between the recombination and the transfer of the carriers, result in this decay in the curve until a stationary state. **Figure 2.9a** shows an example of this behaviour with an emphasis on the characteristics of the peak. The transfer and recombination rate constants alongside the transfer efficacity can be determined in this case according to a model proposed by Parkinson *et al.*[36] and the time constant of the decay is given by expression (2.7):

$$\frac{j(t)-j(\infty)}{j(0)-j(\infty)} = e^{-\frac{t}{\tau}} \quad \text{with} \quad \tau = \frac{1}{k_{rec}+k_{tr}} \qquad (2.7)$$

where τ, k_{rec} and k_{tr} are the time, recombination rate and transfer rate constants, respectively. Moreover, the ratio of the steady state photocurrent to the instantaneous photocurrent observed when the illumination is switched on is given by expression (2.8)[37]:

$$\frac{j(\infty)}{j(0)} = \frac{k_{tr}}{k_{tr}+k_{rec}} = \eta_{tr} \qquad (2.8)$$

These two expressions make it possible to calculate the values of k_{tr}, k_{rec} and η_{tr} (transfer efficacity). We finally highlight that observing this behaviour is an indication of fast kinetics in generating the photocurrent whilst in the case of slow kinetics (**Figure 2.9b**), the peak is not present; an exponential increase/decrease is observed and the rate constants can't be determined.

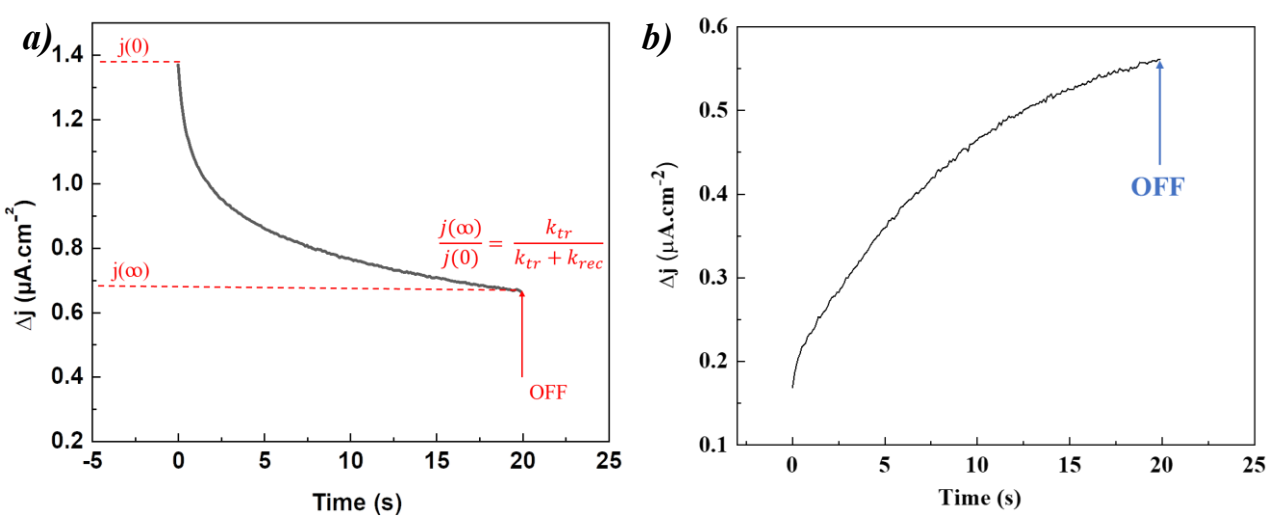

Figure 2.9 : Photocurrent density for Φ_0 = 22 mW.cm^{-2} of (a) $Sr_6Cd_2Sb_6S_{10}O_7$ highlighting *j(0)* and *j(∞)*(taken from Chapter 4) and (b) $Sr_2Sb_2S_3O_2$ with slower kinetics (taken from Chapter 5).

Mott-Schottky test is one way to determine the concentration of the charge carriers (*N*) and the flat band potential (E_{fb}).[38] It can be expressed by the capacity of the following equation (2.9):

$$\frac{1}{C^2} = \frac{2}{eA^2\varepsilon\varepsilon_0 N}\left(V - V_{fb} + \frac{k_B T}{e}\right) \qquad (2.9)$$

where *C* and *A* are the interfacial capacitance and area, respectively; *N* is the number of donors, *e* is the electronic charge, k_B is the Boltzmann constant ($k_B = 8.617303.10^{-5}$ eV. K^{-1}), *V* is the applied voltage, V_{fb} is the flat band potential, *T* is the absolute temperature, ε is the dielectric constant of the semiconductor and ε_0 is the permittivity of free space. **Figure 2.10** shows the plot of ($1/C^2$) against the potential (V) characteristic of a p-type (negative slope) and n-type (positive slope) semiconductor, where the flat band potential V_{fb} can be determined from the intercept of the straight line of the plot on the *V* axis; The number of donors *N* can be found as well from the slope knowing ε and *A*.[38] The extracted value of the flat band is *vs*. the reference electrode (Ag/AgCl), but it can be converted to the RHE scale (E_{RHE}) of the reversible hydrogen electrode[39] with equation (2.10):

$$E_{RHE} = E_{Ag/AgCl} + E^0_{Ag/AgCl} + 0.059.pH \qquad (2.10)$$

where $E^0_{Ag/AgCl\ vs.SHE}$ is the potential of the Ag/AgCl reference electrode with respect to the standard hydrogen electrode (SHE) fixed at 195 mV and the pH of the used electrolyte (5.6 for 0.1 M of Na_2SO_4). Determining the flat band potential (V_{fb}) serves to locate the VB or CB positions for a p-type and n-type semiconductors, respectively[39] as it reflects the position of the Fermi level which lies at 0.1 V lower/higher than the conduction/valence band, respectively.[40,41,42]

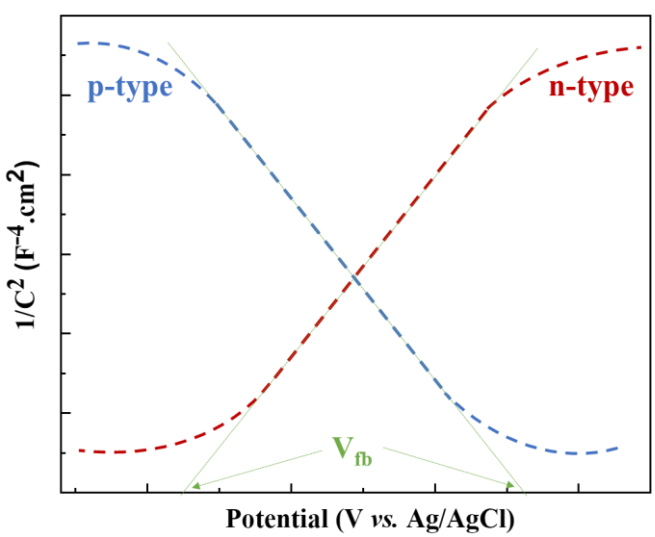

Figure 2.10 : Mott-Schottky plots characteristics for an n-type and p-type semiconductors.

Looking at the relation defining the photocurrent (equation 2.6), we know that several features can influence the photocurrent, including the applied potential (V_{bias}), the intensity of the luminous flux (Φ_0), the choice of the wavelength (λ) and the temperature. The electrochemical characterizations presented in this manuscript were performed in the setup presented in **Figure 2.11**, while investigating the influence of the potential (V_{bias} = 0, 0.2, 0.4, 0.6 and 0.8 V), the wavelengths (λ = 450, 470, 505, 530, 590 and 627 nm) and the luminous flux (solar or UV).

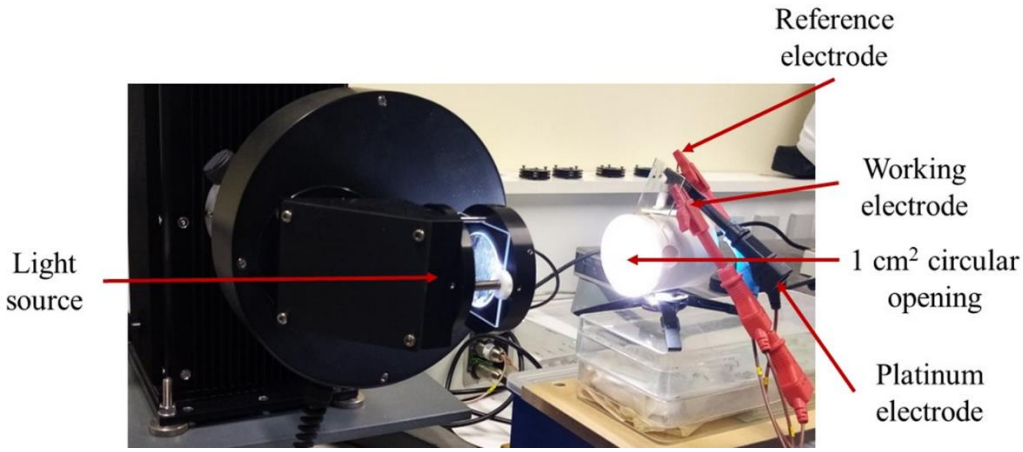

Figure 2.11 : Electrochemical setup used for all photocurrent measurements.

2.1.4. Photocatalysis setup and protocol

All the photocatalytic measurements were conducted in the setup presented in **Figure 2.12**. The aim was to study the photodegradation of Rhodamine B (test molecule, pink colored) under UV (254 nm, 40 W) and solar (100 mW cm^{-2}) irradiations. The photo-reactor consisted of a 200 ml flask of the solution irradiated from above and aluminum foil covers to prevent radiation exposure.

First, the solution (containing 200 mL of Rhodamine B (5×10^{-6} mol dm^{-3}) and 100 mg of the photocatalyst powder) was placed in a sonicator for 20 mins (to break up agglomerates) and stirred for 30 mins in the dark to ensure an appropriate adsorption/desorption equilibrium.[43] The solution was then irradiated with either UV or solar light and samples were taken, at regular intervals to monitor the evolution of the concentration of the photodegraded Rhodamine B by spectrophotometry. The samples were then centrifuged for 20 mins in order to separate any catalyst residue. Absorbance measurements were carried out using a Shimadzu UV-2600 UV-visible spectrophotometer and the percentage of the Rhodamine B's discoloration can be determined:

$$D(\%) = \frac{A_\lambda^0 - A_\lambda}{A_\lambda^0} \times 100 = \frac{C_0 - C_t}{C_0} \times 100 \qquad \text{with} \qquad A_\lambda = \varepsilon_\lambda l C_t \qquad (2.11)$$

where l the length of the sample container (1 cm), ε_λ is the molar extinction coefficient. C_0 and C_t are the concentration of Rhodamine B and A_λ^0 and A_λ are the absorbances at t_0 and t, respectively. In order to get insights to the reaction's kinetics at the solid-liquid interface, the Langmuir-Hinshelwood (LH) model can be applied to determine the apparent rate constant K_{app}.[44] Taking an order 1 for the photodegradation reaction and plotting $\mathrm{Ln}(C_0/C)$ *vs.* time, the value of K_{app} can be directly extracted from the slope according to equation (2.12):

$$v = K_{app} C_A \qquad (2.12)$$

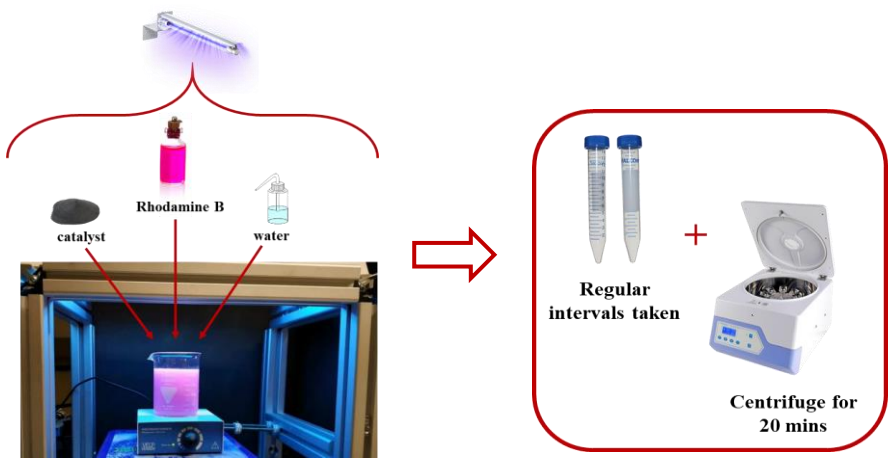

Figure 2.12 : Setup and protocol developed for the photocatalytic measurements.

2.2. Computational methods

In a quantum system with more than one electron/nucleus (N system), the system is so large that the Schrödinger equation can't be analytically solved. Different numerical approximations were developed with the widely used two are: (i) Hartree-Fock and post-Hartree-Fock (MPn, CI, CASSCF) methods based on the electronic wavefunction, differentiating in the Hamiltonian that treats the electronic correlation effect in the post-Hartree-Fock method. (ii) Density functional theory (DFT) that uses electronic charge densities (3D object) instead of wavefunctions and the multielectron contributions are represented by means of an exchange and correlation potential which define the precision of this method.

2.2.1. Electronic Hamiltonian

In order to have information about the electronic, chemical and physical properties of a multielectron quantum system, with *N* electrons, the goal is to solve the Schrödinger equation:

$$\mathrm{H}\Psi = \mathrm{E}\Psi \qquad \text{with} \qquad \hat{H} = \hat{T}_e + \hat{T}_n + \hat{V}_{n-e} + \hat{V}_{e-e} + \hat{V}_{n-n} \qquad (2.13)$$

where *H* is the electronic Hamiltonian; *E* the total energy of the system and Ψ is the wavefunction; $\hat{T}$ is a kinetic energy operator and $\hat{V}$ is the potential energy operator, e/n are the electron and nucleus contribution, respectively and n-e (attractive), e-e and n-n (repulsive) are the contributions for nucleus-electron, electron-electron and nucleus-nucleus respectively.

According to the Born-Oppenheimer approximation, the nuclei have a much larger mass than the electrons; so, their kinetic energy ($\hat{T}_n$) can be neglected, and the nucleus-nucleus repulsion term is considered as a constant $\hat{V}_{n-n}$. The solution of the global Hamiltonian is therefore based on the determination of the electronic Hamiltonian only:

$$\hat{H} = \hat{T}_e + \hat{V}_{n-e} + \hat{V}_{e-e} \qquad (2.14)$$

2.2.2. First principle calculation theory

2.2.2.1. Electronic density

The electron density $\rho(r)$ can be defined as the probability per unit volume of finding an electron in a specific location around an atom or molecule. Unlike the wavefunction, the electron density is an observable and its determination gives insight to the physico-chemical properties of a system. It can be described as a positive function depending upon three spatial variables (*x*, *y*, *z*) and it can be determined by the normalized *N*-electron wavefunction Ψ using equation (2.15):

$$\rho(r) = < \Psi \,|\hat{\rho}(r)|\Psi > \qquad (2.15)$$

where the wavefunction itself depends upon 4*N* variables (3*N* spatial and *N* spin coordinates). Thomas-Fermi theory of atoms and molecules in 1927 was the first attempt to express the electron density, but this model was incomplete and did not answer a number of questions.[45,46] Numerous models[47] were developed later on but the one proposed by Hohenberg and Kohn is the model currently in use.

2.2.2.2. The Hohenberg - Kohn Theorem

The Hohenberg - Kohn theorems were the first to theoretically describe the non-degenerated ground states in an external potential v(r) (electric or magnetic field).[48] The first theorem demonstrates that the electron density uniquely determines the ground state properties of a multi-electron system, based on equation (2.16):

$$E[\rho(\boldsymbol{r})] = F_{HK}[\rho(\boldsymbol{r})] + \int \rho(\boldsymbol{r})\, v_{ext}(\boldsymbol{r})\, d^3\boldsymbol{r} \quad \text{with} \quad F_{HK}[\rho(\boldsymbol{r})] = T_e[\rho(\boldsymbol{r})] + V_{e-e}[\rho(\boldsymbol{r})] \quad (2.16)$$

where F_{HK} is called the Hohenberg-Kohn free energy.

The second Hohenberg - Kohn theorem defines an energy functional for the system and proves that the ground-state electron density minimizes this energy functional. In a way, if $F_{HK}[\rho(r)]$ is known, the electron density of the multi-electron system can be determined.[49]

2.2.2.3. Kohn-Sham equations

The Kohn-Sham equation system is based on a fictitious system of non-interacting particles that generate the same electronic density and is defined by a local effective external potential V_{eff}(r), called the Kohn-Sham potential. This includes the external potential and the effects of the Coulomb interactions between the electrons (exchange and correlation interactions). Therefore, equation (2.16) is now expressed as follow:

$$E[\rho(\boldsymbol{r})] = T_{ref}[\rho(\boldsymbol{r})] + J[\rho(\boldsymbol{r})] + \int \rho(\boldsymbol{r})\, v_{ext}(\boldsymbol{r})\, d^3\boldsymbol{r} + E_{xc}[\rho(\boldsymbol{r})]$$

$$\text{with} \quad J[\rho(\boldsymbol{r})] = \frac{1}{2}\frac{\rho(\boldsymbol{r})\rho(\boldsymbol{r}')}{|\boldsymbol{r}-\boldsymbol{r}'|} d^3r d^3r' \qquad (2.17)$$

where $J[\rho(\boldsymbol{r})]$ is a classical Coulomb interactions term, $T_{ref}[\rho(\boldsymbol{r})]$ is the kinetic energy of the non-interacting particles reference system, $E_{xc}[\rho(\boldsymbol{r})]$ is the exchange and correlation interaction energy and it represents the necessary correction to apply in order to get the exact total energy and it can be expressed as follow:

$$E_{xc} = T - T_{KS} + E_{ee} - E_H \quad (2.18)$$

where T is the exact many-body (KE), T_{KS} is the many-body (KE) of Kohn-Sham (KS) orbitals, E_{ee} is the exact electron-electron interaction and E_H is the Hartree electron-electron interaction. And the reference system can be described as follows:

$$\left\{-\frac{1}{2}\nabla_i^2 + v_{eff}(\boldsymbol{r})\right\}\psi_i(\boldsymbol{r}) = \varepsilon_i\psi_i(\boldsymbol{r}) \qquad (2.19)$$

where ψ_i is the Kohn-Sham orbital, and the external potential $V_{eff}(\boldsymbol{r})$ is a functional derivative of the total energy expressed by:

$$V_{eff}(\boldsymbol{r}) = V_H(\boldsymbol{r}) + V_{xc}(\boldsymbol{r}) + v_{ext}(\boldsymbol{r}) \quad (2.20)$$

where $V_H(\boldsymbol{r})$ and $V_{xc}(\boldsymbol{r})$ are the classic Hartree potential and the exchange and correlation potential, respectively and they are defined as follow:

$$V_H(\boldsymbol{r}) = \int \frac{\rho(\boldsymbol{r}')}{|\boldsymbol{r}-\boldsymbol{r}'|} d^3r' \quad (2.21)$$

$$V_{xc}(\boldsymbol{r}) = \frac{\delta E_{xc}[\rho(\boldsymbol{r})]}{\delta\rho(\boldsymbol{r})} \quad (2.22)$$

2.2.2.4. Exchange-correlation functionals

Various approximations can be used to solve the Kohn-Sham equations; the simplest one being the local density approximation (LDA). This model is based upon the exact exchange energy for a uniform free electron gas and it considers the exchange and correlation effects to be local properties depending on the electronic density only. It is reasonably effective and good for many simple systems but it tends to over-bind atoms (calculating the bonds too short and strong and too small lattice parameters) and it can be expressed as follows:

$$E_{xc}^{LDA}[n(r)] = \int n(r)\varepsilon_{xc}^{hom}[n(r)]dr \quad (2.23)$$

Another improved model is the generalized gradient approximation (GGA), which include the value of the electron density and its derivative (taking into account the strong variations of the electronic density with *r*, i.e. close to the nucleus). It is fairly quick to calculate and it tends to under-bind atoms (makes bonds too weak) but it's better for surfaces and it can be expressed by:

$$E_{xc}^{GGA}[n(r)] = \int n(r)\varepsilon_{xc}^{GGA}[n(r), \nabla n(r)]dr \quad (2.24)$$

There are many GGAs, depending on the parametrization of the data, such as PW91[50], PBE[51], RPBE[52], WC[53], PBEsol.[54] Although these approximations are the most widely used, they tend to fail with Van der Waals bonded, localized electrons and/or strongly correlated materials. In these cases, other approximations were developed such as the Hybrid functionals (e.g. HSE06, B3LYP)[55] or DFT+U, LDA+DMFT, that are more demanding.

2.2.2.4.1. PBE functional

Most of the calculations presented in this work were performed using the PBE exchange and correlation functional of the generalized gradient approximation (GGA), developed by Perdew, Burke and Ernzerhof.[51] The PBE functional is a simple derivation, in which all parameters, including the local spin density (LSD) are fundamental constants. It is close to the PW91 (Perdew-Wang 1991) functional[50], but with smoother potential and easier way to understand and apply.

In addition to retaining the correct features of LSD, the PBE correlation functional combines them with the most energetically important features of gradient-corrected nonlocality. This allowed the resolution of a few additional problems compared to the previous model (i.e. PW91); such as the large number of parameters that induces artificial local minima in potential energy surfaces, as well as the implicit inclusion of exchange effects.

2.2.2.4.2. DFT + U functional

DFT+U method was used in **Chapter 3**, for the iron based oxychalcogenides with strongly correlated *nd* electrons. The Hubbard *U* correction[56] provides a cheap alternative to hybrid functional calculations for improving the description of the electronic structure.[57,58,59]

Several variants of the DFT+U method exist (LDAUTYPE = 1|2|4). The simplified approach (formalism 2) introduced by Dudarev et *al.*[60] was used. This correction is added on the semilocal total energy expression (equation 2.27) that forces the on-site occupancy matrix in the direction of idempotency (either fully occupied or fully unoccupied levels). However, in this formalism the result depends quite strongly on the choice of the effective on-site interaction parameter (U_{eff} = U – J) which is dependent on the orbital being corrected, element, and system;[61,62,63] rather than U (Coulomb repulsion) and J (exchange screening), which are not entered separately.

2.2.3. Calculation method

All the calculations conducted during this work were carried out using the Vienna *ab initio* simulation package (VASP).[64] It is based on density functional theory (DFT) using pseudopotentials and the projector-augmented-wave method.[65] The approach implemented in VASP is based on the local-density approximation with the free energy as a variational quantity and instantaneous electronic ground state is evaluated.

The projector-augmented-wave (PAW) method encoded in VASP was developed by Blöchl[66] by combining ideas from pseudopotential and linearized augmented-plane-wave (LAPW) methods. This formalism introduces a linear transformation from the pseudo (PS) to the all-electron (AE) wave function and derives the PAW total energy functional in a consistent manner to solve the Kohn-Sham (KS) equations. It consists of the fact that if the nuclei are arranged periodically then the potential and the density (measurable properties) are periodic as well; whereas the wavefunction is not measurable, hence quasi-periodic and it is expressed as follow:

$$\psi_k(r) = e^{ik.r}\mu_k(r) \quad (29) \quad \text{with} \quad \mu_k(r) = \sum_G C_{Gk} e^{iG.r} \quad (2.25)$$

where *k* is considered as phase factor, difference of the ψ's phase between the two-unit cells and *G* represents the reciprocal lattice vectors. Therefore, the density is expressed as follows:

$$\rho(r) = \int |\psi_k(r)|^2 d^3k \quad (2.26)$$

where *k* is a quantum number and depending on this number of *k* points, the total energy of the calculation can converge. The *k* points are sampled within the first Brillouin zone (BZ) (Monkhorst-Pack mesh) and the number of points depends on the size of the BZ (The bigger the real space unit cell is, the smaller the BZ and fewer *k*-points are needed).

2.2.3.1. Basics (Planewaves / pseudopotentials)

Planewaves are the basic functions used in the VASP code and are ideal to use for periodic systems, they satisfy Blöchl's theorem. A 3D Fourier basis (also known as plane waves) is used as a way to evaluate the total energy and its derivatives. On the other hand, these planewaves are not accurate in describing the strong variations of the electronic density near the nuclei and this is why they are coupled with the pseudopotentials to get a more accurate description of the electronic structure of the treated material.

When using the pseudopotential approximation, the valence electrons are the ones considered, as they contribute to the chemical bonding and therefore to most of the properties. This contrasts with the core electrons that do not participate in the bonding and so are coarsely modelled and fixed during the calculation and the wavefunction parts closest to the core are almost neglected. **Figure 2.13** represents the use of planewaves and pseudopotentials in function of the core radius, where beneath a certain radius the planewaves are replaced by pseudopotentials (containing

no nodes). During our calculations, we used the projector augmented wave (PAW) potentials, which allowed us to conduct accurate calculations and very similar to the all-electrons code.

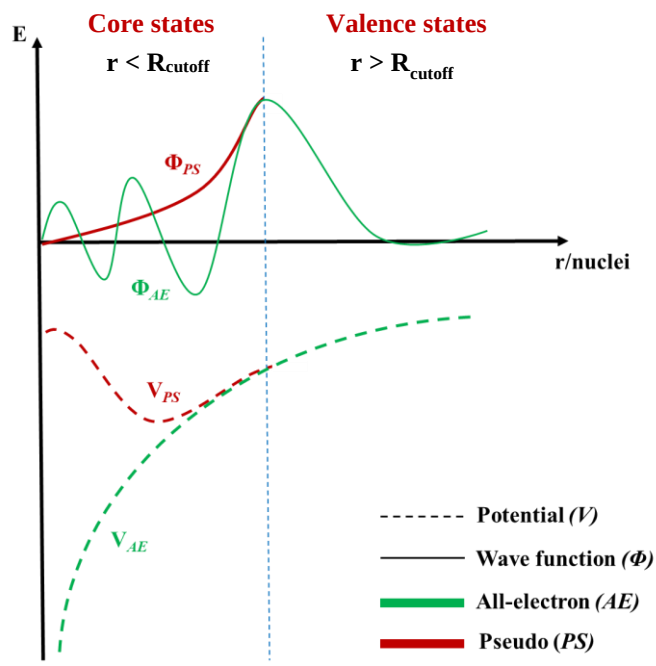

Figure 2.13 : All-electron and pseudo wave functions (solid line) and potentials (dotted line).[67]

2.2.3.2. Hellman-Feyman theorem

The Hellman-Feyman (HF) theorem[68,69] has been a key ingredient of the quantum mechanical treatment of forces acting on nuclei in molecules and solids. According to this theorem the force on nuclei depends on the charge density and can be expressed in terms of the gradient of the total energy. In a fundamental state, the atomic forces and the total energy in the system can therefore be evaluated and described using equation (2.27) and (2.28), respectively:

$$F_\alpha = -\frac{dE}{dR_\alpha} = -\frac{\partial E}{\partial R_\alpha} \qquad (2.27)$$

$$E_{tot} = \frac{1}{2}\sum_{\alpha=1}^{N_z}\sum_{\beta\neq\alpha}\frac{Z_\alpha Z_\beta}{|R_\alpha - R_\beta|} + \sum_{i=1}^{N}\varepsilon_i + \int\left\{\varepsilon_{xc}[\rho(\boldsymbol{r})] - V_{xc}(\boldsymbol{r}) - \frac{1}{2}V_H(\boldsymbol{r})\right\}\rho(\boldsymbol{r})\,d\boldsymbol{r} \qquad (2.28)$$

2.2.3.3. Geometry optimization

An important step in every DFT calculation is to perform a structural or geometry optimization. The energy surface around a minimum is quadratic in small displacements and therefore, can be

determined by the matrix of the second derivatives of the total energy. The simplest is damped molecular dynamics (MD) where while the atoms are moving (according to the atomic forces), they will lose energy to reach a lowest energy state.

According to the Hellman-Feynman theorem, the atomic forces are calculated and a good structure can be found with only reliable forces, but the forces converge more slowly than energies. For the nuclear positions, the electron density and the total energy of the system is calculated. With every step of the calculation, the self-consistent field (SCF) energy calculation is done, the atomic forces are recalculated and the nuclear positions are updated. When the change in atomic forces becomes negligible and the crystalline structure stable (i.e. stable electron density), convergence is reached (degree of SCF $\leq 10^{-6}$ eV/atom for a 'fine' quality).

2.2.3.4. Electronic band structure calculation

The band structure is a good way to visualize the wavevector-dependence of the energy states. The electronic structure is how the electrons are arranged and ordered in space and energy. In the Brillouin zone let's take two limits for the energy of states, electrons with high potentials and electrons with high kinetics. In the case of a material having very localized electrons, i.e. trapped in a very strong potential (caused by the interactions of the electrons with the ions), the kinetics can be neglected and the energy of the wavefunction in this case is independent of *k*:

$$E(k) = \int V(r)|u(r)|^2 d^3r \qquad (2.29)$$

In this case the band structure is isolated and the energy does not vary with the *k*-points. In the opposite case, where the electron has no potential interactions, therefore everything depends on the kinetic energy and our wavefunction can be written now as follows:

$$E(k) = \frac{\hbar^2}{2m}(k+G)^2 \qquad (2.30)$$

The energy then varies quadratically with *k* and it's at its lowest for G = 0; so now we have the energy of each state that varies with *k* which results in an energy band instead of a singular energy (there's a range of energy values we can get depending on where we are in the reciprocal space). In the case of free electrons, we see a parabolic band.

Trying to plot these band structures in 3D is much more complicated and one way to do it is by carefully choosing the directions between the high symmetry points in which the energy varies and this is where the basic idea of a band structure plot lies. In real materials, electrons are neither completely localized nor free, but we still see these features in band structures.

2.2.3.5. Density of states calculation

The band structure is a good way to visualize the dispersion of the energy states (bands) along high symmetry directions. But the transition probability (between states) depends on how many states are available in the initial and final energies. Therefore, the full density of states (DOS) is across the whole Brillouin zone (BZ) and not just the special directions and is expressed as:

$$g(E) = \frac{1}{\Omega_G}\frac{dN}{dE} \qquad (2.31)$$

where Ω_G is the volume of reciprocal space associated with each G-vector. After computing the ground state electronic density with a good *k*-point sampling, the density is fixed and then we find the states at the DOS k-points. The only difference between computing the DOS and the band structure is the choice of sample *k*.

2.2.3.6. Effective masses calculation

The charge carriers' effective masses (for the electrons (m_e^*) and for the holes (m_h^*)) provides essential information to understand the electronic properties of a material. The mobility of the electrons and the holes significantly influences the photocatalytic mechanism efficiency[70,71] in a way that the higher photogenerated mobility favours a higher photocatalytic outcome.[72] VASPKIT program[73] using the VASP code allowed us to extract the corresponding effective mass values. In the case of semiconductors, the CBM and VBM can be approximated as parabolic and the m^* is calculated from one symmetry point to another (**Figure 2.14**) using equation (2.32):

$$\left(\frac{1}{m^*}\right)_{ij} = \frac{1}{\hbar^2}\frac{\partial^2 E_n(k)}{\partial k_i k_j} \qquad (2.32)$$

where $E_n(k)$ corresponds to the n^{-th} electronic band in *k*-space and $\hbar$ is the reduced Planck constant. Usually, band structures show different dispersions of the bands at the CBM and VBM suggesting different mobility of electrons and holes where smaller effective masses are found in the case of

large dispersions (m^* is inversely proportional to the curvature of the electronic dispersion in reciprocal space), as shown in equation (2.32), above.

Prior to the effective masses' extraction, the self-consistent electronic calculation is followed by a non-self-consistent calculation along the high symmetry lines with a fine spacing of *k*-points in reciprocal space. The band dispersion is fitted with a second-order polynomial schematically alongside a third-order polynomial that helps stabilize the fitting. Orientation-dependent effective masses of charge carriers can also be determined using this functionality.[73]

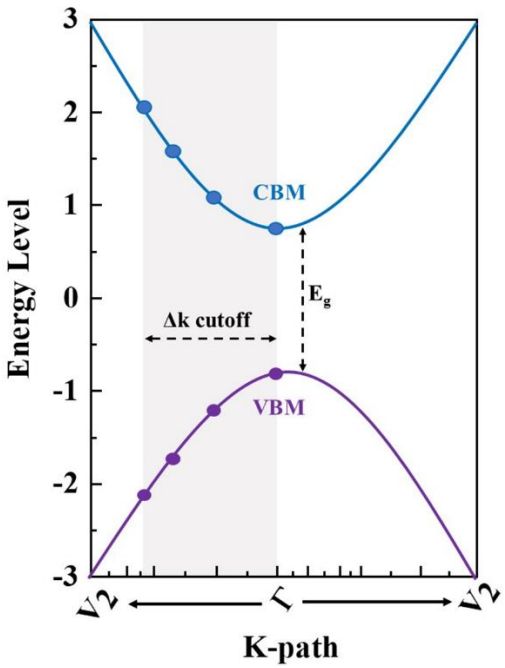

Figure 2.14 : Schematic illustration of the determination of effective masses around the CBM and VBM.

2.2.3.7. Electron localization function

In order to investigate qualitatively different chemical bonds and lone pair electrons, the electron localization function (ELF) can be computed, giving insight into the nodal structure of the molecular orbitals. The total electron density reveals atomic shell structure, electron pairs[74] and is the fundamental independent variable of many-electron theory.[75] Electron localization is fundamentally related to parallel-spin pair probability, through which the effects of Pauli exchange repulsion (no two identical fermions can occupy the same quantum state) are directly reflected.[76] The electron localization function which depends on the total electronic density, its gradient, and the kinetic energy density is expressed by equation (2.33):[77]

$$ELF = (1 + X_\sigma^2)^{-1} \quad \text{with} \quad X_\sigma = {D_\sigma}/{D_\sigma^0} \qquad (2.33)$$

where X_σ is a dimensionless localization index calibrated with respect to the uniform-density electron gas and D_σ^0 is a uniform electron gas with spin-density equal to the local value of $\rho_\sigma(r)$.

Later on, B. Silvi & A. Savin[78] reported a method to classify the different chemical bonds based on a topological analysis of the local-quantum functions related to the Pauli exclusion principle. The localization attractors, defined by the maxima of these functions, can be bonding, non-bonding or core attractors. In particular, electron densities can provide a classification of the different bonds (covalent or ionic) based on the spatial organization of these localization attractors. Whereas shared electron interactions can be characterized based on the bonding attractors.

In addition, based on the calculated ELF, we can determine the critical points that can help determine the electronic charge and volume for selected elements, These calculations were conducted in the Critic2 program[79,80] using the Yu and Trinkle (YT) method.[81]

2.2.4. Crystal Orbital Hamilton Population

Crystal Orbital Hamilton Population (COHP) analysis[,82,83] gives insight to the bonding nature and strength. The calculation is based on rewriting the band structure energy as a sum of orbital pair contributions. The projected p-COHP diagram allows a comparative study by giving access to projected contributions on specific bonds with the dispersion within a specified energy range (bonding, nonbonding and antibonding), and can be defined by expression (2.34):

$$\text{pCOHP}\ (E, K) = \sum_j R\left[P_{\mu j \nu}^{(proj)}(k) H_{\nu\mu}^{(proj)}(k)\right] \times \delta(\varepsilon_j(k) - E) \qquad (2.34)$$

On the other hand, the integral I-COHP diagram represents the nature (bonding/antibonding) and strength of the bond in average (contribution of an atom or a chemical bond to the distribution of one-particle energies) and it is expressed by equation (2.35):

$$\text{IpCOHP}\ (\varepsilon_F) = \int_1^{\varepsilon_F} \text{pCOHP}\ (E)dE \qquad (2.35)$$

The COHP (Crystal Orbital Hamilton Population) analysis was carried out in the framework of the LOBSTER software.[84]

REFERENCES

(1) Ji, S. M.; Choi, S. H.; Jang, J. S.; Kim, E. S.; Lee, J. S. Band Gap Tailored Zn (Nb1− x V x) 2O6 Solid Solutions as Visible Light Photocatalysts. *The Journal of Physical Chemistry C* **2009**, *113* (41), 17824–17830.

(2) Chen, J.; Zhai, Y.; Yu, Y.; Luo, J.; Fan, X. Spatial Separation of Photo-Induced Charge Carriers in a Na3VO2B6O11 Polar Material and Its Enhanced Photocatalytic Activity. *Applied Surface Science* **2021**, *556*, 149809.

(3) Fuierer, P. A.; Newnham, R. E. La2Ti2O7 Ceramics. *Journal of the American Ceramic Society* **1991**, *74* (11), 2876–2881.

(4) Kumari, A.; Vidyasagar, K. Solid-State Synthesis, Structural Variants and Transformation of Three-Dimensional Sulfides, AGaSnS4 (A= Na, K, Rb, Cs, Tl) and Na1. 263Ga1. 263Sn0. 737S4. *Journal of Solid State Chemistry* **2007**, *180* (7), 2013–2019.

(5) Wang, R.; Liang, F.; Wang, F.; Guo, Y.; Zhang, X.; Xiao, Y.; Bu, K.; Lin, Z.; Yao, J.; Zhai, T. Sr6Cd2Sb6O7S10: Strong SHG Response Activated by Highly Polarizable Sb/O/S Groups. *Angewandte Chemie International Edition* **2019**, *58* (24), 8078–8081.

(6) Salter, E. J.; Blandy, J. N.; Clarke, S. J. Crystal and Magnetic Structures of the Oxide Sulfides CaCoSO and BaCoSO. *Inorganic Chemistry* **2016**, *55* (4), 1697–1701.

(7) Panella, J. R.; Chamorro, J.; McQueen, T. M. Synthesis and Structure of Three New Oxychalcogenides: A2O2Bi2Se3 (A= Sr, Ba) and Sr2O2Sb2Se3. *Chemistry of Materials* **2016**, *28* (3), 890–895.

(8) Motohashi, T.; Ueda, T.; Masubuchi, Y.; Takiguchi, M.; Setoyama, T.; Oshima, K.; Kikkawa, S. Remarkable Oxygen Intake/Release Capability of BaYMn2O5+δ: Applications to Oxygen Storage Technologies. *Chem. Mater.* **2010**, *22* (10), 3192–3196. https://doi.org/10.1021/cm100290b.

(9) Sakata, M. t; Cooper, M. J. An Analysis of the Rietveld Refinement Method. *Journal of Applied Crystallography* **1979**, *12* (6), 554–563.

(10) McCusker, L. B.; Von Dreele, R. B.; Cox, D. E.; Louër, D.; Scardi, P. Rietveld Refinement Guidelines. *Journal of Applied Crystallography* **1999**, *32* (1), 36–50.

(11) Monshi, A.; Foroughi, M. R.; Monshi, M. R. Modified Scherrer Equation to Estimate More Accurately Nano-Crystallite Size Using XRD. *World journal of nano science and engineering* **2012**, *2* (3), 154–160.

(12) Pelleg, J.; Elish, E.; Mogilyanski, D. Evaluation of Average Domain Size and Microstrain in a Silicide Film by the Williamson-Hall Method. *Metallurgical and Materials Transactions* **2005**, *36* (11), 3187.

(13) Zak, A. K.; Majid, W. A.; Abrishami, M. E.; Yousefi, R. X-Ray Analysis of ZnO Nanoparticles by Williamson–Hall and Size–Strain Plot Methods. *Solid State Sciences* **2011**, *13* (1), 251–256.

(14) Young, R. A. *The Rietveld Method*; International union of crystallography, 1993; Vol. 5.

(15) Rodriguez-Carvajal, J. Fullprof: A Program for Rietveld Refinement and Profile Matching Analysis of Complex Powder Diffraction Patterns. *Laboratoire Léon Brillouin (CEA-CNRS)* **1991**.

(16) Petříček, V.; Dušek, M.; Palatinus, L. Crystallographic Computing System JANA2006: General Features. *Zeitschrift für Kristallographie-Crystalline Materials* **2014**, *229* (5), 345–352.

(17) Lee, A. Charge Flipping for Routine Structure Solution. *Journal of Applied Crystallography* **2013**, *46* (5), 1306–1315.

(18) Palatinus, L.; Chapuis, G. SUPERFLIP–a Computer Program for the Solution of Crystal Structures by Charge Flipping in Arbitrary Dimensions. *Journal of Applied Crystallography* **2007**, *40* (4), 786–790.

(19) Burla, M. C.; Caliandro, R.; Camalli, M.; Carrozzini, B.; Cascarano, G. L.; De Caro, L.; Giacovazzo, C.; Polidori, G.; Spagna, R. SIR2004: An Improved Tool for Crystal Structure Determination and Refinement. *Journal of Applied Crystallography* **2005**, *38* (2), 381–388.

(20) Howell, P. G. T.; Davy, K. M. W.; Boyde, A. Mean Atomic Number and Backscattered Electron Coefficient Calculations for Some Materials with Low Mean Atomic Number. *Scanning: The Journal of Scanning Microscopies* **1998**, *20* (1), 35–40.

(21) Kubelka, P.; Munk, F. A Contribution to the Optics of Pigments. *Z. Tech. Phys* **1931**, *12* (593), 193.

(22) Tauc, J.; Grigorovici, R.; Vancu, A. Optical Properties and Electronic Structure of Amorphous Germanium. *physica status solidi (b)* **1966**, *15* (2), 627–637.

(23) Murphy, A. B. Band-Gap Determination from Diffuse Reflectance Measurements of Semiconductor Films, and Application to Photoelectrochemical Water-Splitting. *Solar Energy Materials and Solar Cells* **2007**, *91* (14), 1326–1337.

(24) Butler, M.; Ginley, D. Prediction of Flatband Potentials at Semiconductor-electrolyte Interfaces from Atomic Electronegativities. *Journal of the Electrochemical Society* **1978**, *125* (2), 228.

(25) Xu, Y.; Schoonen, M. A. The Absolute Energy Positions of Conduction and Valence Bands of Selected Semiconducting Minerals. *American Mineralogist* **2000**, *85* (3–4), 543–556.

(26) Castelli, I. E.; Landis, D. D.; Thygesen, K. S.; Dahl, S.; Chorkendorff, I.; Jaramillo, T. F.; Jacobsen, K. W. New Cubic Perovskites for One-and Two-Photon Water Splitting Using the Computational Materials Repository. *Energy & Environmental Science* **2012**, *5* (10), 9034–9043.

(27) Cha, S. M.; Nagaraju, G.; Sekhar, S. C.; Yu, J. S. A Facile Drop-Casting Approach to Nanostructured Copper Oxide-Painted Conductive Woven Textile as Binder-Free Electrode for Improved Energy Storage Performance in Redox-Additive Electrolyte. *Journal of Materials Chemistry A* **2017**, *5* (5), 2224–2234.

(28) Memming, R. *Semiconductor Electrochemistry*; John Wiley & Sons, 2015.

(29) Horowitz, G.; Bourrasse, A. Cellules Photo-Électrochimiques à Électrodes Semiconductrices Pour La Conversion et Le Stockage de l'énergie Solaire. *Revue de Physique Appliquée* **1980**, *15* (3), 463–476.

(30) Gärtner, W. W. Depletion-Layer Photoeffects in Semiconductors. *Physical Review* **1959**, *116* (1), 84.

(31) Butler, M. A.; Ginley, D. S. Prediction of Flatband Potentials at Semiconductor-electrolyte Interfaces from Atomic Electronegativities. *Journal of the Electrochemical Society* **1978**, *125* (2), 228.

(32) Shaikh, S. K.; Inamdar, S. I.; Ganbavle, V. V.; Rajpure, K. Y. Chemical Bath Deposited ZnO Thin Film Based UV Photoconductive Detector. *Journal of Alloys and Compounds* **2016**, *664*, 242–249.

(33) Carles, D.; Lefrançois, G.; Vautier, C. INFLUENCE DE L'INTENSITE LUMINEUSE SUR LA PHOTOCONDUCTION DES COUCHES DE SELENIUM AMORPHE. *Le Journal de Physique Colloques* **1982**, *43* (C9), C9-327-C9-330.

(34) Inamdar, S.; Ganbavle, V.; Shaikh, S.; Rajpure, K. Effect of the Buffer Layer on the Metal–Semiconductor–Metal UV Photodetector Based on Al-doped and Undoped ZnO Thin Films with Different Device Structures. *physica status solidi (a)* **2015**, *212* (8), 1704–1712.

(35) Ullrich, B.; Xi, H. Photocurrent Limit in Nanowires. *Optics letters* **2013**, *38* (22), 4698–4700.

(36) Parkinson, B.; Turner, J.; Peter, L.; Lewis, N.; Sivula, K.; Domen, K.; Bard, A. J.; Fiechter, S.; Collazo, R.; Hannappel, T. *Photoelectrochemical Water Splitting: Materials, Processes and Architectures*; Royal Society of Chemistry, 2013.

(37) Peter, L. M. Energetics and Kinetics of Light-Driven Oxygen Evolution at Semiconductor Electrodes: The Example of Hematite. *Journal of Solid State Electrochemistry* **2013**, *17*, 315–326.

(38) Gelderman, K.; Lee, L.; Donne, S. W. Flat-Band Potential of a Semiconductor: Using the Mott–Schottky Equation. *Journal of chemical education* **2007**, *84* (4), 685.

(39) Bott, A. W. Electrochemistry of Semiconductors. *Current Separations* **1998**, *17*, 87–92.

(40) Matsumoto, Y.; Omae, M.; Watanabe, I.; Sato, E. Photoelectrochemical Properties of the Zn-Ti-Fe Spinel Oxides. *Journal of the Electrochemical Society* **1986**, *133* (4), 711.

(41) Kalanur, S. S. Structural, Optical, Band Edge and Enhanced Photoelectrochemical Water Splitting Properties of Tin-Doped WO3. *Catalysts* **2019**, *9* (5), 456.

(42) Lin, L.; Lin, J. M.; Wu, J. H.; Hao, S. C.; Lan, Z. Photovoltage Enhancement of Dye Sensitised Solar Cells by Using ZnO Modified TiO2 Electrode. *null* **2010**, *14* (5), 370–374. https://doi.org/10.1179/143307510X12820854748791.

(43) Weisz, A. D.; Rodenas, L. G.; Morando, P. J.; Regazzoni, A. E.; Blesa, M. A. FTIR Study of the Adsorption of Single Pollutants and Mixtures of Pollutants onto Titanium Dioxide in Water: Oxalic and Salicylic Acids. *Catalysis today* **2002**, *76* (2–4), 103–112.

(44) Ohtani, B. Photocatalysis by Inorganic Solid Materials: Revisiting Its Definition, Concepts, and Experimental Procedures. *Advances in Inorganic Chemistry* **2011**, *63*, 395–430.

(45) Thomas, L. H. The Calculation of Atomic Fields. In *Mathematical proceedings of the Cambridge philosophical society*; Cambridge University Press, 1927; Vol. 23, pp 542–548.

(46) Fermi, E. Statistical Method to Determine Some Properties of Atoms. *Rend. Accad. Naz. Lincei* **1927**, *6* (602–607), 5.

(47) Lieb, E. H.; Simon, B. Thomas-Fermi Theory Revisited. *Physical Review Letters* **1973**, *31* (11), 681.

(48) Argaman, N.; Makov, G. Density Functional Theory: An Introduction. *American Journal of Physics* **2000**, *68* (1), 69–79.

(49) Hohenberg, P.; Kohn, W. Inhomogeneous Electron Gas. *Physical review* **1964**, *136* (3B), B864.

(50) Perdew, J. P.; Wang, Y. Accurate and Simple Analytic Representation of the Electron-Gas Correlation Energy. *Physical review B* **1992**, *45* (23), 13244.

(51) Perdew, J. P.; Burke, K.; Ernzerhof, M. Generalized Gradient Approximation Made Simple. *Physical review letters* **1996**, *77* (18), 3865.

(52) Hammer, B.; Hansen, L. B.; Nørskov, J. K. Improved Adsorption Energetics within Density-Functional Theory Using Revised Perdew-Burke-Ernzerhof Functionals. *Physical review B* **1999**, *59* (11), 7413.

(53) Wu, Z.; Cohen, R. E. More Accurate Generalized Gradient Approximation for Solids. *Physical Review B* **2006**, *73* (23), 235116.

(54) Perdew, J. P.; Ruzsinszky, A.; Csonka, G. I.; Vydrov, O. A.; Scuseria, G. E.; Constantin, L. A.; Zhou, X.; Burke, K. Restoring the Density-Gradient Expansion for Exchange in Solids and Surfaces. *Physical review letters* **2008**, *100* (13), 136406.

(55) Heyd, J.; Scuseria, G. E.; Ernzerhof, M. Hybrid Functionals Based on a Screened Coulomb Potential. *The Journal of chemical physics* **2003**, *118* (18), 8207–8215.

(56) Anisimov, V. I.; Zaanen, J.; Andersen, O. K. Band Theory and Mott Insulators: Hubbard U Instead of Stoner I. *Physical Review B* **1991**, *44* (3), 943.

(57) Kulik, H. J. Perspective: Treating Electron Over-Delocalization with the DFT+ U Method. *The Journal of chemical physics* **2015**, *142* (24), 240901.

(58) Gani, T. Z.; Kulik, H. J. Where Does the Density Localize? Convergent Behavior for Global Hybrids, Range Separation, and DFT+ U. *Journal of chemical theory and computation* **2016**, *12* (12), 5931–5945.

(59) Mori-Sánchez, P.; Cohen, A. J. The Derivative Discontinuity of the Exchange–Correlation Functional. *Physical Chemistry Chemical Physics* **2014**, *16* (28), 14378–14387.

(60) Dudarev, S. L.; Botton, G. A.; Savrasov, S. Y.; Humphreys, C. J.; Sutton, A. P. Electron-Energy-Loss Spectra and the Structural Stability of Nickel Oxide: An LSDA+ U Study. *Physical Review B* **1998**, *57* (3), 1505.

(61) Cococcioni, M.; De Gironcoli, S. Linear Response Approach to the Calculation of the Effective Interaction Parameters in the LDA+ U Method. *Physical Review B* **2005**, *71* (3), 035105.

(62) Mosey, N. J.; Carter, E. A. Ab Initio Evaluation of Coulomb and Exchange Parameters for DFT+ U Calculations. *Physical Review B* **2007**, *76* (15), 155123.

(63) Mosey, N. J.; Liao, P.; Carter, E. A. Rotationally Invariant Ab Initio Evaluation of Coulomb and Exchange Parameters for DFT+ U Calculations. *The Journal of chemical physics* **2008**, *129* (1), 014103.

(64) Sun, G.; Kürti, J.; Rajczy, P.; Kertesz, M.; Hafner, J.; Kresse, G. Performance of the Vienna Ab Initio Simulation Package (VASP) in Chemical Applications. *Journal of Molecular Structure: THEOCHEM* **2003**, *624* (1–3), 37–45.

(65) Kresse, G.; Joubert, D. From Ultrasoft Pseudopotentials to the Projector Augmented-Wave Method. *Physical review b* **1999**, *59* (3), 1758.

(66) Blöchl, P. E. Projector Augmented-Wave Method. *Physical review B* **1994**, *50* (24), 17953.

(67) Kebede, A. Proceedings of the 4th Gondar School of Science and Technology, 3 – 5 January 2014, University of Gondar.

(68) Hellmann, H. Einfuhrung in Die Quantenchemie. **1937**.

(69) Feynman, R. P. Forces in Molecules. *Physical review* **1939**, *56* (4), 340.

(70) Tang, J.; Ye, J. Photocatalytic and Photophysical Properties of Visible-Light-Driven Photocatalyst ZnBi12O20. *Chemical physics letters* **2005**, *410* (1–3), 104–107.

(71) Le Bahers, T.; Rerat, M.; Sautet, P. Semiconductors Used in Photovoltaic and Photocatalytic Devices: Assessing Fundamental Properties from DFT. *The Journal of Physical Chemistry C* **2014**, *118* (12), 5997–6008.

(72) Sato, J.; Kobayashi, H.; Inoue, Y. Photocatalytic Activity for Water Decomposition of Indates with Octahedrally Coordinated D10 Configuration. II. Roles of Geometric and Electronic Structures. *The Journal of Physical Chemistry B* **2003**, *107* (31), 7970–7975.

(73) Wang, V.; Xu, N.; Liu, J.-C.; Tang, G.; Geng, W.-T. VASPKIT: A User-Friendly Interface Facilitating High-Throughput Computing and Analysis Using VASP Code. *Computer Physics Communications* **2021**, *267*, 108033.

(74) Bader, R. F.; Essén, H. The Characterization of Atomic Interactions. *The Journal of chemical physics* **1984**, *80* (5), 1943–1960.

(75) Parr, R. G.; Yang, W. Density-Functional Theory of the Electronic Structure of Molecules. *Annual review of physical chemistry* **1995**, *46* (1), 701–728.

(76) Bader, R. F.; Stephens, M. E. Spatial Localization of the Electronic Pair and Number Distributions in Molecules. *Journal of the American Chemical Society* **1975**, *97* (26), 7391–7399.

(77) Becke, A. D.; Edgecombe, K. E. A Simple Measure of Electron Localization in Atomic and Molecular Systems. *The Journal of chemical physics* **1990**, *92* (9), 5397–5403.

(78) Silvi, B.; Savin, A. Classification of Chemical Bonds Based on Topological Analysis of Electron Localization Functions. *Nature* **1994**, *371* (6499), 683–686.

(79) Otero-de-la-Roza, A.; Johnson, E. R.; Luaña, V. Critic2: A Program for Real-Space Analysis of Quantum Chemical Interactions in Solids. *Computer Physics Communications* **2014**, *185* (3), 1007–1018.

(80) de-la Roza, A. O.; Blanco, M.; Pendás, A. M.; Luana, V. Critic: A New Program for the Topological Analysis of Solid-State Electron Densities. *Computer Physics Communications* **2009**, *180* (1), 157–166.

(81) Wang, H.; Kohyama, M.; Tanaka, S.; Shiihara, Y. Ab Initio Local Energy and Local Stress: Application to Tilt and Twist Grain Boundaries in Cu and Al. *Journal of Physics: Condensed Matter* **2013**, *25* (30), 305006.

(82) Dronskowski, R.; Bloechl, P. E. Crystal Orbital Hamilton Populations (COHP): Energy-Resolved Visualization of Chemical Bonding in Solids Based on Density-Functional Calculations. *The Journal of Physical Chemistry* **1993**, *97* (33), 8617–8624.

(83) Deringer, V. L.; Tchougréeff, A. L.; Dronskowski, R. Crystal Orbital Hamilton Population (COHP) Analysis as Projected from Plane-Wave Basis Sets. *The journal of physical chemistry A* **2011**, *115* (21), 5461–5466.

(84) Maintz, S.; Deringer, V. L.; Tchougréeff, A. L.; Dronskowski, R. LOBSTER: A Tool to Extract Chemical Bonding from Plane-wave Based DFT. **2016**.

Chapter 3

Investigation of photocatalytic properties in layered Iron Oxychalcogenides

Chapter 3: Investigation of photocatalytic properties in layered Iron oxychalcogenides

3.1. Introduction

One of the main objectives of this thesis is investigating the presence of polarity within oxychalcogenide materials and exploring its impact on the photocatalytic activity, specifically for solar range applications. As mentioned previously, performing this reaction under solar light imposes constraints on the band gap size (restricted to 1.23 - 3.1 eV) and the band edge positions (CBM and VBM more negative than the reduction potential of H_2O/H_2 (0 V) and more positive than the oxidation potential of O_2/H_2O (1.23 V), respectively).[1] This has limited the number of materials that can be of use. We previously suggested a potential design strategy for photocatalysts that is based on four principal points: the connectivity, the band structure, the polarity and the cation choice. Having a layered structure can be beneficial for the charge carriers' transport, as well as having a suitable band structure (depending on the O: *Q* (*Q* is a chalcogenide, S or Se) ratio and the contribution of different orbitals) can be key features in having a suitable band gap for the solar range. The impact of polarity and cation choice are yet to be fully explored. Few transition metals oxychalcogenides exist and their exploration as photocatalysts is limited; in addition, iron is cheap and abundant. Therefore, the following chapter will concentrate on investigating four iron-based oxychalcogenides, $La_2O_2Fe_2OQ_2$ and $CaFeOQ$ (Q = S, Se); with an emphasis on the influence of the heteroleptic Fe^{2+} coordination environment, polarity, and the O:*Q* ratio on the photocatalytic properties of these materials.

3.1.1. Polar oxychalcogenides

Oxysulfides and oxyselenides present tuned band gaps to better match the solar spectrum, due to the introduction of softer chalcogenides on the oxide sublattice.[2,3] This has led to different structures compared to the oxides and have received recent attention in several applications.[4,5,6,7,8,9]

In addition, polar units in the structure, promoted by the presence of heteroleptic coordination environments has been suggested to be advantageous in enhancing the charge carriers' separation, giving more efficient photocatalysis.[10,11,12,13]

3.1.2. Transition metal cations

Interest has grown over the years in transition-metal (oxy)pnictides/chalcogenide[14,15,16] especially after the discovery of the unconventional superconductivity in fluoride-doped LaOFeAs with transition temperature T_C = 26 K.[17] These transition metal cations often occupy sites with lower coordination numbers, and can result in layered structures due to anion segregation.[18]

3.1.3. Iron oxychalcogenide phases

The first compound, CaFeOSe, was reported by Han *et al.*[19] its complex microstructure and magnetism were later studied by Cassidy *et al.*[20] The orthorhombic structure of CaFeOSe is built from puckered layers of edge-linked $FeSe_2O_2$ tetrahedra separated by Ca^{2+} layers. Two polymorphs are known, which differ in the orientation of $FeSe_2O_2$ units: a polar polymorph of *Cmc*2_1 symmetry with in-plane polarization and a non-polar, centrosymmetric polymorph of *Pmcn* symmetry (**Figure 3.1**).[20] CaFeOSe behave as an electrical insulator,[21] and it exhibits long-range antiferromagnetic order below 159 K.[20]

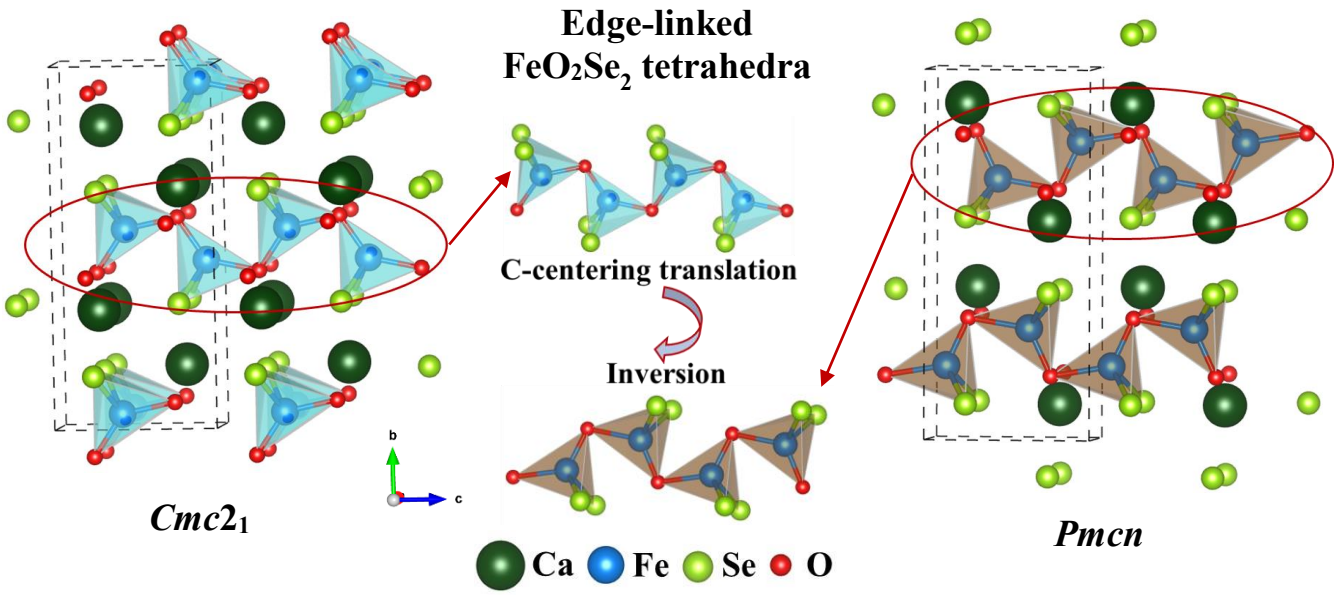

Figure 3.1 : View of CaFeOSe structures with the zigzag layers in the (a) *CmC*2_1 polymorph with C-centering translation and (b) *Pmcn* polymorph with inversion symmetry.

CaFeOS oxysulfide crystallizes in a polar noncentrosymmetric structure of $P6_3mc$ symmetry.[22,23,24,25] Its layered structure (**Figure 3.2**) consists of alternating layers of corner-linked $FeOS_3$ tetrahedra, separated by Ca^{2+} cations. These heteroleptic $FeOS_3$ units are arranged with dipoles parallel to the hexagonal axis[25] (isostructural to CaZnSO).[26,27] CaFeOS is a semiconductor with an antiferromagnetic transition at 70 K.[25] In addition, a computational study reported that CaFeOS can be a promising photovoltaic material with a 24.2 % energy conversion efficiency.[28]

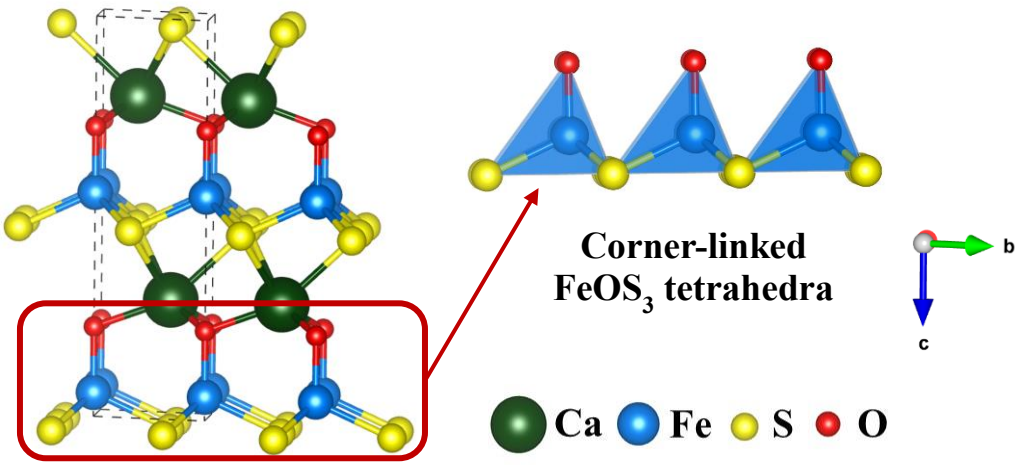

Figure 3.2 : View of CaFeOS structure with the Fe^{2+} based layers along [100] direction.

Finally, the iron oxysulfide and oxyselenide phases $La_2O_2Fe_2OQ_2$ (Q = S, Se) were first explored by Mayer *et al*.[29] They adopt a tetragonal (*I4/mmm* symmetry) anti-$Sr_2MnO_2Mn_2Sb_2$-type structure, where the anion and cation sites are swapped.[30] The structure (**Figure 3.3**) consists of fluorite-like $[La_2O_2]^{2+}$ layers and $[Fe_2OQ_2]^{2-}$ layers stacking along the *c* axis;[31] $[La_2O_2]^{2+}$ layers are formed by edge-sharing La_4O tetrahedra whilst $[Fe_2OQ_2]^{2-}$ layers consist of face-sharing FeO_2Q_4 octahedra where the Fe^{2+} atom is in a centrosymmetric heteroleptic coordination environment.[32,33,34,35] These oxychalcogenides have semiconducting properties (behaving as Mott insulators),[32] and they display antiferromagnetic order below ~ 90 K temperature (T_N depends on Q = S/Se, and La).[35] Band gaps were found to be 0.17-0.19 eV.[32,36] Electronic structure calculations revealed direct band gap aspects[37] and confirmed the contribution of the Fe 3*d* states to the density of states near the Fermi level. Finally, it has been shown that more band narrowing occurs in these phases compared to other iron based oxypnictide such as, LaFeAsO[38] but similar to other iron based chalcogenides such as, FeTe and FeSe.[39]

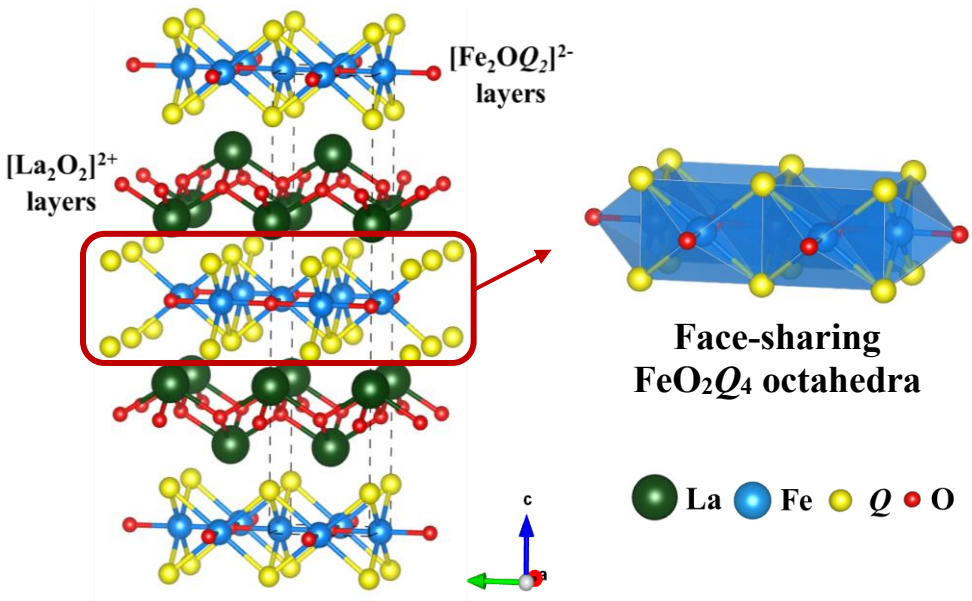

Figure 3.3 : View of $La_2O_2Fe_2OQ_2$ (Q = S, Se) structure with view of the $[Fe_2OQ_2]^{2-}$ layers.

Unfortunately, our attempts to synthesize the centrosymmetric polymorph of CaFeOSe didn't succeed; therefore, for the sake of comparison we chose $La_2O_2Fe_2OQ_2$ polymorphs (easy to synthesize and comparable Fe coordination environments) even with their very narrow band gaps. Thus, in this chapter, these four iron-based oxychalcogenides, $La_2O_2Fe_2OQ_2$ and CaFeOQ (Q = S, Se) will be investigated for their photoelectrochemical (photocurrent measurements) and electronic properties (DFT calculation). First optical band gaps and the band edge positions estimation, determined whether these materials are active or not for applications under solar irradiation. Then their capacity to generate a stable photocurrent was demonstrated with efficient electron-hole separation for CaFeOSe material. Finally, calculation of the effective masses for the non-centrosymmetric CaFeOSe oxyselenide supported the observed photocurrent response.

3.2. Experimental results

3.2.1. Synthesis and preliminary characterization

3.2.1.1. Synthesis and Rietveld Refinement

The four iron oxychalcogenides were prepared by solid-state reactions in evacuated, sealed, quartz tubes. Reagents were stored and manipulated in an argon-filled glovebox. For $La_2O_2Fe_2OQ_2$ (Q = S, Se) (0.5 g) analogues, La_2O_3, Fe and S/Se in the molar ratio 2:2.1:2 was used and the heat treatment consisted of heating to 400°C (1.5°C/min) for 12 h, and then heated to 600 °C (0.5°C/min) and then 850 °C for 12h. For CaFeOQ (Q = S, Se) (0.5 g) analogues, we used a mixture of the precursors CaO, Fe and Se/S in the molar ratio 1:1.05:1. The heat treatment consisted of heating to 750°C at a rate of 5 °C/min for 60 h before quenching the sample for the oxyselenide, and heating to 950°C (0.5°C/min) for 24 h for the oxysulfide.

X-ray powder diffraction (XRPD) data was used to monitor synthesis reactions. Rietveld refinements were carried out using Fullprof software.[40] The background, sample height, lattice parameters, peak profiles, atomic positions and atomic displacement parameters were refined. Vesta software[41] was used to visualize the crystal structure. The good quality of the synthesized samples was confirmed (**Figure 3.4**), and the refined lattice parameters for all phases are gathered in **Table 3.1**.

Table 3.1. Refinement details from Rietveld refinement using room temperature XRPD data.

Parameters		**$La_2O_2Fe_2OS_2$**	**$La_2O_2Fe_2OSe_2$**	**CaFeOS**	**CaFeOSe**
Space group		*I4/mmm*	*I4/mmm*	$P6_3mc$	$Cmc2_1$
Unit cell	***a* (Å)**	4.0438(1)	4.0862(1)	3.7613(1)	3.8925(1)
	***b* (Å)**	4.0438(1)	4.0862(1)	3.7613(1)	13.1878(2)
	***c* (Å)**	17.8995(3)	18.6028(2)	11.3892(2)	5.9260(1)
	***V* (Å^3)**	292.70(1)	310.61(1)	139.54(1)	304.20(1)
Fitting statistics	χ^2	3.86	1.80	1.49	9.02
	R_{exp}	3.32	5.43	5.91	3.39
	R_{wp}	6.53	7.28	7.20	10.2
	R_p	4.70	5.43	5.47	7.16

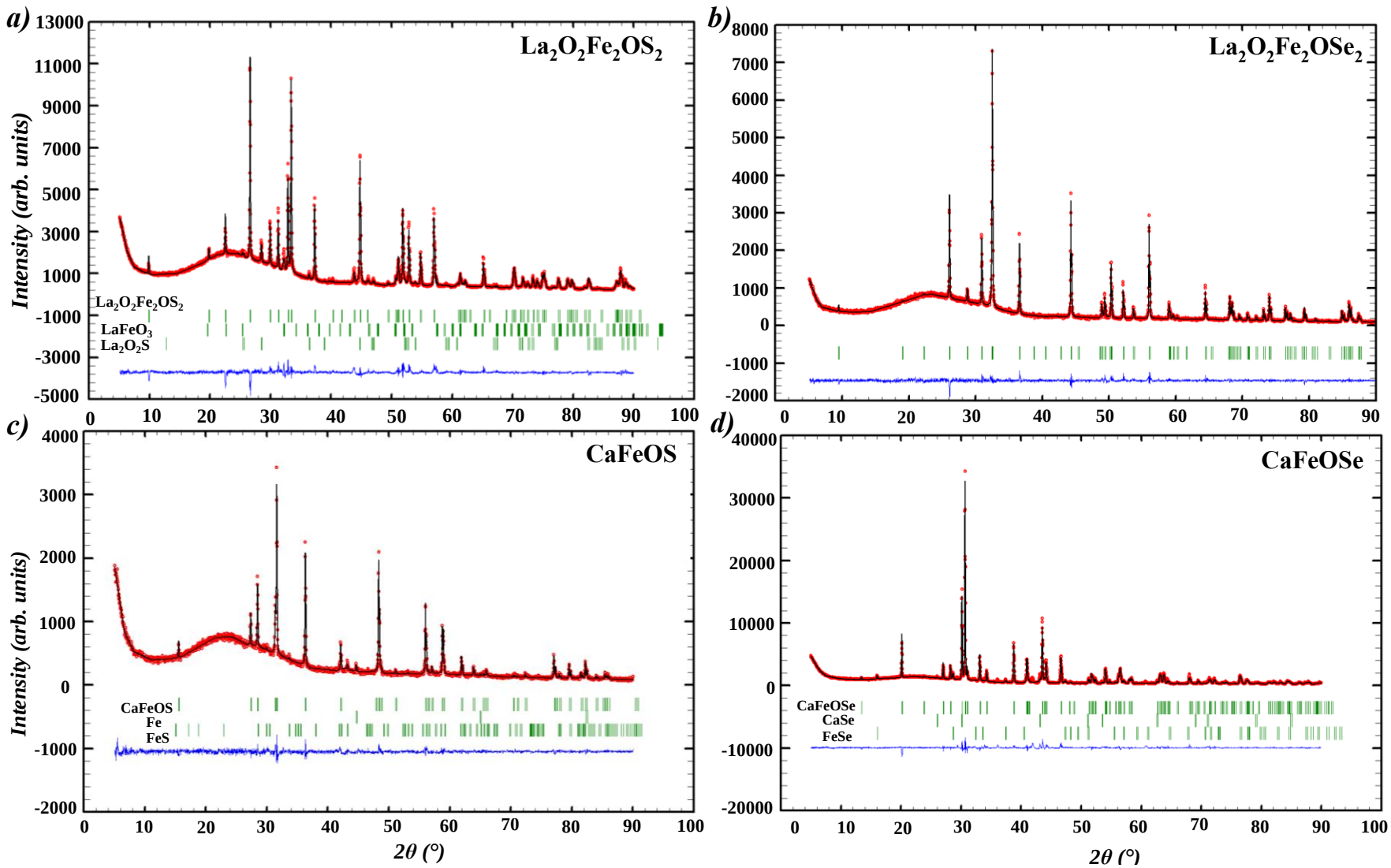

Figure 3.4 : Powder XRD Rietveld refinement profiles: the experimental (red) and the calculated (black) patterns are superimposed; the difference curve and Bragg positions are shown in blue and green, respectively of (a) $La_2O_2Fe_2OS_2$ (88.49%), $LaFeO_3$ (7.30%), La_2O_2S (4.20%); (b) $La_2O_2Fe_2OSe_2$, (c) CaFeOS (95.59%), Fe (0.71%), FeS (3.70%) and (d) CaFeOSe (93.30%), CaSe (2.06%), FeSe (4.65%).

3.2.1.2. Optical band gap and band edges positions

CaFeOS is reported to be an indirect band gap semiconductors (n = 2)[28] and we assumed a direct allowed transition (n = 1/2) for the non-centrosymmetric CaFeOSe (see the results from DFT calculation in **Section 3.2.3**). Tauc plots[42] from our diffuse reflectance measurements (after Kubelka-Munk analysis[43]) suggests optical band gaps of 1.43(1) eV and 2.11(1) eV for CaFeOS and CaFeOSe, respectively (**Figure 3.5**). The band gaps of $La_2O_2Fe_2OQ_2$ (Q = S, Se) are too small to be measured optically, but reported electrical measurements suggest electronic band gaps of 0.17-0.19 eV.[44]

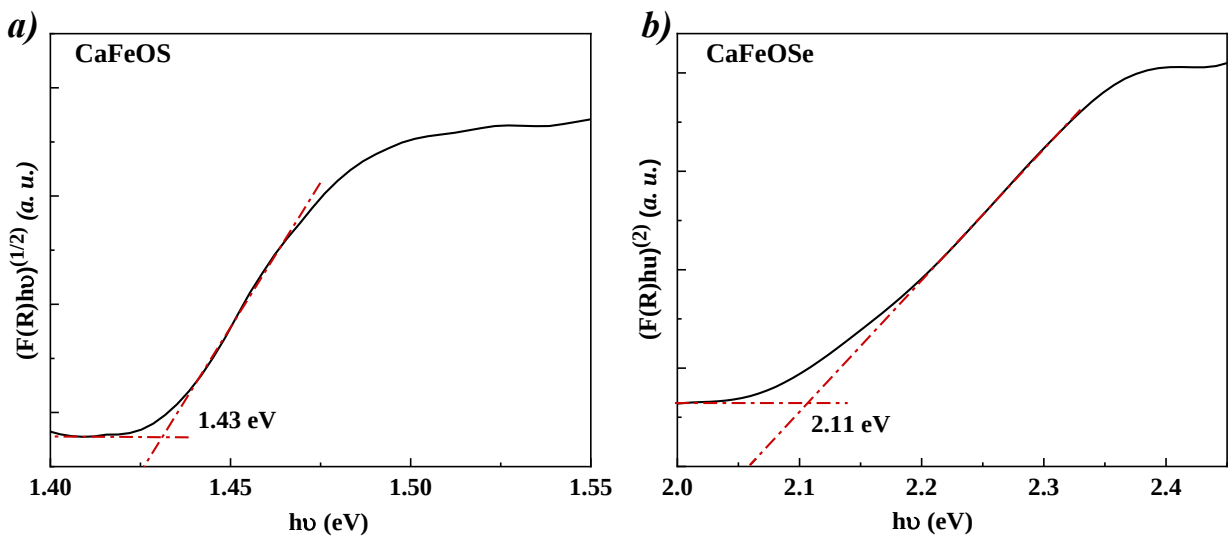

Figure 3.5 : Tauc plot inset to determine the experimental band gap for (a) CaFeOS and (b) CaFeOSe.

The corresponding band edge positions for all four materials were calculated (**Figure 3.6**) in order to check if they encompass the redox potential of water, an essential requirement for photocatalytic water splitting. Therefore, the empirical method based on Mulliken electronegativities proposed by Butler and Ginley[45] was used (**Chapter 2, Section 2.1.2.4**). The summary of the optical band gaps and band edge positions for all materials is listed in **Table 3.2**.

Table 3.2. Optical band gap and the relative band edges position.

Composition	Optical band gap (eV)	Band edges position	
		CB	VB
$La_2O_2Fe_2OS_2$	0.24	0.53(2)	0.72(2)
$La_2O_2Fe_2OSe_2$	0.19	0.48(2)	0.65(2)
CaFeOS	1.43(1)	-0.31(2)	1.12(2)
CaFeOSe	2.11(1)	-0.71(2)	1.4(1)

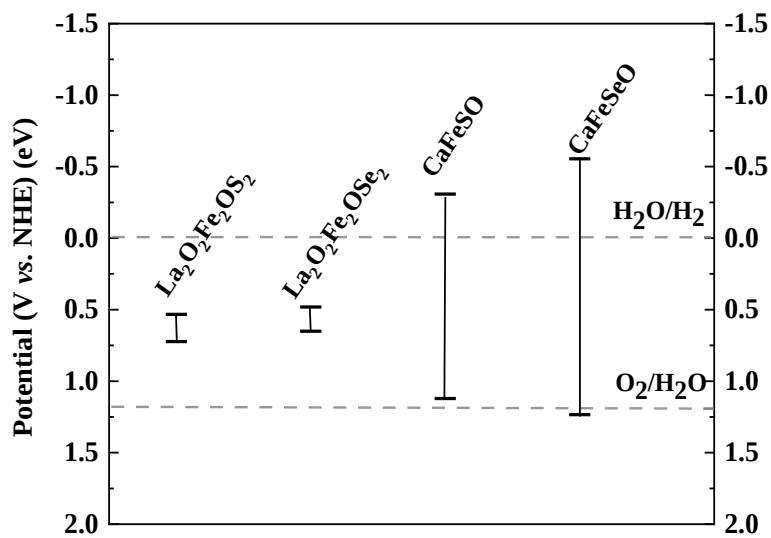

Figure 3.6 : Calculated band edges positions for $La_2O_2Fe_2OS_2$, $La_2O_2Fe_2OSe_2$ CaFeOS and CaFeOSe. The levels of H_2 and O_2 evolution are indicated by dashed lines.

The optical band gaps of CaFeO*Q* (*Q* = S, Se) oxychalcogenides are convenient for solar photocatalysis (1.23 - 3.1 eV), whilst the band gaps of $La_2O_2Fe_2OQ_2$ (*Q* =S, Se) oxychalcogenides are too small for the solar spectrum. These results combined with the band edge positions, suggest that CaFeO*Q* (*Q* =S, Se) oxychalcogenides can be active as photocathodes (well positioned conduction band), making them potential catalysts for half-reactions for solar water splitting. $La_2O_2Fe_2OQ_2$ (*Q*= S, Se) oxychalcogenides cannot be active catalyst in the solar light (conduction and valence band position don't encompass the redox potential of water), which is expected according to their reported band gaps.

3.2.2. Photocurrent measurements

3.2.2.1. Mott-Schottky method to determine the flat band potential

The Mott-Schottky (MS) plot of $1/C^2$ vs. applied potential (**Figure 3.7**) gives insight into the conduction type, the concentration of the charge carriers (*N*) and the flat band potential (V_{fb}).[46,47] Depending on the nature of the observed slope, the flat band potential can be estimated *vs.* Ag/AgCl (reference electrode) or RHE (reversible hydrogen electrode). Then depending on the conduction behaviour, the position of the CB or VB band edge could be determined.[48] The test was performed at 1 kHz and 0 bias voltage.

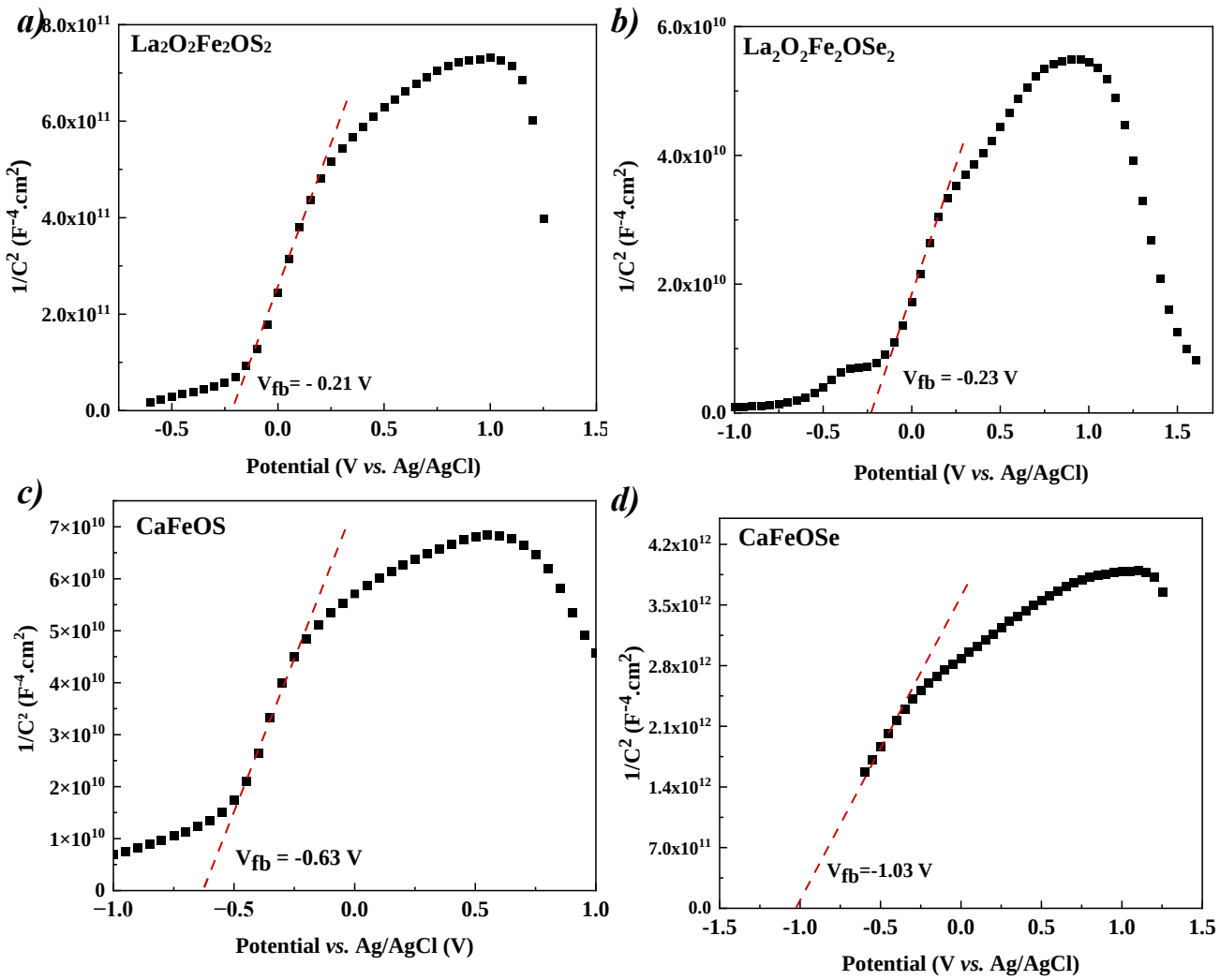

Figure 3.7 : Mott-Schottky plot for (a) $La_2O_2Fe_2OS_2$, (b) $La_2O_2Fe_2OSe_2$, (c) CaFeOS and (d) CaFeOSe deposited on ITO/Glass performed at 1 kHz and V_{bias}= 0 V.

All four compounds gave a positive slope which confirmed the n-type semiconduction. **Table 3.3** gives the estimated flat band potential E_{fb} for $La_2O_2Fe_2OQ_2$ and CaFeO*Q* (*Q* = S, Se) oxychalcogenides *vs.* Ag/AgCl and RHE. In n-type semiconductors, the flat band potential reflects the position of the Fermi level which lies close to the conduction band minimum (CBM) ~ 0.1[49]; therefore the relative CB edge positions were found to be lying at 0.26(1) V for both $La_2O_2Fe_2OQ_2$ phases and at -0.2(1), -0.94(1) V for CaFeOS and CaFeOSe, respectively. Compared with the previously calculated CB positions by the empirical method in **Table 3.2**, the values obtained for $La_2O_2Fe_2OQ_2$ and CaFeO*Q* are similar and confirm the unsuitable position of the conduction bands of $La_2O_2Fe_2OQ_2$ and the suitability of the CaFeO*Q* ones for the solar spectrum.

Table 3.3. Conduction band position *vs.* Ag/AgCl and *vs.* RHE

Composition	**CB position (V) *vs.***	
	Ag/AgCl	RHE
$La_2O_2Fe_2OS_2$	-0.21(1)	0.325(1)
$La_2O_2Fe_2OSe_2$	-0.23(1)	0.295(1)
CaFeOS	-0.63(1)	-0.105(1)
CaFeOSe	-0.75(1)	-0.505(1)

3.2.2.2. Reproducibility measurements

The electrochemical measurements discussed in this section were conducted in the setup described in **Chapter 2**, **Section 2.1.3**. The evolution of the current density ($\Delta j = j_{ill} - j_{dark}$ where j_{ill} and j_{dark} represent the current density under illumination and darkness) was measured for the film with a 450 nm irradiation, under different lamp ignition and extinction cycles (**Figure 3.8**). Under 0 V bias voltage, both $La_2O_2Fe_2OQ_2$ phases were capable of producing a photocurrent; for the oxysulfide (**Figure 3.8a**), it increased linearly from 0.05 to 0.15 µA cm^{-2} for a power density of 22 to 111 mW cm^{-2}, respectively, whilst for the oxyselenide (**Figure 3.8b**) a slightly lower and unstable photocurrent was recorded, reaching a 0.8 µA cm^{-2} for a 111 mW cm^{-2} power density. The transient current has slower kinetics in the oxyselenide case compared to the oxysulfide; this is observed in **Figure 3.8a** and **3.8b**, where the exponential growth is faster for $La_2O_2Fe_2OS_2$. As for the chaotic aspect observed for $La_2O_2Fe_2OSe_2$ in **Figure 3.8b**, this disturbance on the

measurements can be attributed to the film undergoing a chemical degradation or dissolution of the electrode in the electrolyte.

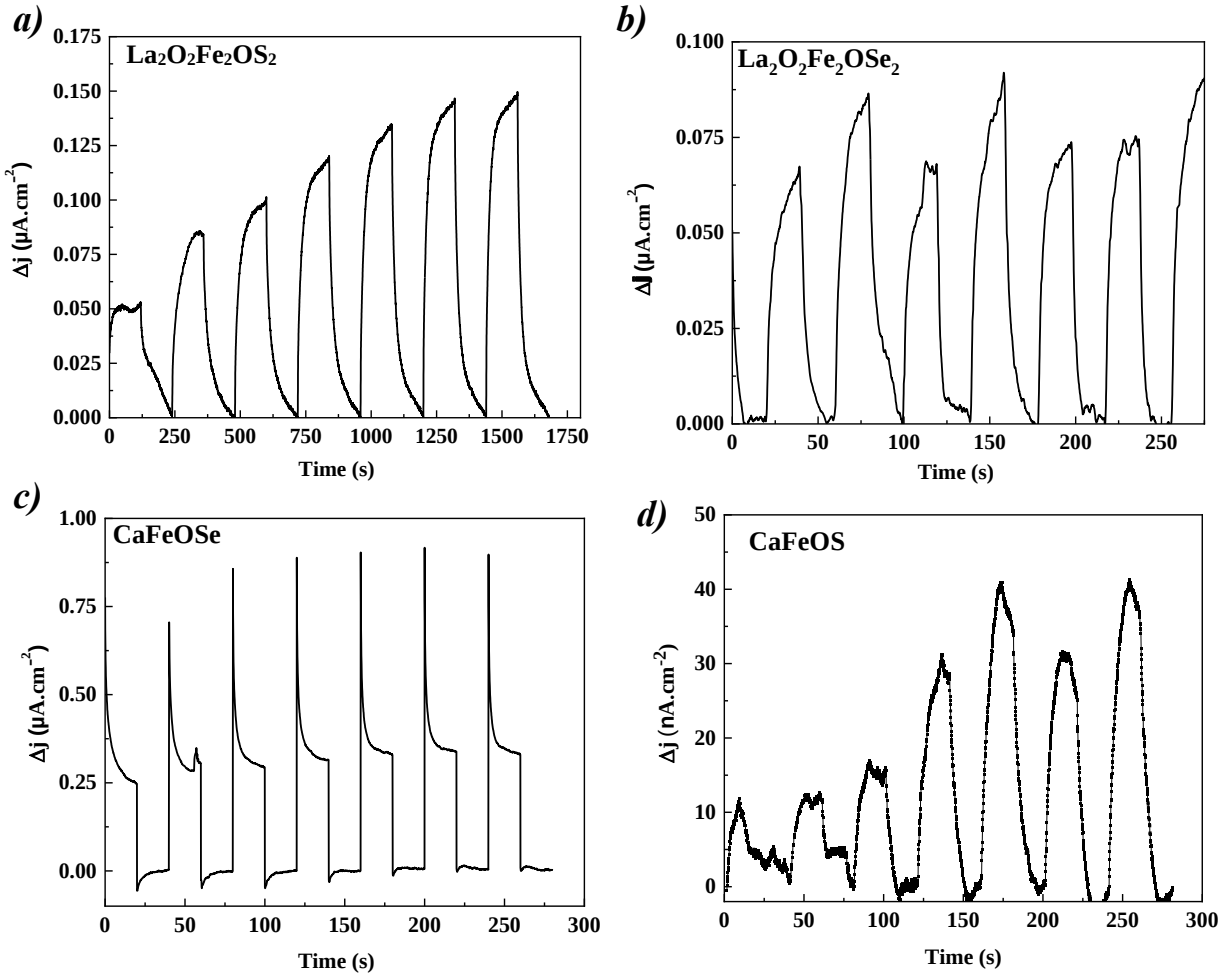

Figure 3.8 : Transient photocurrent response under several light power density (450 nm excitation) of (a) $La_2O_2Fe_2OS_2$, (b) $La_2O_2Fe_2OSe_2$ (c) CaFeOSe (V_{bias}= 0 V in μA.cm^{-2}), and (d) CaFeOS (V_{bias} = 0.6 V in ηA.cm^{-2}).

Under the same conditions (V_{bias} = 0 V and λ = 450 nm), CaFeOSe produced a saturated, yet higher photocurrent increasing from 0.65 to 0.9 μA cm^{-2} for similar power densities (**Figure 3.8c**). Unfortunately, the oxysulfide analogue did not exhibit similar response, instead a much lower (compared to all three phases) and unstable photocurrent was recorded (~ 40 ηA cm^{-2} for 111 mW.cm^{-2} power density) even under a much higher bias voltage (0.6 V) (**Figure 3.8d**). In order to further understand this response, a linear sweep measurement was conducted and **Figure 3.9** shows the observed j-V plot of the CaFeOS phase. A curvature is observed (between 0.7 and 1.4 V), that

can be attributed to an oxidation reaction of either the electrolyte or the prepared film (i.e. CaFeOS powder). Mind that the ions of the electrolyte are inactive (Na^+, SO_4^{2-}), which indicates that the oxidation is happening at the surface of the as-prepared layer of the electrode (CaFeOS powder), thus causing the disruption of the measurements. The potential of this curvature is ~ 0.7 V, compatible with the redox potential of Fe^{2+}/Fe^{3+} to satisfy equation (1):

$$Fe^{2+} \rightarrow Fe^{3+} + e^- \qquad (1)$$

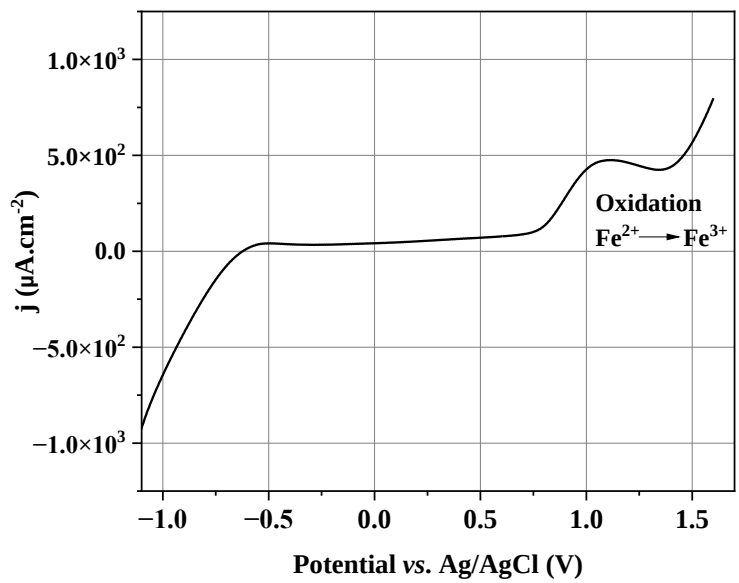

Figure 3.9 : Linear sweep plot for CaFeOS.

Due to the instability of the photocurrent of both and $La_2O_2Fe_2OSe_2$ and CaFeOS, we proceeded to fit the photocurrents recorded for $La_2O_2Fe_2OS_2$ and CaFeOSe phases. The photocurrent increased with the intensity of the luminous flux according to a classical power law.[50] The fitting gives a curve going through the origin with the following equations: $\Delta j = 8.63\times10^{-3}(2)\Phi^{0.60(2)}$ for $La_2O_2Fe_2OS_2$ (**Figure 3.10a**) and $\Delta j = 2.76\times10^{-1}(2)\Phi^{0.05(2)}$ (**Figure 3.10b**) for CaFeOSe.

Information about the trap state in the material can be extracted from the value of the exponent: for an ideal trap-free system, the exponent is equal to 1 and the photocurrent scales linearly with the illumination power; it becomes less than 1 where most of the traps are already filled in and further illumination power cannot effectively increase the photogain.[51] In the case of the oxyselenides, the low values of the exponents (0.05 for CaFeOSe) indicate the presence of many traps in those materials, while $La_2O_2Fe_2OS_2$ presented a much higher exponent (0.60) therefore

fewer traps compared to other oxysulfides such as $Sr_6Cd_2Sb_6S_{10}O_7$ (0.208)[52] and oxyfluorides such as $BiVO_3F$ (0.63).[53] This evolution of the photocurrent according to the luminous flux makes it possible to say that $La_2O_2Fe_2OS_2$ oxysulfide could be used as a photodetector.

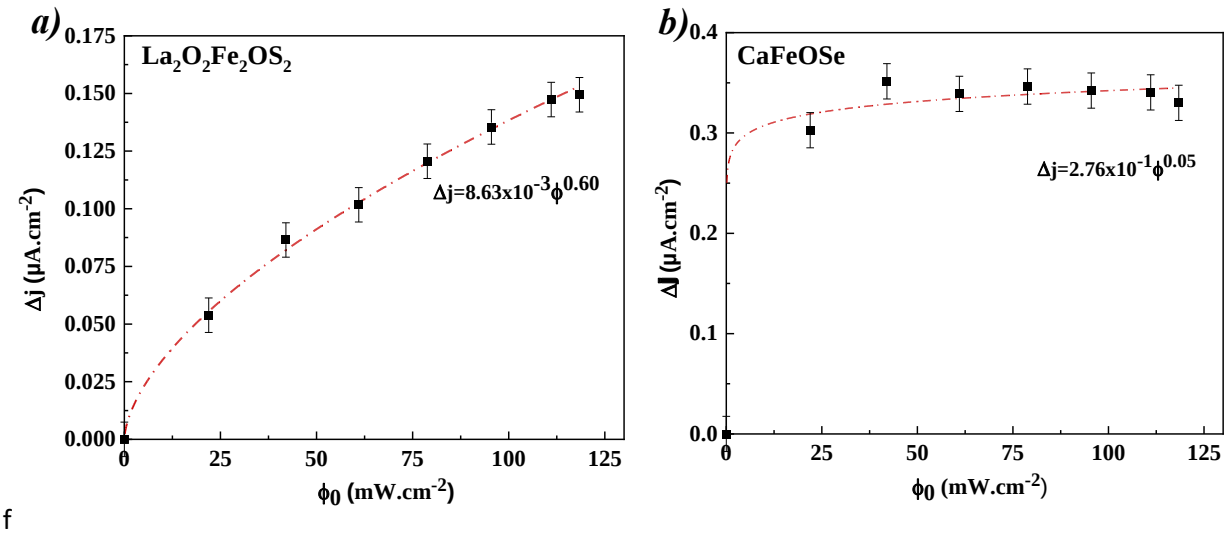

f

Figure 3.10 : Evolution of the photocurrent density with the power density of light (V_{bias}= 0 V under a 450 nm excitation) of (a) $La_2O_2Fe_2OS_2$ and (b) CaFeOSe.

One important point to highlight for CaFeOSe is that its photocurrent response (**Figure 3.8c**) shows a characteristic decay from a "spike" to a steady state during illumination, which can be explained by the fact that the interface is loaded by the charge carriers upon their fast separation (appearance of this peak) followed by the establishment of an equilibrium state between the recombination and the transfer of the carriers (steady state).[54] In this case, i.e. having an exponential decrease in the photocurrent peak, the transfer and recombination constants can be determined using a model proposed by Parkinson *et al*.[55] We calculated a transfer and recombination constant to be 0.35 and 0.55 min^{-1}, respectively (i.e. a transfer efficiency of 40 %, **Figure 3.11a**) for a 0 V bias potential. The transfer efficiency increased drastically to 80 % for a 0.4 V bias potential with a higher transfer constant K_{tr} = 4 min^{-1} and a lower recombination constant K_{rec} = 0.5 min^{-1} (**Figure 3.11b**), which indicates the improved results with a higher voltage appliance. These rate constants calculated for a 0.4 V are much higher compared to other oxychalcogenides such as $Sr_6Cd_2Sb_6S_{10}O_7$ (K_{tr} = 0.25 and K_{rec} = 0.08 min^{-1}), but similar transfer efficiency (η_{tr} = 78%).[56]

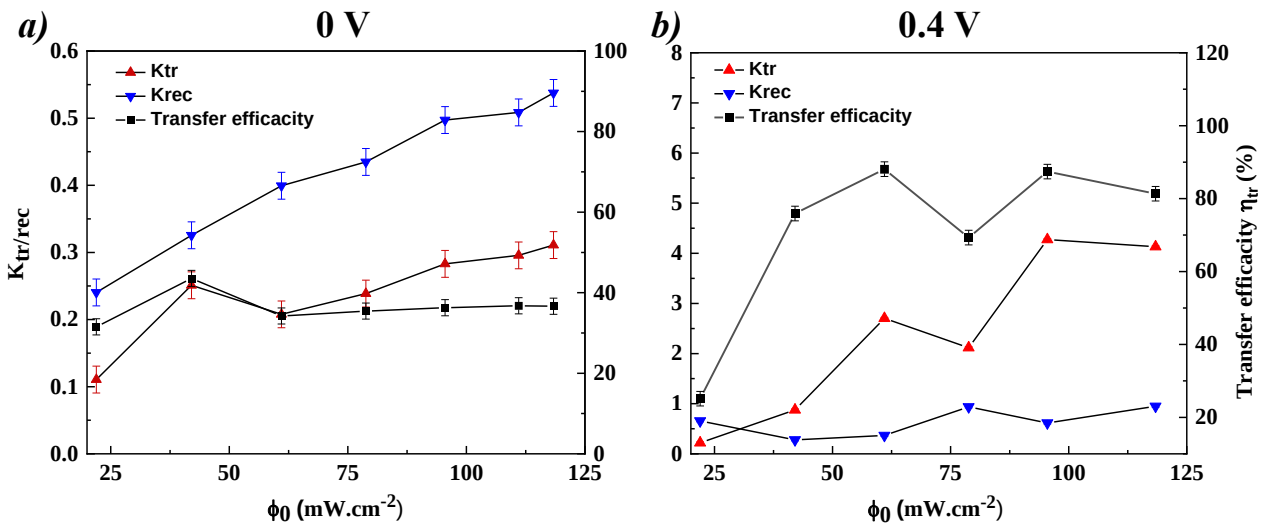

Figure 3.11 : Evolution of the recombination and transfer rate constants k_{tr} and k_{rec} with intensity of light alongside the transfer efficacity η_k by intensity light of CaFeOSe at (a) 0 V and (b) 0.4 V.

3.2.2.3. Influence of the wavelengths

Following on the previous results we obtained for the CaFeOS phase, we proceeded to do the rest of the measurements for $La_2O_2Fe_2OQ_2$ (Q = S, Se) and CaFeOSe phases only. The influence of wavelengths on the photocurrent response for V_{bias}= 0.4 V was studied (**Figure 3.12a, 3.12c and 3.12e**). All three phases demonstrated their capacity to absorb in the visible spectrum (400 – 700 nm). The highest photocurrents (0.22, 0.10, and 0.22 µA cm^{-2} for $La_2O_2Fe_2OS_2$, $La_2O_2Fe_2OSe_2$ and CaFeOSe, respectively) were observed for 470 nm irradiation ($La_2O_2Fe_2OQ_2$) and 450 nm (CaFeOSe) with a decrease occurring towards longer wavelength irradiation. For CaFeOSe, the result is coherent with the material's absorption and the results observed on the Tauc plot (**Figure 3.5**). For $La_2O_2Fe_2OQ_2$ (Q = S, Se) phases with small band gaps (0.17 - 0.19 eV), absorption is in the IR range (700 nm – 1 mm). But these phases absorb in the visible range, which can be explained by the fact that the absorbance can be significant for an energy larger than that of the band gap. In addition, this absorption in the visible spectral zone is due to the absorption of the material which can also help explain the black color of these phases. Similar photocurrent responses were observed for these phases when the test was conducted for V_{bias}= 0 V (**Figure 3.12b, 3.12d and 3.12f**).

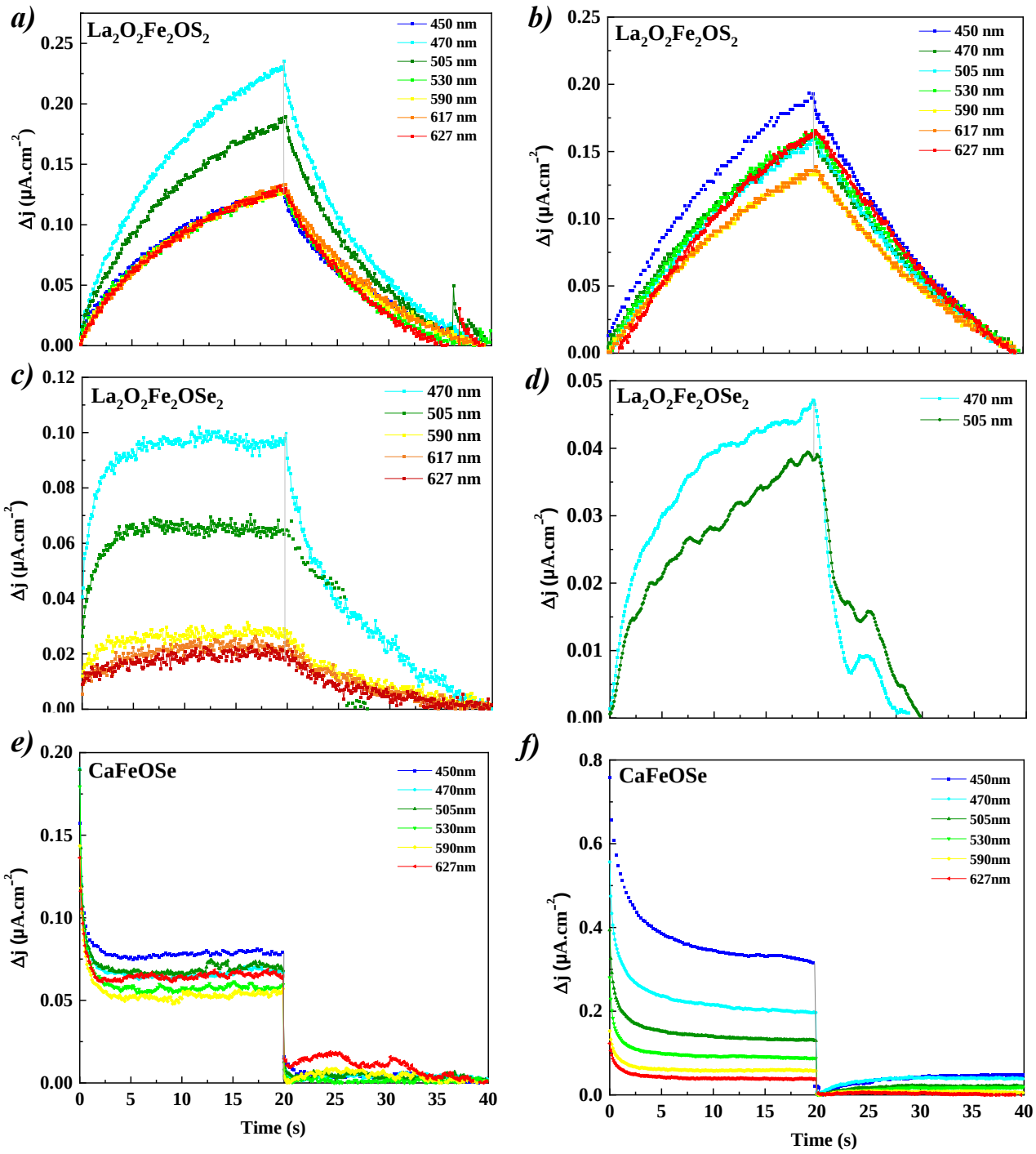

Figure 3.12 : Transient photocurrent response *vs.* wavelengths (constant light intensity ϕ_0=42 mW cm^{-2}) of $La_2O_2Fe_2OQ_2$ and CaFeO*Q* (Q = S, Se) at (a), (c), (e) Bias = 0.4 V and (b), (d), (f) Bias = 0 V.

3.2.2.4. Influence of the applied bias voltage

The applied bias voltage is one of the most important factors that can impact the photocurrent measurements. Therefore, the evolution of the photocurrent for an irradiation of 450 nm and V_{bias} = 0, 0.4, 0.6 and 0.8 V was recorded for the two analogues of $La_2O_2Fe_2OQ_2$ (Q = S, Se) (**Figure 3.13**). A proportional dependency between the photocurrent response and the external potential was observed, consistent with the fact that higher responses are typically observed with increasing voltage. For $La_2O_2Fe_2OSe_2$ (red curve), it looks as if it increases slightly with the potential; but for $La_2O_2Fe_2OSe_2$ (black curve), the change is very little until the highest voltage is applied (0.8 V). This demonstrated the impact of the applied voltage on the materials' performance, where higher voltages result in enhanced performances which could change depending on the material.

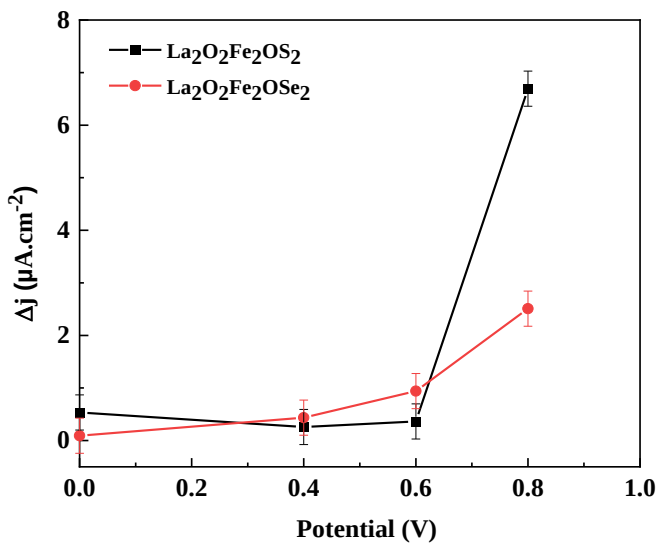

Figure 3.13 : Evolution of the transient photocurrent response vs. potential of $La_2O_2Fe_2OQ_2$ (Q = S, Se).

3.2.2.5. Photocurrent measurements under solar irradiation

By carrying out on/off cycles, the transient photocurrent response under solar illumination (150 W Xenon lamp with AM 1.5G filter – 100 mW.cm^{-2}) was recorded for 0, 0.4 and 0.6 V bias voltages for $La_2O_2Fe_2OQ_2$ (Q = S, Se) oxychalcogenides (**Figure 3.14**). Higher photocurrents were observed for V_{bias}= 0.6 V as expected, 3.55 and 0.55 µA cm^{-2} for $La_2O_2Fe_2OS_2$ and $La_2O_2Fe_2OSe_2$, in **Figure 3.14a and 3.14b**, respectively. A slight instability was observed for the generated

photocurrent upon applying a potential, which may be due to the material's chemical instability in the chosen electrolyte.

Figure 3.14d shows the recorded photocurrents of CaFeOSe for V_{bias}= 0 and 0.4 V: higher values were obtained with no potential (1.45 µA cm^{-2}) than when applying one (0.35 µA cm^{-2}) which is unusual (higher response occurs with higher potential). This could be explained by the degradation of the film; due to the non-ideal semiconductor/electrolyte junction, causing a change in the potential difference across the Helmholtz layer[57] (layer formed by the e^-/h^+ trapped at the surface of the semiconductor or the electrolyte ions). Another possible explanation is the presence of the redox degradation of the phase (oxidation of Fe^{2+} to Fe^{3+}) when increasing the applied potential. Further investigations are required to fully understand this peculiar behaviour.

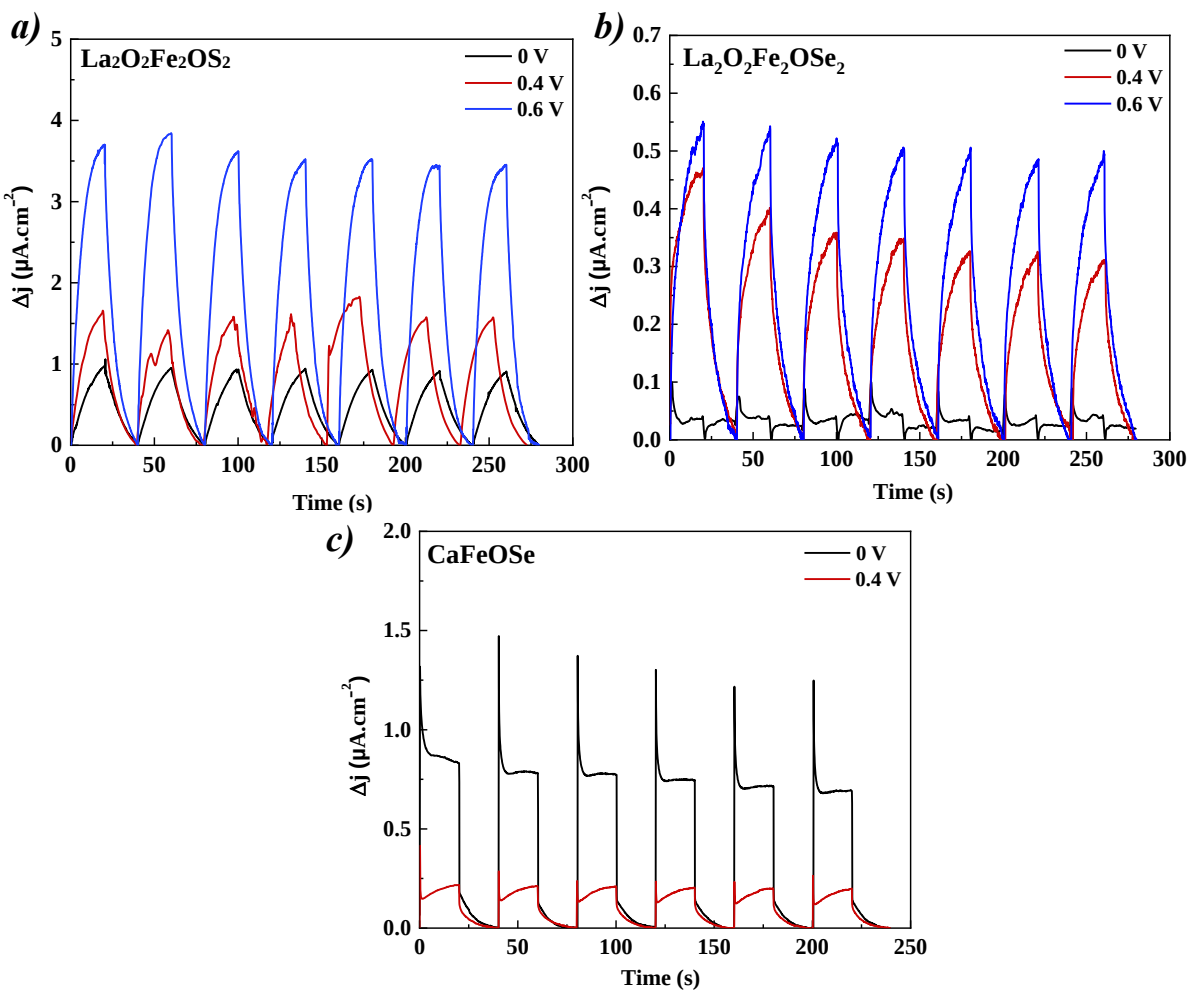

Figure 3.14 : Transient photocurrent response under solar illumination (100 mW.cm^{-2}) for V_{bias}= 0, 0.4 and 0.6 V of (a) $La_2O_2Fe_2OS_2$, (b) $La_2O_2Fe_2OSe_2$ (c) CaFeOSe.

3.2.3. Computational studies

Density functional theory (DFT) calculations were carried out using VASP code[58] in order to investigate the electronic properties of the non-centrosymmetric CaFeOSe oxyselenide, which gave insight into the origin of the interesting photocurrent response we observed during the photoelectrochemical measurements. In order to deal with the strong electronic correlation associated with the 3*d* states of Fe, the GGA plus on-site repulsion U (GGA+ U) method was employed[59] with U_{eff} = 4 eV in an antiferromagnetic configuration.[21] A plane-wave cutoff energy of 550 eV and a threshold of self-consistent-field energy convergence of 10^{-9} eV were used with ƙ-points meshes (13×4×8) in the irreducible Brillouin zone. It converged with residual Hellman-Feynman forces on the atoms smaller than 0.03 eV $Å^{-1}$ and led to a good match with the experimental structure; i.e. within a reasonable error expected for the GGA method. The relaxed structure was used for calculations of the electronic structure and the charge carrier's effective masses.

The band structure of the non-centrosymmetric CaFeOSe oxyselenide is shown in **Figure 3.15a** and focus on the region around the Fermi level at the top of the valence band (VB) and the bottom of the conduction band (CB). A direct band gap of 2.08 eV is obtained for this non-centrosymmetric polymorph of CaFeOSe, which is compatible with the measured optical band gap (**Figure 3.5** in **Section 3.2.1.2**). On the other hand, the oxysulfide CaFeOS has a lower one of 1.16 eV.[28] This decrease in the band gap width is explained by the increase of the *Q*/O ratio around Fe from non-centrosymmetric CaFeOSe (FeO_2Se_2) compared to CaFeOS (FeS_3O). In addition, the smaller radius of sulfur induces a positive chemical pressure due to the shorter Fe-S distances, thus further decreasing the band gap.[60]

The projected densities of states (PDOS) (**Figure 3.15b**) of the non-centrosymmetric CaFeOSe allow the visualization of the contribution of the different atoms to the conduction and valence bands. The Fe 3*d* states lie in the CB starting from ∼2 eV up to ∼6 eV, with the main contribution up to approximately 3.5 eV; whilst these states contribute in the range of −5 to −0.5 eV in the VB. They are found to be hybridizing with the O 2*p* and S 3*p* states, contributing lower (-2 eV) and higher (-0.5 eV) in the VB, respectively (as expected from their electronegativity difference). These observations are similar to the ones reported in the literature for the centrosymmetric polymorph.[19] The bands are rather flat except the $\Gamma \rightarrow Z$ and $\Gamma \rightarrow S$ directions which are more dispersed in the

conduction bands compared to the valence band, which can be related to the contribution of the Fe 3*d* orbitals. The analysis of the fat band plots of the Fe orbitals (spin up and down) in **Figure 15 c-i and 15c-ii** revealed a high spin state.

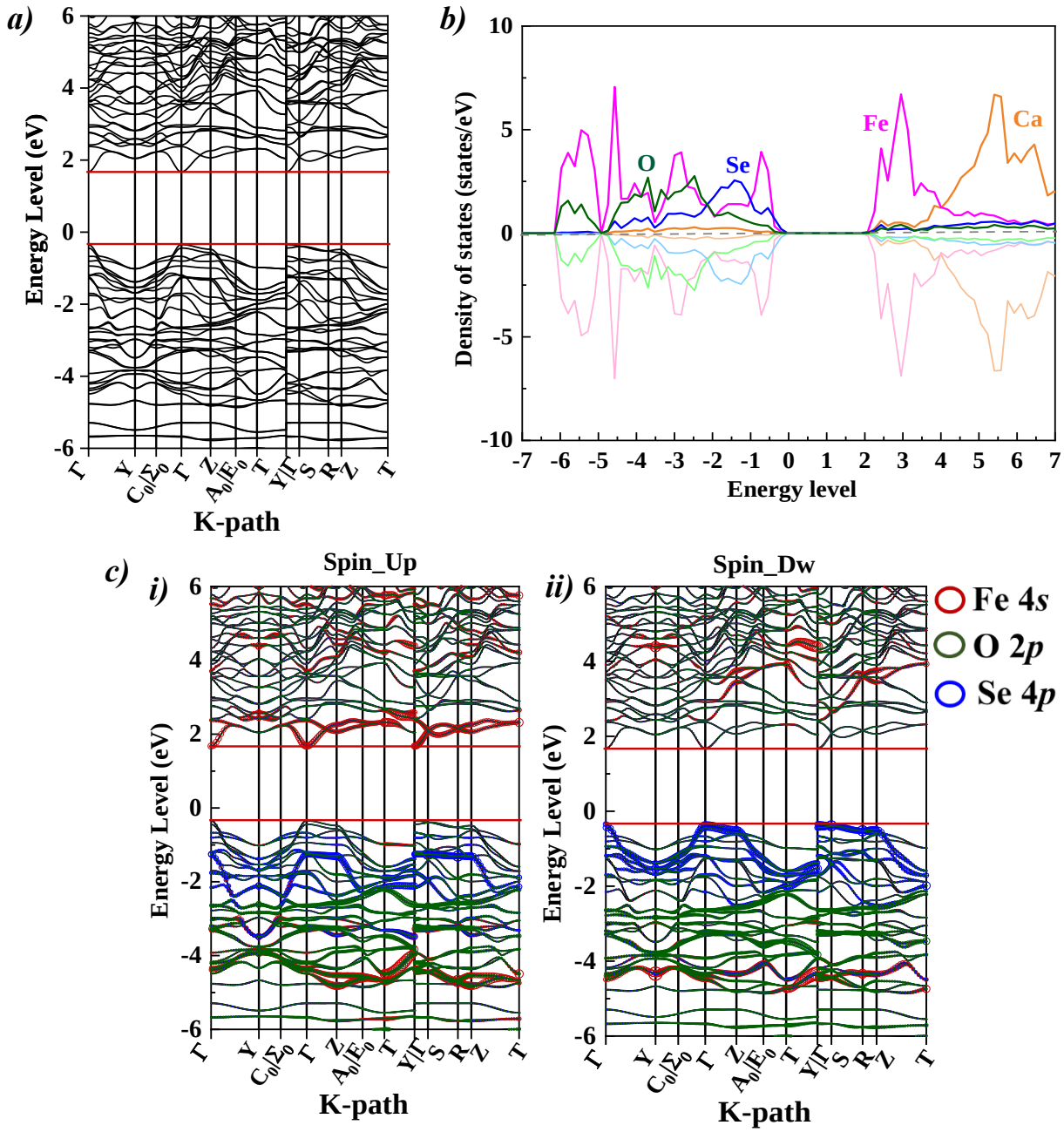

Figure 3.15 : DFT calculations of the non-centrosymmetric polymorph of CaFeOSe with (a) Electronic band structure, (b) projected density of states (PDOS) and (c) fat bands showing the Fe 3*d* states in (i) Spin Up and (ii) Spin Down.

For a quantitative investigation of charge carriers, the effective masses of electrons (m^*_e) and holes (m^*_h) were calculated. We used the effmass software[61] in order to deal with the spin polarized band structure of the CaFeOSe phase. The band structure shows different dispersions of the bands at the CBM and the VBM suggesting different mobility of electrons and holes. The directions near the CBM and VBM were investigated for the extraction of the charge carriers' effective masses.

The lowest value of $m_e^* = 0.342(3)\ m_0$ was found for the electrons in the conduction band for the $\Gamma \rightarrow S$ direction. Heavier effective masses were found for the holes ($m_h^* = 3.616(3)\ m_0$) in the same direction, i.e. within the layers. As the mobility is inversely proportional to the effective mass's values, this indicates a high mobility for the electrons ($m_e^* < 0.5\ m_0$) and a lower one for the holes. This is related to the higher dispersion of the bands in the conduction band compared to the valence band as will be discussed below. In addition, the difference in holes and electrons effective masses has the advantage of ensuring better separation of charge carriers and therefore lowering the rate of electron-hole pairs recombination.

To further discuss the impact of the transition metal in the bands dispersion, it was previously reported that having the *s* orbital character at the CBM by the presence of transition metal cations (Co^{2+}, Ni^{2+}, Fe^{2+} or Mn^{2+}) can lead to competitive effective masses.[62] This is observed in our case as the fat bands analysis for both spin-Up and Spin-Down (**Figure 3.15c)**, shows the contribution of the Fe *s* orbital to the conduction band, hybridized with both Se 4*p* and O 2*p* orbitals.

3.3. Discussion

3.3.1. Band gap width

The materials discussed in this chapter have many features such as the presence of a transition metal (Fe^{2+}), mixed-anion coordination environments of Fe^{2+} cations (FeO_2Q_4 for $La_2O_2Fe_2OQ_2$, $FeOS_3$ for CaFeOS and $FeSe_2O_2$ for CaFeOSe) (**Figure 3.16**) and the layered 2D structures that they adopt (**Figure 3.1, 3.2** and **3.3**). All these characteristics attracted our attention to further explore their potential in photocatalysis and investigate their structure-properties relationship.

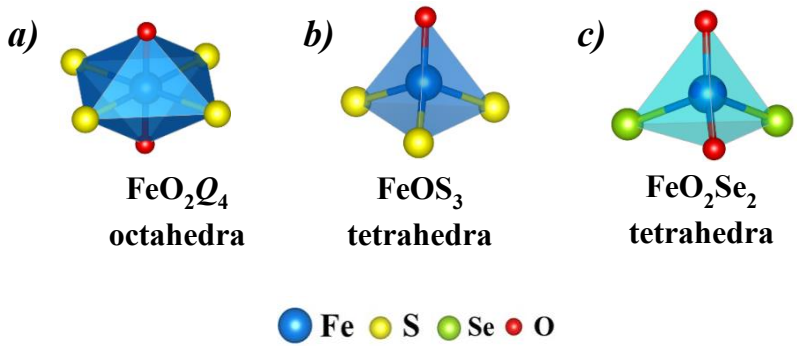

Figure 3.16 : Fe^{2+} coordination environments for (a) $La_2O_2Fe_2OQ_2$, (b) CaFeOS and (c) CaFeOSe.

3.3.1.1. O:*Q* ratio

$La_2O_2Fe_2OQ_2$ phases adopt a band gap of 0.17-0.19 eV[37] whilst CaFeO*Q* oxychalcogenides have larger ones of 1.43 and 2.11 eV for S and Se, respectively. One factor that can play a key role in tuning the band gap is including anions from different rows of the periodic table[4] and this is very much highlighted in the difference between oxides $ZnNb_2O_6$ (3.2 eV),[63] TiO_2 (3.2 eV)[64] and oxysulfides such as $Y_2Ti_2O_5S_2$ (1.9 eV).[65] As mentioned before, the coordination environment of the Fe^{2+} in these materials is different; for instance in $La_2O_2Fe_2OQ_2$ with FeO_2Q_4 units and a Mott insulating character, makes them semiconductors with very small band gaps (too small for ideal photocatalysts). Whilst in CaFeO*Q*, the presence of the pseudo tetrahedral Fe^{2+} ($FeOS_3$ and FeO_2Se_2 for S and Se, respectively) give larger gaps, more suitable for the solar spectrum.

Regarding the CaFeO*Q* phases, CaFeOS (1.43 eV) have slightly greater O:*Q* ratio ($FeOS_3$), compared to CaFeOSe (FeO_2Se_2) with a 2.11 eV band gap size, which could relate to the further decrease of the band gap magnitude of the oxysulfide compared to the oxyselenide. Therefore, the O: *Q* coordination around the cation is one of the key features in the band gap variation, as the

variation of their contributions in the VB or the CB can be influenced in a way that higher *Q* content can lead to further decrease in the band gap.

3.3.1.2. Connectivity

Looking at the reported electronic density of states (DOS) calculations for these phases, it is clear that the Fe 3*d* orbitals are contributing the most near the Fermi level, hybridizing with the O 2*p* and *Q* *np* orbitals to form the maximum of the VB; and in the case of the CaFeO*Q* phases, the contribution of the Ca 4*s* states is negligible.[32,28,19]

The measured band gaps gave such low values compared to other reported transition metal oxychalcogenides such as LaCuOS (3.1 eV),[66] LaOCuTe (2.31 eV)[67] but comparable to $Sr_2CoO_2Cu_2Se_2$ (0.068 eV), $Sr_2CoO_2Ag_2Se_2$ (0.064 eV), and $Sr_2MnO_2Cu_{1.5}Se_2$ (0.073eV).[68] This band gap decrease was addressed in recent reports as a result to the presence of the magnetic elements in the material providing 3*d* orbitals and their interaction with the O/*Q* orbitals in the VB or CB.[69,30]

$La_2O_2Fe_2OQ_2$, $Sr_2CoO_2Cu_2Se_2$ and $Sr_2CoO_2Ag_2Se_2$ adopt similar 2D structure; where the $[Fe_2OQ_2]^{2-}$ layers are formed by face-sharing octahedra with ~180 ° Fe-O-Fe bond angles (**Figure 3.17a**). On the other hand, the oxyselenide CaFeOSe shows deviated Fe-O-Fe angles (~113 °) in the Fe-layers consisting of edge-linked tetrahedra (**Figure 3.17b**). It is possible that having this ~180° bond angle can be advantageous for orbitals overlapping, which can give 3*d* orbitals contributing at lower or higher energy levels, thus tuning the CBM or VBM, resulting in the considerable narrowed band gaps. Finally, in the case of the oxysulfide CaFeOS, the balance between a deviated Fe-S-Fe angle (~104 °) (**Figure 3.17c**) and the choice of sulfur can also be contributing to the tuning of the band gap of this material.

In comparison with other iron chalcogenides such as FeTe and FeSe,[39] they noticed that the Fe-square-lattice unit cell of $La_2O_2Fe_2OSe_2$ was considerably larger than that of either FeTe or FeSe,[70,71] which supported the hypothesis of having more band gap narrowing with larger cation-square lattice. The narrow band gap for $Ba_3Fe_2O_5Cu_2S_2$ (1.03 eV) was also investigated and attributed to the presence of the magnetic trivalent Fe cation.[72]

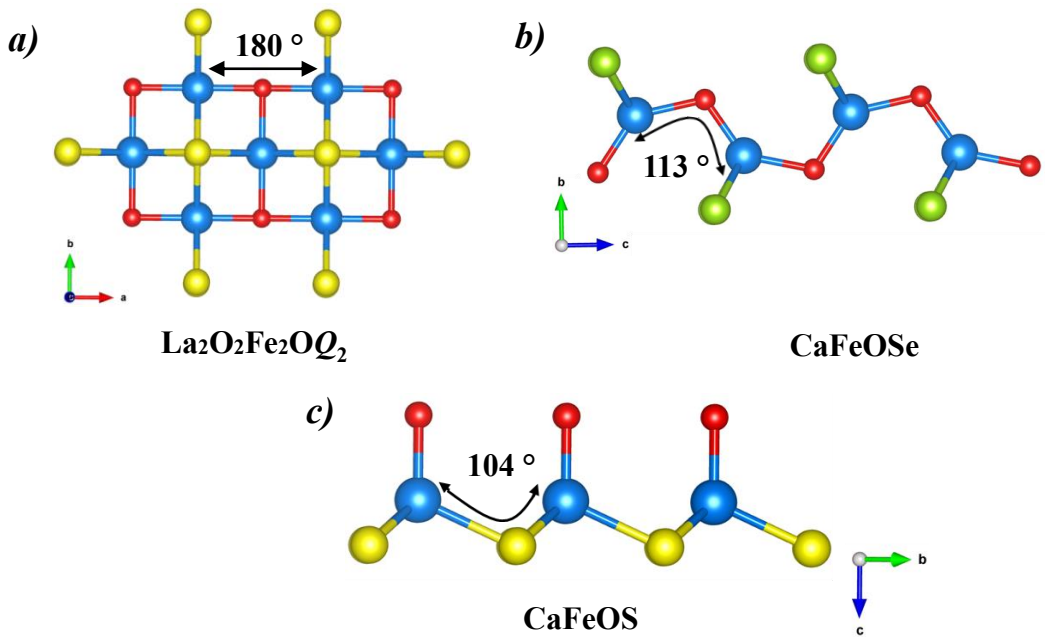

Figure 3.17 : Representation of the M-O/*Q*-M bond angles in (a) $La_2O_2Fe_2OQ_2$ (*Q* = S, Se), (b) CaFeOSe and (c) CaFeOS.

3.3.2. Factors affecting the kinetics observed for the recorded photocurrents

$La_2O_2Fe_2OQ_2$ and CaFeO*Q* (*Q* = S, Se) phases demonstrated their capacity to generate a photocurrent under solar irradiation and in the whole visible spectrum range. These observations were also seen with other oxysulfides such as $Sr_6Cd_2Sb_6S_{10}O_7$ active under solar light.[52]

Figure 3.8c shows a dramatic photocurrent response for CaFeOSe: the spikey peak shape (exponential decay) indicates a fast electron-hole separation and delayed recombination decay. Theory work[13] suggests that polarity within the structure can enhance e^-/h^+ separation and give better kinetics (spikey peak shape). CaFeOSe, prepared here, adopt a polar crystal structure and contain polar FeO_nQ_m units, in contrast to $La_2O_2Fe_2OQ_2$, that adopt a non-polar structure and which show much slower photocurrent responses.

On the other hand, the question remains whether having polar structure or polar units that counts most; thus, we searched other materials showing similar results, such as La_3GaS_5O (*Pnma* symmetry).[73] Using a 300 W Xenon lamp for irradiation, the non-polar La_3GaS_5O demonstrated a photocurrent with fast kinetics of ~ 80 μA under λ > 290 nm and a potential varying between -1.2 to 0.2 V.[73] The common factor between these materials is having a polar coordination for the

photoactive cations: $FeSe_2O_2$ and GaO_3S_4 for CaFeOSe and La_3GaS_5O respectively. This proposes another possible explanation for the enhanced transport properties of the charge carriers which is that having polar coordination environment can be a key factor to have better electron-hole separation than the presence of a polar axis in the crystal structure. This hypothesis is supported by the photocurrent results seen for $La_2O_2Fe_2OQ_2$ analogues (**Figure 3.8a and 3.8b**), with the absence of polar units in their structure, no spikey peaks occurred.

3.3.3. Factors affecting the recorded photocurrent of the oxysulfide CaFeOS

Despite its polar structure, CaFeOS showed relatively poor photocurrent responses due to its low stability during these measurements. It's likely that this photodegradation occurred from incoming oxidation of Fe^{2+}.

According to the literature, the presence of *nd* orbitals could have an impact on the dispersion of the valence and conduction bands; which might result in enhanced charge carriers' transport properties.[74,75] But these metal cations are not always stable in their oxidation state, as they can be reduced or oxidized fast considering the different contributing factors (presence of oxidizable agents), not very beneficial for the photocatalytic activity.

For instance, the use of more electronegative anions (such as oxygen) tends to fully oxidize these cations but pairing them with less electronegative anions (sulfur or selenium) it is possible to stabilize the lower oxidation states.[76] This can also be affected by the O:*Q* ratio, for example, in $FeSe_2O_2$ of CaFeOSe oxyselenide, the presence of Se can result in much higher covalent bond with the Fe in addition to the ionic bonds (presence of more O) compared to $FeOS_3$ of CaFeOS oxysulfide. This is an indication that the stability of CaFeOSe compared to the other phases could be the result of an interplay between the presence of these two anions to stabilize the transition metal cation, giving a much stable oxidation states for the iron in this kind of materials. On the other hand, and as mentioned earlier, these cations may convert to higher oxidation states also when exposed to oxidizers such as oxygen or moisture, which can impact the carrier concentrations.[77]

It was also reported that the photogenerated holes from *d*-bands of transition metal cations could react with oxidizable agents by way of formation of charge transfer-transition complexes which can have major consequences in photoelectrochemistry and photoelectrochemical energy conversion.[78] This was the case of the transition of Mo (IV) to Mo (V), which led to a change in

the crystal geometry. This resulted in a rise of the corresponding electronic levels (due to the liberation of an additional bond) that served as trap for holes which further oxidized the complex formed between the electron donors and the surface states produced by the *d*-holes.[78]

Lastly, the surface morphology is an important factor in controlling the performance of a device constructed from the layered compounds. When the surface of a layered crystal is exposed to the electrolyte, the dangling bonds associated with the unsaturated transition metal or chalcogenide atoms introduce surface states within the band gap. These surface levels can also act as recombination centers for photogenerated electrons and holes.[79] The distinct changes in the composition of the material during the measurements could also affect the oxidation states of these metal cations.[80] For instance, the presence of defect states is usually reported to have a negative effect on the photoactivity because they act as recombination centers for charge carriers. However, under appropriate applied potential, these defect levels can act as electron donor states yielding a photocurrent response under appropriate irradiation.[81]

Therefore, having a metal transition may not yield high-performing semiconductors but can be of big benefit as an ion dopant which could be more efficient for the e^-/h^+ pair recombination rate and enhance the photo-responsiveness of the semiconductor.[81,82,83,84]

We thus unlock some of the key factors to design potential transition metal based oxychalcogenides photocatalysts: First, the band gap magnitude and nature can influence the charge carriers' recombination process, a crucial factor in the photocatalytic reaction. Second, the connectivity can impact the orbitals overlap, which can also influence the band gap narrowing. Finally, the presence of an heteroleptic environment which can lead to a polar unit can be an essential requirement to enhance the charge carrier's separation as we saw from our photocurrent responses. The fact of having a polar structure and its necessity for an improved photocatalytic activity is still to be explored.

3.4. Conclusion

Four iron-based oxychalcogenides were discussed in this chapter, $La_2O_2Fe_2OQ_2$ and CaFeO*Q* (*Q* = S, Se). Their structural and physical properties were investigated by exploring their photoelectric and electronic characteristics. These measurements contributed in determining their potential as photocatalysts and gave us insight into some key features to design transition-metals based oxychalcogenide photocatalysts.

Using UV-visible spectroscopy for CaFeO*Q* (*Q* = S, Se) materials, the optical band gaps was found to be of convenient magnitudes for the solar spectrum (E_g = 1.43 and 2.11 eV for S and Se, respectively). On the other hand, and judging by their reported band gaps, $La_2O_2Fe_2OQ_2$ (*Q* = S, Se) presented small band gaps (0.17 - 0.19 eV), inconvenient for the solar spectrum. Alternately, the band edge positions calculated by the empirical method, revealed that the CaFeO*Q* oxychalcogenides present convenient conduction band positions, which make them active for half reactions in the visible light as photocathodes (reduction reaction).

Looking at the reported electronic properties, specifically the density of states, the O:*Q* ratio around the photoactive cations was found to influence the narrowing of the band gap, where higher chalcogen content further decrease its magnitude. In addition, having M-O-M angles ~ 180 ° can impact the band gap magnitude by further narrowing it.

$La_2O_2Fe_2OQ_2$ and CaFeOSe demonstrated a capacity to generate photocurrents under UV and solar irradiations, even with no applied potential; which is not very common among oxychalcogenides.[85,73] Thus, $La_2O_2Fe_2OQ_2$ and CaFeO*Q* (*Q* = S, Se) can be added to the series of interesting materials for applications under solar light. It is striking to observe the photocurrent response in CaFeOSe that is typical of a material with very efficient electron-hole separation and migration (exponential decay) with slow recombination rates. By comparing with other reported materials, this result could be related to the presence of polarity within the structure.

Therefore, having a layered structure, offered by the presence of a transition metal in a multi-anionic framework, with the presence of noncentrosymmetric units can be beneficial for designing efficient transition-metals based materials for photocatalytic applications in the solar light. On the other hand, these materials can sometimes suffer from an oxidation reaction of the metal cation and this is what was observed for CaFeOS, due to structural and bonding aspects.

REFERENCES

(1) Kong, D.; Zheng, Y.; Kobielusz, M.; Wang, Y.; Bai, Z.; Macyk, W.; Wang, X.; Tang, J. Recent Advances in Visible Light-Driven Water Oxidation and Reduction in Suspension Systems. *Materials Today* **2018**, *21* (8), 897–924.

(2) Cui, J.; Li, C.; Zhang, F. Development of Mixed-Anion Photocatalysts with Wide Visible-Light Absorption Bands for Solar Water Splitting. *ChemSusChem* **2019**, *12* (9), 1872–1888.

(3) Goto, Y.; Seo, J.; Kumamoto, K.; Hisatomi, T.; Mizuguchi, Y.; Kamihara, Y.; Katayama, M.; Minegishi, T.; Domen, K. Crystal Structure, Electronic Structure, and Photocatalytic Activity of Oxysulfides: La2Ta2ZrS2O8, La2Ta2TiS2O8, and La2Nb2TiS2O8. *Inorganic Chemistry* **2016**, *55* (7), 3674–3679.

(4) Kageyama, H.; Hayashi, K.; Maeda, K.; Attfield, J. P.; Hiroi, Z.; Rondinelli, J. M.; Poeppelmeier, K. R. Expanding Frontiers in Materials Chemistry and Physics with Multiple Anions. *Nature communications* **2018**, *9* (1), 1–15.

(5) Ishikawa, A.; Takata, T.; Kondo, J. N.; Hara, M.; Kobayashi, H.; Domen, K. Oxysulfide Sm2Ti2S2O5 as a Stable Photocatalyst for Water Oxidation and Reduction under Visible Light Irradiation (Λ≤ 650 Nm). *Journal of the American Chemical Society* **2002**, *124* (45), 13547–13553.

(6) Miura, A.; Oshima, T.; Maeda, K.; Mizuguchi, Y.; Moriyoshi, C.; Kuroiwa, Y.; Meng, Y.; Wen, X.-D.; Nagao, M.; Higuchi, M. Synthesis, Structure and Photocatalytic Activity of Layered LaOInS 2. *Journal of Materials Chemistry A* **2017**, *5* (27), 14270–14277.

(7) Kabbour, H.; Sayede, A.; Saitzek, S.; Lefevre, G.; Cario, L.; Trentesaux, M.; Roussel, P. Structure of the Water-Splitting Photocatalyst Oxysulfide α-LaOInS 2 and Ab Initio Prediction of New Polymorphs. *Chemical Communications* **2020**, *56* (11), 1645–1648.

(8) Wang, Q.; Nakabayashi, M.; Hisatomi, T.; Sun, S.; Akiyama, S.; Wang, Z.; Pan, Z.; Xiao, X.; Watanabe, T.; Yamada, T. Oxysulfide Photocatalyst for Visible-Light-Driven Overall Water Splitting. *Nature materials* **2019**, *18* (8), 827–832.

(9) Zhao, L. D.; Berardan, D.; Pei, Y. L.; Byl, C.; Pinsard-Gaudart, L.; Dragoe, N. Bi 1− x Sr x CuSeO Oxyselenides as Promising Thermoelectric Materials. *Applied Physics Letters* **2010**, *97* (9), 092118.

(10) Dong, X.-D.; Zhang, Y.-M.; Zhao, Z.-Y. Role of the Polar Electric Field in Bismuth Oxyhalides for Photocatalytic Water Splitting. *Inorganic Chemistry* **2021**, *60* (12), 8461–8474.

(11) Lou, Z.; Wang, P.; Huang, B.; Dai, Y.; Qin, X.; Zhang, X.; Wang, Z.; Liu, Y. Enhancing Charge Separation in Photocatalysts with Internal Polar Electric Fields. *ChemPhotoChem* **2017**, *1* (5), 136–147.

(12) Dong, X.-D.; Yao, G.-Y.; Liu, Q.-L.; Zhao, Q.-M.; Zhao, Z.-Y. Spontaneous Polarization Effect and Photocatalytic Activity of Layered Compound of BiOIO3. *Inorganic Chemistry* **2019**, *58* (22), 15344–15353.

(13) Vonrüti, N.; Aschauer, U. Band-Gap Engineering in AB (O x S 1− x) 3 Perovskite Oxysulfides: A Route to Strongly Polar Materials for Photocatalytic Water Splitting. *Journal of Materials Chemistry A* **2019**, *7* (26), 15741–15748.

(14) Dai, P.; Hu, J.; Dagotto, E. Magnetism and Its Microscopic Origin in Iron-Based High-Temperature Superconductors. *Nature Physics* **2012**, *8* (10), 709–718.

(15) Dagotto, E. Colloquium: The Unexpected Properties of Alkali Metal Iron Selenide Superconductors. *Reviews of modern physics* **2013**, *85* (2), 849.

(16) Stewart, G. R. Superconductivity in Iron Compounds. *Reviews of Modern Physics* **2011**, *83* (4), 1589.

(17) Kamihara, Y.; Watanabe, T.; Hirano, M.; Hosono, H. Iron-Based Layered Superconductor La [O1-x F x] FeAs (X= 0.05− 0.12) with T C= 26 K. *Journal of the American Chemical Society* **2008**, *130* (11), 3296–3297.

(18) Stock, C.; McCabe, E. E. The Magnetic and Electronic Properties of Oxyselenides—Influence of Transition Metal Ions and Lanthanides. *Journal of Physics: Condensed Matter* **2016**, *28* (45), 453001.

(19) Han, F.; Wang, D.; Malliakas, C. D.; Sturza, M.; Chung, D. Y.; Wan, X.; Kanatzidis, M. G. (CaO)(FeSe): A Layered Wide-Gap Oxychalcogenide Semiconductor. *Chemistry of Materials* **2015**, *27* (16), 5695–5701.

(20) Cassidy, S. J.; Batuk, M.; Batuk, D.; Hadermann, J.; Woodruff, D. N.; Thompson, A. L.; Clarke, S. J. Complex Microstructure and Magnetism in Polymorphic CaFeSeO. *Inorganic Chemistry* **2016**, *55* (20), 10714–10726.

(21) Lai, K. T.; Komarek, A. C.; Fernandez-Diaz, M. T.; Chang, P.-S.; Huh, S.; Rosner, H.; Kuo, C.-Y.; Hu, Z.; Pi, T.-W.; Adler, P. Canted Antiferromagnetism on Rectangular Layers of Fe2+ in Polymorphic CaFeSeO. *Inorganic Chemistry* **2017**, *56* (8), 4271–4279.

(22) JHA, A.; Igiehon, U. O.; Grieveson, P. Carbothermic Reduction of Pyrrholite in the Presence of Lime for Production of Metallic Iron. I: Phase Equilibria in the Fe-Ca-SO System. *Scandinavian journal of metallurgy* **1991**, *20* (5), 270–278.

(23) Selivanov, E. N.; Chumarev, V. M.; Gulyaeva, R. I.; Mar'evich, V. P.; Vershinin, A. D.; Pankratov, A. A.; Korepanova, E. S. Composition, Structure, and Thermal Expansion of Ca3Fe4S3O6 and CaFeSO. *Inorganic materials* **2004**, *40* (8), 845–850.

(24) Jin, S. F.; Huang, Q.; Lin, Z. P.; Li, Z. L.; Wu, X. Z.; Ying, T. P.; Wang, G.; Chen, X. L. Two-Dimensional Magnetic Correlations and Partial Long-Range Order in Geometrically Frustrated CaOFeS with Triangle Lattice of Fe Ions. *Physical Review B* **2015**, *91* (9), 094420.

(25) Delacotte, C.; Perez, O.; Pautrat, A.; Berthebaud, D.; Hebert, S.; Suard, E.; Pelloquin, D.; Maignan, A. Magnetodielectric Effect in Crystals of the Noncentrosymmetric CaOFeS at Low Temperature. *Inorganic chemistry* **2015**, *54* (13), 6560–6565.

(26) Petrova, S. A.; Mar'Evich, V. P.; Zakharov, R. G.; Selivanov, E. N.; Chumarev, V. M.; Udoeva, L. Y. Crystal Structure of Zinc Calcium Oxysulfide. In *Doklady Chemistry*; Kluwer Academic Publishers-Plenum Publishers, 2003; Vol. 393, pp 255–258.

(27) Sambrook, T.; Smura, C. F.; Clarke, S. J.; Ok, K. M.; Halasyamani, P. S. Structure and Physical Properties of the Polar Oxysulfide CaZnOS. *Inorganic chemistry* **2007**, *46* (7), 2571–2574.

(28) Zhang, Y.; Lin, L.; Zhang, J.-J.; Huang, X.; An, M.; Dong, S. Exchange Striction Driven Magnetodielectric Effect and Potential Photovoltaic Effect in Polar CaOFeS. *Physical Review Materials* **2017**, *1* (3), 034406.

(29) Mayer, J. M.; Schneemeyer, L. F.; Siegrist, T.; Waszczak, J. V.; Van Dover, B. New Layered Iron-Lanthanum-Oxide-Sulfide And-Selenide Phases: Fe2La2O3E2 (E= S, Se). *Angewandte Chemie International Edition in English* **1992**, *31* (12), 1645–1647.

(30) Clarke, S. J.; Adamson, P.; Herkelrath, S. J.; Rutt, O. J.; Parker, D. R.; Pitcher, M. J.; Smura, C. F. Structures, Physical Properties, and Chemistry of Layered Oxychalcogenides and Oxypnictides. *Inorganic chemistry* **2008**, *47* (19), 8473–8486.

(31) Freelon, B.; Yamani, Z.; Swainson, I.; Flacau, R.; Karki, B.; Liu, Y. H.; Craco, L.; Laad, M. S.; Wang, M.; Chen, J. Magnetic and Structural Properties of the Iron Oxychalcogenides La 2 O 2 Fe 2 O M 2 (M= S, Se). *Physical Review B* **2019**, *99* (2), 024109.

(32) Zhu, J.-X.; Yu, R.; Wang, H.; Zhao, L. L.; Jones, M. D.; Dai, J.; Abrahams, E.; Morosan, E.; Fang, M.; Si, Q. Band Narrowing and Mott Localization in Iron Oxychalcogenides La 2 O 2 Fe 2 O (Se, S) 2. *Physical review letters* **2010**, *104* (21), 216405.

(33) McCabe, E. E.; Stock, C.; Rodriguez, E. E.; Wills, A. S.; Taylor, J. W.; Evans, J. S. O. Weak Spin Interactions in Mott Insulating La 2 O 2 Fe 2 OSe 2. *Physical Review B* **2014**, *89* (10), 100402.

(34) Oogarah, R. K.; Suard, E.; McCabe, E. E. Magnetic Order and Phase Transition in the Iron Oxysulfide La2O2Fe2OS2. *Journal of Magnetism and Magnetic Materials* **2018**, *446*, 101–107.

(35) Free, D. G.; Evans, J. S. Low-Temperature Nuclear and Magnetic Structures of La 2 O 2 Fe 2 O Se 2 from x-Ray and Neutron Diffraction Measurements. *Physical Review B* **2010**, *81* (21), 214433.

(36) Lei, H.; Bozin, E. S.; Llobet, A.; Ivanovski, V.; Koteski, V.; Belosevic-Cavor, J.; Cekic, B.; Petrovic, C. Magnetism in La 2 O 3 (Fe 1− x Mn x) 2 Se 2 Tuned by Fe/Mn Ratio. *Physical Review B* **2012**, *86* (12), 125122.

(37) Jin, G.; Wang, Y.; Dai, X.; Ren, X.; He, L. Strong Charge and Spin Fluctuations in La 2 O 3 Fe 2 Se 2. *Physical Review B* **2016**, *94* (7), 075150.

(38) Singh, D. J.; Du, M.-H. Density Functional Study of LaFeAsO 1− x F x: A Low Carrier Density Superconductor near Itinerant Magnetism. *Physical Review Letters* **2008**, *100* (23), 237003.

(39) Subedi, A.; Zhang, L.; Singh, D. J.; Du, M.-H. Density Functional Study of FeS, FeSe, and FeTe: Electronic Structure, Magnetism, Phonons, and Superconductivity. *Physical Review B* **2008**, *78* (13), 134514.

(40) Rodriguez-Carvajal, J. Fullprof: A Program for Rietveld Refinement and Profile Matching Analysis of Complex Powder Diffraction Patterns. *Laboratoire Léon Brillouin (CEA-CNRS)* **1991**.

(41) Momma, K. *Visualization for Electronic and Structural Analysis*; 2019.

(42) Tauc, J.; Grigorovici, R.; Vancu, A. Optical Properties and Electronic Structure of Amorphous Germanium. *physica status solidi (b)* **1966**, *15* (2), 627–637.

(43) Kubelka, P.; Munk, F. A Contribution to the Optics of Pigments. *Z. Tech. Phys* **1931**, *12* (593), 193.

(44) Giovannetti, G.; de'Medici, L.; Aichhorn, M.; Capone, M. La 2 O 3 Fe 2 Se 2: A Mott Insulator on the Brink of Orbital-Selective Metallization. *Physical Review B* **2015**, *91* (8), 085124.

(45) Butler, M.; Ginley, D. Prediction of Flatband Potentials at Semiconductor-electrolyte Interfaces from Atomic Electronegativities. *Journal of the Electrochemical Society* **1978**, *125* (2), 228.

(46) Leroy, S.; Blach, J.-F.; Huvé, M.; Léger, B.; Kania, N.; Henninot, J.-F.; Ponchel, A.; Saitzek, S. Photocatalytic and Sonophotocatalytic Degradation of Rhodamine B by Nano-Sized La2Ti2O7 Oxides Synthesized with Sol-Gel Method. *Journal of Photochemistry and Photobiology A: Chemistry* **2020**, *401*, 112767. https://doi.org/10.1016/j.jphotochem.2020.112767.

(47) Gelderman, K.; Lee, L.; Donne, S. W. Flat-Band Potential of a Semiconductor: Using the Mott–Schottky Equation. *Journal of chemical education* **2007**, *84* (4), 685.

(48) Bott, A. W. Electrochemistry of Semiconductors. *Current Separations* **1998**, *17*, 87–92.

(49) Lin, L.; Lin, J. M.; Wu, J. H.; Hao, S. C.; Lan, Z. Photovoltage Enhancement of Dye Sensitised Solar Cells by Using ZnO Modified TiO2 Electrode. *null* **2010**, *14* (5), 370–374. https://doi.org/10.1179/143307510X12820854748791.

(50) Shaikh, S. K.; Inamdar, S. I.; Ganbavle, V. V.; Rajpure, K. Y. Chemical Bath Deposited ZnO Thin Film Based UV Photoconductive Detector. *Journal of Alloys and Compounds* **2016**, *664*, 242–249.

(51) Zhao, Q.; Wang, W.; Carrascoso-Plana, F.; Jie, W.; Wang, T.; Castellanos-Gomez, A.; Frisenda, R. The Role of Traps in the Photocurrent Generation Mechanism in Thin InSe Photodetectors. *Materials Horizons* **2020**, *7* (1), 252–262.

(52) Al Bacha, S.; Saitzek, S.; McCabe, E. E.; Kabbour, H. Photocatalytic and Photocurrent Responses to Visible Light of the Lone-Pair-Based Oxysulfide Sr6Cd2Sb6S10O7. *Inorganic Chemistry* **2022**.

(53) Mentré, O.; Juárez-Rosete, M. A.; Saitzek, S.; Aguilar-Maldonado, C.; Colmont, M.; Arévalo-López, Á. M. S= 1/2 Chain in BiVO3F: Spin Dimers versus Photoanodic Properties. *Journal of the American Chemical Society* **2021**, *143* (18), 6942–6951.

(54) LEROY, S. Etude Des Propriétés Photocatalytiques et Photoélectriques Du Dititanate de Lanthane (La2Ti2O7) à Structure Pérovskite En Feuillets et Son Utilisation Dans Des Hétérojonctions Tout Oxyde Pour La Conversion d'énergie.

(55) Parkinson, B.; Turner, J.; Peter, L.; Lewis, N.; Sivula, K.; Domen, K.; Bard, A. J.; Fiechter, S.; Collazo, R.; Hannappel, T. *Photoelectrochemical Water Splitting: Materials, Processes and Architectures*; Royal Society of Chemistry, 2013.

(56) Al Bacha, S.; Saitzek, S.; McCabe, E. E.; Kabbour, H. Photocatalytic and Photocurrent Responses to Visible Light of the Lone-Pair-Based Oxysulfide Sr6Cd2Sb6S10O7. *Inorganic Chemistry* **2022**, *61* (46), 18611–18621.

(57) Uosaki, K.; Kita, H. Effects of the Helmholtz Layer Capacitance on the Potential Distribution at Semiconductor/Electrolyte Interface and the Linearity of the Mott-Schottky Plot. *Journal of The Electrochemical Society* **1983**, *130* (4), 895–897.

(58) Sun, G.; Kürti, J.; Rajczy, P.; Kertesz, M.; Hafner, J.; Kresse, G. Performance of the Vienna Ab Initio Simulation Package (VASP) in Chemical Applications. *Journal of Molecular Structure: THEOCHEM* **2003**, *624* (1–3), 37–45.

(59) Dudarev, S. L.; Botton, G. A.; Savrasov, S. Y.; Humphreys, C.; Sutton, A. P. Electron-Energy-Loss Spectra and the Structural Stability of Nickel Oxide: An LSDA+ U Study. *Physical Review B* **1998**, *57* (3), 1505.

(60) Almoussawi, B.; Kageyama, H.; Roussel, P.; Kabbour, H. Versatile Interplay of Chalcogenide and Dichalcogenide Anions in the Thiovanadate Ba7S (VS3O) 2 (S2) 3 and Its Selenide Derivatives: Elaboration and DFT Meta-GGA Study. *ACS Organic & Inorganic Au* **2023**.

(61) Whalley, L. D. Effmass: An Effective Mass Package. *Journal of Open Source Software* **2018**, *3* (28), 797.

(62) Hautier, G.; Miglio, A.; Waroquiers, D.; Rignanese, G.-M.; Gonze, X. How Does Chemistry Influence Electron Effective Mass in Oxides? A High-Throughput Computational Analysis. *Chemistry of Materials* **2014**, *26* (19), 5447–5458.

(63) Kormányos, A.; Thomas, A.; Huda, M. N.; Sarker, P.; Liu, J. P.; Poudyal, N.; Janáky, C.; Rajeshwar, K. Solution Combustion Synthesis, Characterization, and Photoelectrochemistry of CuNb2O6 and ZnNb2O6 Nanoparticles. *The Journal of Physical Chemistry C* **2016**, *120* (29), 16024–16034.

(64) Hashimoto, K.; Irie, H.; Fujishima, A. TiO2 Photocatalysis: A Historical Overview and Future Prospects. *Japanese journal of applied physics* **2005**, *44* (12R), 8269.

(65) Denis, S. G.; Clarke, S. J. Two Alternative Products from the Intercalation of Alkali Metals into Cation-Defective Ruddlesden–Popper Oxysulfides. *Chemical Communications* **2001**, No. 22, 2356–2357.

(66) Ueda, K.; Inoue, S.; Hosono, H.; Sarukura, N.; Hirano, M. Room-Temperature Excitons in Wide-Gap Layered-Oxysulfide Semiconductor: LaCuOS. *Applied Physics Letters* **2001**, *78* (16), 2333–2335.

(67) Liu, M. L.; Wu, L. B.; Huang, F. Q.; Chen, L. D.; Ibers, J. A. Syntheses, Crystal and Electronic Structure, and Some Optical and Transport Properties of LnCuOTe (Ln= La, Ce, Nd). *Journal of Solid State Chemistry* **2007**, *180* (1), 62–69.

(68) Jin, S.; Chen, X.; Guo, J.; Lei, M.; Lin, J.; Xi, J.; Wang, W.; Wang, W. Sr2Mn3Sb2O2 Type Oxyselenides: Structures, Magnetism, and Electronic Properties of Sr2 A O2 M 2Se2 (A= Co, Mn; M= Cu, Ag). *Inorganic Chemistry* **2012**, *51* (19), 10185–10192.

(69) Guo, Z.; Sun, F.; Yuan, W. Chemical Intercalations in Layered Transition Metal Chalcogenides: Syntheses, Structures, and Related Properties. *Crystal Growth & Design* **2017**, *17* (4), 2238–2253.

(70) Hsu, F.-C.; Luo, J.-Y.; Yeh, K.-W.; Chen, T.-K.; Huang, T.-W.; Wu, P. M.; Lee, Y.-C.; Huang, Y.-L.; Chu, Y.-Y.; Yan, D.-C. Superconductivity in the PbO-Type Structure α-FeSe. *Proceedings of the National Academy of Sciences* **2008**, *105* (38), 14262–14264.

(71) Bao, W.; Qiu, Y.; Huang, Q.; Green, M. A.; Zajdel, P.; Fitzsimmons, M. R.; Zhernenkov, M.; Chang, S.; Fang, M.; Qian, B. Tunable (δ π, δ π)-Type Antiferromagnetic Order in α-Fe (Te, Se) Superconductors. *Physical review letters* **2009**, *102* (24), 247001.

(72) Zhang, H.; Jin, S.; Guo, L.; Shen, S.; Lin, Z.; Chen, X. Bandgap Narrowing in the Layered Oxysulfide Semiconductor Ba3Fe2O5Cu2S2: Role of FeO2 Layer. *Chinese Physics B* **2016**, *25* (2), 026101.

(73) Ogisu, K.; Ishikawa, A.; Shimodaira, Y.; Takata, T.; Kobayashi, H.; Domen, K. Electronic Band Structures and Photochemical Properties of La− Ga-Based Oxysulfides. *The Journal of Physical Chemistry C* **2008**, *112* (31), 11978–11984.

(74) Ogisu, K.; Ishikawa, A.; Teramura, K.; Toda, K.; Hara, M.; Domen, K. Lanthanum–Indium Oxysulfide as a Visible Light Driven Photocatalyst for Water Splitting. *Chemistry letters* **2007**, *36* (7), 854–855.

(75) Hisatomi, T.; Okamura, S.; Liu, J.; Shinohara, Y.; Ueda, K.; Higashi, T.; Katayama, M.; Minegishi, T.; Domen, K. La 5 Ti 2 Cu 1− x Ag x S 5 O 7 Photocathodes Operating at Positive Potentials during Photoelectrochemical Hydrogen Evolution under Irradiation of up to 710 Nm. *Energy & Environmental Science* **2015**, *8* (11), 3354–3362.

(76) Stevanović, V.; Hartman, K.; Jaramillo, R.; Ramanathan, S.; Buonassisi, T.; Graf, P. Variations of Ionization Potential and Electron Affinity as a Function of Surface Orientation: The Case of Orthorhombic SnS. *Applied Physics Letters* **2014**, *104* (21), 211603.

(77) Brandt, R. E.; Stevanović, V.; Ginley, D. S.; Buonassisi, T. Identifying Defect-Tolerant Semiconductors with High Minority-Carrier Lifetimes: Beyond Hybrid Lead Halide Perovskites. *Mrs Communications* **2015**, *5* (2), 265–275.

(78) Tributsch, H. Hole Reactions from D-energy Bands of Layer Type Group VI Transition Metal Dichalcogenides: New Perspectives for Electrochemical Solar Energy Conversion. *Journal of the Electrochemical Society* **1978**, *125* (7), 1086.

(79) Kam, K. K.; Parkinson, B. A. Detailed Photocurrent Spectroscopy of the Semiconducting Group VIB Transition Metal Dichalcogenides. *The Journal of Physical Chemistry* **1982**, *86* (4), 463–467.

(80) Augustynski, J.; Balsenc, L.; Hinden, J. X-Ray Photoelectron Spectroscopic Studies of RuO2-based Film Electrodes. *Journal of the Electrochemical Society* **1978**, *125* (7), 1093.

(81) Hamilton, J. W. J.; Byrne, J. A.; McCullagh, C.; Dunlop, P. S. M. Electrochemical Investigation of Doped Titanium Dioxide. *International Journal of Photoenergy* **2008**, *2008*, 631597. https://doi.org/10.1155/2008/631597.

(82) Leung, L. K.; Komplin, N. J.; Ellis, A. B.; Tabatabaie, N. Photoluminescence Studies of Silver-Exchanged Cadmium Selenide Crystals: Modification of a Chemical Sensor for Aniline Derivatives by Heterojunction Formation. *The Journal of Physical Chemistry* **1991**, *95* (15), 5918–5924.

(83) Kiwi, J.; Gratzel, M. Heterogeneous Photocatalysis: Enhanced Dihydrogen Production in Titanium Dioxide Dispersions under Irradiation. The Effect of Magnesium Promoter at the Semiconductor Interface. *The Journal of Physical Chemistry* **1986**, *90* (4), 637–640.

(84) Palmisano, L.; Augugliaro, V.; Sclafani, A.; Schiavello, M. Activity of Chromium-Ion-Doped Titania for the Dinitrogen Photoreduction to Ammonia and for the Phenol Photodegradation. *The Journal of Physical Chemistry* **1988**, *92* (23), 6710–6713.

(85) Shi, Y.-F.; Li, X.-F.; Zhang, Y.-X.; Lin, H.; Ma, Z.; Wu, L.-M.; Wu, X.-T.; Zhu, Q.-L. [(Ba19Cl4)(Ga6Si12O42S8)]: A Two-Dimensional Wide-Band-Gap Layered Oxysulfide with Mixed-Anion Chemical Bonding and Photocurrent Response. *Inorganic chemistry* **2019**, *58* (10), 6588–6592.

Chapter 4

Photocatalytic and Photocurrent Responses to visible light of the lone-pair-based oxysulfide $Sr_6Cd_2Sb_6O_7S_{10}$

Chapter 4: Photocatalytic and photocurrent responses to visible light of the lone-pair-based oxysulfide $Sr_6Cd_2Sb_6S_{10}O_7$

4.1. Introduction

The previous chapter focused on the investigation of $3d^6$ Fe^{2+} oxychalcogenides. These phases present certain structural aspects (layers) and coordination environments (heteroleptic environments) that seemed favourable for the photocurrent and photocatalytic measurements. Although a photocurrent response was observed for all four samples, the band gap magnitude and the band edge positions were not always convenient. $La_2O_2Fe_2OQ_2$ presented very narrow band gaps compared to CaFeO*Q* (*Q* = S, Se), which could be related to the cation-anion interactions and the structures' connectivity.

Therefore, the investigation in this chapter is focused on the p-block cation Sb^{3+} with the $5s^2$ 'inert pair'. The presence of these pairs is known to favour lower-symmetry (often polar) coordination environments; on the other hand, their activity can be tuned by the anion choice and coordination.

4.1.1. Revised lone pair model

For heavier elements (group 14th-16th), relativistic effects and ionic factors can cause the contraction of the valence ns^2 orbitals (contraction increases with the increase of the atomic number) which can explain the origin of the 'inert effect' seen for these p-block elements.[1,2] In addition, their presence can induce oriented dipoles thus causing deviations from centrosymmetric coordination environments; which can help in designing piezoelectric, ferroelectric and NLO materials.[3] **Figure 4.1** show the crystal structure of a lone pair oxide and chalcogenide systems, where SnTe (**Figure 4.1a**) crystallizes in a higher symmetry (*Fm*-3*m*), with non-bonding $5s^2$ electrons.[4] Whilst the presence of a second Jahn-Teller distortion could further stabilize the lone pair (stronger lone pair effect) in lower symmetry structures with further ionic bonds, for instance SnO (**Figure 4.1b**).[5]

Lone pair cations, such as bismuth $6s^2$ electrons pairs, with a tendency to lower the symmetry could be the origin of having intrinsic polarization within the structure.[6] The presence of a (heavy)

"lone pair" cation such as Bi^{3+}, Sb^{3+}, Sn^{2+} was also found to be a key feature in designing photocatalytic and photovoltaic materials[7,8,9] In fact, the presence of the $5s^2$ or $6s^2$ lone pair of electrons, and its relative energy to anion *p* orbitals, can determine the energy (and degree of delocalisation) of states at the top of the valence band which are key to explaining the optical response of these materials. These hypotheses were discussed in the work of Kavanagh *et al.* in $Sn_2SbS_2I_3$ chalcohalide[10] and Wang et *al.* in antimony chalcogenide semiconductors.[11]

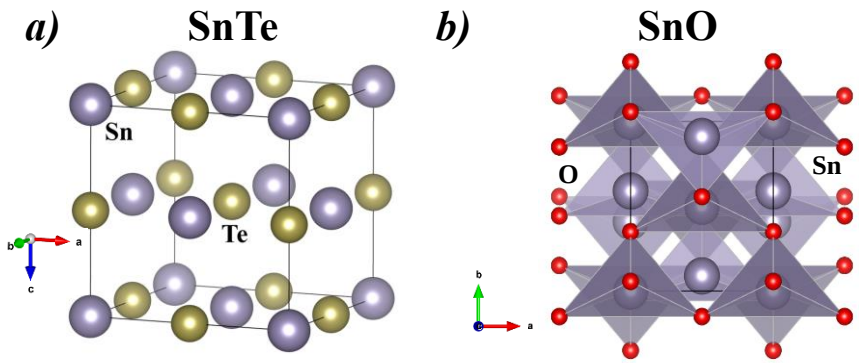

Figure 4.1 : (a) high symmetry structure of SnTe and (b) second order Jahn-Teller structure of SnO.

To explain the origin of the formation of lone pairs, two models were discussed: classical and revised lone pair model. In the classical lone pair model proposed by Orgel[12,13], they considered the lone pair to be derived from an on-site mixing of non-bonding cation *s/p* orbitals. But these orbitals can't be mixed on cations occupying sites with inversion symmetry, and so this mixing provides the electronic driving force for distortions leading to non-centrosymmetric coordination environments for many $5s^2$ and $6s^2$ cations. But this model is incomplete and does not provide an understanding of the nature of the stereochemically active lone pair and why it forms in some materials and why it does not form in others. This is where the revised lone pair model was developed[4] and it can be summarized as follows: i) strong interaction between the cation *s* and anion *p* orbitals results in high-energy anti-bonding states with a considerable degree of cation *s* character at the top of the upper valence band, and ii) the distortion of the crystal structure to allow for the interaction of the nominally empty cation *p* states with the antibonding orbitals resulting in the familiar lone pair asymmetric electron density (**Figure 4.2**).

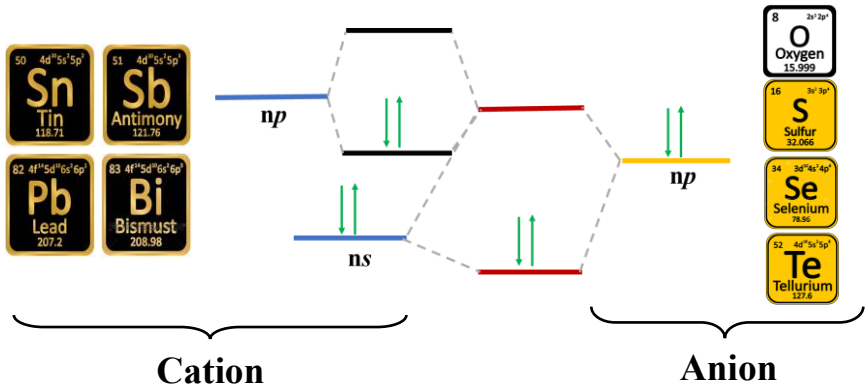

Figure 4.2 : Molecular orbital representation showing the lone pair states derived from the hybridization of cationic n*s* and n*p* states with the anionic n*p* states.

As mentioned previously, the energy of the chalcogen (S/Se) *p* orbitals has an impact on the stereochemical activity of lone pairs which can influence the separation of the charge carriers. DFT studies discussed the variation of this stereochemical activity in function of the lone pair coordination environments (Sb^{3+} (**Figure 4.3a**)[11] and Sn^{2+} (**Figure 4.3b**)[14]). The anionic substitution of oxygen can be used to fine-tune the energy-positioning of the electron lone pair-derived orbitals.[15] The energetic binding of these lone pair cations and of the chalcogenide *p* states can determine the strength of hybridization and the resulting stabilization of the antibonding states at the top of the valence bands, in a way that it increases as one moves down the periodic table.

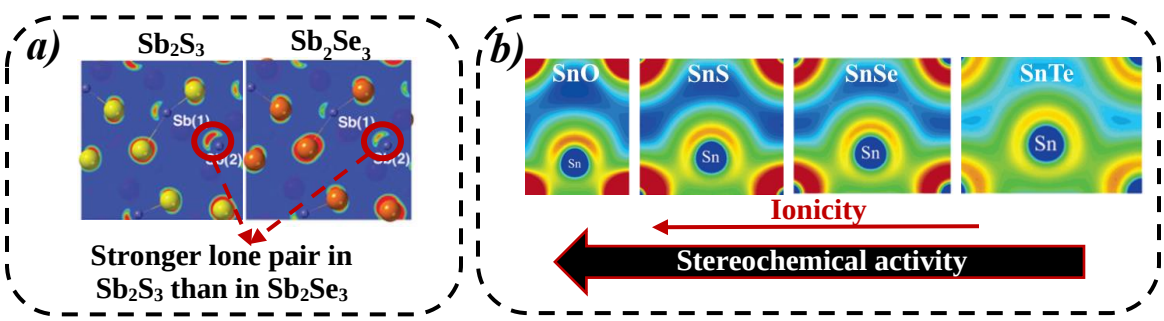

Figure 4.3 : (a) Partial charge densities of Sb_2S_3 and Sb_2Se_3.Taken from ref.[11] (b)Variation of the electron density contour maps for SnO, SnS, SnSe, and SnTe. Taken from ref. [14]

4.1.2. Polarisation

Highly-polarizable materials are favourable for photoelectric conversion due to their efficient charge separation. The presence of a local electrical field can facilitates the transfer of the photo-

generated pairs to different active sites leading to an improved e^-/h^+ separation.[16,17,18,19] This enhanced charge carriers' separation can give better photoactivity[20] (e.g. polar $Na_3VO_2B_6O_{11}$).[21]

4.1.3. $Sr_6Cd_2Sb_6S_{10}O_7$

The oxysulfide $Sr_6Cd_2Sb_6S_{10}O_7$ reported by Wang *et al.* contains Sb^{3+} $5s^2$ cations in both homoleptic ($Sb(1)S_5$ and $Sb(3)O_3$) and heteroleptic ($Sb(2)OS_4$) coordination environments (**Figure 4.4a**).[15] With a band gap of 1.89 eV and polar crystal structure, it has potential for photocatalytic behaviour. It crystallizes in the polar space group *Cm* with a structure built up from zigzag $^2_\infty[CdSb_2OS_5]^{4-}$ layers. These zigzag layers are separated by pseudo-chains of $^1_\infty[Sb(3)O_{2.5}]^{2-}$ composed of [seesaw-shaped /C_{2v}] $[Sb(3)O_4]^{5-}$ units linked via their half-occupied (disorded) O(4) sites (**Figure 4.4b**). The zigzag $^2_\infty[CdSb_2OS_5]^{4-}$ layers are built from $^1_\infty[CdS_3]^{4-}$ chains which are corner-linked to edge-shared chains of $^1_\infty[Sb(1)OS_3]^{3-}$ and $^1_\infty[Sb(2)OS_2]^{3-}$. Electronic structure calculations indicate that Sr, O and Cd contribute little to the band edges, whilst the Sb(1) and Sb(2) sites (and particularly the $5s^2$ pair from the $Sb(2)OS_4$ units) are responsible for the NLO activity. In addition, $Sr_6Cd_2Sb_6S_{10}O_7$ displayed a type-I phase-matchable second harmonic generation (SHG) response (d_{eff} = 27.4 pmV^{-1}) under laser irradiation at 2.09 mm.[15]

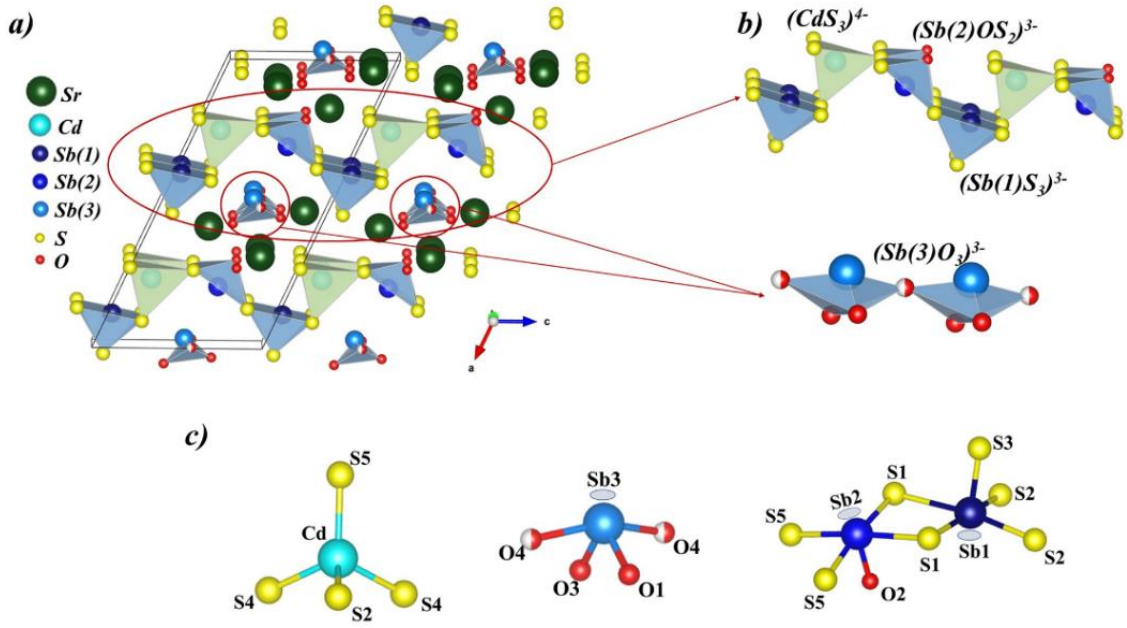

Figure 4.4 : (a) View of $Sr_6Cd_2Sb_6S_{10}O_7$. (b) Zigzag layer formed of $[CdS_3]^{4-}$ tetrahedra and the mixed anion tetragonal pyramids of antimony $[SbOS_2]^{3-}/[SbS_3]^3$, pseudo-chains composed of $[Sb(3)O_3]^{3-}$ motifs joined by half-occupied O(4) vertices (c) coordination environments of Cd and Sb ions.

More recently, the oxyselenide analogue $Sr_6Cd_2Sb_6O_7Se_{10}$ and its photoelectric properties were reported.[22] It is isostructural to the oxysulfide with an indirect band gap of a smaller magnitude (1.55 eV), suitable for photoelectric conversion. SHG measurements revealed the intense polarization within the structure compared to the oxysulfide. It also demonstrated an improved charge carrier's separation with much longer recombination lifetime of 76.5 µs. Electrochemical measurements showed excellent photoelectric properties with broadband photoresponse and stable reproducibility.[22] These findings, were consistent with our work, and complement our study by further showing how the anions *Q* in Sb*Q*$_5$ units can tune the band-edge structure in these photoactive materials.

We decided to further investigate the structure-properties relationship of $Sr_6Cd_2Sb_6S_{10}O_7$ by combining experimental and computational studies. We focused on exploring the relative importance of the anion in tuning the band gap and giving polar coordination environments, and the relationship with the Sb^{3+} $5s^2$ lone pair and its activity.

4.2. Experimental results

4.2.1. Synthesis and preliminary characterization

4.2.1.1. Synthesis and Rietveld Refinement

A sample of $Sr_6Cd_2Sb_6S_{10}O_7$ (1 g) was synthesized from a stoichiometric mixture of the reagents SrS/CdS/Sb_2O_3/Sb/S (Alfa Aesar 99.5%). The heat treatment consisted of heating to 700°C at a rate of 1.15°C/min dwelling for 48 h before cooling to room temperature. After this procedure a red powder was obtained (**Figure 4.5**).

Figure 4.5 : Diagram of the solid-state synthesis of $Sr_6Cd_2Sb_6S_{10}O_7$

High quality XRPD data confirmed the formation of a high-quality sample of $Sr_6Cd_2Sb_6S_{10}O_7$. Rietveld refinements were carried out using Fullprof software[23] in the *Cm* space group. The background, sample height, lattice parameters, peak profiles (pseudo-Voight), atomic positions and atomic displacement parameters were refined.[24] As depicted in **Figure 4.6**, Rietveld analysis led to very good reliability factors and was in good agreement with the model of *Cm* symmetry reported by Wang et al.[15] The refined atomic positions are given in **Table 4.1**.

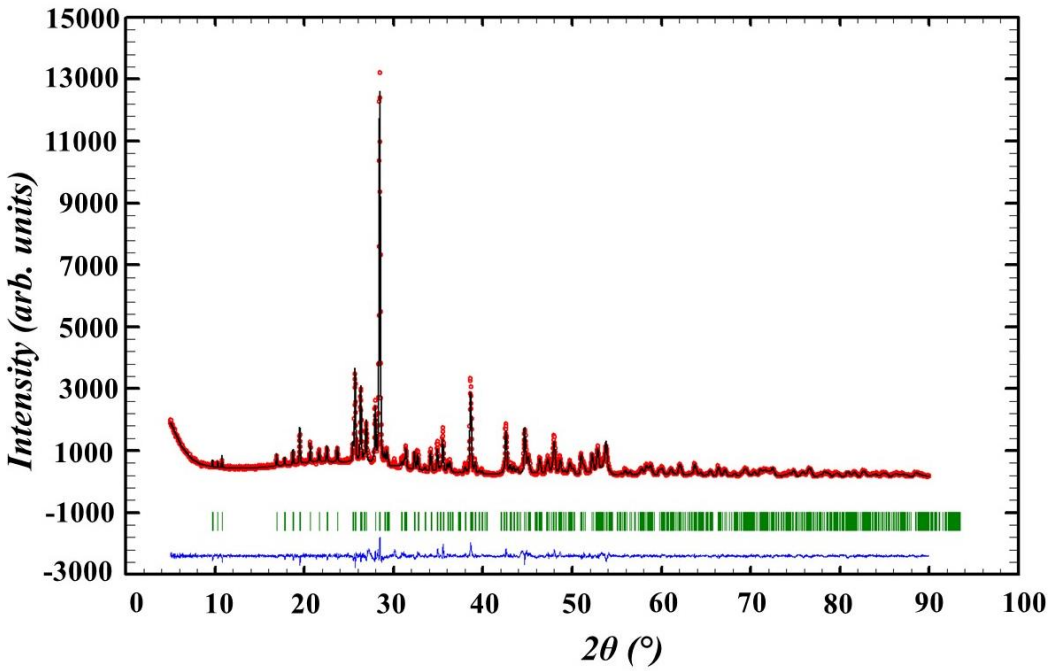

Figure 4.6 : Powder XRD Rietveld refinement profiles: the experimental (red) and the calculated (black) patterns are superimposed; the difference curve and Bragg positions are shown in blue and green, respectively.

Table 4.1. Refinement details from Rietveld refinement using lab XRPD data for $Sr_6Cd_2Sb_6S_{10}O_7$ using *Cm* model; *a* = 18.9653(4) Å, *b* = 4.0531(1) Å, *c* = 10.0392(2) Å, β = β = 114.873(1) °; R_p = 6.01 %, R_{wp} = 7.78 %, R_{exp} = 4.55 % and χ^2 = 2.92.

Atom	Wyckoff site	*x*	*y*	*z*	U_{iso} (Å^2)	Site occupancy
Sb1	*2a*	0.4(1)	0	0.1(4)	0.019(1)	1
Sb2	*2a*	0.3(1)	1	0.6(4)	0.019(1)	1
Sb3	*2a*	0.5(1)	1	0.6(4)	0.019(1)	1
Cd1	*2a*	0.3(1)	0.5	0.2(4)	0.003(3)	1
Sr1	*2a*	0.7(1)	1	0.8(4)	0.005(1)	1
Sr2	*2a*	0.5(1)	1.5	0.9(4)	0.005(1)	1
Sr3	*2a*	0.6(1)	0.5	0.4(4)	0.005(1)	1
S1	*2a*	0.4(1)	1.5	0.8(4)	0.005(3)	1
S2	*2a*	0.4(1)	0.5	0.3(4)	0.005(3)	1
S3	*2a*	0.5(1)	0	0.1(4)	0.005(3)	1
S4	*2a*	0.2(1)	0	0.0(4)	0.005(3)	1
S5	*2a*	0.2(1)	0.5	0.4(4)	0.005(3)	1
O1	*2a*	0.6(1)	1	0.5(4)	0.011(5)	1
O2	*2a*	0.2(1)	1	0.7(4)	0.011(5)	1
O3	*2a*	0.6(1)	1	0.8(4)	0.011(5)	1
O4	*2a*	0.5(1)	0.5	0.7(4)	0.011(5)	0.5

4.2.1.2. Optical band gap and band edges positions

The magnitude and nature of the band gap of $Sr_6Cd_2Sb_6S_{10}O_7$ were measured by diffuse reflectance UV-visible spectroscopy. **Figure 4.7a** shows reflectance *vs*. wavelength for $Sr_6Cd_2Sb_6S_{10}O_7$. The reflectance data were analysed using the Kubelka-Munk function.[25] A Tauc plot (**Figure 4.7a**) $[F(R)h\upsilon]^{1/n}$ *vs*. $[h\upsilon]$ (where $h\upsilon$ is the photon energy),[26] gives insight into the nature of the band gap: $Sr_6Cd_2Sb_6S_{10}O_7$ is reported to be an indirect band gap semiconductor (hence n = 2) and a tangent to the inflection point on the Tauc plot gives an optical band gap E_g = 2.01(2) eV. This is in fairly close agreement with that reported by Wang *et al.* (1.89 eV).[15]

To estimate the band edge positions, we adopted the empirical method based on the Mulliken electronegativities developped by Butler and Ginley[27] (Further details on this method can be found in **Chapter 2**). Our calculations revealed a conduction band (CB) edge lying at -0.26 eV and a valence band (VB) edge lying at 1.64 eV, confirming that the band edge positions of $Sr_6Cd_2Sb_6S_{10}O_7$ encompass the redox potential of water (**Figure 4.7b**), an essential requirement for photocatalytic water splitting.

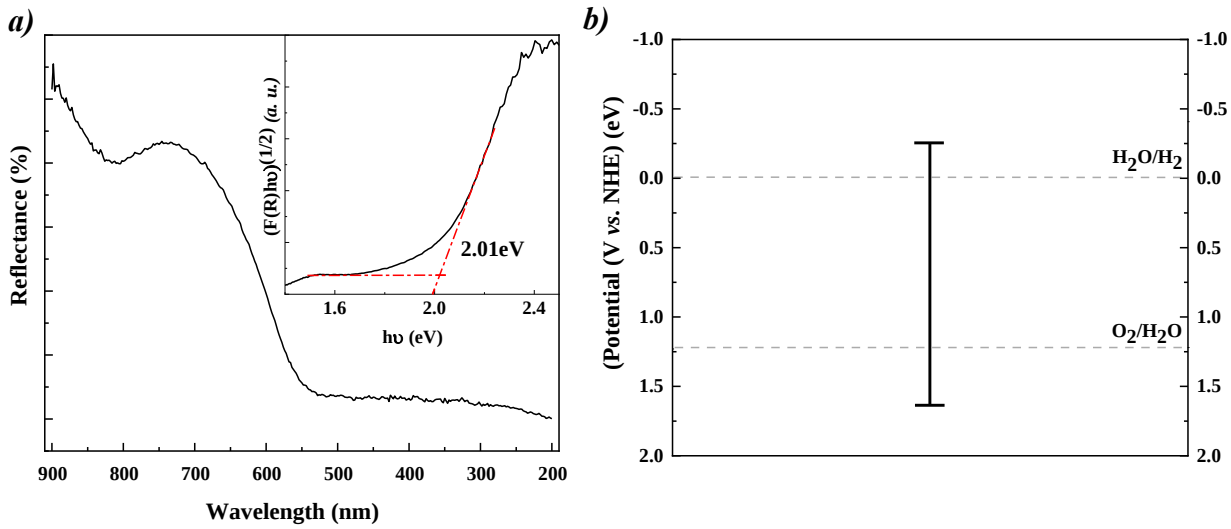

Figure 4.7 : (a) Diffuse-reflectance spectra with a Tauc plot inset to determine the experimental band gap for $Sr_6Cd_2Sb_6S_{10}O_7$ and (b) band edge position estimated for $Sr_6Cd_2Sb_6S_{10}O_7$.

4.2.2. Photocurrent measurements

Different experimental approaches were tested in order to perform the electrochemical measurements, this included different polymers for the working electrode preparation and different electrolytes. We first performed the measurements on a film prepared with dimethylformamide (DMF) polymer in a sodium sulfate (Na_2SO_4) electrolyte. Even though good photocurrent responses were observed, we noticed film degradation after 4 hours. We thought that the film is not stable in the chosen electrolyte solution, we therefore decided to test other solutions, including a mixture of Na_2SO_3 and Na_2S. Whilst a better film stability was clearly seen, we noticed a loss in the performance efficiency, this part on the stability will be discussed later in **Section 4.2.2.5**. The last approach we decided to try is to change the polymer used, to see if the film does not degrade during the whole duration of the experiment. We chose the polyvinylidene fluoride (PVDF) polymer following this protocol: the photocatalyst $Sr_6Cd_2Sb_6S_{10}O_7$ is dispersed in PVDF (polyvinylidene fluoride) binder (in a 2:1 ratio), then deposited evenly on an ITO/glass substrate and an aqueous 0.1 M Na_2SO_4 solution was employed as electrolyte. The results discussed in this chapter are the ones observed during the experiments conducted using the last protocol (protocol 3). **Table 4.2** gives the main results we obtained for all three approaches, in terms of reproducibility, wavelength influence, response under sunlight and photocorrosion. **Appendix 2, Section 2.1** presents the major results plots we obtained for the first and the second protocols.

Table 4.2. Different protocols adopted for the photocurrent measurement with the principle results observed for the different tests.

			Reproductibility	Wavelengths	Sunlight	Photocorrosion
1	**-Drop Casting (DMF) -Electrolyte (Na_2SO_4)**		*λ = 450 nm and V_{bias} = 0.6 V *Photocurrent of 0.4 $\mu A.cm^{-2}$ *Fast separation (Spikey peak) *K_{tr}>>K_{rec} (0.075>>0.03) *Transfert efficacity (η_k = 68%)	*V_{bias} = 0.6 V *Decrease in the photocurrent when increasing λ *Best efficiency (0.28 $\mu A.cm^{-2}$) in the blue spectral zone (450-505 nm).	*V_{bias}= 0.4/0.6/0.8/1 V *Continuous decay Photocurrent of 0.1 $\mu A.cm^{-2}$	*Clear degradation of film efficiency after 4 hours. *Photocurrent of 0.4 - 0.015 $\mu A.cm^{-2}$
2	**-Drop Casting (DMF) -Electrolyte (SO_4^{2-} /SO_3^{2-}/S^{2-})**		*λ = 450 nm and V_{bias} = 0.6 V *Photocurrent of 0.14 $\mu A.cm^{-2}$ *Loss of the spikey peak *Decrease in the performance.	*V_{bias} = 0.6 V *Decrease in the photocurrent when increasing λ *Best efficiency (0.08 $\mu A.cm^{-2}$) in the blue spectral zone (450-505 nm).	*V_{bias} = 0.6/0.8/1 V *Lighter degradation *Photocurrent of 0.08 $\mu A.cm^{-2}$	*Gradual stabilization after 4 days. *Photocurrent of 0.1-0.06 $\mu A.cm^{-2}$
3	**-Drop Casting (PVDF) -Electrolyte (Na_2SO_4)**	**0 V**	*λ = 450 nm *Photocurrent off 0.1 $\mu A.cm^{-2}$ *Loss of the spikey peak	*Decrease in the photocurrent when increasing λ *Best efficiency (0.06 $\mu A.cm^{-2}$) in the blue spectral zone (450-505 nm).	*Reproductible and stable photocurrent of 0.1 $\mu A.cm^{-2}$	*Stable photocurrent
		0.4 V	*λ = 450 nm *Photocurrent of 1.25 $\mu A.cm^{-2}$ *Fast separation (Spikey peak) *K_{tr}>>K_{rec} (0.25>>0.08) *Transfert efficacity=78%	*Decrease in the photocurrent when increasing λ *Best efficiency (1.2 $\mu A.cm^{-2}$) in the blue spectral zone (450-505 nm).	*Gradual stabilization of the photocurrent (2.25 $\mu A.cm^{-2}$).	*Slight degradation of film efficiency

4.2.2.1. Reproducibility measurement

The chronoamperometry measurements (current density variation Δj between illumination and dark cycles) were carried out on a $Sr_6Cd_2Sb_6S_{10}O_7$ film for 0.4 V and 0 V bias voltages and under an excitation of 450 nm (**Figure 4.8**). Starting at 0.4 V in **Figure 4.8a-i**, a significant change in transient photocurrent is observed when the underside of the working electrode is illuminated: the photocurrent generated increases from 0.65 to 0.95 µA.cm^{-2} for a power density of 22 to 111 mW.cm^{-2}, respectively. The photocurrent generated increases with the intensity of the luminous flux according to a classical power law[28] (**Figure 4.8a-ii**). The power law fitting gives a curve going through the origin with an equation of $\Delta j = 3.52\times10^{-1}\phi^{0.21}$. The value of the exponent provides the information of traps present in the sample. Indeed, for an ideal trap-free system, the exponent is equal to 1 and the photocurrent scales linearly with the illumination power. But for trapped states, the exponent becomes smaller than 1 (as for high powers most of the traps are already filled in and further illumination power cannot effectively increase the photogain).[29] Thus, in the present case, the low value of the exponent indicates the presence of many traps in the compound. The photocurrent response (**Figure 4.8a-i**) shows also a characteristic decay from a "spike" to a steady state during illumination. The presence of this spike is explained by the rapid separation of the electron/hole pairs under illumination, then the establishment of an equilibrium state between the recombination and the transfer of the carriers.

The previous test was performed under the same excitation of 450 nm but this time for a 0 V bias voltage, and a clear stable photocurrent was observed (**Figure 4.8b-i**). Between different illumination and dark cycles, the generated photocurrent increased with the intensity of the luminous flux from 0.045 to 0.95 µA.cm^{-2}, according to a classical power law (same as before). Although the characteristic ‘spike’ shape of the peaks (observed at 0.4 V bias voltage, **Figure 4.8a-i**) was lost, the exponent obtained from the fitting of the power law in this case is higher (0.47), indication of a decrease in the trap states (**Figure 4.8b-ii**).

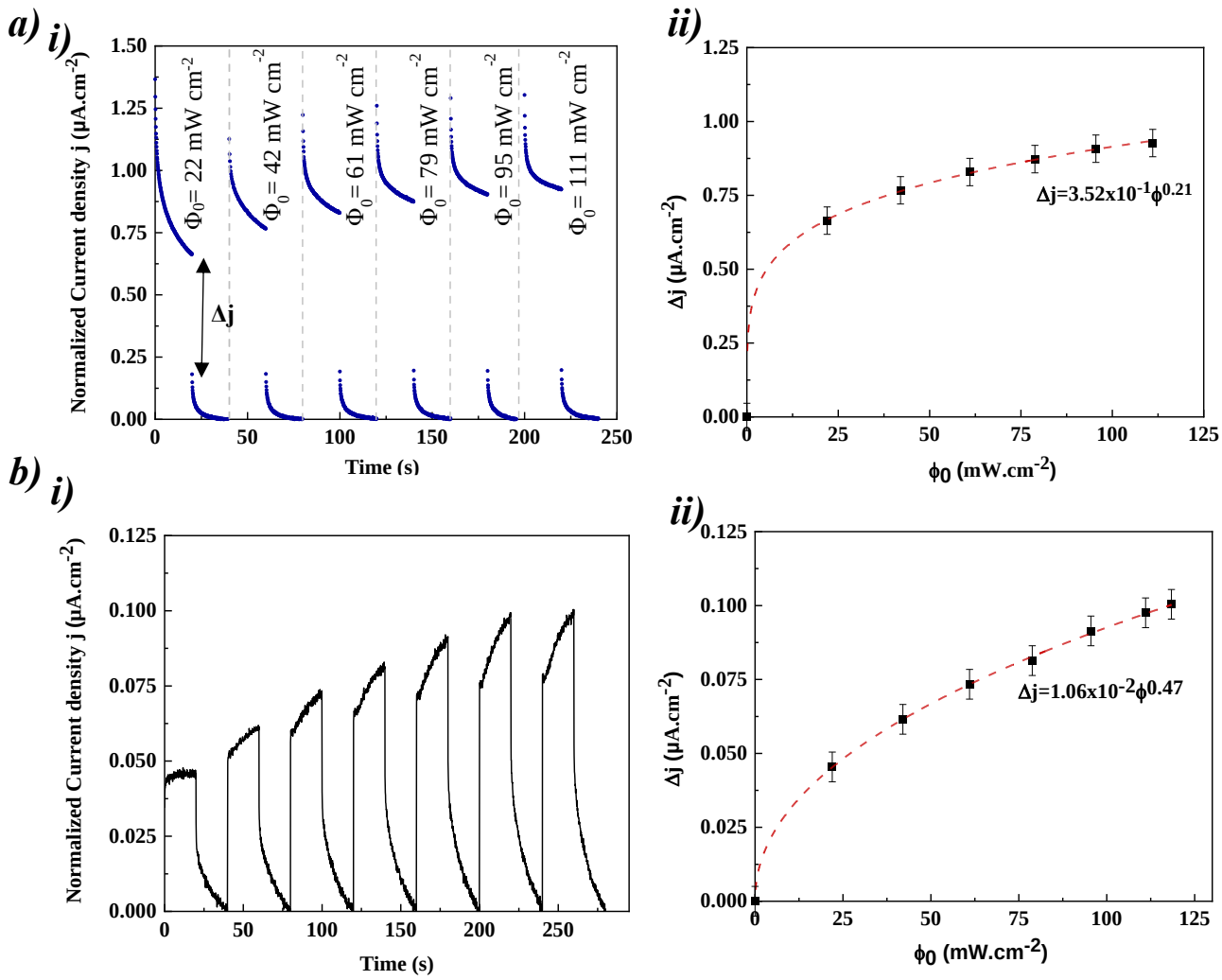

Figure 4.8 : (a) V_{bias}=0.4 V under a 450 nm excitation and (b) V_{bias}=0 V under a 450 nm excitation with i) transient photocurrent response and ii) evolution of the photocurrent density the power density of light.

Having this current spikey peak shape allowed us to determine the transfer and recombination constants k_{tr} and k_{rec} as well as the transfer efficacity η_k. Parkinson *et al.*[30] proposed a model (**Figure 4.9a)** that considers the presence of the two phenomena (transfer and recombination) which made it possible to calculate the rate constants from the modeling of the exponential decrease of the peak. In fact, when the semiconductor is illuminated, the e^--h^+ pairs separate quickly, which is the origin of having this spike at first. This is followed by an exponential decrease caused by the progressive equilibrium between the two phenomena until a stationary state is reached. Using the following equations, k_{tr} and k_{rec} are determined:

$$\frac{j(t)-j(\infty)}{j(0)-j(\infty)} = e^{-\frac{t}{\tau}} \quad (4.1)$$

$$\frac{j(\infty)}{j(0)} = \frac{k_{tr}}{k_{tr}+k_{rec}} \quad (4.2)$$

where $\tau = (k_{tr} + k_{rec})^{-1}$, *j(0)* is the instant density of the photocurrent and *j(∞)* the one at the final stationary state. Like we mentioned previously, having this current shape indicates fast kinetics, while in the case of slow kinetics this shape is not observable, which makes it difficult to calculate different rate constants. We therefore deduced the transfer and recombination constants to be are 0.25 and 0.08 min^{-1}, respectively giving a transfer efficiency of 78 % (**Figure 4.9b**).

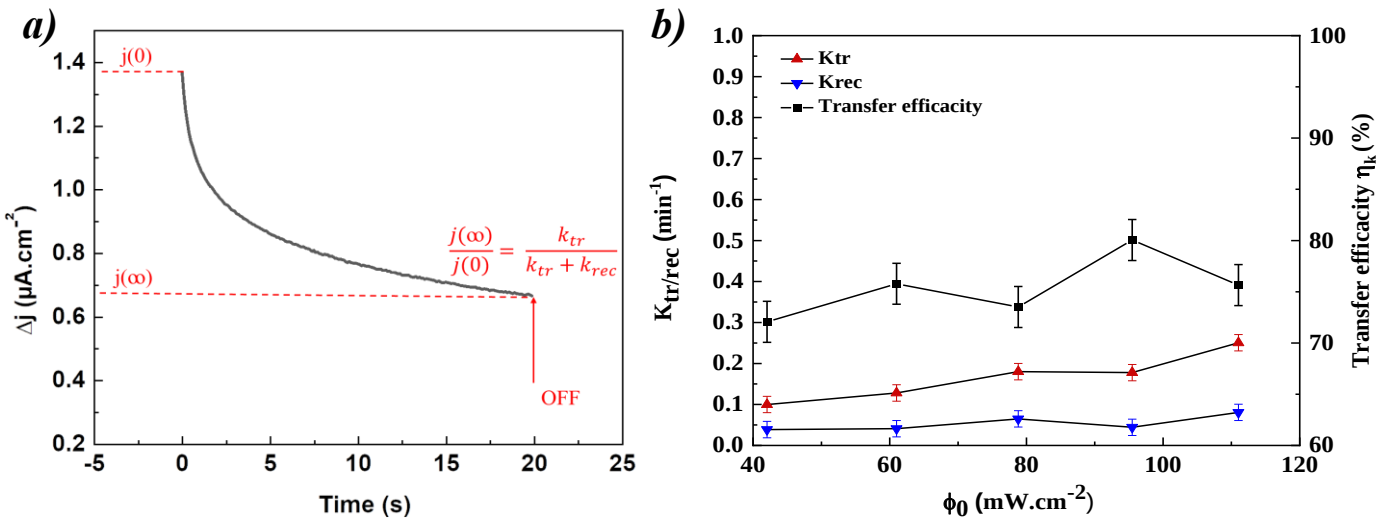

Figure 4.9 : (a) Photocurrent density of $Sr_6Cd_2Sb_6S_{10}O_7$ for Φ_0 = 22 mW.cm^{-2} highlighting *j(0)* and *j(∞)* and (b) evolution of the recombination and transfer rate constants k_{tr} and k_{rec} with intensity of light alongside the transfer efficacity η_k by intensity light.

4.2.2.2. Influence of the wavelengths

We continued our investigations by analyzing the influence of different wavelengths on the photocurrent response, and this was performed under two bias voltages (0.4 and 0 V). $Sr_6Cd_2Sb_6S_{10}O_7$ is red colored, therefore it should absorb in the complementary spectral zone which is the blue (450 - 505 nm). The transient photocurrent response recorded for V_{bias} = 0.4 V *vs.* wavelength is shown in **Figure 4.10a**, where the highest response is observed for an irradiation at 450 nm, which is expected because of the materials' absorption. Lower photocurrents are observed for longer wavelength (lower energy) irradiation. This variation is consistent with the decrease in

absorbance observed on the Tauc plot (**Figure 4.7a**) where we saw that $Sr_6Cd_2Sb_6S_{10}O_7$ absorbs in the visible light spectrum (E_g = 2.01 eV/ 616 nm), explaining its red color complementary to the blue light absorbed. Similar results were observed when we performed the test at 0 V bias voltage (**Figure 4.10b**). A higher photocurrent response is also observed at 450 nm (0.065 µA.cm^{-2}) and lower values occurred at longer wavelengths.

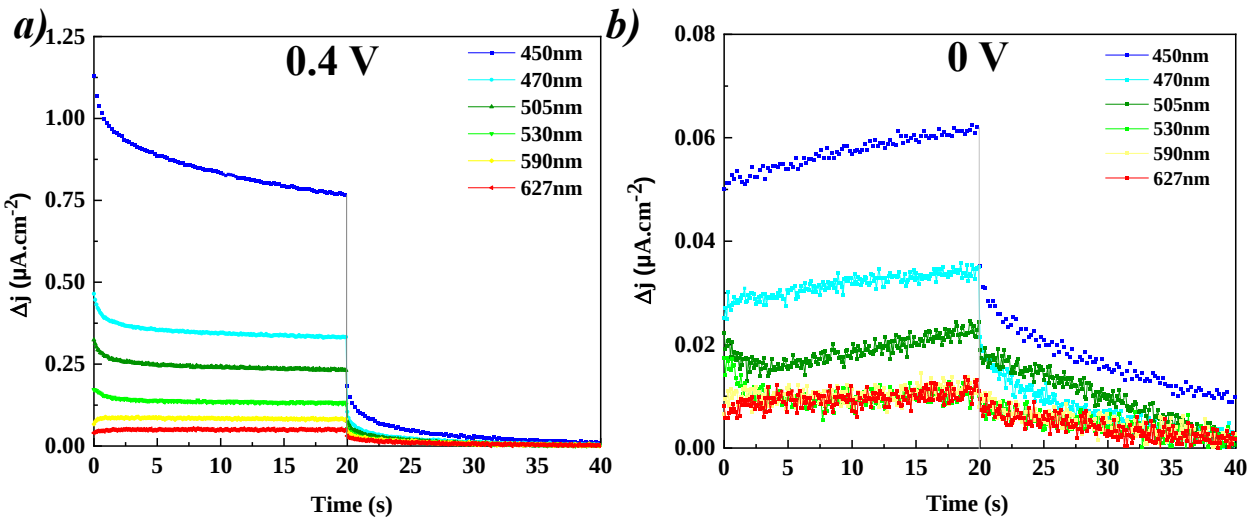

Figure 4.10 : Evolution of the photocurrent density the power density of light of $Sr_6Cd_2Sb_6S_{10}O_7$ for bias voltage of (a) 0.4 V and (b) 0 V.

4.2.2.3. Photocurrent measurements under solar irradiation

One particular challenge is to find materials that demonstrate an activity under solar irradiation, and one way to do that is to measure a material's capacity to generate a photocurrent. We therefore submitted the prepared film to solar illumination (150 W Xenon lamp with AM 1.5G filter – 100 mW.cm^{-2}), and we recorded the evolution of the transient photocurrent by carrying out on/off cycles for two different bias voltages, 0 and 0.4 V (**Figure 4.11a**). A clear decrease in the performance is seen comparing between the two voltages (~2.7 to ~0.2 µA.cm^{-2} for 0.4 and 0 V, respectively). We also noticed a slight decrease in the value of the generated photocurrent for 0.4 V but it remains more stable when no potential is applied (red curve). This decrease indicates a photocorrosion phenomenon which may be due to a material or chemical instability within the electrolyte used.

Trying to understand the origin of having this decrease, we investigated the kinetics of the transient photocurrent evolving between 0 V and 0.4 V (**Figure 4.11b**), and this was done for a 3200 mins exposure time. We saw that without applied a potential the kinetics are slow and no spike is observed. This behaviour can be explained by the carrier trapping effect induced by surface defects.[31] Higher potentials de-trapping is facilitated by the induced electric field.

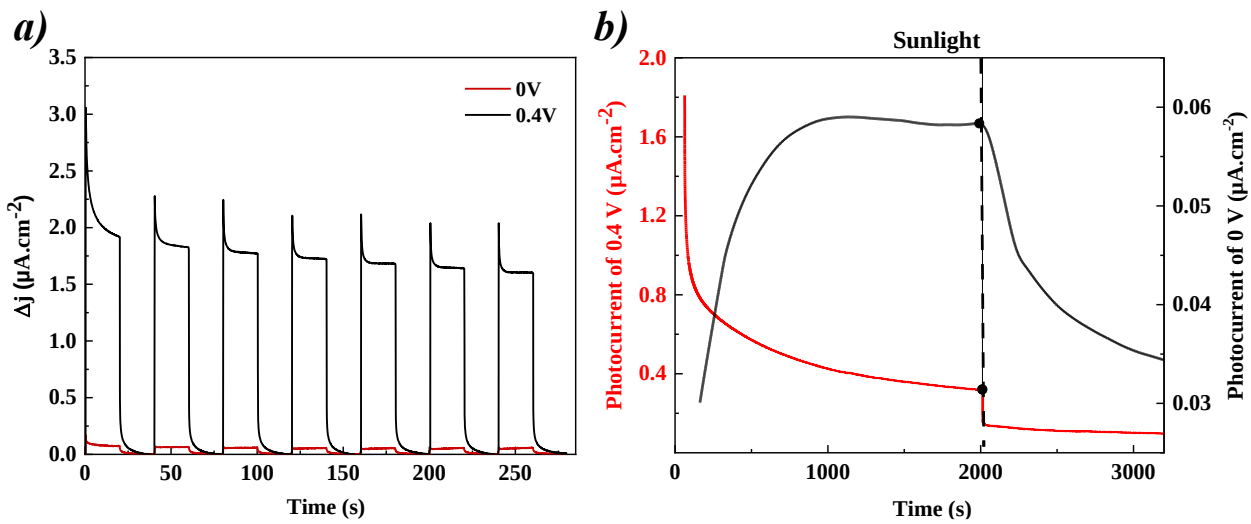

Figure 4.11 : (a) Transient photocurrent response under solar illumination (100 mW.cm^{-2}) for V_{bias}=0.4 V and V_{bias}=0V. (b) Current density variation at 0V and 0.4V under solar light excitation and a 3200s exposure time.

4.2.2.4. Mott-Schottky method to determine the flat band potential

Figure 4.12a presents the Mott-Schottky (MS)[32] plot of $1/C^2$ *vs.* applied potential for $Sr_6Cd_2Sb_6S_{10}O_7$, the positive slope confirms the n-type semiconducting behaviour with a flat band potential E_{fb} estimated to be -0.46(1) V *vs*. Ag/AgCl (reference electrode) or 0.13(2) V *vs*. RHE (reversible hydrogen electrode). This estimated position of the flat band potential gives insight into the position of the CB or VB edge depending on the conduction behaviour.[33] The flat band potential reflects the position of the Fermi level which lies close to the conduction band minimum (CBM) ~ 0.1 in a n-type semiconductor.[34] This calculated value is close to the calculated CB edge position using the empirical method based on Mulliken electronegativities (**Figure 4.7b**) in **Section 4.2.1.2**.

Figure 4.12b presents the linear sweep voltammetry recorded for $Sr_6Cd_2Sb_6S_{10}O_7$, where the current is measured while the potential between the working electrode and the reference

electrode is swept linearly in time under dark and light illumination. Depending on the variation of the intensity of the photocurrent nature, anodic (positive potential) or cathodic (negative potential), the semiconduction type can be determined. Judging from the previous results, we chose to perform the test under 450 nm excitation and between the variation of the j-v curves, we noticed an anodic photocurrent which indicate n-type semiconduction of $Sr_6Cd_2Sb_6S_{10}O_7$, consistent with the results of the Mott-Schottky test.

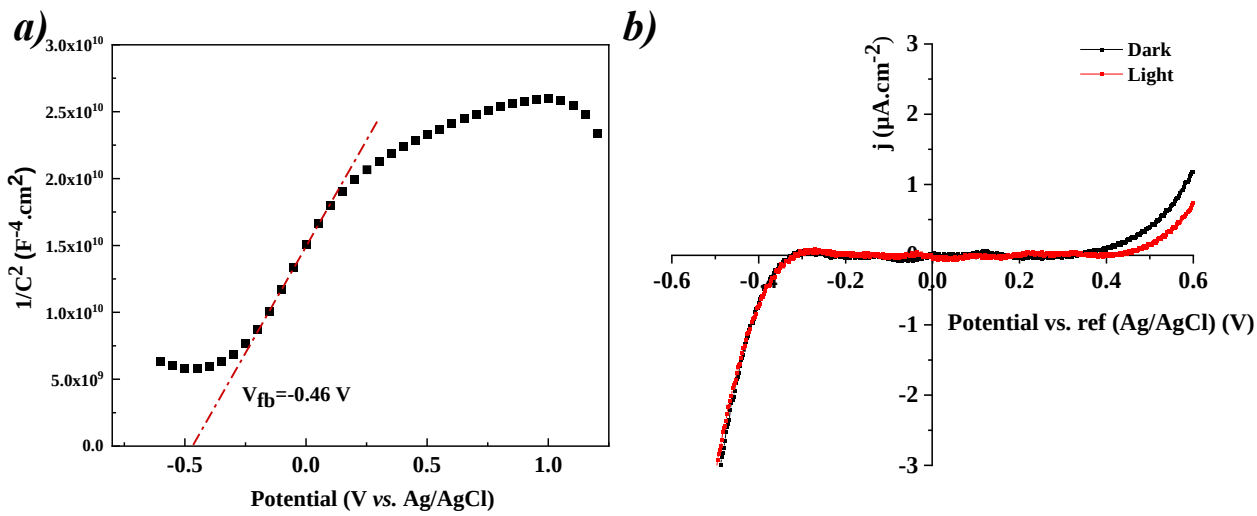

Figure 4.12 : (a) Mott-Schottky plot for $Sr_6Cd_2Sb_6S_{10}O_7$ deposited on ITO/Glass performed at 1000 Hz. (b) Current density j-V between dark and illumination cycles (λ=450 nm; 20 mW.cm^{-2}) recorded on $Sr_6Cd_2Sb_6S_{10}O_7$/ITO/glass film

4.2.2.5. Influence of electrolytes on the performance and stability

As we previously mentioned in **Section 4.2.2.3**. a slight photocorrosion was observed during the photocurrent measurements under solar irradiation. To further understand the degradation described above in Na_2SO_4 electrolyte, we considered other electrolyte solutions, including a mixture of 0.1 M Na_2SO_3 and 0.01 M Na_2S. In fact, we thought that the presence of sulfite anions SO_3^{2-} ions can stabilize the oxysulfide phase; according to the literature they are considered as hole scavengers which can prevent photocorrosion.[35] This hypothesis was confirmed by the recorded photocurrent in **Figure 4.13**, although the photocurrent was lower for this Na_2SO_3/Na_2S electrolyte (**Figure 4.13a**) the film was stable even over four days (**Figure 4.13b**), indicating a significant reduction in photocorrosion compared with the Na_2SO_4 electrolyte.

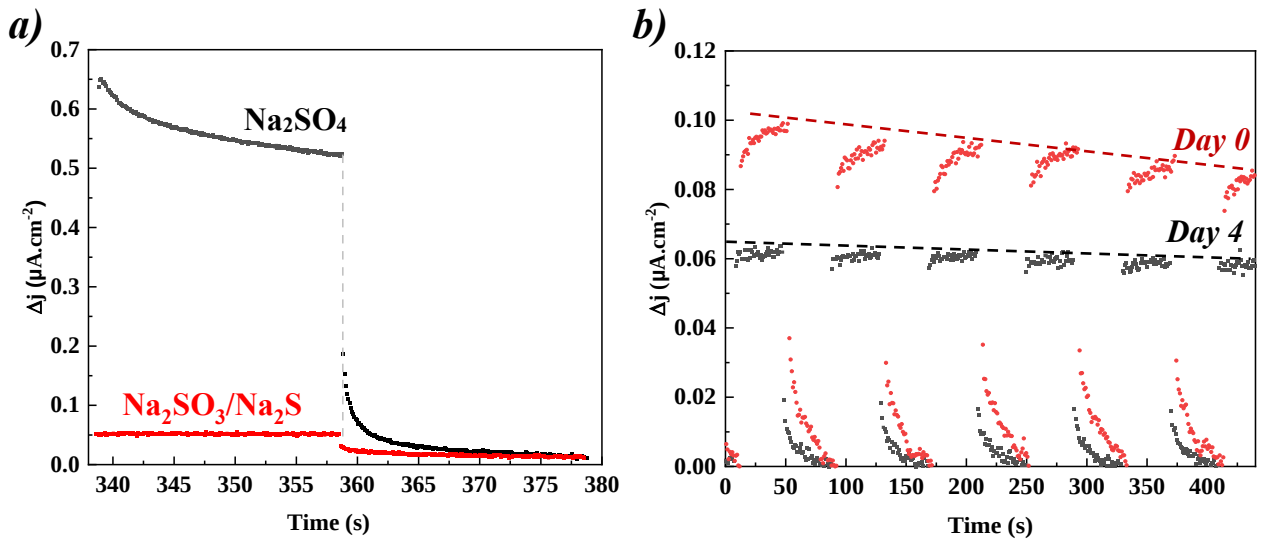

Figure 4.13 : (a) Electrolyte influence (Na_2SO_4, Na_2SO_3/Na_2S) on the transient photocurrent response of $Sr_6Cd_2Sb_6S_{10}O_7$ (b) Transient photocurrent response of $Sr_6Cd_2Sb_6S_{10}O_7$ in Na_2SO_3/Na_2S electrolyte on Day0 and Day4.

We investigated the stability of our material further by varying the pH of the solution. We prepared three different solutions with three different pH (5.5, 10 and 2). After adding $Sr_6Cd_2Sb_6S_{10}O_7$ powder and stirring for a limited time, we evacuated the powder from the solution (**Figure 4.14a**). The samples purity was then checked by X-ray powder diffraction (**Figure 4.14b**). All the electrochemical measurements were performed in the electrolyte (Na_2SO_4) that was used during the measurements. With a pH = 5.5 (grey curve), no change in the XRPD pattern was detected, whilst a degradation of $Sr_6Cd_2Sb_6S_{10}O_7$ occurred for acidic (blue curve) or basic (red curve) solutions. These results confirm the degradation and the instability of the oxysulfide in aqueous solutions as observed in the electrochemical experiments.

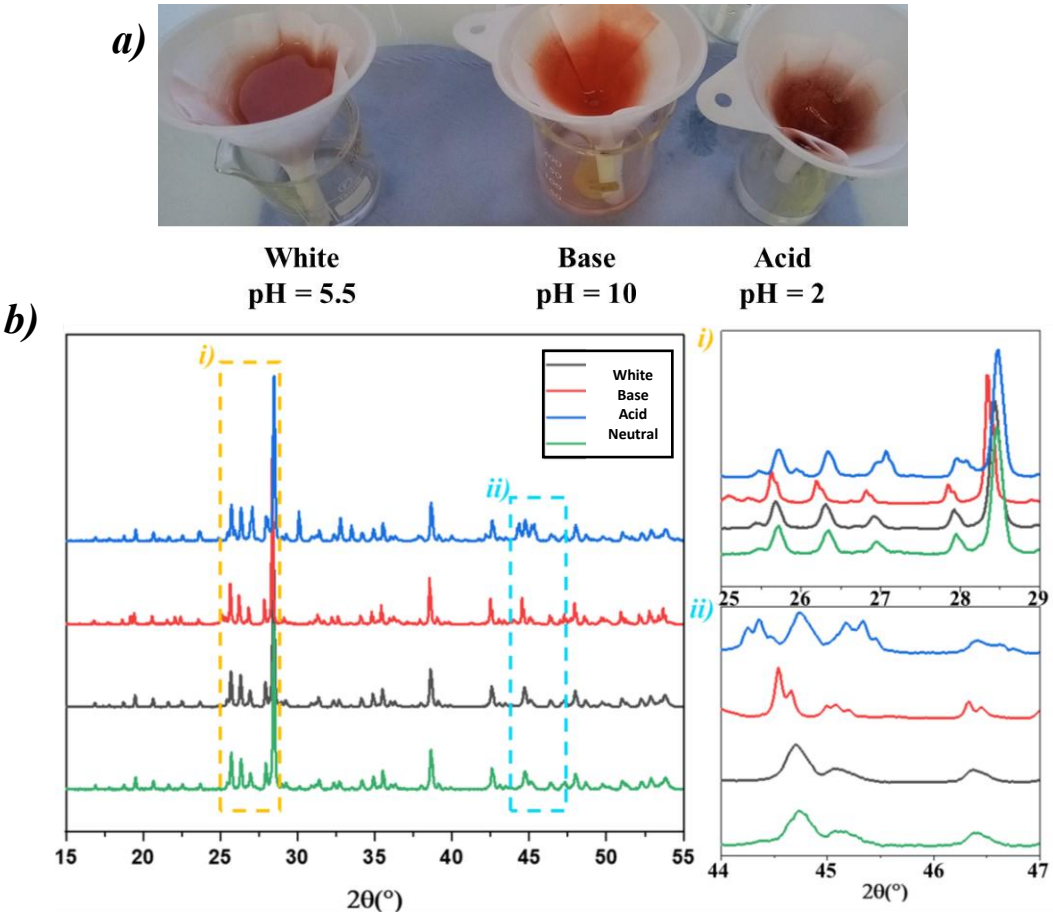

Figure 4.14 : (a) Powder of $Sr_6Cd_2Sb_6S_{10}O_7$ placed in acidic, basic and neutral pH. (b) X-ray powder diffraction (XRPD) data of dried powder of $Sr_6Cd_2Sb_6S_{10}O_7$ after being in a basic and neutral pH.

4.2.3. Photocatalytic activity

To quantify the photocatalytic efficiency of $Sr_6Cd_2Sb_6S_{10}O_7$, we carried out a study of the photodegradation of Rhodamine B by following the kinetics by UV-visible spectroscopy based on the maximum absorption of the dye (λ = 565 nm). This experiment was done using a photo-reactor consisting of 200 ml flask containing 100 mL of Rhodamine B (2×10^{-6} mol dm^{-3}) and 100 mg of $Sr_6Cd_2Sb_6S_{10}O_7$ powder; which is irradiated from above with a 40 W UV lamp (254 nm). The solution was stirred for 30 min in the dark to ensure an appropriate adsorption/desorption equilibrium, before the experiment. For an ideal photocatalyst, the degradation of Rhodamine B (measured by the discoloration of the solution) should increase with time until it saturates at 100% when all the dye has been degraded. Photocatalysis by $Sr_6Cd_2Sb_6S_{10}O_7$ only gave 75 % degradation (**Figure 4.15a**), which may reflect instability of the oxysulfide in these wet conditions, changes in

surface structure or pollution of adsorption sites by reaction intermediates reducing efficiency, but this has yet to be fully explored. Looking through literature, other lone pair-based materials, such as Bi_2MO_6 (M = W, Mo) showed a 90% and 51% Rhodamine B degradation, respectively.[36]

To describe the photocatalytic kinetics at the solid−liquid interface, the Langmuir−Hinshelwood (LH) model was used,[37] taking an order 1 for the photodegradation reaction and plotting $Ln(C_0/C)$ *vs.* time to determine the apparent rate constant (k_{app}). **Figure 4.15b** shows the Langmuir-Hinshelwood kinetic plot for the first run of the $Sr_6Cd_2Sb_6S_{10}O_7$ photocatalyst. Despite a latency time of 20 min at the start of the reaction, a linear evolution with an apparent rate constant of 9.0×10^{-3} min^{-1} is observed, comparable with other photocatalysts (typically 10^{-2} min^{-1})[32] and (10^{-3} min^{-1})[36], indicating good kinetic performance of $Sr_6Cd_2Sb_6S_{10}O_7$.

Several factors can influence the process and the outcome of the photocatalytic activity, such as the mass of the catalyst and the concentration of the chosen colored solution to degradate, the temperature and the pH, as well as the microstructure and the morphology of the semiconductor, and its stability in the electrolyte. In the case of having lone pairs, we noticed that despite the greater lone pair activity of Bi^{3+} based materials (Bi_2MO_6, M = W, Mo), the calculated rate constants (6.3×10^{-3} min^{-1} for Bi_2WO_6 and 1.7×10^{-3} min^{-1} for Bi_2MoO_6) are still comparable to $Sr_6Cd_2Sb_6S_{10}O_7$ with lower lone pair activity. This suggests that whilst a higher stereochemical activity might reduce the electronic band gap,[38,39] its influence on the rate of the photodegradation is difficult to compare directly as several other structural parameters may play a role (including polarity).

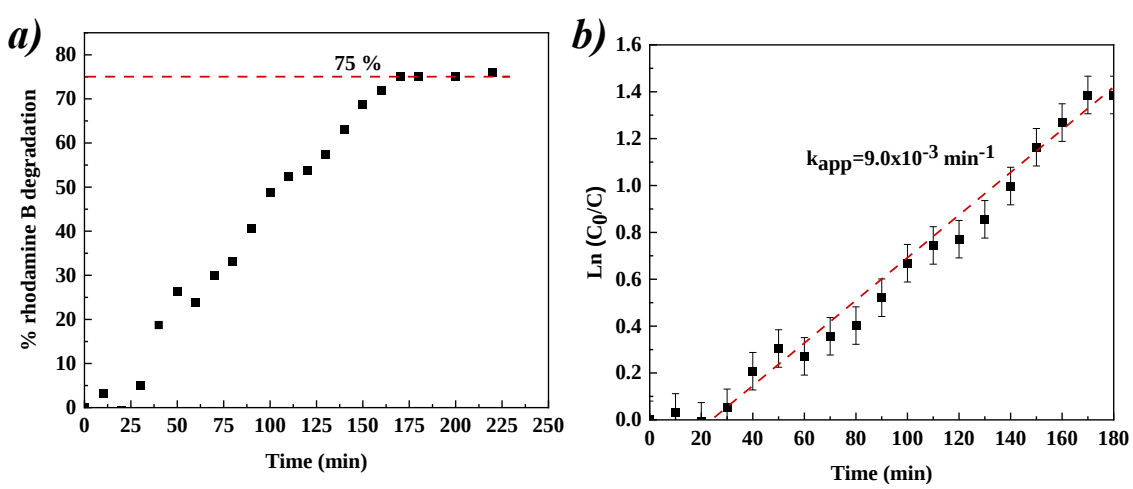

Figure 4.15: Percentage of discoloration of Rhodamine B on $Sr_6Cd_2Sb_6S_{10}O_7$ photocatalyst.

4.2.4. Computational studies

4.2.4.1. Band structure and effective masses calculation

DFT calculations were carried out to investigate the electronic properties of $Sr_6Cd_2Sb_6S_{10}O_7$ (**Figure 4.16**). The structure of the oxysulfide includes the half-occupied O(4) site, making computation studies more challenging. A (a×2b×c) supercell of *Cm* symmetry was used to accommodate this, which led to a disorder-free structure.[40,15] Full geometry optimizations were carried out using a plane-wave energy cutoff of 550 eV with *k*-points meshes (3×7×6) in the irreducible Brillouin zone. The resulting optimized structure was of *Pc* space group which was consistent with the experimental one, details of different atomic positions are given in **Appendix 2**, **Section 2.2**. The calculated electronic band structure for $Sr_6Cd_2Sb_6S_{10}O_7$ revealed the indirect band gap of 1.39 eV, slightly smaller than the experimental value (due to the well-known tendency of the GGA approximation (with PBE functional used here) to underestimate band gaps.[41] The valence band maximum and conduction band minimum are positioned at B (0; 0; 0.5) and Γ (0; 0; 0) points, respectively, see **Figure 4.16**.

A very important factor in photocatalysis is enhancing charge carrier mobility and minimizing their recombination rate. One way to investigate this mobility is by calculating the corresponding effective masses. The charge carrier's mobility is inversely proportional to their effective mass: the lower their effective mass, the higher their mobility. VASP allowed us to compute the electrons and holes effective masses from the band structure at high symmetry points, according to different chosen K-paths.

In order to have a quantitative investigation of charge carriers, the effective masses of electrons (m^*_e) and of holes (m^*_h) were calculated[42] using the following equation near the CBM and the VBM:

$$\left(\frac{1}{m^*}\right)_{ij} = \frac{1}{\hbar^2}\frac{\partial^2 E_n(k)}{\partial k_i k_j} \tag{4.3}$$

where $E_n(k)$ corresponds to the n^{-th} electronic band in *k*-space. Prior to the effective masses' extraction, the self-consistent electronic calculation was followed by a non-self-consistent calculation along the high symmetry lines with a fine spacing of 0.02 $Å^{-1}$ of *k*-points in reciprocal space. The band structure shows different dispersions of the bands at the CBM and VBM

suggesting different mobility of electrons and holes. Since the VBM is located at B and the CBM at Γ, we investigated the directions Γ → B and B → D very near to the Γ or B points, both related to directions within the layers (intralayer). We have also investigated directions between the layers (interlayer) with Y2 → Γ for m_e^* (**Figure 4.16**).

The lowest value of $m_e^* = 0.22\ m_0$ was found for the electrons in the conduction band for intralayer directions, while for interlayers we find much higher value of $m_e^* = 5.44\ m_0$. It shows the anisotropy of the charge carriers' mobility with easier transport within the layers as expected from the structure. Values below 0.5 m_0 (as found for electrons here) are usually considered as very low and indicative of a high mobility. As the mobility is inversely proportional to the effective mass this indicates a high electron mobility compared with other oxysulfides such as BiCuOS (0.59 m_0) and BiAgOS (0.68 m_0).[43] The hole mass was obtained by fitting bands at the valence band maximum and in contrast they are found to be heavier with a mass of 6.50 m_0 indicating lower hole mobility compared to the electrons. The difference in holes and electrons effective masses has the advantage of ensuring better separation of charge carriers and therefore a low rate of the electron-hole pairs recombination.

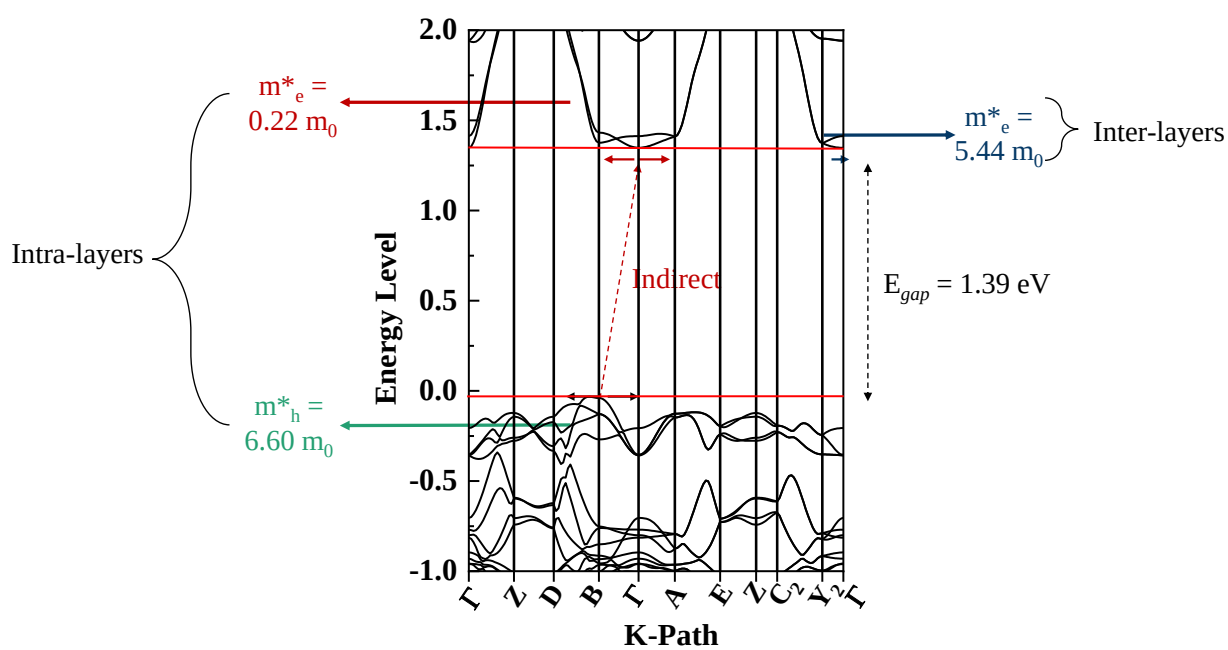

Figure 4.16 : Calculated band structure for $Sr_6Cd_2Sb_6S_{10}O_7$, showing the different electrons and holes effective masses extracted for the intra and inter-layers.

4.2.4.2. Partial density of states calculation

The total and partial projected densities of states (DOS and PDOS) of $Sr_6Cd_2Sb_6S_{10}O_7$ were previously discussed by Wang et *al.*[15] Focusing on the region around the Fermi level, we saw that the orbitals near this selected region are mainly dominated by Sb, S and O states, while Sr and Cd states make a minimal contribution.

We also computed the density of states (**Figure 4.17**) and it was consistent with the reported results.[15] The Sb 5*p* states dominate the conduction band minimum, lying from ~1.4 eV up to ~3 eV, while the Sb 5*s* states lie in the valence band (in the range of -3 to -0.1 eV), hybridizing with the O 2*p* and S 3*p* to form the maximum of the valence band. Similar Sb 5*s* contribution to the top of the valence band was also observed for several antimony based compound including α-Sb_2O_3, β-Sb_2O_3, γ-Sb_2O_3, α-Sb_2O_4 and β-Sb_2O_4 oxides[44] and Sb_2S_3 and Sb_2Se_3 chalcogenide semiconductors.[11]

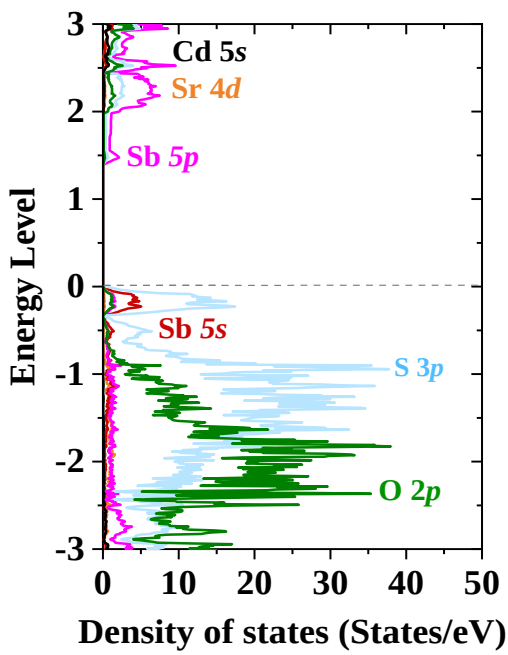

Figure 4.17 : Projected DOS of $Sr_6Cd_2Sb_6S_{10}O_7$ is shown for the Sr 3*d*, Sb 5*s*, Sb 5*p*, S 3*p* and O 2*p* states. The Fermi level is set to 0.

The $Sr_6Cd_2Sb_6S_{10}O_7$ structure has three different coordination environments for the antimony Sb^{3+}. Therefore, investigation of the orbital distribution of the Sb in the different antimony containing groups allowed us to understand the effect of the sulfur: oxygen (S:O) ratio on the properties. **Figure 4.18** shows the partial density of states for the three different Sb entities ($Sb(1)S_5$, $Sb(2)OS_4$ and $Sb(3)O_3$). The homoleptic $Sb(3)O_3$ entity contributes lower between -1 and -2 eV, and the other two $Sb(1)S_5$ and $Sb(2)OS_4$ entities contribute the most to the top of the valence band, between (0 and ~ -1 eV). These results indicate that the Sb 5*s* - *Q np* (*Q* = O, S, Se) hybridization plays a key role in tuning the band gap, highlighting a suitable O:*Q* ratio to reduce the band gap up to the visible range.

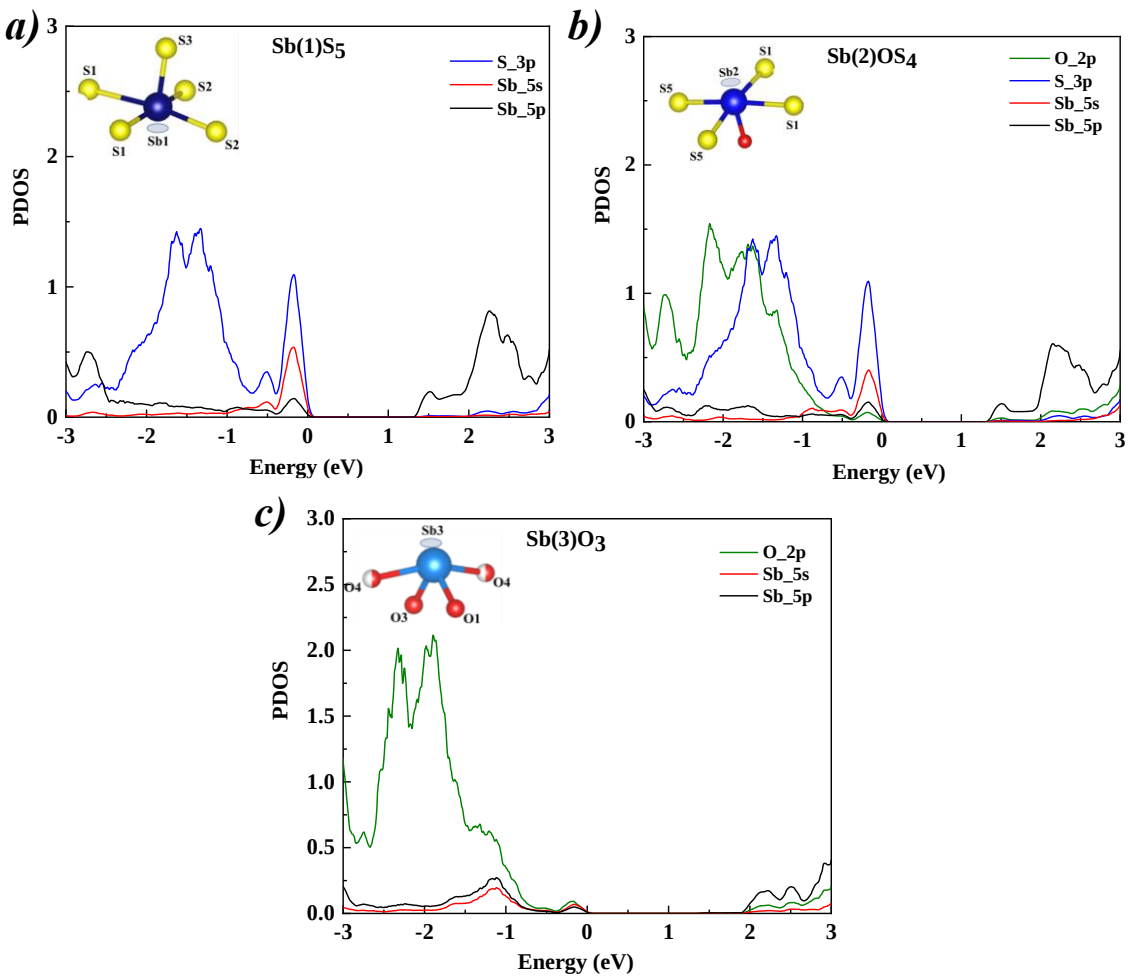

Figure 4.18: Partial density of states (PDOS) (a) of $Sb(1)S_5$ and (b) of $Sb(2)S_4O$ and (c) of $Sb(3)O_3$.

4.2.4.3. Crystal Orbital Hamiltonian Population (COHP)

Crystal Orbital Hamiltonian Population (COHP) has also been computed and pictures the bonding nature and strength (**Figure 4.19**). It is particularly interesting to focus on top of the VBM where the states related to the lone pair formation are found as described for the partial density of states. From the Fermi level E_F down to about -2 eV/-3 eV, filled antibonding interactions between Sb 5*s* and S 3*p* and/or O 2*p* states are found. These interactions are responsible for the stereoactive lone pair, consistent with the revised lone pair model.[4,45] Considering the different antimony sites, the $5s^2$ antibonding states for $Sb(1)S_5$ units remain relatively high in energy, immediately below the E_F. In contrast, for $Sb(2)OS_4$ and $Sb(3)O_3$ sites with more O^{2-} anions in the Sb^{3+} coordination sphere, stronger Sb^{3+} $5s^2$ – O 2*p* hybridisation occurs. This gives increased stabilisation of Sb^{3+} $5s^2$ electrons (see the lower energy antibonding states between -2.0 and -3.5 eV) for the Sb(2) and Sb(3) sites, alongside increased localization.

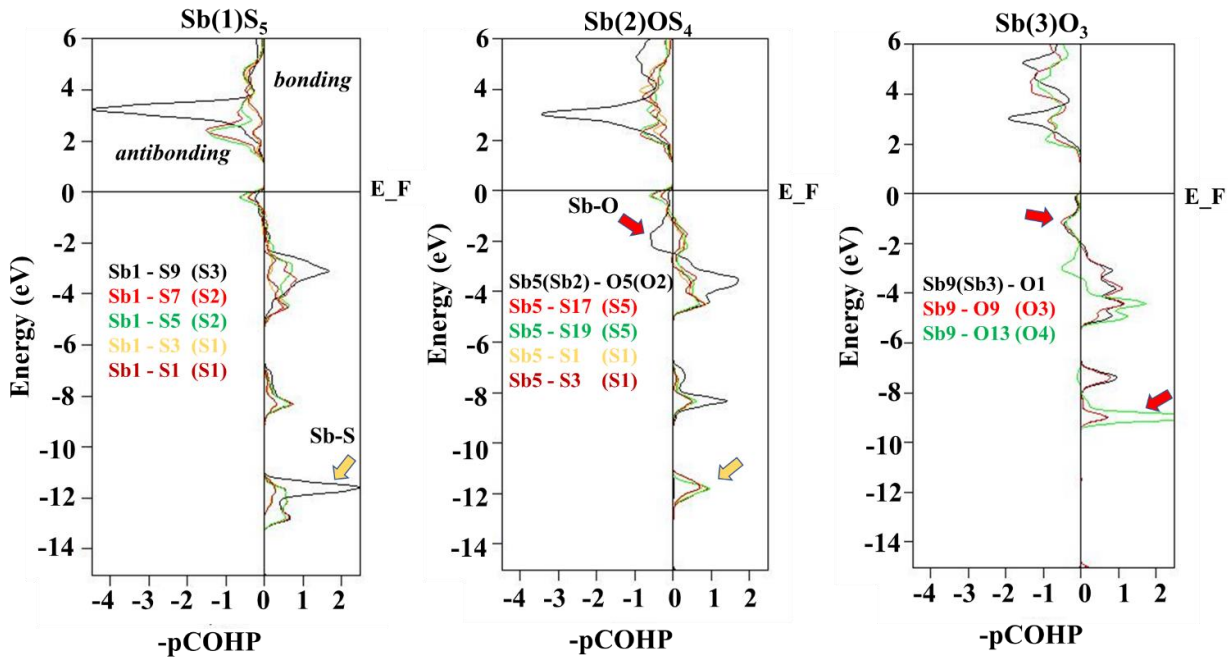

Figure 4.19 : COHP analysis for the bonds formed by $Sb(1)S_5$, $Sb(2)OS_4$ and $Sb(3)O_4$ (from left to right) with their ligands with the color codes indicated on the plots. The numbering of the atoms in the legend is that of the supercell in *P*1 used for the calculations.

Based on the calculated electronic density and the electron localization function ELF (discussed later in **Section 4.2.4.4**), the Critic2 program[46,47] using the Yu and Trinkle (YT) method[48] was used

to determine the critical points of the ELF and to obtain the electronic charge and volume within the basins (wells). **Table 4.3** gives the calculated positions, distances to the corresponding antimony atom, volumes and charges of the electronic lone pairs. The DFT calculated volume of the lone pairs has the trend $Sb(3)O_3$ > $Sb(2)S_4O$ > $Sb(1)S_5$ indicating that the most ionic interactions lead to a greater stereoactivity as reported in previous studies.[49]

The calculated Sb-(LP) distances range from 0.823 Å for Sb(1)-LP1 (full sulfide coordination) to 1.142 Å for Sb(3)-LP3 (full oxide coordination) and with an intermediate distance of 0.875 Å for Sb(2)-LP2 (mixed anion coordination). The calculated electronic charges are 3.55 e^-, 3.77 e^- and 2.88 e^- for Sb(1), Sb(2) and Sb(3) lone pairs, respectively. Despite its greater volume, the lower charge is found for Sb(3) in $Sb(3)O_3$. Charges reported with the same method are for instance reported by Poupon *et al.*: for oxotellurate (IV) compounds[50,51] with a typical lone pair charge of 2.71 e^-. These findings reflect increasing delocalization of Sb^{3+} lone pair with increasing oxide coordination, consistent with the density of states calculations reported for $Sr_6Cd_2Sb_6O_7Se_{10}$.[22]

Table 4.3. Description of the Lone Pairs: positions, Sb-E distances, charges and volumes.

Electronic lone pair	Position			Distance to Sb (Å)	Charge (e^-)	Volume (Å^3)
	x	*y*	*z*			
E1 ($Sb(1)S_5$)	0.847(5)	0.25(3)	0.987(9)	0.823(2)	3.55(6)	20.44(4)
E2 ($Sb(2)OS_4$)	0.340(4)	0.5(1)	0.562(6)	0.875(8)	3.37(4)	21.13(1)
E3 ($Sb(3)O_3$)	0.420(2)	0.953(5)	0.475(8)	1.142(4)	2.88(9)	23.54(5)

Different approaches can be used to represent the Kohn-Sham orbitals, and that may lead to different results if we consider the literature, therefore the comparison is not straightforward if not based on similar approaches. In the current study we focused on a comparative analysis of the lone pairs. Regarding the results of the COHP calculations we identified the $Sb(3)O_3$ as the entity contributing the most to the anisotropy and the polarization field (lower antibonding interactions, more stable lone pair), while $Sb(1)S_5$ contributes the most to the band edges (supported by the partial density of states calculations). Both of these factors are crucial for enhanced photoconduction properties, therefore better photocatalytic activity.

4.2.4.4. Electron localization function and stereochemical activity calculation

Electron localization function (ELF) reflects localized electron pairs and gives insight into different bonds and lone pair electrons.[52] Therefore by computing this ELF it allowed us to investigate the nodal structure of the molecular orbitals of $Sr_6Cd_2Sb_6O_7S_{10}$ (**Figure 4.20**). Looking at the local coordination geometry around the Sb^{3+} cations, the distorted lone pair of antimony is clearly observed. As the environment changes the Sb^{3+} $5s^2$ pair size changes, which indicates that the lone pair is sensitive to the O:S ratio. As expected based on the revised lone pair model,[4,45] and COHP calculations (**Figure 4.19**), the size of the lone pair increases with the O ratio increasing.

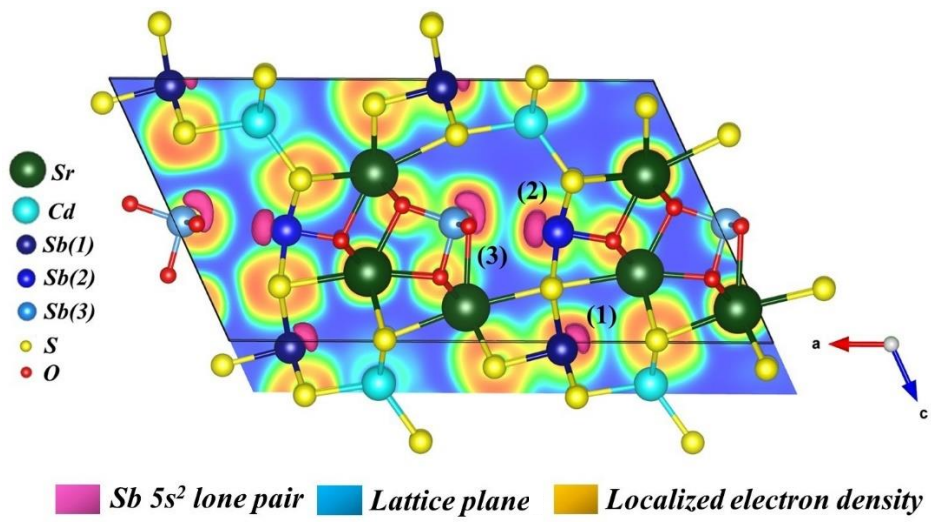

Figure 4.20 : DFT-computed ELF for the three different Sb coordination, $Sb(1)S_5$, $Sb(2)OS_4$ and $Sb(3)O_3$.

Hu *et al.*[53] described an approach useful to quantify the stereochemical activity of lone pair electrons using the following equation:

$$R_{SCA} = I(Sb - s)/I(Sb - p) \tag{4.4}$$

where R_{SCA} is the ratio of Sb-*s* states to Sb-*p* states, and *I(Sb-s)/I(Sb-p)* is the integrated PDOS from a specified energy level (point where the intensity of Sb-*s* and Sb-*p* is equivalent) to the Fermi level (**Figure 4.21a**). As the revised lone pair model indicates, the filled antibonding interactions between Sb *5s* and S *3p* and/or O *2p* states are responsible for the stereoactive lone pair and are located close to the top of the valence band.[45,4] Therefore the method is a simple calculation of the

stereochemical activity ratio based on a simple comparison of the *s* and *p* states of the Sb cation near the Fermi level (between the two green arrows on **Figure 4.21a**).

The stereochemical activity ratio R_{SCA} was calculated for $Sb(1)S_5$, $Sb(2)S_4O$ and $Sb(3)O_3$ to be 0.57, 0.59 and 0.64, respectively (**Table 4.4**). The smaller R_{SCA} is for the Sb fully coordinated by sulfur (0.568) and the bigger one is obtained for the Sb fully coordinated with the oxygen (0.641), confirming the proportional relationship between the stereochemical activity of lone pair electrons with the O:S ratio (**Figure 4.21c**). These findings are also consistent with the results obtained from the COHP results and the calculated volumes and distances to Sb which increase upon increasing the oxygen ratio.

Table 4.4. Integrated PDOS from a specified energy level to the fermi level and the calculated stereochemical activity factor for different antimony entities.

	$Sb(1)S_5$ entity	**$Sb(2)S_4O$ entity**	**$Sb(3)O_3$ entity**
I (Sb-s)	1.40	1.39	1.28
I (Sb-p)	2.46	2.35	1.99
R_{SCA}	0.57	0.59	0.64

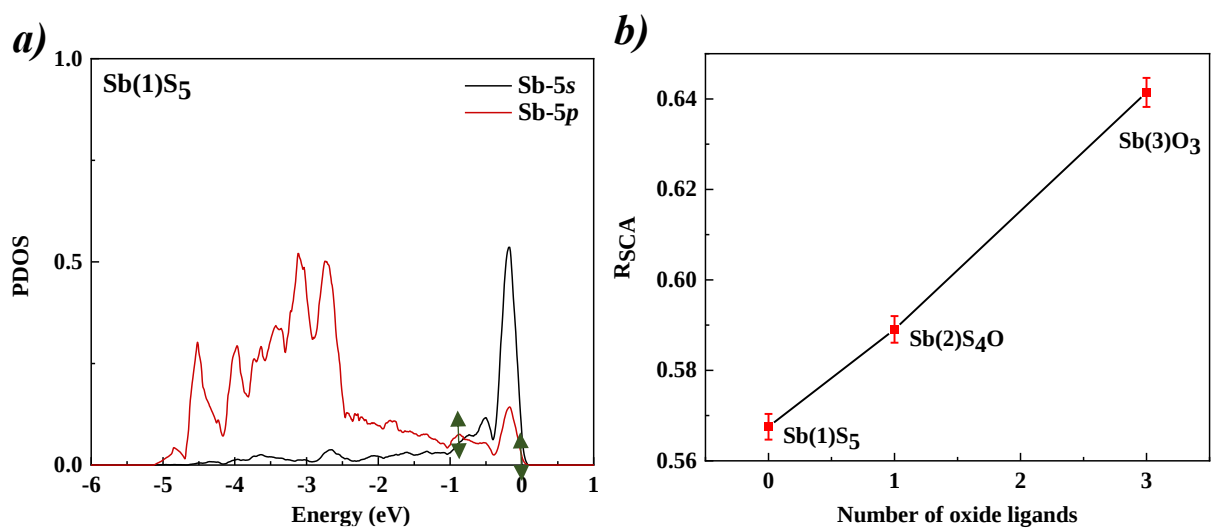

Figure 4.21 : (a) Example of comparison of PDOS of Sb-5*s* and Sb-5*p* in $Sb(1)S_5$, between energy levels marked with green arrows. and (b) Relationship between stereochemical activity factor R_{SCA} and number of oxide ligands.

4.3. Discussion

4.3.1. Tuning the size of the band gap

One of the key characteristics of $Sr_6Cd_2Sb_6S_{10}O_7$ is its reduced band gap of 1.89 eV, suitable for the visible spectrum;[15] compared to other antimony Sb^{3+} oxides such as α-Sb_2O_3 (3.38 eV), β-Sb_2O_3 (2.25 eV), γ-Sb_2O_3 (2.55 eV).[44] While the VBM of these phases are mainly composed of O 2*p* states, the VBM in $Sr_6Cd_2Sb_6S_{10}O_7$ consists of S 3*p* and O 2*p* orbitals hybridizing with Sb 5*s* states. The presence of this anion mixing has led to an increase in the relative energies of the antibonding orbitals, which resulted in an increase in the valence band edge, decreasing then the band gap. This first result emphasises the potential to tune band gaps by including anions from different rows of the periodic table in mixed-anion systems, as in oxysulfides. Note that its recently reported oxyselenide analogue $Sr_6Cd_2Sb_6O_7Se_{10}$[22] revealed a slightly smaller gap (1.55 eV); this confirms that the nature of chalcogenide has an influence on tuning the band gap, where a less electronegative element contributes higher in the VBM, decreasing the band gap furthermore.

4.3.2. Factors affecting photocurrent response and photocatalytic activity

$Sr_6Cd_2Sb_6S_{10}O_7$ demonstrated the capacity of generating an efficient photocurrent under solar and UV irradiation with efficient electron-hole separations (judging by the observed peak shapes). However, the presence of oxide and sulfide anions alone isn't sufficient for a photocurrent response under sunlight irradiation; for instance $[(Ba_{19}Cl_4)(Ga_6Si_{12}O_{42}S_8)]$ and $LaGaS_2O$, with heteroleptic Ga^{3+} coordination environments, require irradiation by higher-energy UV light before a photocurrent response is observed.[54,55] We therefore wanted to look deeper into investigating the structure-properties relationship in this material.

For the sake of comparison, we looked at the photocurrent results reported for the oxyselenide analogue.[22] A much higher photocurrent response (50 $\mu A.cm^{-2}$ under 700 nm excitation and bias = 5 V) was measured for $Sr_6Cd_2Sb_6O_7Se_{10}$ than for $Sr_6Cd_2Sb_6S_{10}O_7$ (0.95 $\mu A.cm^{-2}$ under a 450 nm excitation and bias = 0 V, **Figure 4.8**). This difference can be attributed to the higher bias voltage (5 V) used for measurements on the oxyselenide (compared with bias voltage of 0.4 and 0 V used for measurements on $Sr_6Cd_2Sb_6S_{10}O_7$ that we reported above), as higher responses are typically observed with increased voltage.

4.3.2.1. Polarity

A key question is whether the polar structure or polar units are what actually contributes to these enhanced photoelectric properties. The points we concluded were based on interpreting the obtained peak shapes for the recorded photocurrents. It's useful to compare $Sr_6Cd_2Sb_6S_{10}O_7$ with other oxysulfides demonstrating similar photocurrent behaviour (spikey peaks i.e. fast kinetics) such as La_3GaS_5O.[55] Whilst $Sr_6Cd_2Sb_6S_{10}O_7$ adopts a polar crystal structure (of *Cm* symmetry),[15] La_3GaS_5O crystallises with a non-polar structure (of *Pnma* symmetry).[55] On the other hand, both phases have polar coordination environments for the photoactive cations, arising from the presence of the stereochemical activity lone pair of antimony favouring lower-symmetry sites in $Sr_6Cd_2Sb_6S_{10}O_7$,[15] and the presence of the heteroleptic GaO_3S_4 coordination in La_3GaS_5O.[55] A potential suggestion is that the presence of a polar coordination environment around the photo-active cation can be of greater influence on enhancing electron-hole separation than having a polar crystal structure. In addition to the results previously discussed in **Chapter 3**, the question remains whether the presence of polar units or polar structure is more important.

Both $Sr_6Cd_2Sb_6Q_{10}O_7$ (Q = S, Se) phases demonstrated good photoelectric performances with efficient charge carrier transport properties (slow recombination rates) in both analogues. The oxyselenide didn't show as fast kinetics as the oxysulfide. This difference in the kinetics can be attributed to the slightly higher dipole moments in the case of the oxysulfide ($[SbOS_4]^{7-}$ 15.5 D > $[SbS_5]^{7-}$ 12.7 D)[15] compared to the oxyselenide, $[SbOSe_4]^{7-}$ 15 D > $[SbSe_5]^{7-}$ 11.9 D. This illustrates another aspect of the influence of the chalcogenide in the material.

4.3.2.2. $5s^2$ lone pair activity

A key feature in the photocatalytic activity of $Sr_6Cd_2Sb_6S_{10}O_7$ is the $5s^2$ lone pair on Sb^{3+} sites. The presence of the $5s^2$ or $6s^2$ pairs favours lower symmetry coordination environments which can give rise to polarization within the structure.[10,19] Corey *et al*,[56] and more recently Wang *et al*[57] have shown that the stereochemical activity of the Sb^{3+} $5s^2$ lone pair increases with increasing electronegativity of the chalcogenide in the binary chalcogenides Sb_2Q_3 (Q = O, S, Se, Te).[56,57] This is consistent with the COHP analysis and the ELF plot (**Figure 4.19 and 4.20**) and with the R_{SCA} factors reflecting the stereochemical activity[53] determined for $Sb(1)S_5$, $Sb(2)OS_4$ and $Sb(3)O_3$ (**Figure 4.21b**). The stereochemical activity is comparable to that reported for arsenic sulfides (typically 0.59 – 0.73)[58] but lower than that reported for bismuth oxides[53] with smaller energy

difference between cation ns^2 and anion valence *np* orbitals. This supports the fact that the anion nature can influence the stereoactivity of the lone pairs. The Sb^{3+} $5s^2$ contributes to the density of states at the top of the valence band, thus playing a key role in reducing the band gap towards the energy of solar irradiation, and the extent of its stereochemical activity is reflected in the energy range of these states.[57] This can be the origin of having anisotropic effects (effective masses and mobility) thus improved electrons and holes transport properties.[57] Similar results were observed for Bi-based compounds that present a $6s^2$ stereoactive lone pair.[59]

$Sr_6Cd_2Sb_6S_7O_{10}$ oxysulfide contains two types of coordination environment for the antimony cations, homoleptic ($Sb(1)S_5$ and $Sb(3)O_3$) and heteroleptic ($Sb(2)OS_4$). Predominantly homoleptic cation coordination are found in oxysulfides, but more mixing of anions depending on the nature of the specific combination of cations and anions can lead to heteroleptic coordination environments.[60] The influence of heteroleptic coordination environments are not fully explored in terms of photocatalysis and electrons/holes separation.[61] Orbital distribution of the Sb in different antimony containing groups showed that Sb(3) fully coordinated by O gives lower energy occupied Sb(3) states and makes little contribution to the band edges, while Sb(1) and Sb(2) states (with sulfide ions in their coordination environments) contribute more to the band edges. This is especially true for $Sb(1)S_5$ which contributes most to the top of the valence band (particularly Sb $5s^2$ electron pair) due to the higher energy S 3*p* states with the less electronegative sulfide coordination compared with oxide-sulfide coordination. This demonstrates the sensitivity of the lone pair stereoactivity towards the O:S ratio.

4.3.3. Charge carriers mobilities

The photocurrent results can also be linked to the electronic properties of the material, particularly the charge carriers' mobilities. By computing the effective masses along the high symmetry points near the CBM and VBM, we gain insight into the origin of this property. First, we noticed that the computed electrons effective masse is low (0.22 m_0) along the B $\rightarrow$ D (0, $^1/_2$, $^1/_2$ plane; parallel to the Sb-S layers) direction, whilst it increased drastically (5.44 m_0) along the $Y_2 \rightarrow \Gamma$ direction ($^1/_2$, 0, 0 plane; perpendicular to the Sb-S layers). Sb 5*p* orbitals are contributing most to the CBM, so by looking at their overlap for instance at the Y point (along *a* axis, across the layers), the orbitals are hardly overlapping which can be causing the increased electron effective mass along this direction, therefore the decrease in their mobility (**Figure 4.22a**).

On the other hand, looking at **Figure 4.22b**, at the D point (along *b* axis within the layers), orbitals are fairly diffuse along *a* and *b* axis (red arrows), resulting in more delocalization due to the mixing of the Sb 5*p* – S 3*p* states, thus lower m_e* values. This highlights one important characteristic for oxychalcogenides, as the presence of layers tends to facilitate the mobility of the charge carriers. Other than that, CdS is intensively studied as n-type semiconductor,[62,63,64,65] and the presence of the Cd orbitals can also be advantageous for the interesting electrons behaviour, but in our compound they are higher in energy.

Regarding the hole's mobility, we looked at the valence band, specifically the Sb 5*s* – S 3*p* orbitals. Much as the $Sb(3)O_3$ orbitals are low in energy, the SbS_5 and $SbOS_4$ sites have orbitals at the top of the VB. At the D point (**Figure 4.22b**), these entities seem fairly separated which can lead to a decrease in the orbital overlap (black dotted box), causing then the increase in the effective masses value we got (6.6 m_0). At the B point (0, 0, $^1/_2$ plane; parallel to the zigzag layers), a lower effective mass was obtained (m_h*= 0.751 m_0), as we can see higher delocalization of the Sb 5*s* – S 3*p* occurred along *a* axis (**Figure 4.22c**).

Having this difference in the effective masses can effectively reduce the recombination of photogenerated electrons and holes, thus improving photocatalytic performance. This was consistent with the obtained recombination constant (0.08 min^{-1}). In addition, as we identified previously the contribution of the $Sb(3)O_3$ entity to the anisotropic effects such as the observed difference in the effective masses, the presence of the highly electronegative oxygen can also be another reason for having a minimized recombination rate. A study on $Bi_2TiO_4F_2$ oxyfluoride supported this point, where the presence of F^- ion (strongly electronegative) was found to effectively reduce the recombination of photogenerated electrons and holes.[66]

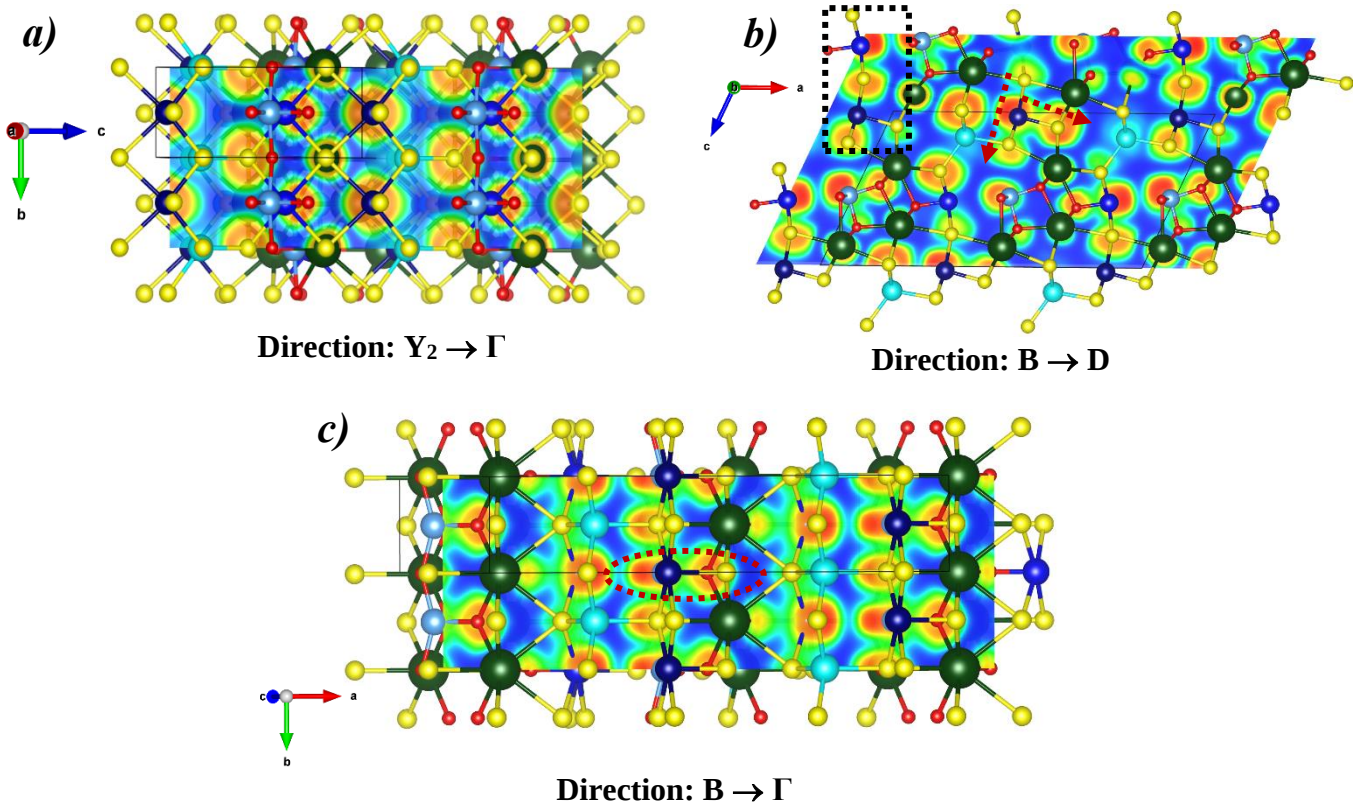

Figure 4.22 : Orbital overlap in $Sr_6Cd_2Sb_6O_7S_{10}$ along the directions (a) $Y_2 \rightarrow \Gamma$ (i.e. $^1/_2$, 0, 0 plane), (b) $B \rightarrow D$ (i.e. 0, $^1/_2$, $^1/_2$ plane) and (c) $B \rightarrow \Gamma$ (i.e. 0, 0, $^1/_2$ plane).

4.3.4. Solutions/pH for photocurrent measurements

The choice of the electrolyte (nature and pH) is an important factor that can directly influence the photoelectrochemical measurements. It is crucial that the electrolyte doesn't interact with the working electrode; the ions have to be electro-inactive in a way that the redox couple of water is the only one involved during the measurements. Hence chemical stability of the material can influence the electrolyte choice. In addition, when the semiconductor is brought into contact with an electrolyte, a potential gradient is established at the interface and charges appear at the surface of the semiconductor. The origin of these charges could be electrons/holes trapped at the surface of the semiconductor or the electrolyte ions that adsorb on the surface. This forms a layer called the Helmholtz layer,[67] and as long as the potential difference across this Helmholtz layer remains almost unchanged when the applied potential is changed, the semiconductor/electrolyte junction is ideal.

Our investigation of the chemical stability of $Sr_6Cd_2Sb_6S_7O_{10}$ (**Figure 4.14**) revealed a narrow stability range (pH = 5.5), making it not very stable compared to other materials. For instance, $LaFeO_3$ oxide maintained its chemical stability in pH varying between 5 to 14.[68] This indicates the importance of knowing the chemical stability of the tested material to avoid decomposition (as observed from XRPD results in Figure **4.14b**).

Our first electrolyte choice was a classical sodium sulfate (0.1 mol. L^{-1}) with electro-inactive Na^+ and SO_4^{2-} ions. Whilst interesting results were obtained using this electrolyte, photocorrosion occurred. In our case, we noticed that the photocorrosion occurred upon applying a potential (0.4 V), which can be due to a change in the Helmholtz layer.

Attempts to stabilize the phase by adding sulfite anions (SO_3^{2-}), reduced the photocorrosion, but it reduced the performance as well. As hole scavengers, these SO_3^{2-} ions might have stabilized the Helmholtz layer by balancing the potential difference across whilst adjusting the electrons/holes ratio trapped at the surface. Thus, the combination of these tests confirm that the nature of the electrolyte and the contact electrolyte-electrode can further be optimized for obtaining enhanced photoelectrochemical outcome.

Therefore, the good photocatalytic activity and the good electron-holes separation that we observed for our $Sr_6Cd_2Sb_6S_7O_{10}$ oxysulfide could be an equilibrium between first the Sb $5s^2$ lone pair that contributes to a better electron-hole separation, second the S:O ratio in the heteroleptic groups within the structure, in a way to have the sulfide (lower electronegativity) to increase the valence band resulting in a decrease in the band gap into the visible range and on the other hand the oxygen to stabilize the lone pair electrons and reduce the recombination of the photogenerated electrons and holes due to its higher electronegativity.

4.4. Conclusion

In conclusion, $Sr_6Cd_2Sb_6S_{10}O_7$ oxysulfide can be a promising candidate for water-splitting photocatalysis, under UV and solar irradiations. This phase was previously reported for its interesting non-linear optical properties that are related to its many characteristic, that can be interesting features for designing efficient photocatalysts. We were particularly intersted in investigating two major traits: the presence of the stereochemically-active lone pair of antimony and of the various coordination environments around this cation, both homoleptic (SbO_3 and SbS_5) and heteroleptic ($SbOS_4$).

Primarily, regarding our experimental results, by means of diffuse reflectance we saw that the presence of mixed anions within the material can be effective in tuning the band gap of these systems to be suitable for the visible spectrum. Simultaneously, the obtained photoelectrochemical results highlighted the capacity of $Sr_6Cd_2Sb_6S_{10}O_7$ to generate photocurrents on a large range of wavelengths as well as under solar irradiation, with or without external voltage. These measurements also confirmed the very efficient electron-hole separation and migration (spikey peak shapes for the recorded photocurrents) with a 78% transfer efficacity related to the decreased recombination rate (0.08 min^{-1}). Moreover, $Sr_6Cd_2Sb_6S_{10}O_7$ was capable of photodegrading the Rhodamine B under UV irradiation with a good rate constant, that is comparable with other reported photocatalysts.

DFT calculations gave us insight to the electronic properties of our material, which allowed us to understand the results we observed experimentally. Starting with the reduced band gap, that can be attributed to the presence of the sulfur 3*p* orbitals of the SbS_5 and SbS_4O contributing most to the top of the valence band. The calculated effective masses of the charge carriers revealed different mobility, particularly very mobile electrons (with an effective mass below 0.5 m_0); which support the behaviour we saw in the photocurrent measurements and link to the low recombination rate as well. By means of electron localization function, we saw that the SbS_5 and $SbOS_4$ units (contributing to the VBM) are largely separated therefore diminishing their overlapping, which can be the origin of having the low mobility exhibited by the holes.

We also noticed that this mixing in anions can be important for tuning the stereochemical activity of lone pairs electrons; this was confirmed by our COHP calculations that displayed the different antibonding interactions involving Sb^{3+} 5*s* and anion *np* states just below the Fermi level.

In fact, we found that the lone pair stereoactivity is sensitive to the O/S ratio in the Sb coordination environment, in a way to increase with the increase of the ionicity of the anion. We therefore concluded that the most ionic entity ($Sb(3)O_3$) is the most polar Sb site, contributing the most to the polar nature and enhancing electron-hole separation, whilst $Sb(1)S_5$ entities contribute most to the DOS at the VBM.

This study demonstrates the importance of lone pairs in designing photocatalytic materials, and the balance between the cation site polarity and energies of cation valence states that can be tuned by anion substitution. It also highlights some key features useful for designing efficient photocatalysts with interesting charge carriers' transport properties.

REFERENCES

(1) Das, A.; Das, U.; Das, A. K. Relativistic Effects on the Chemical Bonding Properties of the Heavier Elements and Their Compounds. *Coordination Chemistry Reviews* **2023**, *479*, 215000.

(2) Thayer, J. S. Relativistic Effects and the Chemistry of the Heavier Main Group Elements. *Relativistic methods for chemists* **2010**, 63–97.

(3) Liang, F.; Kang, L.; Lin, Z.; Wu, Y. Mid-Infrared Nonlinear Optical Materials Based on Metal Chalcogenides: Structure–Property Relationship. *Crystal growth & design* **2017**, *17* (4), 2254–2289.

(4) Walsh, A.; Payne, D. J.; Egdell, R. G.; Watson, G. W. Stereochemistry of Post-Transition Metal Oxides: Revision of the Classical Lone Pair Model. *Chemical Society Reviews* **2011**, *40* (9), 4455–4463.

(5) Stoltzfus, M. W.; Woodward, P. M.; Seshadri, R.; Klepeis, J.-H.; Bursten, B. Structure and Bonding in SnWO4, PbWO4, and BiVO4: Lone Pairs vs Inert Pairs. *Inorganic chemistry* **2007**, *46* (10), 3839–3850.

(6) Sayama, K.; Nomura, A.; Zou, Z.; Abe, R.; Abe, Y.; Arakawa, H. Photoelectrochemical Decomposition of Water on Nanocrystalline BiVO 4 Film Electrodes under Visible Light. *Chemical Communications* **2003**, No. 23, 2908–2909.

(7) Ok, K. M. Functional Layered Materials with Heavy Metal Lone Pair Cations, Pb 2+, Bi 3+, and Te 4+. *Chemical Communications* **2019**, *55* (85), 12737–12748.

(8) Handy, J. V.; Zaheer, W.; Rothfuss, A. R.; McGranahan, C. R.; Agbeworvi, G.; Andrews, J. L.; García-Pedraza, K. E.; Ponis, J. D.; Ayala, J. R.; Ding, Y. Lone but Not Alone: Precise Positioning of Lone Pairs for the Design of Photocatalytic Architectures. *Chemistry of Materials* **2022**.

(9) Suzuki, H.; Kunioku, H.; Higashi, M.; Tomita, O.; Kato, D.; Kageyama, H.; Abe, R. Lead Bismuth Oxyhalides PbBiO2X (X= Cl, Br) as Visible-Light-Responsive Photocatalysts for Water Oxidation: Role of Lone-Pair Electrons in Valence Band Engineering. *Chemistry of Materials* **2018**, *30* (17), 5862–5869.

(10) Kavanagh, S. R.; Savory, C. N.; Scanlon, D. O.; Walsh, A. Hidden Spontaneous Polarisation in the Chalcohalide Photovoltaic Absorber Sn 2 SbS 2 I 3. *Materials horizons* **2021**, *8* (10), 2709–2716.

(11) Wang, X.; Li, Z.; Kavanagh, S. R.; Ganose, A. M.; Walsh, A. Lone Pair Driven Anisotropy in Antimony Chalcogenide Semiconductors. *Physical Chemistry Chemical Physics* **2022**, *24* (12), 7195–7202.

(12) Orgel, L. EJ Chem. Soc. 1958, 4186. Dunitz, J. D.; Orgel. *L. E. Adv. Inorg. Chem. Radiochem* **1960**, *2* (1).

(13) Orgel, L. E. 769. The Stereochemistry of B Subgroup Metals. Part II. The Inert Pair. *Journal of the Chemical Society (Resumed)* **1959**, 3815–3819.

(14) Walsh, A.; Watson, G. W. Influence of the Anion on Lone Pair Formation in Sn (II) Monochalcogenides: A DFT Study. *The Journal of Physical Chemistry B* **2005**, *109* (40), 18868–18875.

(15) Wang, R.; Liang, F.; Wang, F.; Guo, Y.; Zhang, X.; Xiao, Y.; Bu, K.; Lin, Z.; Yao, J.; Zhai, T. Sr6Cd2Sb6O7S10: Strong SHG Response Activated by Highly Polarizable Sb/O/S Groups. *Angewandte Chemie International Edition* **2019**, *58* (24), 8078–8081.

(16) Chen, F.; Huang, H.; Guo, L.; Zhang, Y.; Ma, T. The Role of Polarization in Photocatalysis. *Angewandte Chemie International Edition* **2019**, *58* (30), 10061–10073.

(17) Dong, X.-D.; Zhang, Y.-M.; Zhao, Z.-Y. Role of the Polar Electric Field in Bismuth Oxyhalides for Photocatalytic Water Splitting. *Inorganic Chemistry* **2021**, *60* (12), 8461–8474.

(18) Lou, Z.; Wang, P.; Huang, B.; Dai, Y.; Qin, X.; Zhang, X.; Wang, Z.; Liu, Y. Enhancing Charge Separation in Photocatalysts with Internal Polar Electric Fields. *ChemPhotoChem* **2017**, *1* (5), 136–147.

(19) Dong, X.-D.; Yao, G.-Y.; Liu, Q.-L.; Zhao, Q.-M.; Zhao, Z.-Y. Spontaneous Polarization Effect and Photocatalytic Activity of Layered Compound of BiOIO3. *Inorganic Chemistry* **2019**, *58* (22), 15344–15353.

(20) Guo, Y.; Shi, W.; Zhu, Y. Internal Electric Field Engineering for Steering Photogenerated Charge Separation and Enhancing Photoactivity. *EcoMat* **2019**, *1* (1), e12007.

(21) Chen, J.; Zhai, Y.; Yu, Y.; Luo, J.; Fan, X. Spatial Separation of Photo-Induced Charge Carriers in a Na3VO2B6O11 Polar Material and Its Enhanced Photocatalytic Activity. *Applied Surface Science* **2021**, *556*, 149809.

(22) Wang, R.; Wang, F.; Zhang, X.; Feng, X.; Zhao, C.; Bu, K.; Zhang, Z.; Zhai, T.; Huang, F. Improved Polarization in the Sr6Cd2Sb6O7Se10 Oxyselenide through Design of Lateral Sublattices for Efficient Photoelectric Conversion. *Angewandte Chemie* **2022**.

(23) Rodriguez-Carvajal, J. Fullprof: A Program for Rietveld Refinement and Profile Matching Analysis of Complex Powder Diffraction Patterns. *Laboratoire Léon Brillouin (CEA-CNRS)* **1991**.

(24) Pitschke, W.; Hermann, H.; Mattern, N. The Influence of Surface Roughness on Diffracted X-Ray Intensities in Bragg–Brentano Geometry and Its Effect on the Structure Determination by Means of Rietveld Analysis. *Powder Diffraction* **1993**, *8* (2), 74–83.

(25) Kubelka, P.; Munk, F. A Contribution to the Optics of Pigments. *Z. Tech. Phys* **1931**, *12* (593), 193.

(26) Tauc, J.; Grigorovici, R.; Vancu, A. Optical Properties and Electronic Structure of Amorphous Germanium. *physica status solidi (b)* **1966**, *15* (2), 627–637.

(27) Butler, M.; Ginley, D. Prediction of Flatband Potentials at Semiconductor-electrolyte Interfaces from Atomic Electronegativities. *Journal of the Electrochemical Society* **1978**, *125* (2), 228.

(28) Shaikh, S. K.; Inamdar, S. I.; Ganbavle, V. V.; Rajpure, K. Y. Chemical Bath Deposited ZnO Thin Film Based UV Photoconductive Detector. *Journal of Alloys and Compounds* **2016**, *664*, 242–249.

(29) Zhao, Q.; Wang, W.; Carrascoso-Plana, F.; Jie, W.; Wang, T.; Castellanos-Gomez, A.; Frisenda, R. The Role of Traps in the Photocurrent Generation Mechanism in Thin InSe Photodetectors. *Materials Horizons* **2020**, *7* (1), 252–262.

(30) Parkinson, B.; Turner, J.; Peter, L.; Lewis, N.; Sivula, K.; Domen, K.; Bard, A. J.; Fiechter, S.; Collazo, R.; Hannappel, T. *Photoelectrochemical Water Splitting: Materials, Processes and Architectures*; Royal Society of Chemistry, 2013.

(31) Hwang, I.; McNeill, C. R.; Greenham, N. C. Drift-Diffusion Modeling of Photocurrent Transients in Bulk Heterojunction Solar Cells. *Journal of Applied Physics* **2009**, *106* (9), 094506.

(32) Leroy, S.; Blach, J.-F.; Huvé, M.; Léger, B.; Kania, N.; Henninot, J.-F.; Ponchel, A.; Saitzek, S. Photocatalytic and Sonophotocatalytic Degradation of Rhodamine B by Nano-Sized La2Ti2O7 Oxides Synthesized with Sol-Gel Method. *Journal of Photochemistry and Photobiology A: Chemistry* **2020**, *401*, 112767. https://doi.org/10.1016/j.jphotochem.2020.112767.

(33) Bott, A. W. Electrochemistry of Semiconductors. *Current Separations* **1998**, *17*, 87–92.

(34) Lin, L.; Lin, J. M.; Wu, J. H.; Hao, S. C.; Lan, Z. Photovoltage Enhancement of Dye Sensitised Solar Cells by Using ZnO Modified TiO2 Electrode. *null* **2010**, *14* (5), 370–374. https://doi.org/10.1179/143307510X12820854748791.

(35) Zhou, L.; Zhang, H.; Sun, H.; Liu, S.; Tade, M. O.; Wang, S.; Jin, W. Recent Advances in Non-Metal Modification of Graphitic Carbon Nitride for Photocatalysis: A Historic Review. *Catalysis Science & Technology* **2016**, *6* (19), 7002–7023.

(36) Belver, C.; Adán, C.; Fernández-García, M. Photocatalytic Behaviour of Bi2MO6 Polymetalates for Rhodamine B Degradation. *Catalysis Today* **2009**, *143* (3), 274–281. https://doi.org/10.1016/j.cattod.2008.09.011.

(37) Ohtani, B. Photocatalysis by Inorganic Solid Materials: Revisiting Its Definition, Concepts, and Experimental Procedures. *Advances in Inorganic Chemistry* **2011**, *63*, 395–430.

(38) Lucid, A.; Iwaszuk, A.; Nolan, M. A First Principles Investigation of Bi2O3-Modified TiO2 for Visible Light Activated Photocatalysis: The Role of TiO2 Crystal Form and the Bi3+ Stereochemical Lone Pair. *Materials science in semiconductor processing* **2014**, *25*, 59–67.

(39) Iwaszuk, A.; Nolan, M. SnO-Nanocluster Modified Anatase TiO 2 Photocatalyst: Exploiting the Sn (II) Lone Pair for a New Photocatalyst Material with Visible Light Absorption and Charge Carrier Separation. *Journal of Materials Chemistry A* **2013**, *1* (22), 6670–6677.

(40) Chang, H.-Y.; Kim, S.-H.; Halasyamani, P. S.; Ok, K. M. Alignment of Lone Pairs in a New Polar Material: Synthesis, Characterization, and Functional Properties of Li2Ti (IO3) 6. *Journal of the American Chemical Society* **2009**, *131* (7), 2426–2427.

(41) Perdew, J. P.; Burke, K.; Ernzerhof, M. Generalized Gradient Approximation Made Simple. *Physical review letters* **1996**, *77* (18), 3865.

(42) Wang, V.; Xu, N.; Liu, J.-C.; Tang, G.; Geng, W.-T. VASPKIT: A User-Friendly Interface Facilitating High-Throughput Computing and Analysis Using VASP Code. *Computer Physics Communications* **2021**, *267*, 108033.

(43) Gamon, J.; Giaume, D.; Wallez, G.; Labégorre, J.-B.; Lebedev, O.; Al Rahal Al Orabi, R.; Haller, S.; Le Mercier, T.; Guilmeau, E.; Maignan, A. Substituting Copper with Silver in the BiMOCh Layered Compounds (M= Cu or Ag; Ch= S, Se, or Te): Crystal, Electronic Structure, and Optoelectronic Properties. *Chemistry of Materials* **2018**, *30* (2), 549–558.

(44) Allen, J. P.; Carey, J. J.; Walsh, A.; Scanlon, D. O.; Watson, G. W. Electronic Structures of Antimony Oxides. *The Journal of Physical Chemistry C* **2013**, *117* (28), 14759–14769.

(45) Payne, D. J.; Egdell, R. G.; Walsh, A.; Watson, G. W.; Guo, J.; Glans, P.-A.; Learmonth, T.; Smith, K. E. Electronic Origins of Structural Distortions in Post-Transition Metal Oxides: Experimental and Theoretical Evidence for a Revision of the Lone Pair Model. *Physical review letters* **2006**, *96* (15), 157403.

(46) Otero-de-la-Roza, A.; Johnson, E. R.; Luaña, V. Critic2: A Program for Real-Space Analysis of Quantum Chemical Interactions in Solids. *Computer Physics Communications* **2014**, *185* (3), 1007–1018.

(47) de-la Roza, A. O.; Blanco, M.; Pendás, A. M.; Luana, V. Critic: A New Program for the Topological Analysis of Solid-State Electron Densities. *Computer Physics Communications* **2009**, *180* (1), 157–166.

(48) Wang, H.; Kohyama, M.; Tanaka, S.; Shiihara, Y. Ab Initio Local Energy and Local Stress: Application to Tilt and Twist Grain Boundaries in Cu and Al. *Journal of Physics: Condensed Matter* **2013**, *25* (30), 305006.

(49) Walsh, A.; Watson, G. W. Influence of the Anion on Lone Pair Formation in Sn (II) Monochalcogenides: A DFT Study. *The Journal of Physical Chemistry B* **2005**, *109* (40), 18868–18875.

(50) Poupon, M.; Barrier, N.; Petit, S.; Clevers, S.; Dupray, V. Hydrothermal Synthesis and Dehydration of CaTeO3 (H2O): An Original Route to Generate New CaTeO3 Polymorphs. *Inorganic Chemistry* **2015**, *54* (12), 5660–5670.

(51) Poupon, M.; Barrier, N.; Petit, S.; Boudin, S. A New β-CdTeO 3 Polymorph with a Structure Related to α-CdTeO 3. *Dalton Transactions* **2017**, *46* (6), 1927–1935.

(52) Silvi, B.; Savin, A. Classification of Chemical Bonds Based on Topological Analysis of Electron Localization Functions. *Nature* **1994**, *371* (6499), 683–686.

(53) Hu, C.; Mutailipu, M.; Wang, Y.; Guo, F.; Yang, Z.; Pan, S. The Activity of Lone Pair Contributing to SHG Response in Bismuth Borates: A Combination Investigation from Experiment and DFT Calculation. *Physical Chemistry Chemical Physics* **2017**, *19* (37), 25270–25276.

(54) Shi, Y.-F.; Li, X.-F.; Zhang, Y.-X.; Lin, H.; Ma, Z.; Wu, L.-M.; Wu, X.-T.; Zhu, Q.-L. [(Ba19Cl4)(Ga6Si12O42S8)]: A Two-Dimensional Wide-Band-Gap Layered Oxysulfide with Mixed-Anion Chemical Bonding and Photocurrent Response. *Inorganic chemistry* **2019**, *58* (10), 6588–6592.

(55) Ogisu, K.; Ishikawa, A.; Shimodaira, Y.; Takata, T.; Kobayashi, H.; Domen, K. Electronic Band Structures and Photochemical Properties of La− Ga-Based Oxysulfides. *The Journal of Physical Chemistry C* **2008**, *112* (31), 11978–11984.

(56) Carey, J. J.; Allen, J. P.; Scanlon, D. O.; Watson, G. W. The Electronic Structure of the Antimony Chalcogenide Series: Prospects for Optoelectronic Applications. *Journal of Solid State Chemistry* **2014**, *213*, 116–125.

(57) Wang, X.; Li, Z.; Kavanagh, S. R.; Ganose, A. M.; Walsh, A. Lone Pair Driven Anisotropy in Antimony Chalcogenide Semiconductors. *arXiv preprint arXiv:2109.08117* **2021**.

(58) Yin, R.; Hu, C.; Lei, B.-H.; Pan, S.; Yang, Z. Lone Pair Effects on Ternary Infrared Nonlinear Optical Materials. *Physical Chemistry Chemical Physics* **2019**, *21* (9), 5142–5147.

(59) Mohn, C. E.; Stølen, S. Influence of the Stereochemically Active Bismuth Lone Pair Structure on Ferroelectricity and Photocalytic Activity of Aurivillius Phase Bi 2 WO 6. *Physical Review B* **2011**, *83* (1), 014103.

(60) Orr, M.; Hebberd, G. R.; McCabe, E. E.; Macaluso, R. T. Structural Diversity of Rare-Earth Oxychalcogenides. *ACS Omega* **2022**.

(61) Kageyama, H.; Hayashi, K.; Maeda, K.; Attfield, J. P.; Hiroi, Z.; Rondinelli, J. M.; Poeppelmeier, K. R. Expanding Frontiers in Materials Chemistry and Physics with Multiple Anions. *Nature communications* **2018**, *9* (1), 1–15.

(62) Li, Q. H.; Gao, T.; Wang, T. H. Optoelectronic Characteristics of Single CdS Nanobelts. *Applied Physics Letters* **2005**, *86* (19), 193109.

(63) Gao, T.; Li, Q. H.; Wang, T. H. CdS Nanobelts as Photoconductors. *Applied Physics Letters* **2005**, *86* (17), 173105.

(64) Dong, L.; Jiao, J.; Coulter, M.; Love, L. Catalytic Growth of CdS Nanobelts and Nanowires on Tungsten Substrates. *Chemical Physics Letters* **2003**, *376* (5–6), 653–658.

(65) Gao, T.; Wang, T. Catalyst-Assisted Vapor− Liquid− Solid Growth of Single-Crystal Cds Nanobelts and Their Luminescence Properties. *The Journal of Physical Chemistry B* **2004**, *108* (52), 20045–20049.

(66) Wang, S.; Huang, B.; Wang, Z.; Liu, Y.; Wei, W.; Qin, X.; Zhang, X.; Dai, Y. A New Photocatalyst: Bi 2 TiO 4 F 2 Nanoflakes Synthesized by a Hydrothermal Method. *Dalton Transactions* **2011**, *40* (47), 12670–12675.

(67) Uosaki, K.; Kita, H. Effects of the Helmholtz Layer Capacitance on the Potential Distribution at Semiconductor/Electrolyte Interface and the Linearity of the Mott-Schottky Plot. *Journal of The Electrochemical Society* **1983**, *130* (4), 895–897.

(68) Boumaza, S.; Boudjellal, L.; Brahimi, R.; Belhadi, A.; Trari, M. Synthesis by Citrates Sol-Gel Method and Characterization of the Perovskite LaFeO 3: Application to Oxygen Photo-Production. *Journal of Sol-Gel Science and Technology* **2020**, *94*, 486–492.

Appendix 2

2.1. Photocurrent results plots obtained for different photocurrent protocols

2.1.1. Protocol 1: Drop Casting (DMF) in (Na_2SO_4) electrolyte

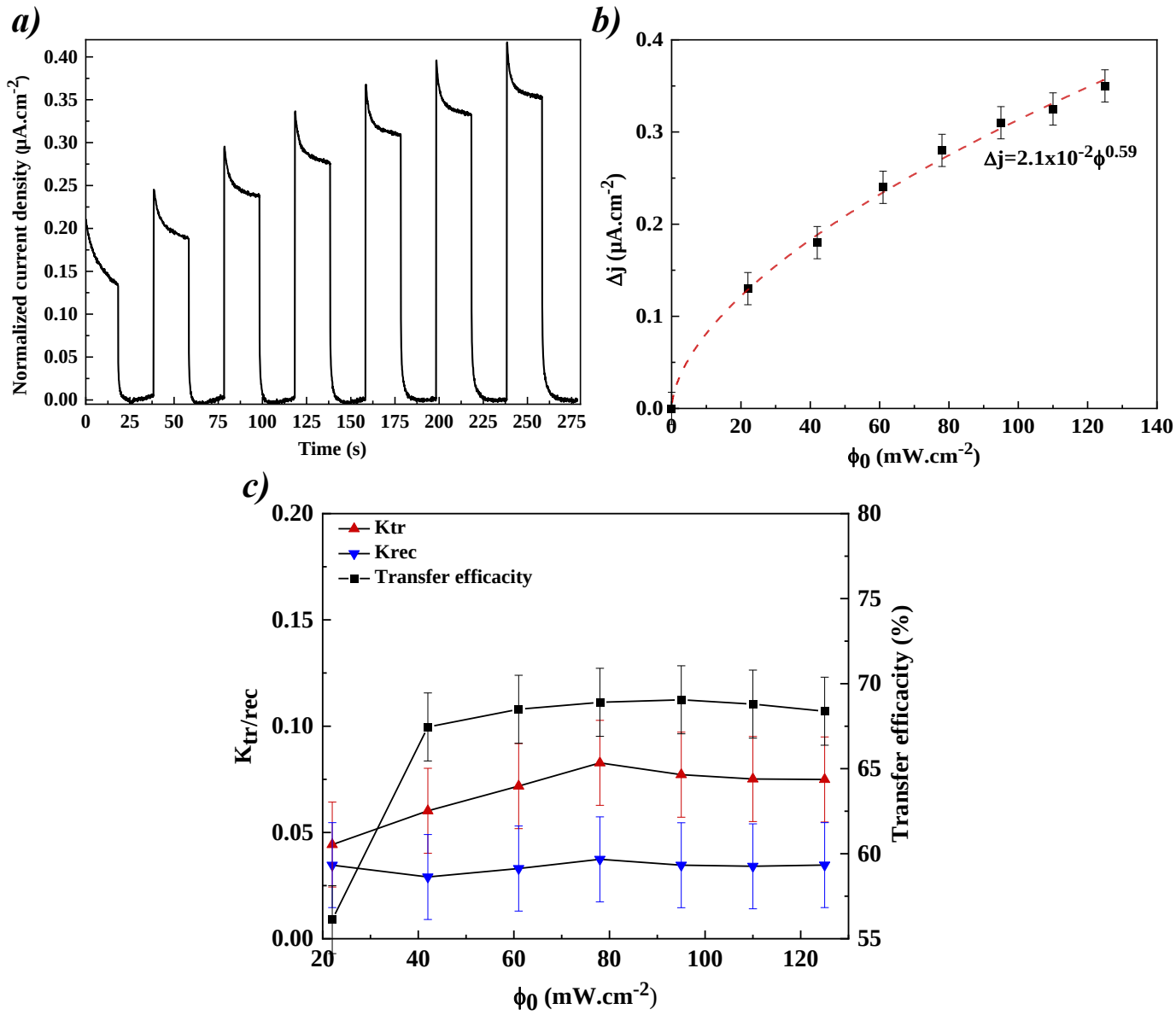

Figure 2.1 : (a) Transient photocurrent response for $Sr_6Cd_2Sb_6S_{10}O_7$ with V_{bias}=0.6 V under a 450 nm excitation, (b) evolution of the photocurrent density the power density of light and (c) evolution of the recombination and transfer rate constants k_{tr} and k_{rec} with intensity of light alongside the transfer efficacity η_k by intensity light.

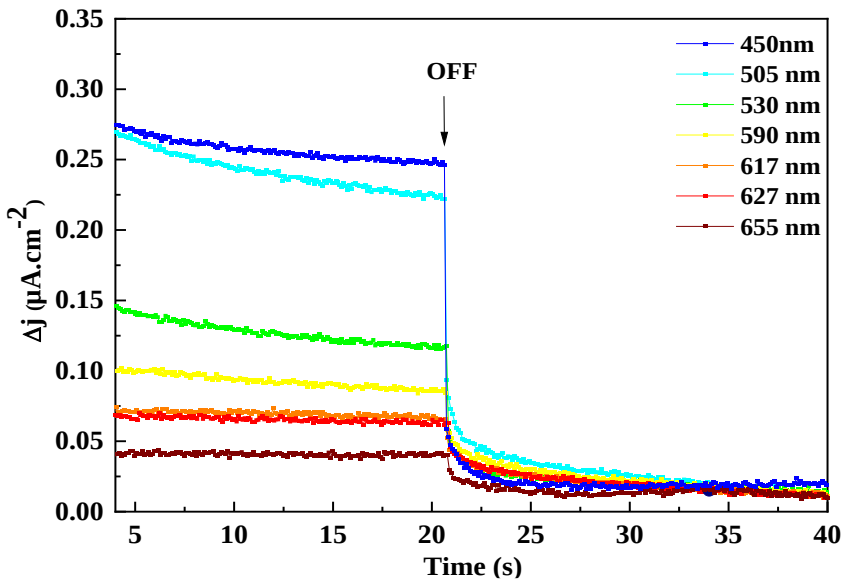

Figure 2.2 : Evolution of the photocurrent density the power density of light of $Sr_6Cd_2Sb_6S_{10}O_7$ for bias voltage of 0.6 V

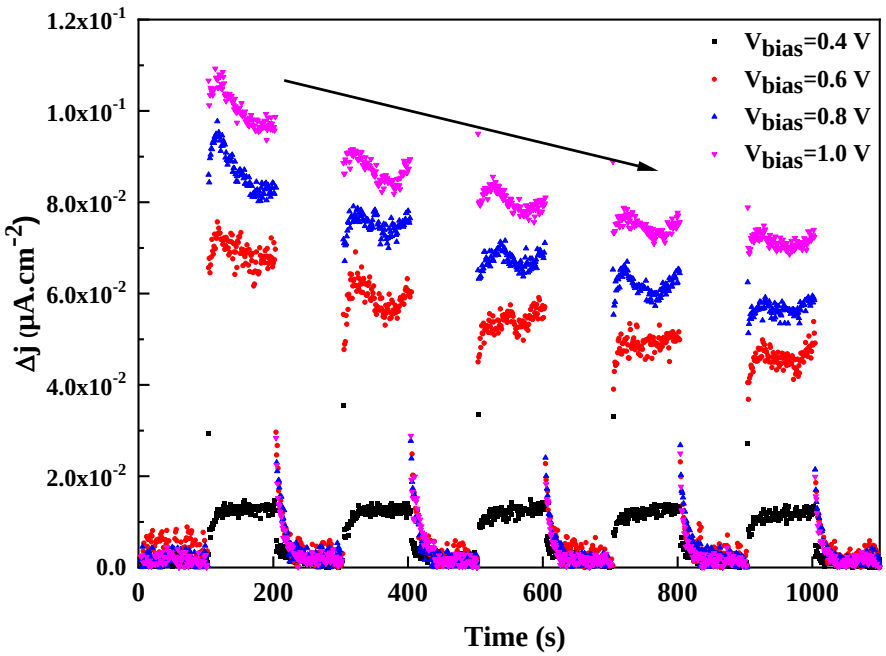

Figure 2.3 : Transient photocurrent response under solar illumination (100 mW.cm^{-2}) for V_{bias}= 0.4, 0.6, 0.8 and 1.0 V.

2.1.2. Protocol 2: Drop Casting (DMF) in ($SO_4^{2-}/SO_3^{2-}/S^{2-}$) electrolyte

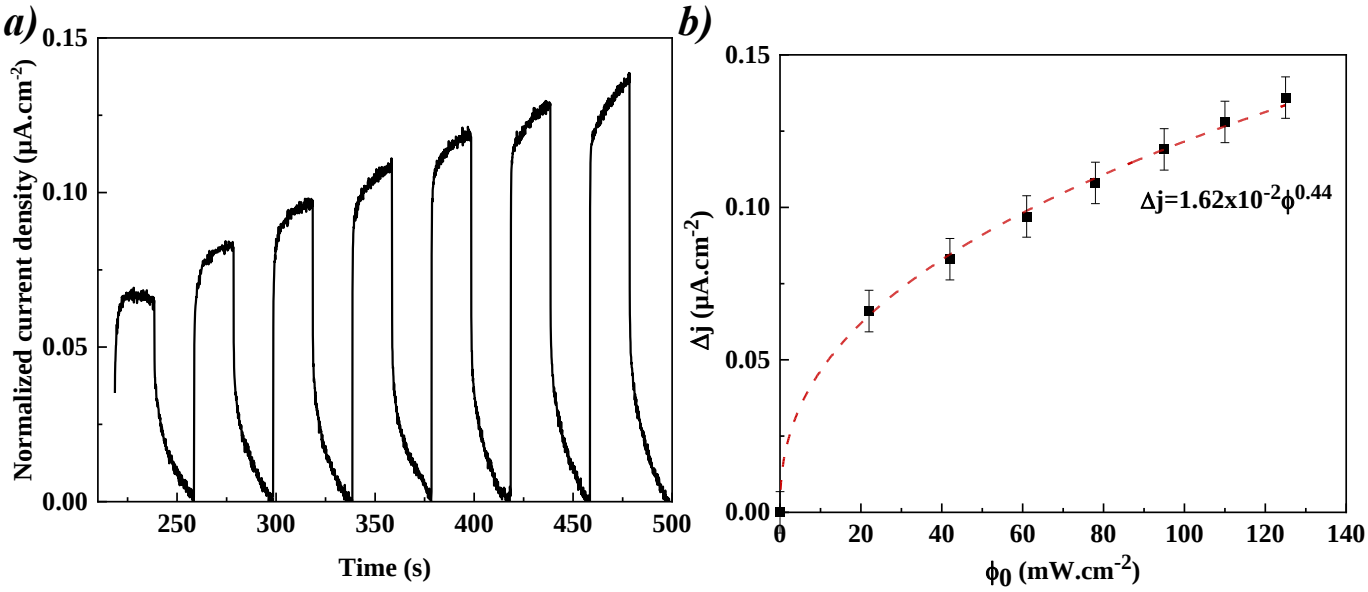

Figure 2.4 : (a) Transient photocurrent response for $Sr_6Cd_2Sb_6S_{10}O_7$ with V_{bias}=0.6 V under a 450 nm excitation and (b) evolution of the photocurrent density the power density of light.

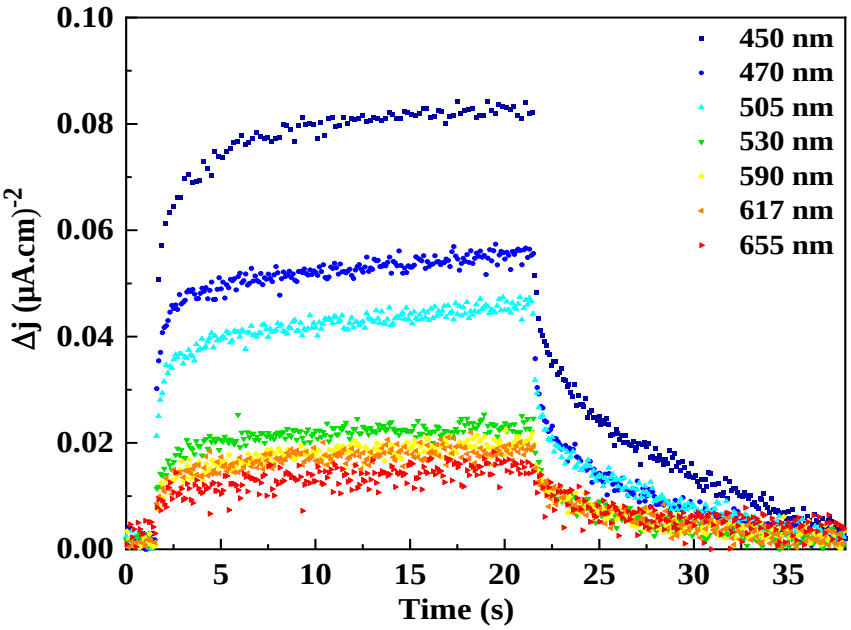

Figure 2.5 : Evolution of the photocurrent density the power density of light of $Sr_6Cd_2Sb_6S_{10}O_7$ for bias voltage of 0.6 V

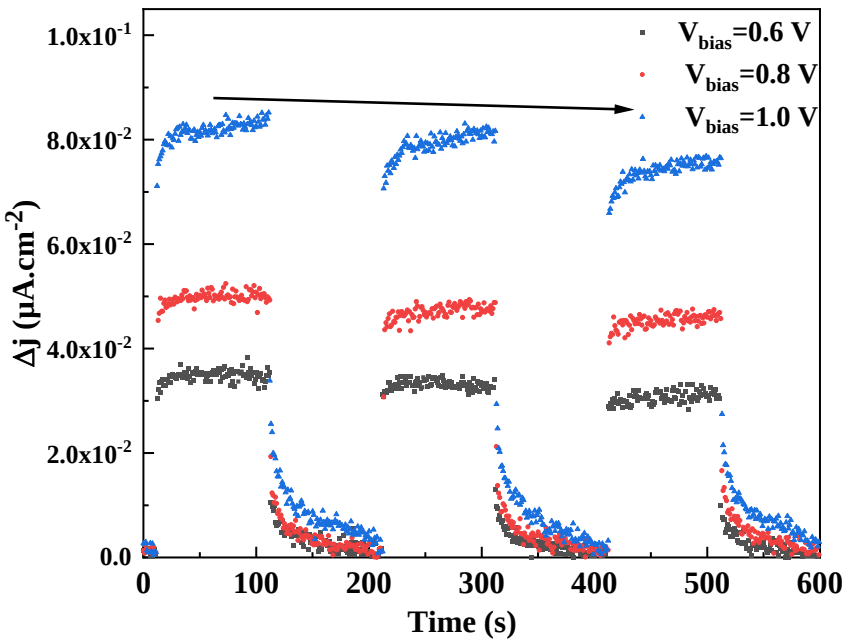

Figure 2.6 : Transient photocurrent response under solar illumination (100 mW.cm^{-2}) for V_{bias}= 0.6, 0.8 and 1.0 V.

2.2. DFT calculations for $Sr_6Cd_2Sb_6S_{10}O_7$

Table 2.1. Atomic positions of the optimized supercell $a\times2b\times c$ structure of $Sr_6Cd_2Sb_6S_{10}O_7$ given here for *P*1 (the space group of the supercell is *Pc*). Optimized cell parameters are a = 19.2631 Å, b = 8.10615 Å, c = 10.1812 Å, β = 115.26° and V= 1437.77 Å^3.

Atom	Wyckoff site	*x/a*	*y/b*	*z/c*
Sb1	*1a*	0.39384	0.00021	0.03020
Sb2	*1a*	0.89384	0.24979	0.03020
Sb3	*1a*	0.39356	0.49981	0.03007
Sb4	*1a*	0.89356	0.75020	0.03007
Sb5	*1a*	0.30024	0.00055	0.58288
Sb6	*1a*	0.80024	0.24945	0.58288
Sb7	*1a*	0.30110	0.49951	0.58275
Sb8	*1a*	0.80110	0.75049	0.58275
Sb9	*1a*	0.47983	0.01058	0.52718
Sb10	*1a*	0.97983	0.23942	0.52718
Sb11	*1a*	0.47983	0.48938	0.52712
Sb12	*1a*	0.97983	0.76062	0.52712
Sr1	*1a*	0.68064	-0.00224	0.72998
Sr2	*1a*	0.18064	0.25224	0.72998
Sr3	*1a*	0.68075	0.50224	0.72993
Sr4	*1a*	0.18075	0.74776	0.72993

Sr5	*1a*	0.53344	0.25010	0.85904
Sr6	*1a*	0.03344	-0.00010	0.85904
Sr7	*1a*	0.53860	0.74988	0.88701
Sr8	*1a*	0.03860	0.50012	0.88701
Sr9	*1a*	0.59223	0.25007	0.35837
Sr10	*1a*	0.09223	-0.00007	0.35837
Sr11	*1a*	0.59267	0.74992	0.35457
Sr12	*1a*	0.09267	0.50008	0.35457
Cd1	*1a*	0.25844	0.24841	0.15751
Cd2	*1a*	0.75845	0.00159	0.15751
Cd3	*1a*	0.25938	0.75156	0.15867
Cd4	*1a*	0.075938	0.49844	0.15867
S1	*1a*	0.35986	0.25059	0.79427
S2	*1a*	0.85986	-0.00059	0.79427
S3	*1a*	0.36119	0.74940	0.79546
S4	*1a*	0.86119	0.50060	0.79546
S5	*1a*	0.40576	0.24907	0.21362
S6	*1a*	0.90576	0.00093	0.21362
S7	*1a*	0.40692	0.75083	0.21076
S8	*1a*	0.90692	0.49917	0.21076
S9	*1a*	0.53255	0.00659	0.09505
S10	*1a*	0.03255	0.24341	0.09505
S11	*1a*	0.53256	0.49344	0.09531
S12	*1a*	0.03256	0.75656	0.09531
S13	*1a*	0.20704	-0.00036	0.98480
S14	*1a*	0.70704	0.25036	0.98480
S15	*1a*	0.21073	0.50038	0.98989
S16	*1a*	0.71073	0.74962	0.98989
S17	*1a*	0.23221	0.24973	0.38208
S18	*1a*	0.73221	0.00027	0.38208
S19	*1a*	0.23265	0.75028	0.38256
S20	*1a*	0.73265	0.49972	0.38256
O1	*1a*	0.56741	-0.00308	0.47685
O2	*1a*	0.06741	0.25308	0.47685
O3	*1a*	0.56740	0.50307	0.47678
O4	*1a*	0.06740	0.74693	0.47678
O5	*1a*	0.20619	-0.00008	0.61344
O6	*1a*	0.70619	0.25008	0.61344
O7	*1a*	0.20665	0.50009	0.61204
O8	*1a*	0.70665	0.74991	0.61204
O9	*1a*	0.54554	-0.02642	0.73671
O10	*1a*	0.04554	0.27642	0.73671
O11	*1a*	0.54549	0.52645	0.73656
O12	*1a*	0.04549	0.72355	0.73656
O13	*1a*	0.49246	0.25002	0.58319
O14	*1a*	0.99246	-0.00002	0.58319

Chapter 5

Investigating the Photocatalytic and Photocurrent Responses of $Sr_2Sb_2O_2Q_3$ (Q = S, Se) oxychalcogenides exhibiting very low charge carriers' effective masses

Chapter 5: Investigating the Photocatalytic and Photocurrent Responses of $Sr_2Sb_2O_2Q_3$ (Q = S, Se) oxychalcogenides exhibiting very low charge carrier effective masses

5.1. Introduction

In the previous two chapters, we discussed two different cation choices (transition metals in **Chapter 3** and lone pair cations in **Chapter 4**) in oxychalcogenides and investigated their potential as photocatalysts for water-splitting. After these two studies, some key features in designing efficient materials for photocatalysis were unlocked: i) polarity (units or structure) is favourable for fast electron-holes separation and ii) the contribution of the lone pair orbitals to the density of states results in more suitable band gap for solar water-splitting compared with transition metals. Therefore, in the following chapter, our investigation on lone pair-based systems continued, in particular $Sr_2Sb_2O_2Q_3$ (Q = S, Se) oxychalcogenides, with different composition and structural features to the one previously discussed. $Sr_6Cd_2Sb_6O_7Q_{10}$ (Q = S, Se) oxychalcogenides[1,2] are characterized by the presence of the highly oriented $^1{}_\infty[CdQ_3]^{4-}$ chains, in addition reports suggested that these units can act as charge reservoirs.[2] On the other hand, $Sr_2Sb_2O_2Q_3$ (Q = S, Se) systems don't show this characteristic and to that end, these phases were studied, specifically to further investigate the impact of the CdQ units on the photocatalytic properties.

5.1.1. Chalcogenide choice

Due to the different electronegativities of chalcogenide (S^{2-} and Se^{2-}) compared to the oxide, it is possible to tune the band gap magnitude to match the solar spectrum.[3] In addition to the various properties the layered oxychalcogenide family may exhibit;[4,5] depending on the judicious choice of ions, these materials can contain heteroleptic (O^{2-} and Q^{2-}) coordination environments that are often polar. This can impact the e^-/h^+ separation, giving better photocatalytic performance.[6,2,7]

5.1.2. Charge carriers' mobility

Another important feature for photocatalysis is the charge carriers' dynamics, their effective masses thus their mobility; which can have an impact on the semiconductor performance.[8,9] For example, oxides with a difference in their charge carriers effective masses exhibit a difference in character between the VB and the CB;[10] as the VB tends to be flat because of the localized oxygen *p* character, therefore large effective masses, whilst the CB is more dispersive because of the contribution of cations, giving low electron effective masses.[11,12] In a typical post-transition metal-based oxide semiconductor with low electron and hole effective masses, the CBM is highly dispersed because of the unoccupied *s* orbitals of the post-transition metal and the orbitals of the neighboring cations overlapping;[13] whilst the VBM is dispersed due to the interaction of the occupied post transition metal 5*s*/3*d* orbitals with anion *p* orbitals.[14,15,16,17] On the other hand, a recent study on tin oxyselenide demonstrated that the higher VBM dispersion can be due to the delocalized O 2*p* orbitals hybridizing with Se 4*p* and Sn 5*s* orbitals leading to enhanced carrier mobility; $SnSe_xO_{1-x}$ (m_h*= 0.58, 0.93, 1.99 for x = 0.22, 0.56 and 0.74 respectively).[18] Whilst for oxysulfides, such as tetragonal-ZrOS (0.24 m_0) and cubic-ZrOS (0.37 m_0), the highly dispersed CBM consisted of the Zr 4*d* orbitals forming an antibonding state with O 2*p* orbitals and the shallower VBM consisted of the S 3*p* orbitals varying depending on the S-S separation.[19]

5.1.3. $Sr_2Sb_2O_2Q_3$ (*Q* = S, Se) oxychalcogenides

This chapter focuses on the new oxysulfide $Sr_2Sb_2O_2S_3$, isostructural to the previously reported oxyselenide $Sr_2Sb_2O_2Se_3$.[20] Both contain heteroleptic $SbOQ_4$ units with stereochemically-active $5s^2$ electron pairs, similar to $Sr_6Cd_2Sb_6O_7Q_{10}$ (*Q* = S, Se). The low-dimensional structure of the antimony oxyselenide alongside two other composition ($Sr_2O_2Bi_2Se_3$, $Ba_2O_2Bi_2Se_3$) was determined by Panella *et al*[20] from X-ray powder diffraction data, and it was found to crystallize in the non-polar space group $P2_1/c$ (a = 9.4243(1) Å, b = 4.05708(5) Å, c = 13.3415(1) Å and β = 121.9549(7) °) for $Sr_2Sb_2O_2Se_3$. The structure is shown in **Figure 5.1** and it consists of double chains of edge-linked $SbSe_4O$ square-based pyramids, arranged in ribbons along the *b* direction; which are connected to each other by apically bonded oxygen atoms in the SrO units. As highlighted by the red dotted square in **Figure 5.1**, within a strip of square pyramids, one row of the $SbSe_4O$ points up while the neighboring unit points down. Looking through literature, very little characterization has been reported for the $A_2O_2B_2Se_3$ series. Temperature-dependent

resistance data revealed insulating behaviour for all three phases. Heat capacity data exhibited low energy phonon modes in the two bismuth phases compared to the antimony phase, a commonly associated feature with the presence of the bismuth lone pairs.[21]

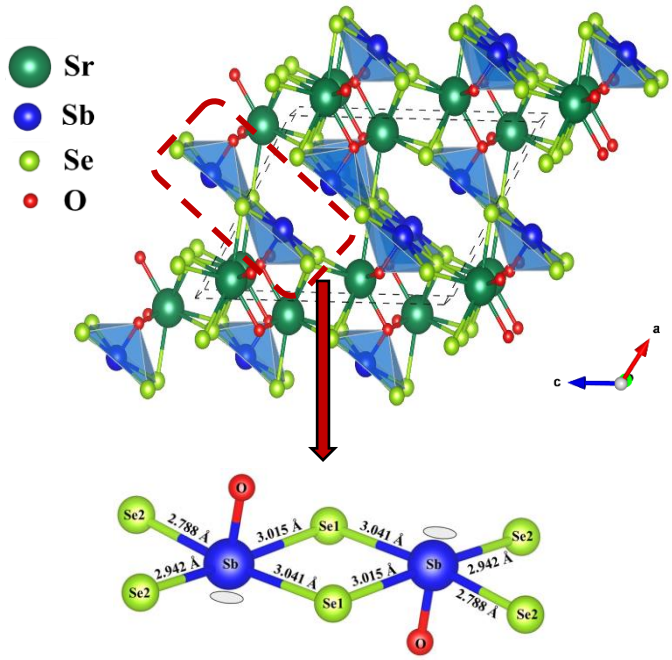

Figure 5.1 : View of the $P2_1/c$ model of $Sr_2Sb_2O_2Se_3$ reported by Panella et al.[20]

Accordingly, in the following chapter, experimental and computational studies were combined to investigate the structural and physical properties of $Sr_2Sb_2O_2Q_3$ (Q = S, Se) oxychalcogenides. By means of X-ray diffraction and electron microscopy, the intriguing structure of both phases was explored. Density functional theory revealed interesting charge carriers' properties and efficient role of the lone pair. The photoactivity of $Sr_2Sb_2O_2Q_3$ was studied in terms of: i) photocatalysis (degradation of Rhodamine B under UV light or under solar simulator lamp) and ii) photocurrent response with interesting activity highlighted over a wide wavelength range and solar irradiation with and without external potential. Finally, band gap values and band edge positions proved these oxychalcogenides to be promising candidates for water splitting using solar energy.

5.2. Experimental results

5.2.1. Structural details

5.2.1.1. Structure solution and description

Small single crystals of $Sr_2Sb_2O_2S_3$ were first identified by serendipity in some attempts to prepare another compound, namely $Sr_6Zn_2Sb_6O_7S_{10}$. The structure solution was carried out using XRD data obtained from a rectangular shaped orange single crystal. The unit cell parameters a = 13.048(1) Å, b = 3.9559(3) Å, c = 9.3143(6) Å and β = 122.498(4) ° and the space group $C2/m$ (No.12) were determined. Refinement was carried out with the Jana2006 program[22] based on a structure solution obtained using the charge-flipping method;[23,24] resulting in the structure of the desired $Sr_2Sb_2O_2S_3$ phase.

The structure consisted of double chains of edge-linked SbS_4O square-based pyramid separated with the Sr atoms. Although the structure is non-polar, the antimony is present in a polar coordination environment. This particular heteroleptic environment is found in other oxychalcogenides, such as $Sr_6Cd_2Sb_6S_{10}O_7$[7,1] and its oxyselenide analogue.[2]

Figure 5.2 shows the precession obtained for 3 different (*hkl*) planes from the diffraction data used for the structure solution discussed above. We noticed additional spots in the 0*kl* plane, which can be an indication of the presence of a more complex structure (modulation). Electron diffraction TEM (discussed later in **Section 5.2.1.2**) was used to get more insight into the nature of the modulation. Since this modulation is not observed in the PXRD experiment (due to both the local scale of the SAED probe and the roughly stronger interaction of electrons with latter compared to X-rays), only an average structure can be proposed which we particularly used in the DFT calculations (presented in **Section 5.3.5**).

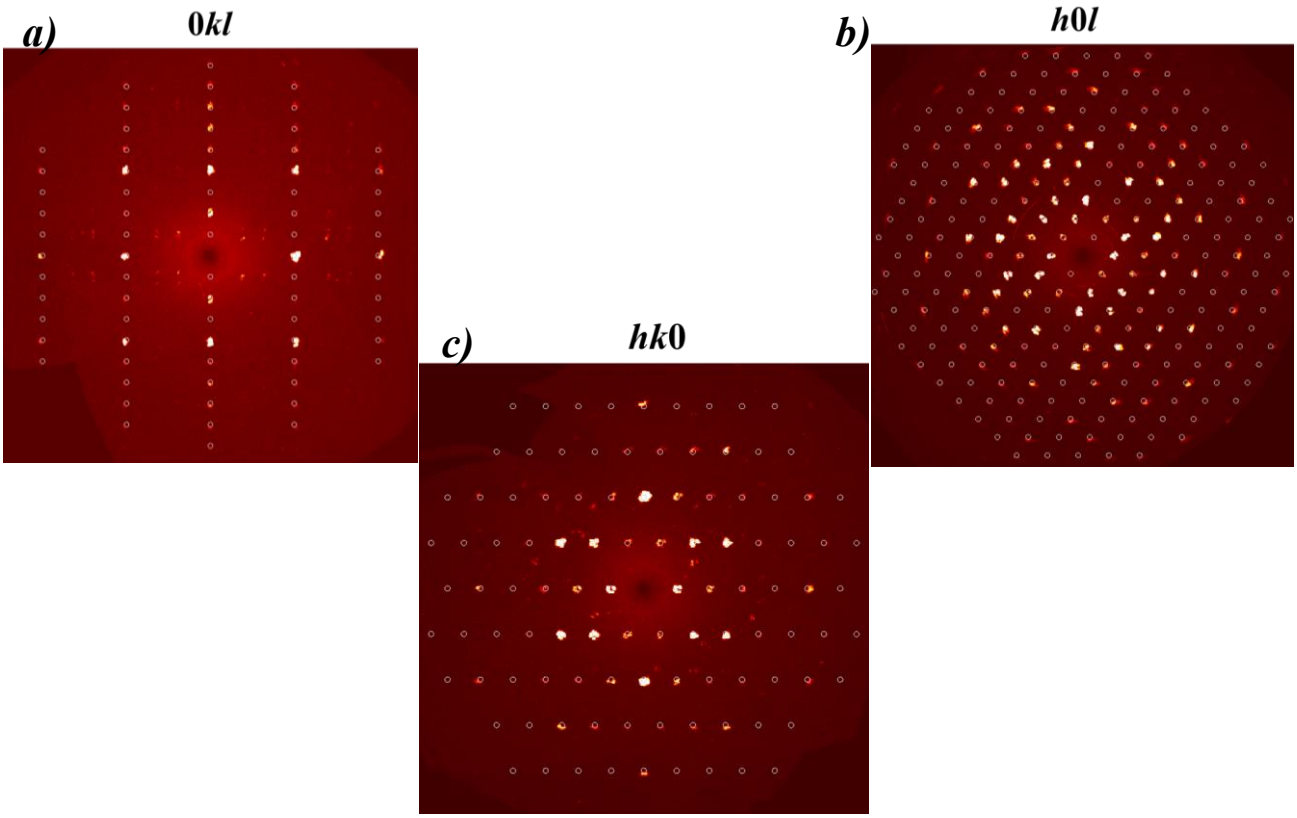

Figure 5.2 : Single-crystal XRD data collection for $Sr_2Sb_2O_2S_3$ of (a) (0*kl*) plane. (b) (*h*0*l*) plane. (c) (*hk*0) plane.

5.2.1.2. Electron microscopy

The work presented in this section was conducted in collaboration with other co-workers within the MISSP group, crystallographer Pr. Pascal Roussel and microscopist Pr. Marielle Huvé.

The commensurate approximation that we found for the $Sr_2Sb_2O_2S_3$ crystal (*C*2/*m*) is similar to the one reported for $Sr_2Sb_2O_2Se_3$ (and $A_2Bi_2O_2Se_3$ *A* = Sr, Ba) of $P2_1/c$ symmetry by Panella *et al*[20]; where the two phases exhibit the same cell but with different centering conditions. Rietveld refinements discussed later in **Section 5.2.2.1**. using the *C*2/*m* and $P2_1/c$ models gave similarly good fits to the data; giving some ambiguity as to the best description for the commensurate approximation of the crystal structure. A complementary electron diffraction study was conducted in order to clarify the dispute. For that purpose, data were collected along [100], [001] and [101] zone axes for both samples. The main spots could be indexed by a monoclinic unit cell (a≈13.05 Å b≈3.95 Å c≈9.32 Å β =122 °) for both compounds (**Figure 5.3**), which can relate to the one

reported for $Sr_2O_2Sb_2Se_3$ in the $P2_1/c$ space group[20], through the transformation matrix (001, $0\bar{1}0$, 100). However, in **Figure 5.3c**, $21\bar{2}$ and $12\bar{1}$ reflections are systematically absent which could be an indication of the better consistency of a *C*-centred model with our diffraction data, and that the actual cell is a≈13.05 Å b≈3.95 Å c≈9.32 Å β =122° with *C*-centering.

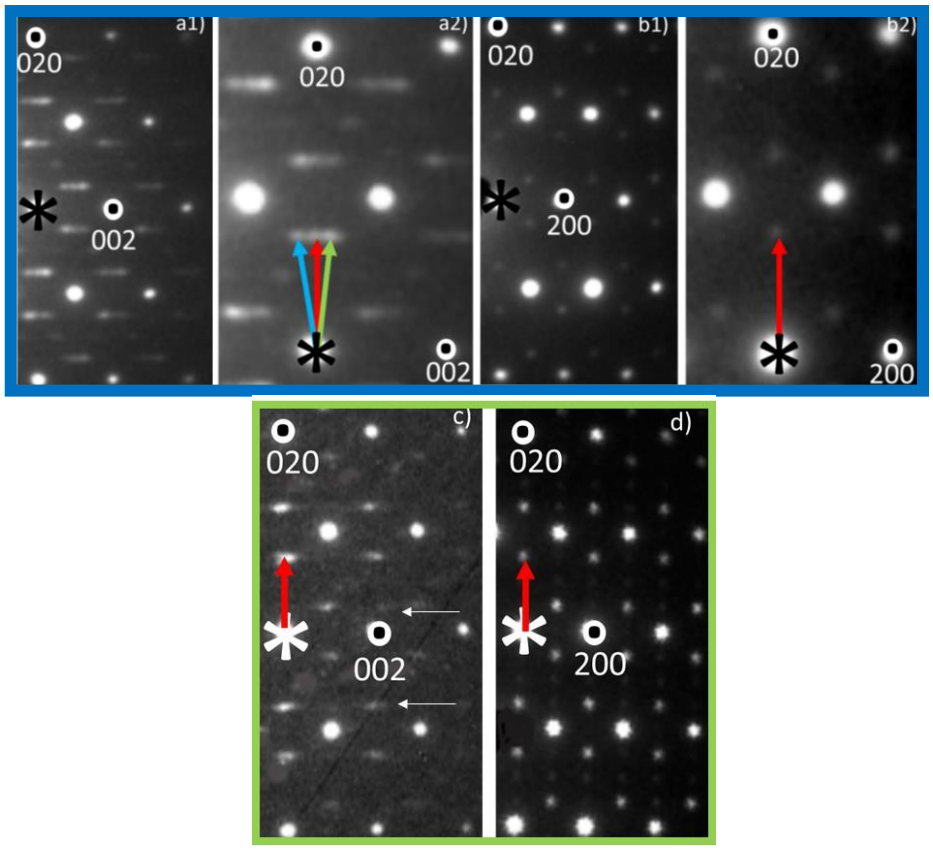

Figure 5.3 : For $Sr_2Sb_2O_2S_3$, (a1) [100] zone axis pattern and (a2) corresponding enlargement showing three modulation vectors: q_1=≈0.74b* (red), q_2≈0.74b*+ 0.28(a*+c*) (green) and q_3≈0.74b*- 0.28(a*+c*) (blue arrow). (b1) [001] zone axis pattern and (b2) corresponding enlargement confirming the modulation vector along b*. For $Sr_2Sb_2O_2Se_3$, (c) [100] zone axis pattern showing a modulation vector (q_1≈0.72b*) with a poorly defined component along a*. (d) [001] zone axis pattern confirming the component of the modulation vector along b*.

Additional weak spots and streaks were also observed on certain crystallites, this made us believe that an additional ordering could be present in these phases; in particular, an incommensurate modulation of the crystal structures. Indeed, for the oxysulfide phase (blue box), additional spots can be indexed by an incommensurate modulation vector q_1≈0.74b*, as highlighted on the [100], [001] and [101] zone axis patterns (ZAP) (red arrows) in **Figure 5.3a** and **5.3b**. In

addition, two other modulation vectors were also indexed q_2=0.74b*+0.279(a*+c*) and q_3=0.74b*-0.279(a*+c*) (blue and green arrows) in the same lattice which can indicate the possibility of slightly different orders from one domain to the other. Alternately for the oxyselenide phase (green box), the component along *a** is weak and is represented by a deformation of the round spots into oval, shown in white arrows in **Figure 5.3c**. This suggests smaller incommensurate modulation away from the commensurate structure which might explain why early reports on the oxyselenide phases did not mention it.[20] In summary, this electron diffraction study shows that:

- The actual space group is probably *C*2/*m* and not $P2_1/c$ (extinction of the $21\bar{2}$ and $12\bar{1}$ spots)
- The actual structure is more complex than the average structure reported one on the oxyselenide analogue[20] (additional orders can co-exist in the phase).

5.2.2. Synthesis and preliminary characterization

5.2.2.1. Synthesis and polycrystalline phase analysis

Single-phase samples of $Sr_2Sb_2O_2Q_3$ (*Q* = S, Se) (1 g) were synthesized by solid-state reaction from stoichiometric mixtures of the precursors: SrS/Sb_2O_3/Sb/S (Alfa Aesar 99.5%) in the molar ratio 2:0.667:0.667:1 for the oxysulfide and SrO/Sb/Se (Alfa Aesar 99.5%) in the molar ratio 2:2:3 for the oxyselenide. Thermal treatment consisted on heating up to 700 °C and 800 °C for $Sr_2Sb_2O_2S_3$ and $Sr_2Sb_2O_2Se_3$, respectively at a rate of 70 °C/h and dwelling for 48 h before cooling down to room temperature. Upon grinding the pellets, orange and black powders were obtained for the oxysulfide and the oxyselenide, respectively (**Figure 5.4**).

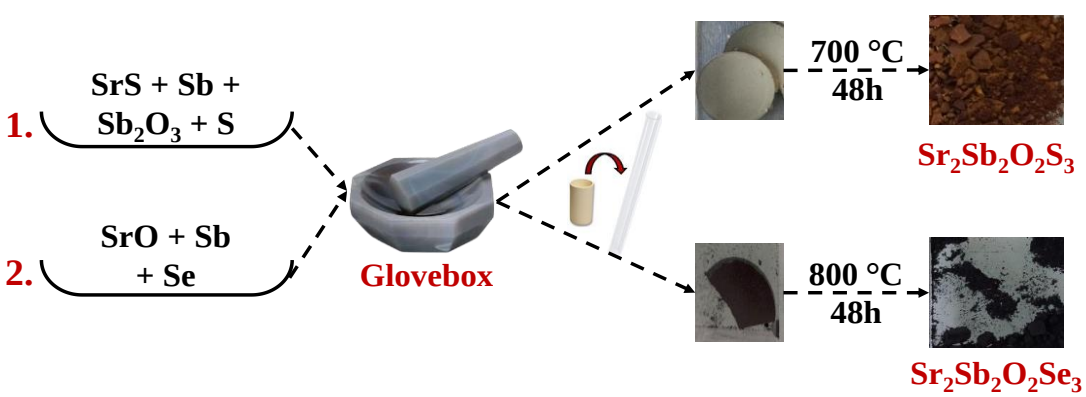

Figure 5.4 : Schematic diagram of the solid-state synthesis of $Sr_2Sb_2O_2Q_3$ (*Q* = S, Se) oxychalcogenides.

High-purity samples were obtained. Single crystals were detected in both preparations, and using EDX analysis the expected stoichiometry for both compositions was confirmed (**Figure 5.5**) and revealed the atomic ratios of the Sr, Sb and S/Se contents (**Table 5.1**).

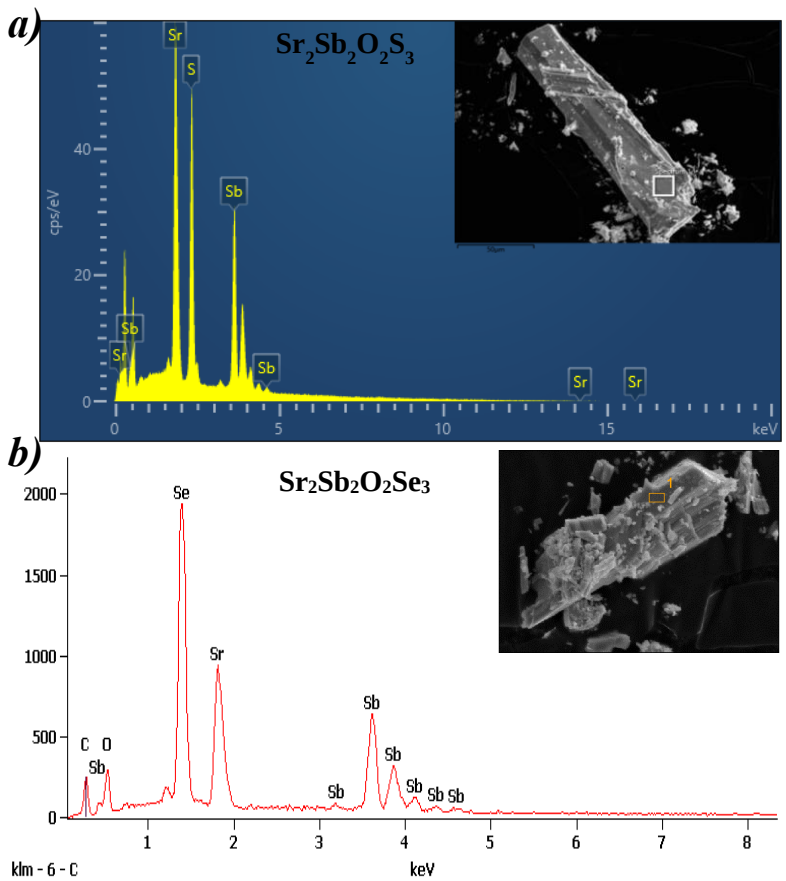

Figure 5.5 : Spectrum of the EDX analysis for crystals of (a) $Sr_2Sb_2O_2S_3$ and (b) $Sr_2Sb_2O_2Se_3$.

Table 5.1. Atomic ratios of the Sr, Sb and S/Se content in $Sr_2Sb_2O_2Q_3$ (Q =S, Se) crystals.

Phase	Sr	Sb	S/Se
Stoichiometric ratio	28.7	28.7	42.6
$Sr_2Sb_2O_2S_3$	28.3(1)	29.0(1)	42.7(1)
$Sr_2Sb_2O_2Se_3$	28.47(1)	28.99(2)	42.54(2)

Rietveld refinements were carried out in different symmetry models ($P2_1/c$, $C2/m$, $C2$ and Cm) using Fullprof software.[25] The background, sample height, lattice parameters, peak profiles, atomic positions and a global atomic displacement parameter (per phase) were refined, which demonstrated the high quality of the prepared samples. Note that preferred orientation was observed in some data, which could be a result of the samples' preparation method, but we dealt with it using a March-Dollase function along the (010) direction;[26] and all sites were constrained in order to have same atomic displacement parameters. Preliminary XRPD data for $Sr_2Sb_2O_2S_3$ indicated a model consistent with the previously reported Se analogue, $Sr_2Sb_2O_2Se_3$,[20] in the $P2_1/c$ space group with, as expected, a slightly smaller unit cell volume (room temperature volume = 405.07(2) Å^3, compared with 432.81 Å^3 for $Sr_2Sb_2O_2Se_3$) (**Figure 5.6** and **Tables 5.2-5.3**). Similarly, refinements using XRPD data for $Sr_2Sb_2O_2Se_3$ confirmed that a good quality sample had been prepared (**Figure 5.7** and **Tables 5.4-5.5**).

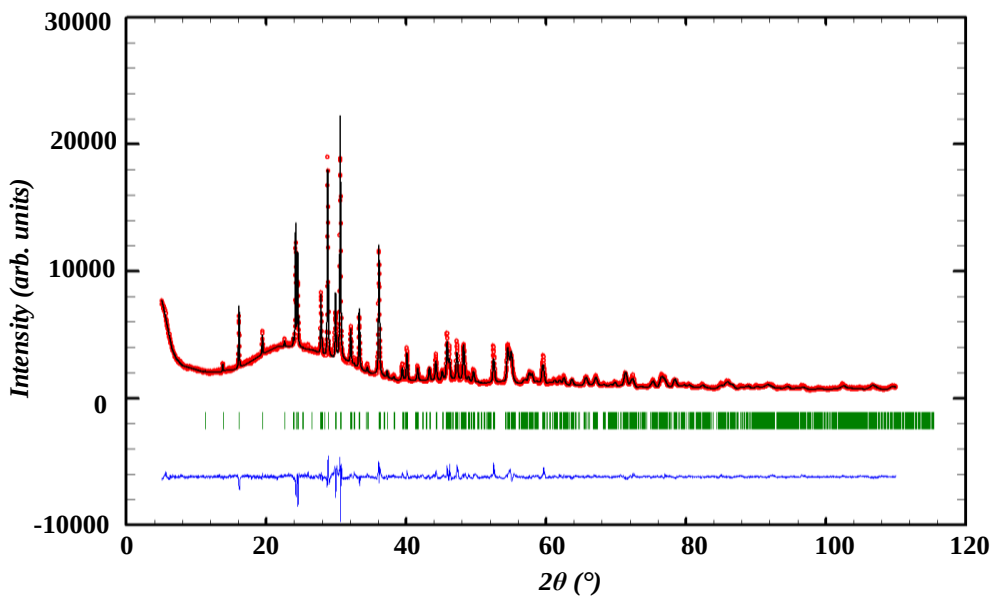

Figure 5.6 : Rietveld refinement profiles for $Sr_2Sb_2O_2S_3$ in the $P2_1/c$ space group: the experimental (red) and the calculated (black) patterns are superimposed; the difference curve is represented in blue and Bragg positions in green. A March-Dollase function was used to model preferred orientation along the <010> direction.

Table 5.2. Refinement details from Rietveld refinement using lab XRPD data for $Sr_2O_2Sb_2S_3$ using $P2_1/c$ model; a = 9.3142(2) Å, b = 3.9547(1) Å, c = 13.0417(3) Å, β = 122.519(1) °, V = 405.04(1) Å^3, R_p = 4.85 %, R_{wp} = 6.56 %, R_{exp} = 2.40, R_f = 7.31, χ^2 = 7.46.

Atom	Wyckoff site	*x*	*y*	*z*	U_{iso} (Å^2)
Sr	*4e*	0.3859(4)	0.002(3)	0.0947(3)	0.0011(5)
Sb	*4e*	0.1441(4)	-0.010(2)	0.7057(3)	0.0011(5)
S1	*4e*	0.312(1)	0.067(3)	0.3792(7)	0.0011(5)
S2	*2a*	0	0	0	0.0011(5)
O	*4e*	0.352(2)	0.045(9)	0.678(1)	0.0011(5)

Table 5.3. Bond distances (Å) for $Sr_2Sb_2O_2S_3$ following the Rietveld refinement in the space group $P2_1/c$.

Atoms 1,2	$d_{1,2}$ (Å)	Atoms 1,2	$d_{1,2}$ (Å)
Sr-O	2.64(1)	Sb-S2	2.979(5)
Sr-S1	3.03(1)	Sb-S1	2.61(1)
Sr-S2	3.110(3)	S1-O	3.22(2)
Sb-O	2.16(2)	S1-S1	3.26(9)
O-O	3.08(3)	S2-O	3.35(2)

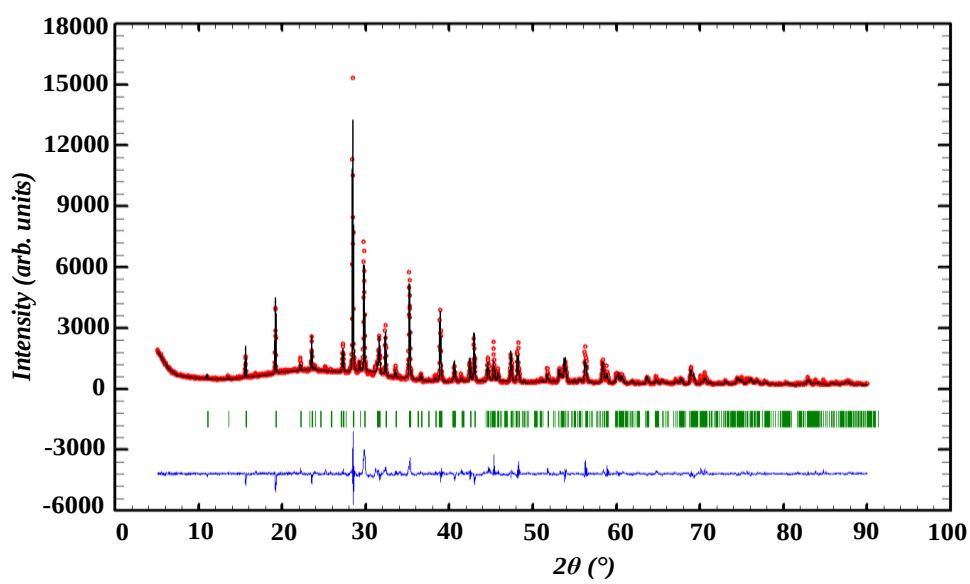

Figure 5.7 : Rietveld refinement profiles for $Sr_2Sb_2O_2Se_3$ in the $P2_1/c$ space group: the experimental (red) and the calculated (black) patterns are superimposed; the difference curve is represented in blue and Bragg positions in green. A March-Dollase function was used to model preferred orientation along the <010> direction.

Table 5.4. Refinement details from Rietveld refinement using lab XRPD data for $Sr_2O_2Sb_2Se_3$ using $P2_1/c$ model; a = 9.4253(4)Å, b = 4.0582(2) Å, c = 13.3461(5) Å, β = 121.931(1) °, volume = 433.25(3) Å^3; R_p = 9.73 %, R_{wp} = 13.1 %, R_{exp} = 4.21, R_f = 10.8, χ^2 = 9.63.

Atom	Wyckoff site	*x*	*y*	*z*	U_{iso} (Å^2)
Sr	*4e*	0.3926(6)	0.013(8)	0.1035(3)	0.0057(7)
Sb	*4e*	0.1417(5)	-0.011(5)	0.7005(4)	0.0057(7)
Se1	*4e*	0.3061(6)	0.030(5)	0.3789(4)	0.0057(7)
Se2	*2a*	0	0	0	0.0057(7)
O	*4e*	0.335(3)	0.91(3)	0.673(1)	0.0057(7)

Table 5.5. Bond distances (Å) for $Sr_2Sb_2O_2Se_3$ following the Rietveld refinement in the space group $P2_1/c$.

Atoms 1,2	$d_{1,2}$ (Å)	Atoms 1,2	$d_{1,2}$ (Å)
Sb-Se1	2.82(2)	Sb-O	2.06(3)
Sr-Se2	3.20(5)	Sr-O	2.73(2)
Sb-Se2	3.02(1)	O-O	3.35(1) ×2
Sr-Se1	3.45(2)	Se2-O	3.22(6)
Se1-Se1	3.372(5)	Se1-O	3.41(6)

Given the suggestion of a higher symmetry $C2/m$ model from electron diffraction (**Section 5.2.1.2**), ISODISTORT[27] was used to explore possible structures for $Sr_2Sb_2O_2Q_3$. The $C2/m$ symmetry model with Sr, Sb, S(1) and O on *4i* sites (x 0 z) and S(2) on the *2a* site (0 0 0) (**Figure 5.8**), is related to the $P2_1/c$ symmetry model through the transformation matrix (001, $0\bar{1}0$, 100). By using a Y_2^+ irrep, the higher symmetry model ($C2/m$) (34 parameters) can undergo a distortion involving displacement of ions along the short ≈ 4 Å axis (along [010]) to break the mirror plane *m* (half-way along the *b* axis), which can give additional degrees of freedom along [010] for Sr, Sb, S(1) and O atoms, resulting in the lower symmetry model ($P2_1/c$) (38 parameters). This primitive model has further degrees of freedom (four additional parameters), with Sr, Sb, S(1) and O on 4e sites (x y z) and S(2) on the 2a site (0 0 0).

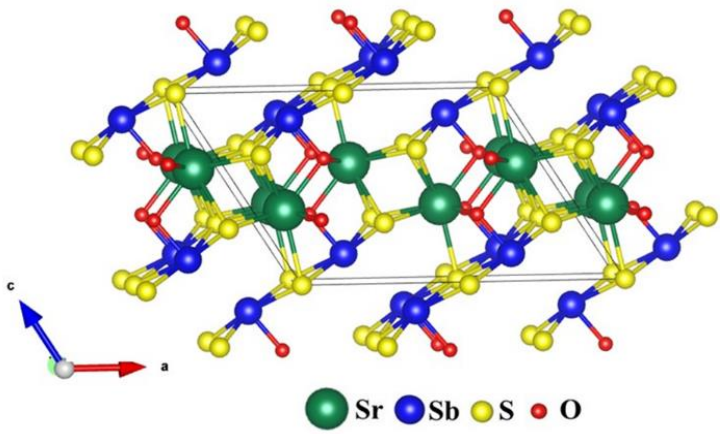

Figure 5.8 : Illustration of the model refined in *C*2/*m* symmetry for $Sr_2O_2Sb_2S_3$ with Sr, O, Sb and S ions shown in green, red, blue and yellow, respectively.

Rietveld refinements using XRPD data were also done in the *C*-centered monoclinic model (*C*2/*m*) using the cell, $a \approx 13.05$ Å, $b \approx 3.95$ Å, $c \approx 9.32$ Å and $\beta = 122$ °. **Figures 5.9, 5.10** and **Tables 5.6-5.9** confirm the good fits obtained for the collected data on both samples. Similar to the previous refinements, all sites were constrained to have same atomic displacement parameters. In the absence of additional reflections, or problems with our model, the *C*2/*m* model seems the best description to describe the commensurate approximation of the $Sr_2Sb_2S_3O_2$ structure.

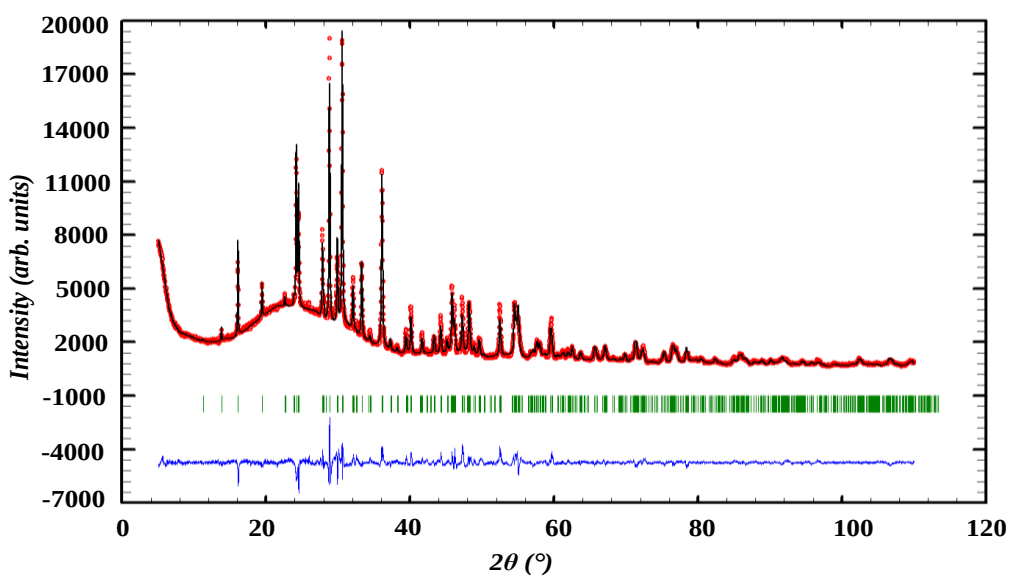

Figure 5.9 : Rietveld refinement profiles for $Sr_2O_2Sb_2S_3$ in the *C*2/*m* space group: the experimental (red) and the calculated (black) patterns are superimposed; the difference curve is represented in blue and Bragg positions in green. A March-Dollase function was used to model preferred orientation along the <010> direction.

Table 5.6. Refinement details from Rietveld refinement using lab XRPD data for $Sr_2O_2Sb_2S_3$ using *C*2/*m* model; *a* = 13.0415(3) Å, *b* = 3.9545(1) Å, *c* = 9.3136(2) Å, β = 122.520(1) °, V= 405.05(1) Å^3, R_p = 4.86 %, R_{wp} = 6.46 %, R_{exp} = 2.38, R_f = 4.82, χ^2 = 7.35.

Atom	Wyckoff site	*x*	*y*	*z*	U_{iso} (Å^2)
Sr	*4i*	0.0946(3)	0	0.3860(4)	0.0032(3)
Sb	*4i*	0.7055(3)	0	0.1442(4)	0.0032(3)
S1	*4i*	0.3778(6)	0	0.3132(9)	0.0032(3)
S2	*2a*	0	0	0	0.0032(3)
O	*4i*	0.678(1)	0	0.341(2)	0.0032(3)

Table 5.7. Bond distances (Å) for $Sr_2Sb_2O_2S_3$ following the Rietveld refinement in the space group *C*2/*m*.

Atoms 1,2	$d_{1,2}$ (Å)	Atoms 1,2	$d_{1,2}$ (Å)
Sr-O	2.40(1) ×2	Sb-S2	3.005(2) ×2
Sr-S1	3.2110(7) ×2	Sb-S1	2.763(4) ×2
Sr-S2	3.11(3)	S1-O	3.310(1) ×2
Sb-O	2.05(2)	O-O	3.20(1) ×2
S1-S1	3.216(7)	S2-O	3.39(1) ×2

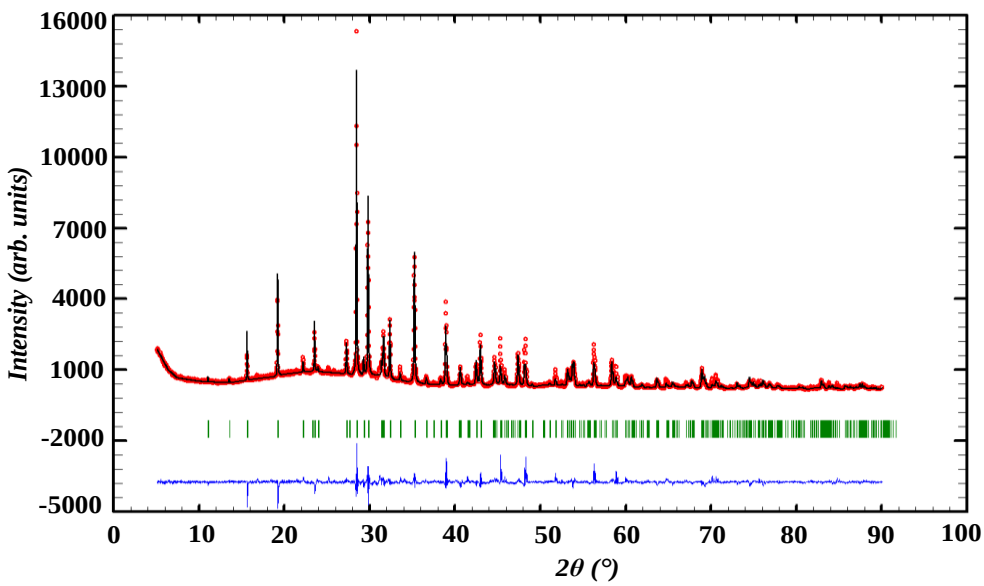

Figure 5.10 : Rietveld refinement profiles for $Sr_2O_2Sb_2Se_3$ in the *C*2/*m* space group: the experimental (red) and the calculated (black) patterns are superimposed; the difference curve is represented in blue and Bragg positions in green. A March-Dollase function was used to model preferred orientation along the <010> direction.

Table 5.8. Refinement details from Rietveld refinement using lab XRPD data for $Sr_2O_2Sb_2Se_3$ using *C*2/*m* model; *a* = 13.3436(3)Å, *b* = 4.0562(1) Å, *c* = 9.4224(2) Å, β = 121.932(1) °, volume = 432.81(2) Å^3; R_p = 8.50 %, R_{wp} = 11.7 %, R_{exp} = 4.27, R_f = 9.83, χ^2 = 9.49.

Atom	Wyckoff site	*x*	*Y*	*Z*	U_{iso} (Å^2)
Sr	*4i*	0.1024(4)	0	0.3908(6)	0.0031(7)
Sb	*4i*	0.7009(4)	0	0.1424(5)	0.0031(7)
Se1	*4i*	0.3803(4)	0	0.3077(6)	0.0031(7)
Se2	*2a*	0	0	0	0.0031(7)
O	*4i*	0.674(1)	0	0.351(3)	0.0031(7)

Table 5.9. Bond distances (Å) for $Sr_2Sb_2O_2Se_3$ following the Rietveld refinement in the space group *C2/m.*

Atoms 1,2	$d_{1,2}$ (Å)	Atoms 1,2	$d_{1,2}$ (Å)
Sr-O	2.35(1) ×2	Sb-Se1	2.885(4) ×2
Sb-O	2.18(3)	Sb-Se2	3.049(3) ×2
Sr-Se2	3.179(5)	O-O	3.18(2) ×2
Sr-Se1	3.398(7) ×2	Se1-Se1	3.33(5)

As mentioned before, other related structures were also considered using ISODISTORT[27] such as *C*2 and *Cm* symmetry models. The refinement details for both models can be found in **Appendix 3, Section 3.1**.

5.2.2.2. Optical band gap and band edges positions

Optical properties of the polycrystalline $Sr_2Sb_2O_2S_3$ and $Sr_2Sb_2O_2Se_3$ phases were investigated by measuring the reflectance using UV-Visible spectroscopy. Reflectance *vs.* wavelength analysis is shown in **Figure 5.11**. The Kubelka-Munk transformation $F(R)=(1-R)^{(1/n)}/2R$[28] was applied to the reflectance and the optical band gap E_g, was determined using the Tauc plot method[29] by drawing $[F(R)h\upsilon]^{1/n}$ vs. $[h\upsilon]$ (where *hv* is the photon energy). Assuming a direct allowed transition (n = 1/2) (see the results from DFT calculation, presented below), E_g was determined to be 2.44(1) eV and 1.72(1) eV for $Sr_2Sb_2O_2S_3$ and $Sr_2Sb_2O_2Se_3$, respectively; convenient for the solar spectrum, and comparable with other reported mixed-anion materials including oxynitrides

$LaTiO_2N$ (2.1 eV),[30] $XNbO_2N$ (X= Ca, Sr, Ba, La)[31] and lone-pair containing oxyfluorides Bi_2NbO_5F (2.86 eV), Bi_2TaO_5F (2.95 eV).[32]

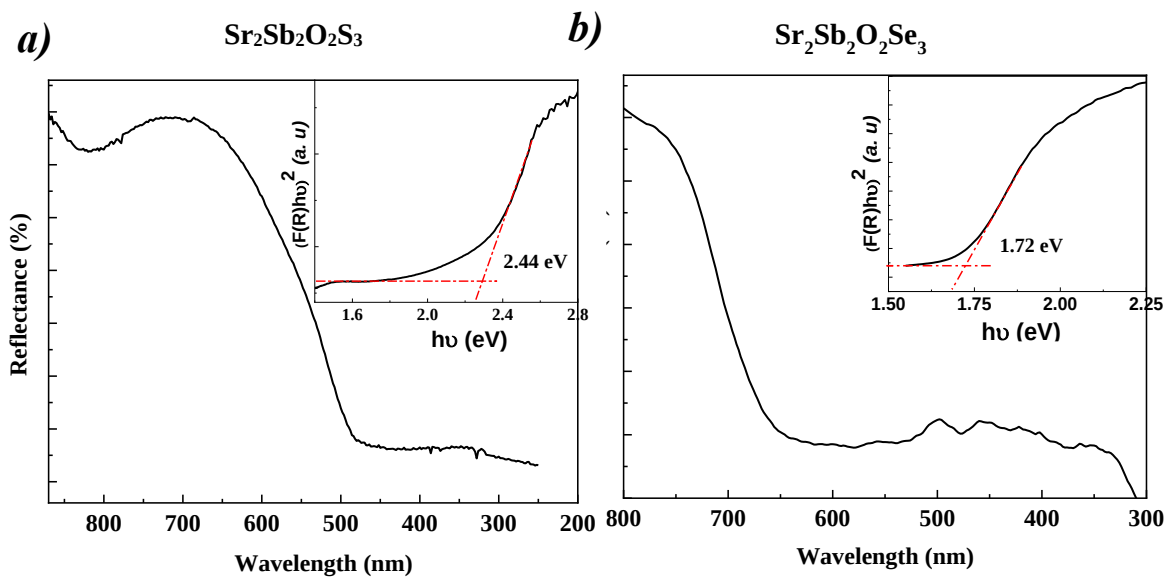

Figure 5.11 : Diffuse-reflectance spectra with a Tauc plot inset to determine the experimental band gap of a) $Sr_2Sb_2O_2S_3$ and b) $Sr_2Sb_2O_2Se_3$.

After estimating the magnitude of the band gap, we estimated the conduction and valence band edge positions (**Figure 5.12**) using the empirical method based on Mulliken electronegativities proposed by Butler and Ginley,[33] and further described by Xu and Schoonen[34] (see **Section 2.1.2.4** in **Chapter 2**). Our calculations using this method confirm that the band edges for $Sr_2Sb_2O_2S_3$ and $Sr_2Sb_2O_2Se_3$ are appropriate for the redox potential of water and are consistent with the band edge positions determined experimentally from Mott-Schottky measurements (discussed later in **Section 5.3.3.4)**.

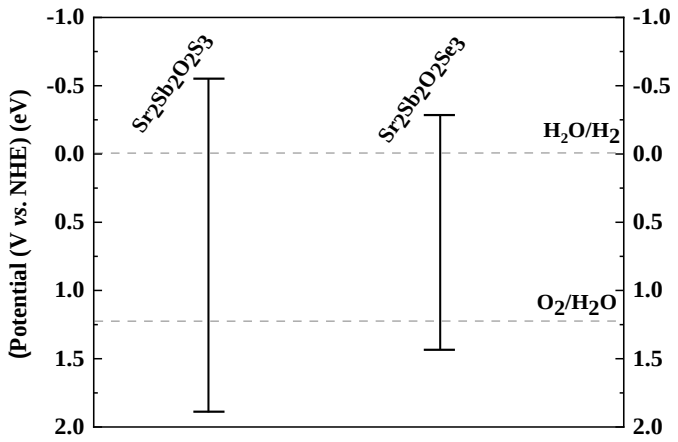

Figure 5.12 : Calculated band edges positions for $Sr_2Sb_2O_2S_3$ and $Sr_2Sb_2O_2Se_3$; The levels of H_2 and O_2 evolution are indicated by dashed lines.

5.2.2.3. Thermal analysis

Different synthesis temperatures were tried in an effort to prepare a pure sample of the oxysulfide. At 700 °C a high quality sample was obtained, but increasing the temperature by 50 °C gave a red powder, suggesting either sample decomposition or phase change.

In order to get additional information, we tried to solve the structure of the obtained red phase using the collected XRD data in Jana2006 program[22] but with the problem of peak/profile overlapping we managed to just identify the unit cell (a = 12.6542 Å, b = 17.3486 Å, c = 11.0075 Å, β = 92.405°) in the monoclinic $C2_1/c$ symmetry model. Pawley refinement gave a good fit (**Figure 5.13a**) and EDX analysis on the obtained red powder (**Figure 5.13b**) revealed a slight decrease in the sulfur content (Sb: 29.9, Sr: 29.81, S: 40.29) comparing to the stoichiometric atomic percentages (Sb: 28.7, Sr: 28.7, S: 42.6). We therefore decided to investigate its thermal stability to gain more insight into the nature of this change upon the temperature increase.

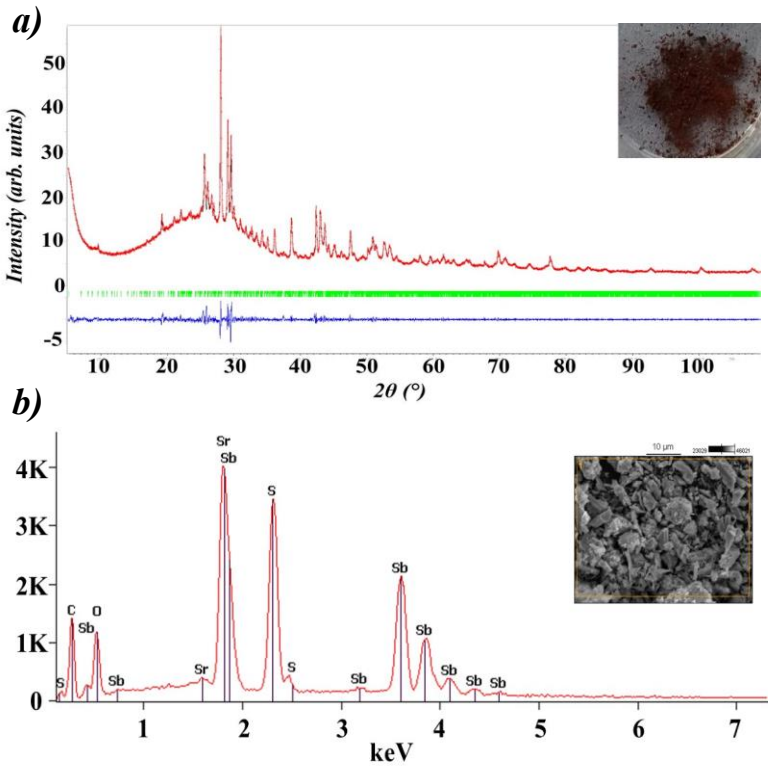

Figure 5.13 : (a) Powder XRD Pawley refinement profiles for the red powder in the $C2_1/c$ space group: the experimental (red) and the calculated (black) patterns are superimposed; the difference curve is represented in blue and Bragg positions in green. (b) Spectrum of the EDX analysis of a $Sr_2Sb_2O_2S_3$ powder annealed at 800 °C.

The thermal stability of the $Sr_2Sb_2O_2S_3$ oxysulfide was studied under argon using TGA coupled with TDA (**Figure 5.14**). The evolved gases were monitored by an Omnistar quadrupole mass spectrometer (Pfeiffer). The atmosphere was controlled by evacuating and filling the thermobalance with the carrier gas before the sample was heated to 1000 °C at a rate of 5 °C/min. $Sr_2Sb_2O_2S_3$ remained stable up to ~ 700 °C in argon and we don't observe any mass loss at ~ 600 °C that is typical of oxysulfides due to sulfur evaporation.[35] No weight loss was associated with the endothermic peak at ~ 735 °C on the TDA curve (lower panes), suggesting a phase transition at this temperature. Above 800 °C, two weight losses were detected coupled with three exothermic combined peaks indicating a phase degradation.

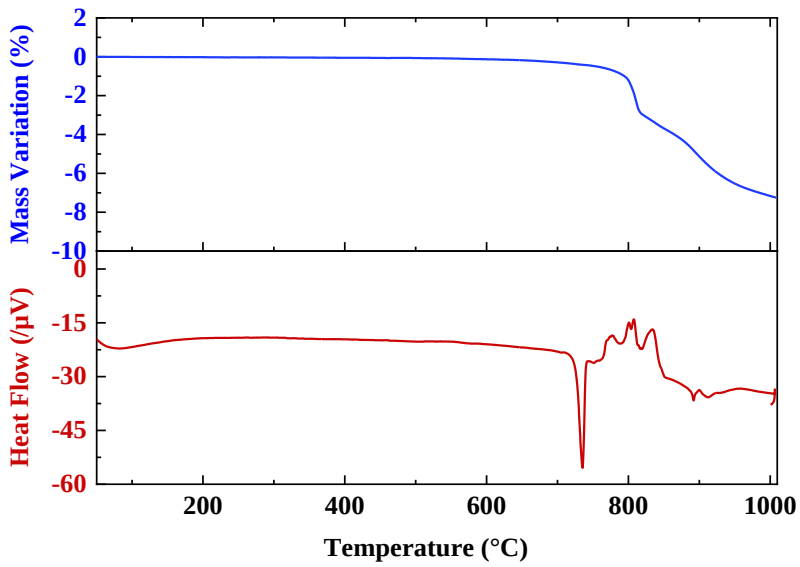

Figure 5.14 : (a) TGA (upper panes) coupled with TDA (lower panes) of $Sr_2Sb_2O_2S_3$ under argon.

To investigate possible phase degradation, TGA was coupled with MS (**Figure 5.15a**) using the same conditions (under argon, in the range 25-1000 °C). No loss of water was observed (no signal at *m/z* 18). Signals were measured (lower panes) at *m/z* 64 (SO_2^+), *m/z* 48 (SO^+) and *m/z* 44 (CO_2) allowing the evolved gases to be identified. A sharp mass loss (8.1 %) occurs at around 800 °C, close to the theoretical mass loss expected for the loss of 1 molecule of sulfur monoxide (SO) (8.8 %). This was confirmed by EDX (**Figure 5.15b**) on the residue after TGA-MS measurements where the atomic percentages corresponding to the sulfur element decreased (S: 37.70 %). One possible explanation for this is that the reducing atmosphere could favour reduction to metallic antimony and formation of oxides and sulfides of strontium (e.g. $Sr_2O_2Sb_2S_3 \rightarrow SrO(s) + SrS_2(s) + 3Sb(s) + SO(g)$).

Further structural details on the orange $Sr_2Sb_2O_2S_3$ and the red $Sr_xSb_yO_zS_u$ phases, including unit cell parameters, EDX atomic percentages, SEM images and Pawley refinement plots can be found in **Appendix 3, Section 3.2**.

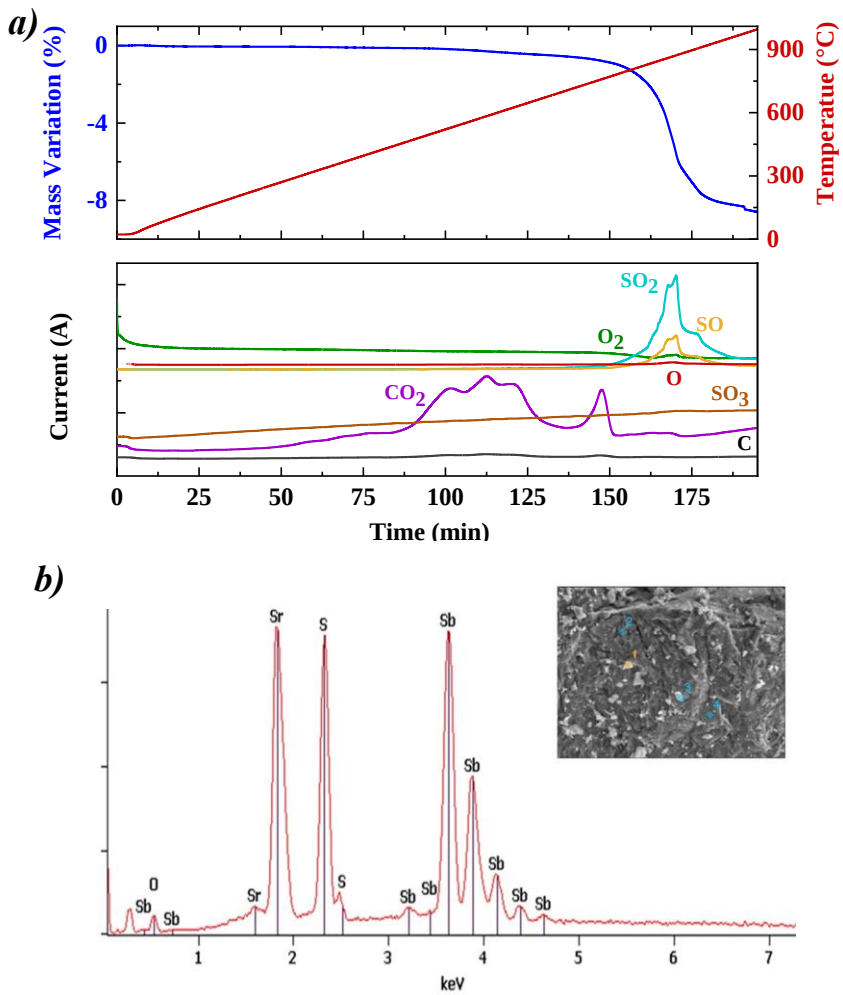

Figure 5.15 : (a) TGA (upper pane) coupled with mass spectrometry (lower panes) of $Sr_2Sb_2O_2S_3$ under argon. (b) Spectrum of the EDX analysis of a $Sr_2Sb_2O_2S_3$ TGA residue.

5.2.3. Photocurrent measurements

5.2.3.1. Reproducibility measurements

The electrochemical measurements were performed using the setup and protocol described in **Chapter 2**. The variation in the current density Δj as the difference between the illuminated (j_{ill}) and the dark current densities (j_{dark}) were carried out for $Sr_2Sb_2O_2Q_3$ (Q = S, Se) thick films with several irradiances under 450 nm and 0.4 bias voltage (**Figure 5.16**). For $Sr_2Sb_2O_2S_3$ (**Figure 5.16a**), the transient photocurrent increased from 5.5×10^{-1} for a 22 mW.cm^{-2} power density to 8.2×10^{-1} µA cm^{-2} for 42 mW.cm^{-2} for 111 mW.cm^{-2}. **Figure 5.16b** presents the evolution of the photocurrent Δj with the intensity of the luminous flux Φ_0 according to a classical power law[36]

giving a curve going through the origin with an equation of $\Delta j = 3.52\times10^{-1}\Phi^{0.18}$. For an ideal trap-free system, the exponent is equal to 1. In our case, the fitting gives a non-unity (i.e. 0.18(2)) exponent, indicating that for high powers most of the traps are already filled in and further illumination power cannot effectively increase the photogain.[37]

The photocurrent responses of the previously reported $Sr_2Sb_2O_2Se_3$[20] were also investigated under the same conditions (0.4 V bias voltage and under an excitation of 450 nm). The current density variation Δj in **Figure 5.16c** shows a linear increase occurring in the transient photocurrent under different illumination and dark cycles going from 0.8 to 1.1 µA.cm^{-2} for a power density of 22 to 111 mW.cm^{-2}. Similar to the oxysulfide, the generated photocurrent increased with the intensity of the luminous flux according to a classical power law[36] (**Figure 5.16d**) giving a curve going through the origin with an equation of $\Delta j = 6.17\times10^{-2}\phi^{0.58}$. As mentioned before, the value of the exponent provides the information of the traps present in the sample. In $Sr_2Sb_2O_2Se_3$ the exponent value (0.58(1)) is low, indicating the presence of many traps (although fewer than $Sr_2Sb_2O_2S_3$ with exponents of 0.18(1) for 0.4 V).

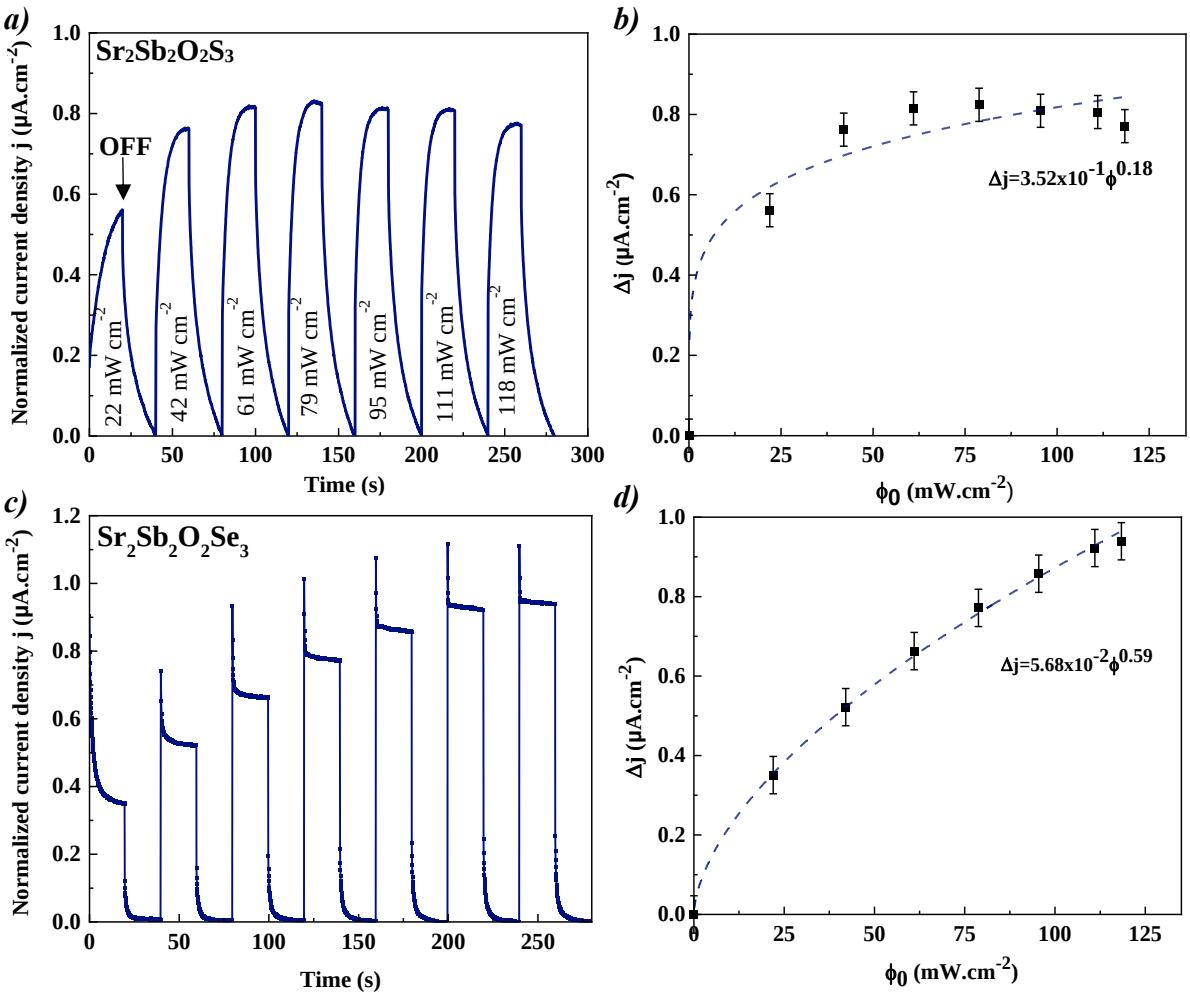

Figure 5.16 : (a) Transient photocurrent response (V_{bias}=0.4 V under a 450 nm excitation) and (b) Evolution of the photocurrent density the power density of light of $Sr_2Sb_2O_2S_3$. (c) Transient photocurrent response (V_{bias}=0.4 V under a 450 nm excitation) and (d) Evolution of the photocurrent density the power density of light of $Sr_2Sb_2O_2Se_3$

The same photocurrent measurements were performed for both materials without external bias voltage (**Figure 5.17**). For $Sr_2Sb_2O_2S_3$, the transient photocurrent in **Figure 5.17a** increased from 1.7×10^{-1} for a 22 mW.cm^{-2} power density to 2.2×10^{-1} µA cm^{-2} for 42 mW.cm^{-2} and kept increasing more slowly until reaching a stable photocurrent of 2.65×10^{-1} µA cm^{-2} for 111 mW.cm^{-2}. However, the trend remains the same with a power law (**Figure 5.17b**) and an equation of $\Delta j = 8.10\times10^{-2}\Phi^{0.25}$. In our case, the fitting gives a non-unity (i.e. 0.25(2)) exponent, suggesting a complex process of electron-hole generation, recombination and trapping within the sample. Moreover, for high light intensities, the photocurrent becomes independent of the light intensity received. This

effect can be due to a saturation of the photo-generated electron-hole pairs and/or a limitation of mobility in the layer.[38] For $Sr_2Sb_2O_2Se_3$, a higher transient photocurrent was measured (**Figure 5.17c**), 2.8 µA cm^{-2} for 111 mW.cm^{-2}. The power law fitting was less appropriate for this oxyselenide, indicating that the generated photocurrent tends toward a saturation value very early (**Figure 5.17d**).

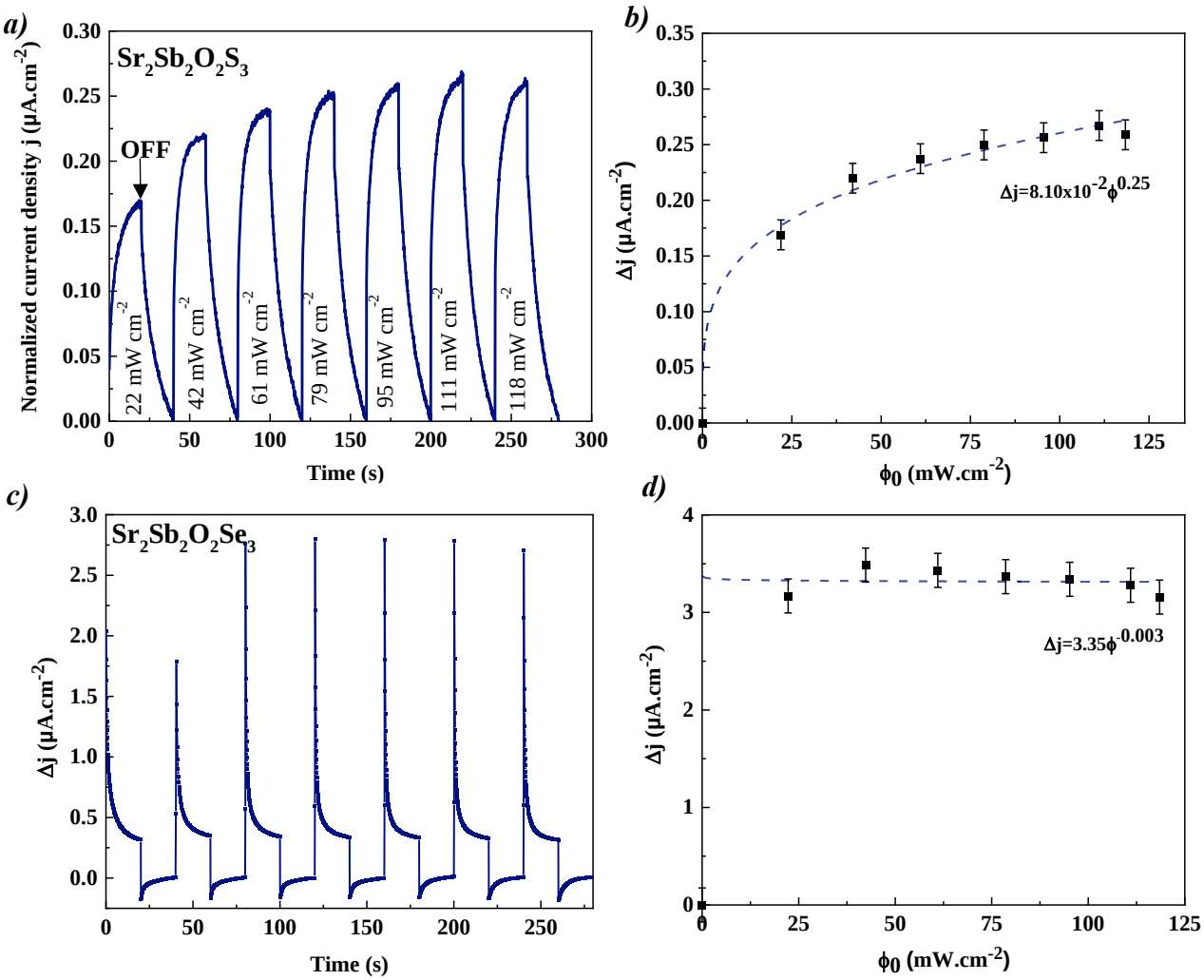

Figure 5.17 : (a) Transient photocurrent response (V_{bias}=0 V under a 450 nm excitation) and (b) Evolution of the photocurrent density the power density of light of $Sr_2Sb_2O_2S_3$. (c) Transient photocurrent response (V_{bias}=0 V under a 450 nm excitation) and (d) Evolution of the photocurrent density the power density of light of $Sr_2Sb_2O_2Se_3$

Unlike the oxysulfide, the photocurrent response registered for $Sr_2Sb_2O_2Se_3$ for 0.4 V (**Figure 5.16c**) and 0 V (**Figure 5.17c**) shows the characteristic decay from a "spike", which can be explained by the rapid separation of the electron/hole pairs under illumination, then the establishment of an equilibrium state between the recombination and the transfer of the carriers. In fact, at 0.4 V, the photocurrent peak is more square and shorter than that observed at 0 V, indicating more ideal behaviour at 0.4 V, as the equilibrium is reached faster (giving a more square peak), and minimal recombination occurs (shorter peak). We can also note that without applied potential, the photocurrent generated tends toward a saturation value from 42 mW.cm^{-2} (**Figure 5.17d**). Whilst at V_{bias} = 0.4 V, we observe classical power law behaviour (**Figure 5.16d**) without reaching saturation.

To understand this behaviour, it is possible in the case of a 'spike' to calculate the transfer and recombination constants according to a model proposed by Parkinson *et al.*[39,40]. More details about this calculation can be found in **Chapter 2**, **section 2.1.3.2**. This model was applied to extract the values of k_{tr}, k_{rec} as a function of light intensity for V_{bias} = 0 and 0.4 V (**Figure 5.18**). At 118 mW.cm^{-2}, the rate constants at 0.4 V are k_{tr} = 7 min^{-1} and K_{rec} = 1.5 min^{-1} (i.e. a transfer efficiency of 85 %, **Figure 5.18a**), and k_{tr} = 0.1 min^{-1} and K_{rec} = 1.3 min^{-1} (i.e. a transfer efficiency of 10 %, **Figure 5.18b**) at 0 V.

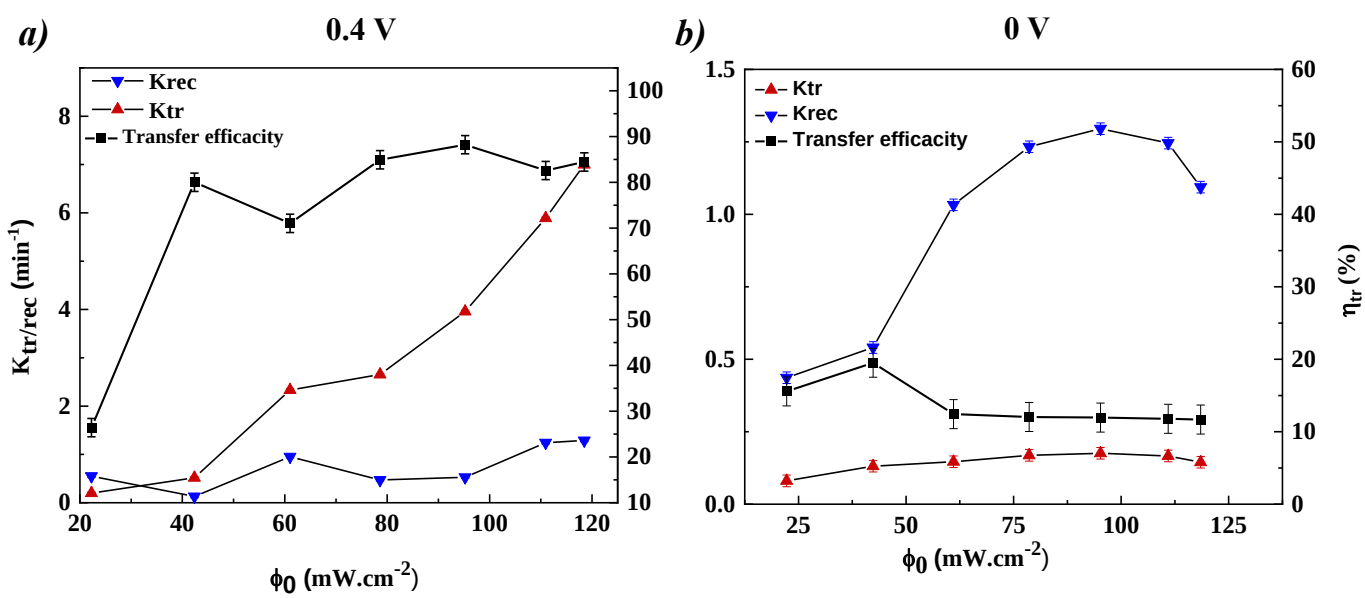

Figure 5.18 : Evolution of the recombination and transfer rate constants k_{tr} and k_{rec} with intensity of light alongside the transfer efficacity η_k by intensity light of $Sr_2Sb_2O_2Se_3$ at Bias (a) 0.4 V and (b) 0 V.

5.2.3.2. Influence of the wavelengths

The produced photocurrent is naturally linked to the material's absorption, therefore for an orange ($Sr_2Sb_2O_2S_3$) and grey ($Sr_2Sb_2O_2Se_3$) powder, the best efficiency should be observed in the complementary color spectral area between 450-505 nm for the oxysulfide and the whole spectral range for the oxyselenide, respectively. This was confirmed when we recorded the variation of the transient photocurrent Δj for V_{bias}= 0.4 V *vs.* wavelength (**Figure 5.19**). For $Sr_2Sb_2O_2S_3$, the highest photocurrent (**Figure 5.19a**) is observed at 505 nm and it decreased towards the longest wavelengths (590 - 627 nm).

As for $Sr_2Sb_2O_2Se_3$, the photocurrent dependency on the wavelengths in **Figure 5.19b**, we noticed similar response to the one recorded for its oxysulfide analogue. The best efficiency was seen for 450 nm excitation with the highest photocurrent value of 1.95 µA.cm^{-2} and decreasing proportionally towards bigger wavelengths. However, we observed the presence of significant photocurrent over the entire spectral range (450 to 655 nm) unlike the oxysulfide where the photocurrent drops drastically from 590 nm, logical considering the sample's color.

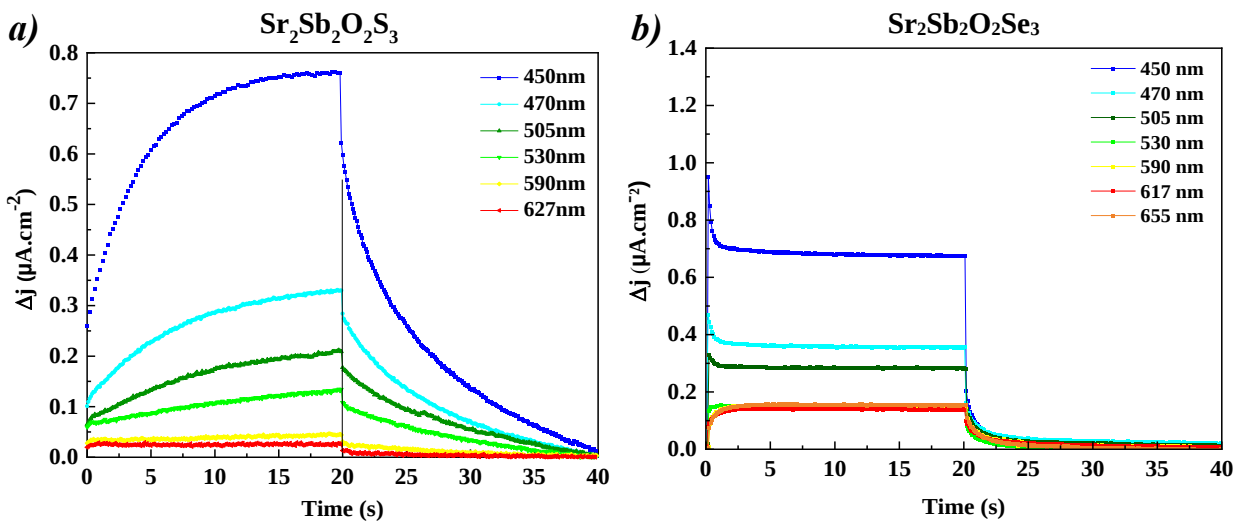

Figure 5.19 : Transient photocurrent response vs. wavelengths (constant light intensity ϕ_0=42 mW cm^{-2} and Bias = 0.4 V) of (a) $Sr_2Sb_2O_2S_3$ and (b) $Sr_2Sb_2O_2Se_3$.

5.2.3.3. Photocurrent measurements under solar irradiation

Both photoelectrodes were submitted to solar irradiation (150 W Xenon lamp with AM 1.5G filter – 100 mW.cm^{-2}) and the transient photocurrent response was recorded under different on/off cycles (**Figure 5.20**). For $Sr_2Sb_2O_2S_3$, two bias voltages (0 and 0.4 V) were tried out and **Figure 5.20a** shows the recorded response. For 0 V: a photocurrent of 3.2×10^{-1} µA cm^{-2} is obtained with a slight decrease in the value upon increasing the power density, until stability at the end with a 2.7×10^{-1} µA cm^{-2} value. Whilst for a 0.4 V potential, a higher photocurrent is obtained (1.60 µA cm^{-2}) but with a clear decrease (1.15 µA cm^{-2}) at higher power densities. This behaviour indicates the presence of progressive corrosion within the thick film in the chosen electrolyte which may be accentuated by the applied potential. The difference between the responses recorded under sunlight with both potentials (0.4 and 0 V), is consistent with the reproducibility test under 450 nm excitation. This hypothesis is still to be explored by other tests, including testing other electrolytes.

Figure 5.20b shows the response obtained when irradiating the photoelectrode of $Sr_2Sb_2O_2Se_3$ to solar irradiation under 0.4 V bias voltage. We can observe a good response of the photocurrent produced during the ON/OFF cycles with a very slight decrease in the photocurrent. This result shows better photostability of the oxyselenide compared to the sulfur-based analogue.

Although a photocorrosion may be occurring upon applying a potential in the case of the oxysulfide, the capacity of both materials to generate a photocurrent under sunlight without potential is rarely observed for this family of materials. For instance, $[(Ba_{19}Cl_4)(Ga_6Si_{12}O_{42}S_8)]$ generates a transient photocurrent response when subjected to ultraviolet light excitation[41] and $LaGaS_2O$ electrode produces an anodic photocurrent only under UV light.[42]

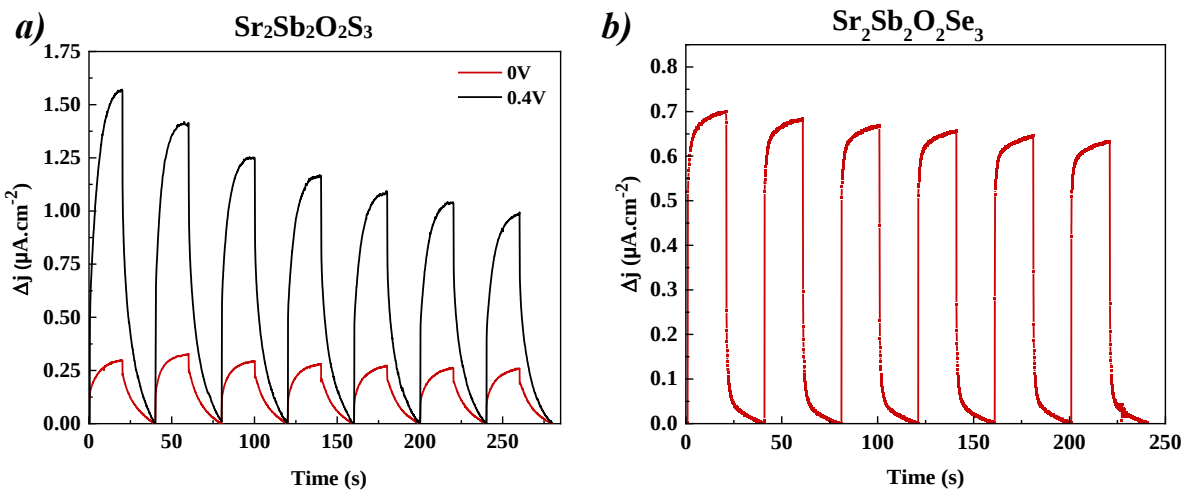

Figure 5.20 : (a) Transient photocurrent response under solar illumination (100 mW.cm^{-2}) for V_{bias}= 0 and 0.4 V of $Sr_2Sb_2O_2S_3$. (b) Transient photocurrent response under solar illumination (100 mW.cm^{-2}) for V_{bias}= 0.4 V of $Sr_2Sb_2O_2Se_3$.

5.2.3.4. Mott-Schottky method to determine the flat band potential

The last electrochemical measurement performed for both compounds was a Mott-Schottky test: the (MS) plot of 1/C^2 *vs.* applied potential shown in **Figure 5.21** indicates the conduction type, the concentration of the charge carriers (*N*) and the flat band potential (E_{fb}).[43] The positive gradient in the Mott-Schottky plot of 1/C^2 *vs.* V for $Sr_2Sb_2O_2S_3$ (**Figure 5.21a**) is consistent with n-type semiconducting behaviour and a flat band potential E_{fb} of -1.15 V *vs*. Ag/AgCl (reference electrode) or -0.625 V *vs*. RHE (reversible hydrogen electrode).[44] A potential measured with respect to Ag/AgCl ($E_{Ag/AgCl}$) can be converted to the RHE scale (E_{RHE}) with expression (5.1):

$$E_{RHE} = E_{Ag/AgCl} + E^0_{Ag/AgCl} + 0.059.pH \qquad (5.1)$$

where $E^0_{Ag/AgCl\ vs.SHE}$ is the potential of the Ag/AgCl reference electrode with respect to the standard hydrogen electrode (SHE) fixed at 195 mV. The pH of 0.1 M Na_2SO_4 electrolyte is 5.6.

The Mott-Schottky plot for $Sr_2Sb_2O_2Se_3$ (**Figure 5.21b**) is also consistent with n-type semiconducting behaviour and a flat band potential E_{fb} of -1.0 V *vs*. Ag/AgCl (reference electrode) or -0.475 V *vs*. RHE (reversible hydrogen electrode). Depending on the conduction type, the flat band potential serves to locate the valence and conduction band edge positions[44] as it reflects the position of the Fermi level which lies at 0.1 V lower than the conduction band for the n-type

semiconductors.[45,46,47] Thus, this calculated value is close to the calculated CB band edge position using the empirical method previously discussed in **Section 5.3.2.2**.

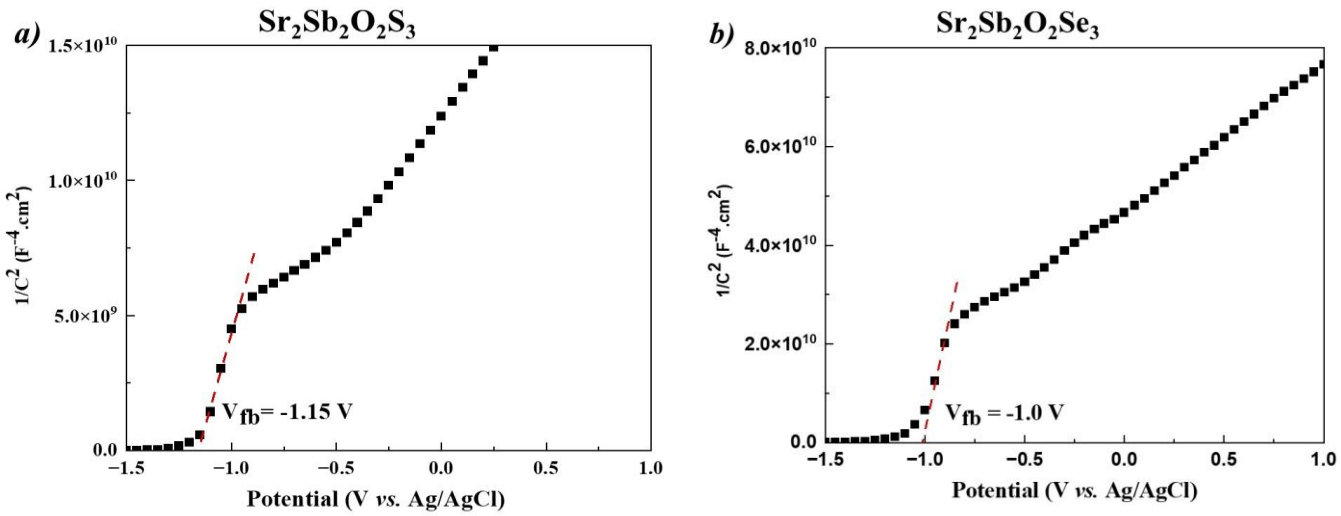

Figure 5.21 : (a) Mott-Schottky plot for $Sr_2Sb_2O_2S_3$ deposited on ITO/Glass performed at 100 Hz. (b) Mott-Schottky plot for $Sr_2Sb_2O_2Se_3$ deposited on ITO/Glass performed at 1 KHz.

In summary, both $Sr_2Sb_2O_2Q_3$ phases exhibited n-type semiconduction, with a capacity to generate a photocurrent with or without an applied bias voltage. Whilst $Sr_2Sb_2O_2Se_3$ demonstrated fast kinetics (spikey peak shapes), the oxysulfide analogue revealed slower kinetics. In addition, and according to a classical power law, both the oxysulfide and the oxyselenide revealed the presence of many traps within their system and $Sr_2Sb_2O_2Se_3$ tending toward a rapid saturation at bias = 0 V. Finally, $Sr_2Sb_2O_2Q_3$ oxychalcogenides were active under solar irradiation.

5.2.4. Photocatalytic activity

For the photodegradation experiment, the photo-reactor is similar to the one described previously, but the solution consisted of 200 mL of Rhodamine B (5×10^{-6} mol dm^{-3}) and 100 mg of the photocatalyst powder ($Sr_2Sb_2O_2Q_3$ (Q = S, Se)). In this case, 20 mins stirring in a sonicator was added in order to break up agglomerates before it was stirred for 30 mins in the dark to ensure an appropriate adsorption/desorption equilibrium. Both UV (254 nm, 40 W) and solar (100 mW cm^{-2}) irradiations were used as sources of incident light. Then, samples were taken, at regular intervals to monitor the evolution of the concentration of the photodegraded Rhodamine B by spectrophotometry (**Figure 5.22**).

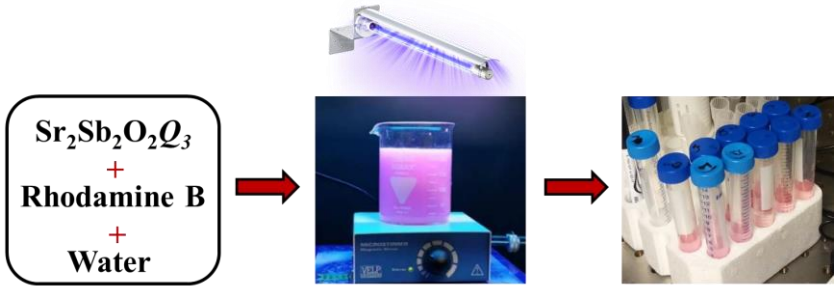

Figure 5.22 : Photocatalytic measurements example of $Sr_2Sb_2O_2S_3$

UV-vis spectroscopy was used to follow the kinetics of the photodegradation of Rhodamine B, based on the maximum absorption, allowing the photocatalytic efficiency of $Sr_2Sb_2O_2Q_3$ (Q = S, Se) phases to be quantified. The photocatalytic kinetics at the solid-liquid interface were described using the Langmuir-Hinshelwood model (LH),[48] taking an order 1 for the photodegradation reaction and plotting $Ln(C_0/C)$ *vs.* time to determine the apparent speed constant (k_{app}). **Figure 5.23** shows the corresponding kinetic plots for $Sr_2Sb_2O_2Q_3$ (Q = S, Se) photocatalysts under UV and solar irradiations. Under UV light, both photocatalysts exhibited similar efficiency: linear evolution occurred with apparent speed constants of 2.28×10^{-2} min^{-1} and 1.79×10^{-2} min^{-1} for $Sr_2Sb_2O_2Se_3$ and $Sr_2Sb_2O_2S_3$ respectively. These results reveal good kinetic performances for both phases and are comparable with other photocatalysts (typically 10^{-2} min^{-1}), such as $La_2Ti_2O_7$[43] and $Sr_6Cd_2Sb_6S_{10}O_7$.[7,1]

The performance of both materials decreased under solar irradiation but its striking that quite significant activity was still observed for $Sr_2Sb_2O_2Se_3$ (with $k_{app} = 6.45\times10^{-3}$ min^{-1}). It should be noted that it was difficult to disperse the $Sr_2Sb_2O_2S_3$ phase in solution, and 20 minutes sonication was needed to break up agglomerates and give the best photocatalytic efficiency. $Sr_2Sb_2O_2Se_3$ showed better dispersion (less sonication was needed), and the maximum efficiency is reached more quickly. The kinetics of the photodegradation reaction can be influenced by the microstructure and the morphology of the photocatalyst as well as its stability in the chosen electrolyte; nonetheless structural parameters (such as polarity, lone pairs) can also influence the outcome of the reaction.

The photocatalytic efficiency of $Sr_2Sb_2O_2Q_3$ under solar light ($k = 4.78\times10^{-4}$, 6.45×10^{-3} min^{-1} for S and Se, respectively) is comparable with other reported oxychalcogenides such as BiCuOQ

(Q = S, Se).[49] BiCuOS demonstrated the capacity to degradate 55% of an organic pollutant (Congo Red) in aqueous solution under visible light in 70 mins and k = 9.1×10^{-3} min^{-1}.[49]

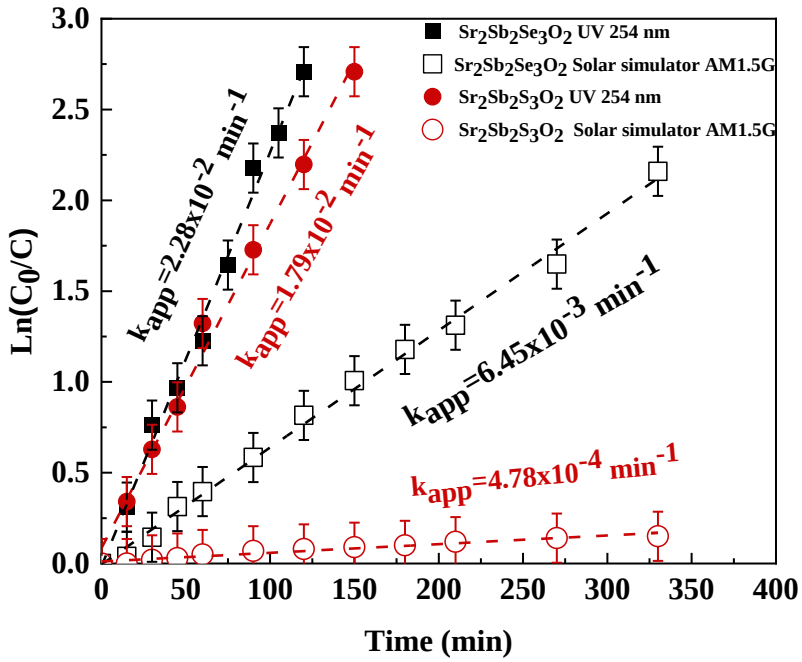

Figure 5.23 : Langmuir-Hinshelwood kinetic plot for the degradation of Rhodamine B on $Sr_2Sb_2O_2Q_3$ (Q = S, Se) under UV (254 nm, 40 W) and Solar (100 $mW.cm^{-2}$) irradiation.

Unfortunately, during these photoelectrochemical studies, significant photocorrosion was observed for $Sr_2Sb_2O_2S_3$ upon applying a bias voltage (**Figures 5.16a** and **5.20a**). However, XRPD patterns of the powder before and after the catalysis show only slight broadening of peaks (which could indicate lower crystallinity) but little change is observed by XRPD (**Figure 5.24** and **Table 5.10**).

Table 5.10. Unit Cell parameters from Rietveld refinement using room temperature XRPD data of $Sr_2Sb_2O_2S_3$ dried powder i) after synthesis, ii) after photocurrent measurements and iii) after photocatalysis measurements.

	a	*b*	*c*	β	volume
i) Reference	13.0414(3) Å	3.9547(1) Å	9.3141(2) Å	122.519(1) °	405.06(2) $Å^3$
ii) Potential	13.0386(3) Å	3.9546(1) Å	9.3134(2) Å	122.518(1) °	404.93(1) $Å^3$
iii) Catalysis	13.0404(4) Å	3.9524(1) Å	9.3116(3) Å	122.510(1) °	404.73(2) $Å^3$

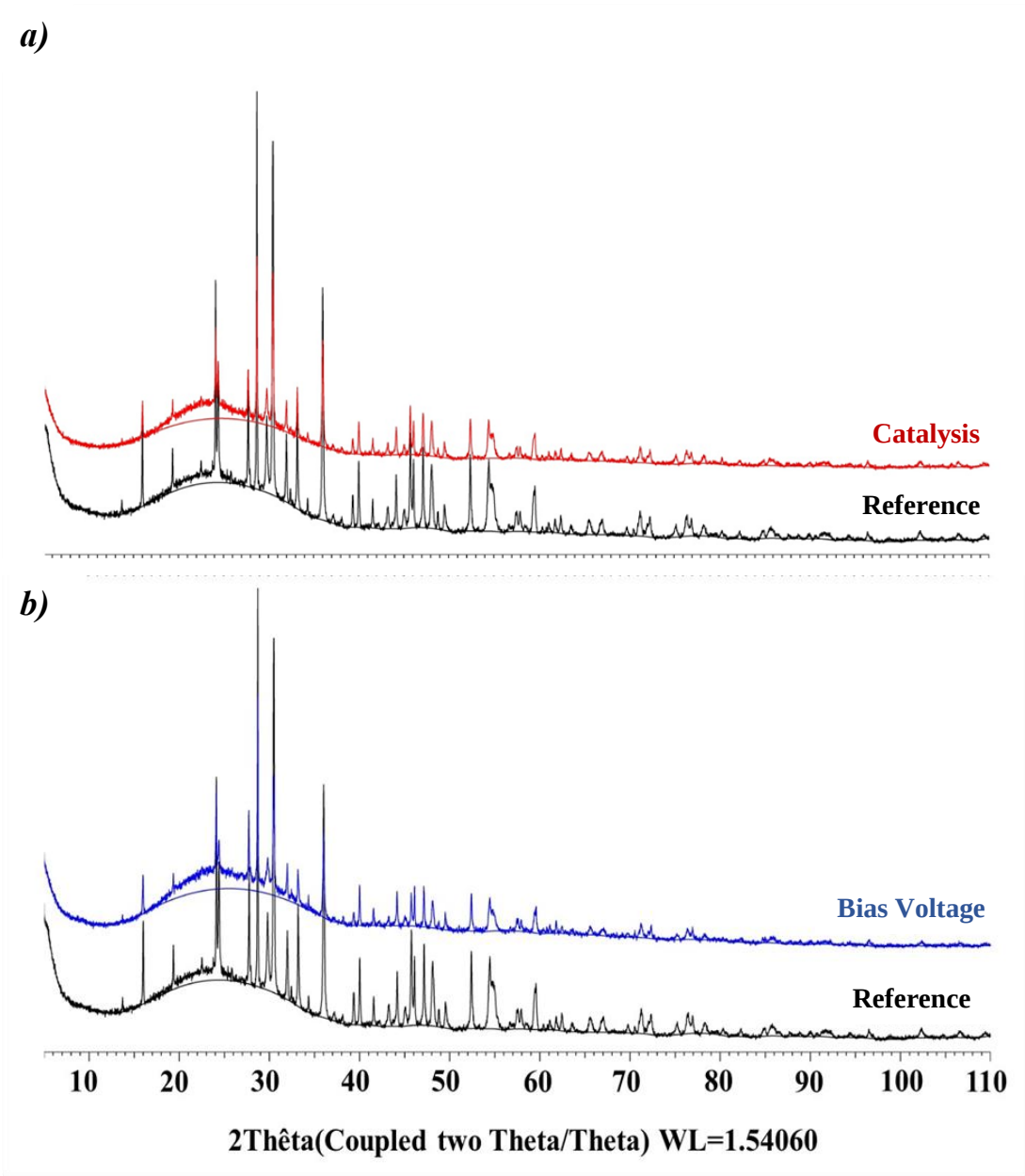

Figure 5.24 : Collected X-ray powder diffraction (XRPD) data of dried powder of $Sr_2Sb_2O_2S_3$ after (a) photocatalytic test and (b) test under an applied bias voltage and a 450 nm excitation.

SEM analysis was also carried out on the after-test samples to investigate the grain size and shape (**Figure 5.25**) and indicated that crystallite size remains comparable. Therefore, photocorrosion cannot be attributed to a structural change but rather to a progressive deterioration (dissolution) of the photoelectrode in the electrolyte. Future work to optimise the electrolyte and film stability would be worthwhile.

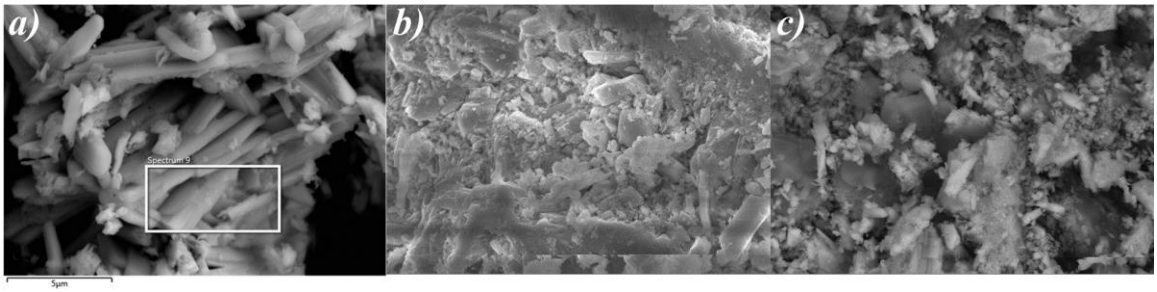

Figure 5.25 : SEM images of $Sr_2Sb_2O_2S_3$ dried powder a) after synthesis, b) after photocurrent measurements and c) after photocatalysis measurements.

We note that the protocol adopted for the photodegradation tests was our second attempt and the results showed here were the best we observed. The first photocatalytic measurement was done in the same photo-reactor, but in this case the solution was stirred for 30 min in the dark to ensure an appropriate adsorption/desorption equilibrium without prior treatment in the sonicator for 20 mins. A latency time of 30 mins was observed before any degradation occurred, which was not efficient. Further details on the protocol and results observed for $Sr_2Sb_2O_2S_3$ oxysulfide using this protocol can be found in **Appendix 3, Section 3.3**.

5.2.5. Computational studies

5.2.5.1. Density functional theory (DFT)

For the DFT calculations, full geometry optimizations for both $Sr_2Sb_2O_2Q_3$ (Q = S, Se) were carried out using a plane-wave energy cutoff of 550 eV and a threshold of the self-consistent-field energy convergence of 10^{-6} eV with k-points meshes (3×13×4) and (4×13×3) in the irreducible Brillouin zone for both $C2/m$ and $P2_1/c$ models. The relaxed structure was a good match with the experimental structure, and it was used for calculations of the electronic band structure, the charge carrier's effective masses and the density of states. Vesta software[50] was used to visualize the crystal structure and the localized electron densities. In the following section, the DFT calculations using the $C2/m$ model will be discussed; and the results obtained for the $P2_1/c$ model can be found in **Appendix 3, Section 3.4**.

The electronic band structures and properties of the $C2/m$ models of $Sr_2Sb_2O_2Q_3$ were investigated, which revealed direct band gaps of 1.08 eV and 0.73 eV for Q = S, Se, respectively.

These are smaller than the experimental optical band gaps (2.44(1) eV and 1.72(1) eV measured for $Sr_2Sb_2O_2S_3$ and $Sr_2Sb_2O_2Se_3$, respectively) discussed above. This might be explained by the GGA approximation (with PBE functional used here) well known to underestimate band gaps.[51] **Figures 5.26a** and **5.26d** show the calculated electronic band structure for $Sr_2Sb_2O_2Q_3$ with valence band maximum and conduction band minimum at the Γ point (0; 0; 0) for both Q = S, Se.

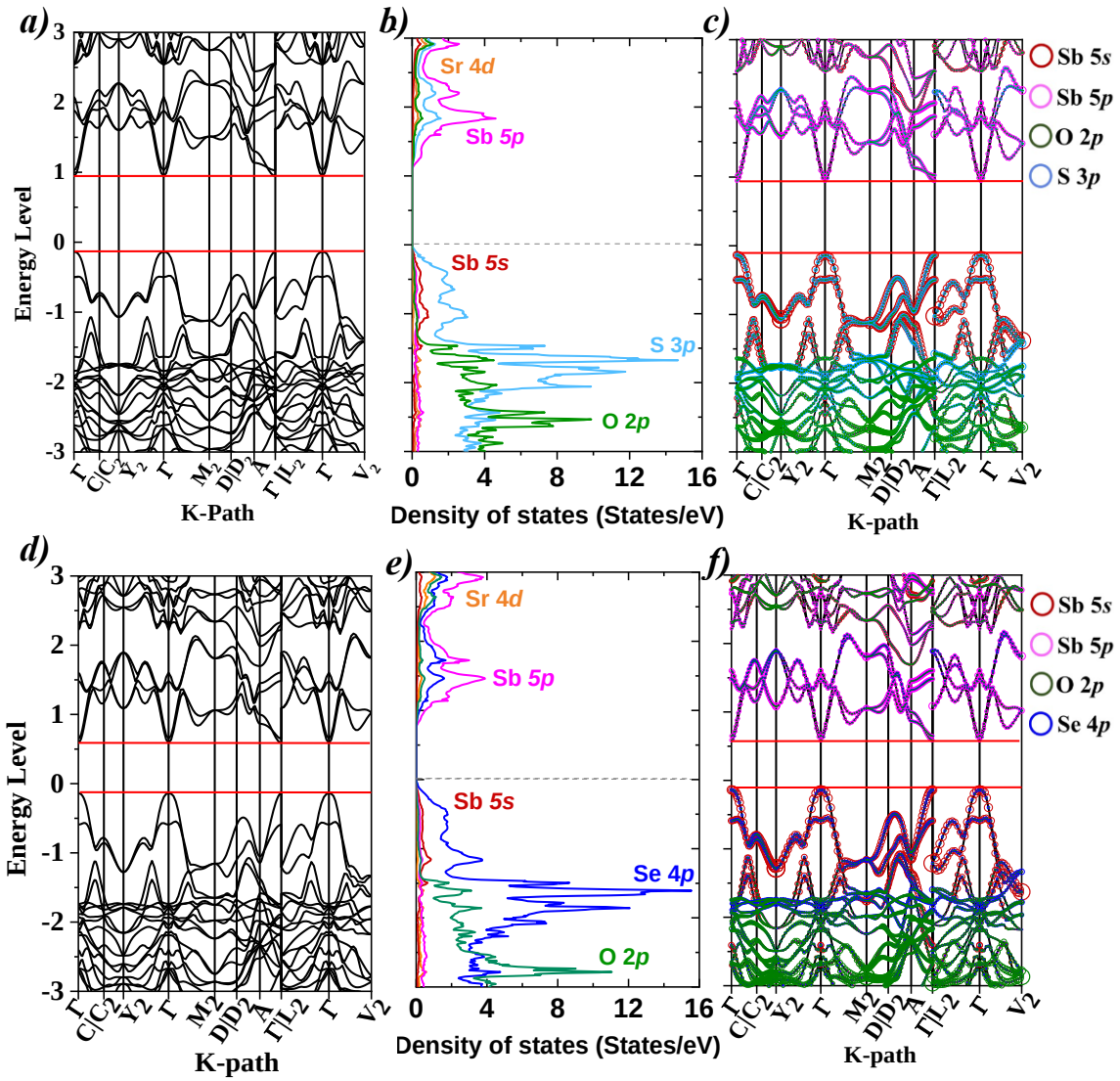

Figure 5.26 : (a) and (d) Electronic band structure, (b) and (e) Projected DOS is shown for the Sr 4*d*, Sb 5*s*, Sb 5*p*, S 3*p*/ Se 4*p* and O 2*p* states. The Fermi level is set to 0, (c) and (f) Fat bands showing the Sb 5*s*, Sb 5*p*, O 2*p* and S 3*p* states, calculated in the *C*2/*m* model for $Sr_2Sb_2O_2S_3$ and $Sr_2Sb_2O_2Se_3$, respectively.

The projected densities of states are shown in **Figures 5.26b** and **5.26e** focusing on the region around the Fermi level of the valence and conduction band. The orbitals near this selected region are mainly dominated by Sb and S/Se states, while Sr and O states make a minimal contribution. The Sb 5*p* states dominate the conduction band minimum, lying from ~1 eV up to ~3 eV, while the Sb 5*s* states lie in the valence band (in the range of -1.5 to -0.1 eV), hybridizing with the O 2*p* and S 3*p*/Se 4*p* to form the maximum of the valence band. This orbital contribution to both bands was also confirmed by the plot of the fat bands (**Figure 5.26c** and **5.26f**), and similar results have been reported for $Sm_2Ti_2S_2O_5$,[52] and $Ln_2Ti_2S_2O_5$.[53] Similar Sb 5*s* contribution to the top of the valence band was also observed for several antimony based compounds including $Sr_6Cd_2Sb_6S_{10}O_7$ oxysulfide,[7,54] α-Sb_2O_3, β-Sb_2O_3, γ-Sb_2O_3, α-Sb_2O_4 and β-Sb_2O_4 oxides[55] and Sb_2S_3 and Sb_2Se_3 chalcogenide semiconductors.[56] This Sb 5*s* - *Q np* (*Q* = O, S, Se) hybridization plays a key role in reducing the band gap into the visible range.

In order to have a quantitative investigation of the charge carriers' mobilities, the effective masses of electrons (m^*_e) and of holes (m^*_h) were calculated[57] using the following equation near the CBM and the VBM at Γ (0; 0; 0):

$$\left(\frac{1}{m^*}\right)_{ij} = \frac{1}{\hbar^2}\frac{\partial^2 E_n(k)}{\partial k_i k_j} \tag{5.2}$$

where $E_n(k)$ corresponds to the n^{-th} electronic band in *k*-space. Prior to the effective masses' extraction, the self-consistent electronic calculation was followed by a non-self-consistent calculation along the high symmetry lines. Different dispersions were observed at the CBM and VBM, which suggests different mobility of electrons and holes. We investigated the directions within the layers, Γ → A, Γ → V_2, Γ → L_2, Γ → M_2 and Γ → Y_2, very near to the Γ point, since the VBM and the CBM are located at Γ for both phases.

The calculations revealed low effective masses for both oxyselenide and oxysulfide phases (**Table 5.11**), with particularly low values for electrons (0.160(2) m_0 for Γ → V_2) and holes (0.303(3) m_0 for Γ → A) effective masses for the oxyselenide. The carrier mobility is inversely proportional to the effective mass; therefore, this high mobility makes the oxyselenide particularly attractive for efficient photoconduction and photocatalysis applications. These values are lower than those reported for related oxyselenide and oxysulfide materials (m_e^* values of 0.59 m_0, 0.68 m_0 for BiCuOS and BiAgOS, respectively;[58] m_h^* of 0.24 m_0 and 0.37 m_0 for c-ZrOS and t-ZrOS,

respectively;[19] m_e^*= 1.6(2) m_0 for LaCuOSe;[59] m_h^*= 0.58, 0.93, 1.99 m_0 for $SnSe_xO_{1-x}$).[18] The high mobilities reflect the high dispersion at the VBM and CBM, influenced by both the high covalency (particularly for the oxyselenide), and the presence of the stereochemically-active $5s^2$ electron pair on Sb^{3+} ions (as discussed further below).

Table 5.11. Calculated electron (m_e^*) and hole (m_h^*) effective mass, m_0 being the free electron mass for $Sr_2Sb_2O_2Q_3$ for *C*2/*m* model.

Directions	$Sr_2Sb_2O_2S_3$		$Sr_2Sb_2O_2Se_3$	
	m_e/m_0	m_h/m_0	m_e/m_0	m_h/m_0
$\Gamma \rightarrow Y_2$	0.316(7)	0.735(5)	0.253(2)	0.504(2)
$\Gamma \rightarrow M_2$	0.469(1)	1.839(3)	0.402(3)	1.259(6)
$\Gamma \rightarrow L_2$	0.292(2)	0.674(1)	0.240(5)	0.484(7)
$\Gamma \rightarrow V_2$	0.188(6)	0.866(7)	0.160(2)	0.559(2)
$\Gamma \rightarrow A$	0.692(2)	0.435(3)	0.526(7)	0.303(3)

The Sb 5*s* - *Q* n*p* hybridisation relates to the Sb $5s^2$ lone pair and its stereochemical activity. The valence electron density map projected on the (010) plane is shown in **Figure 5.27a** and **5.27b** giving insight into the stereoactivity of the Sb^{3+} lone pair within the $O(S,Se)_4$ heteroleptic environment. It has been demonstrated that the stereochemical activity of the lone pairs can give rise to anisotropic effects (effective masses and mobility) therefore can be effective for enhancing the separation and the transfer of electrons and holes.[56] Similar results were observed for Sb-based compounds[60] such as $Sr_6Cd_2Sb_6S_7O_{10}$,[7,54] $Sr_6Cd_2Sb_6Se_7O_{10}$[2] and bismuth based materials.[61]

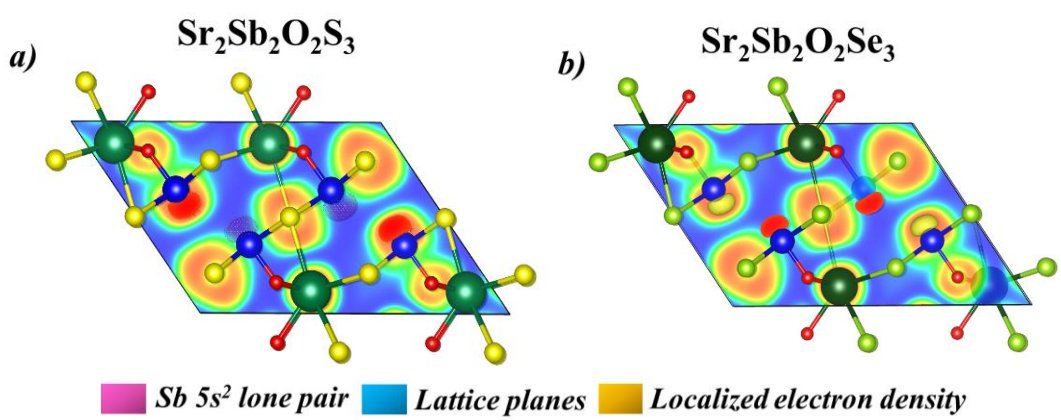

Figure 5.27 : Electron localization function (ELF) projected on the (010) lattice plane and 0.91 isosurface of DFT plots of (a) $Sr_2Sb_2O_2S_3$ and (b) $Sr_2Sb_2O_2Se_3$.

To quantify this stereochemical activity, a universal method described by Hu *et al.*[62,63] was adopted. This method was used for different lone pair systems, such as arsenic sulfides[64] and bimuth borates.[63] By simply comparing the *s* and *p* states of the Sb cation near the Fermi level (**Figure 5.28a and 5.28c**) (filled antibonding interactions responsible for the stereoactive lone pair[65,66]), PDOS from a specified energy level (point where the intensity of Sb-*s* and Sb-*p* is equivalent) to the Fermi level (**Figure 5.28b and 5.28d**) are integrated. Details of the calculation are given in **Table 5.12**. In our previous study on $Sr_6Cd_2Sb_6S_{10}O_7$,[7] we found a R_{SCA} of 0.57, 0.59, 0.64 for SbS_5, SbS_4O and SbO_3, respectively. These values are comparable to the ones calculated for the $Sr_2Sb_2O_2Q_3$ phases (R_{SCA} = 0.68 and 0.54 for S and Se, respectively). This is an indication that the presence of a heteroleptic environment (coordinated with both sulfide/selenide and oxide anions) around the antimony influence the stereochemical activity of the lone pair; in a way that with increasing the anion ionicity, this activity increases (O > S > Se).

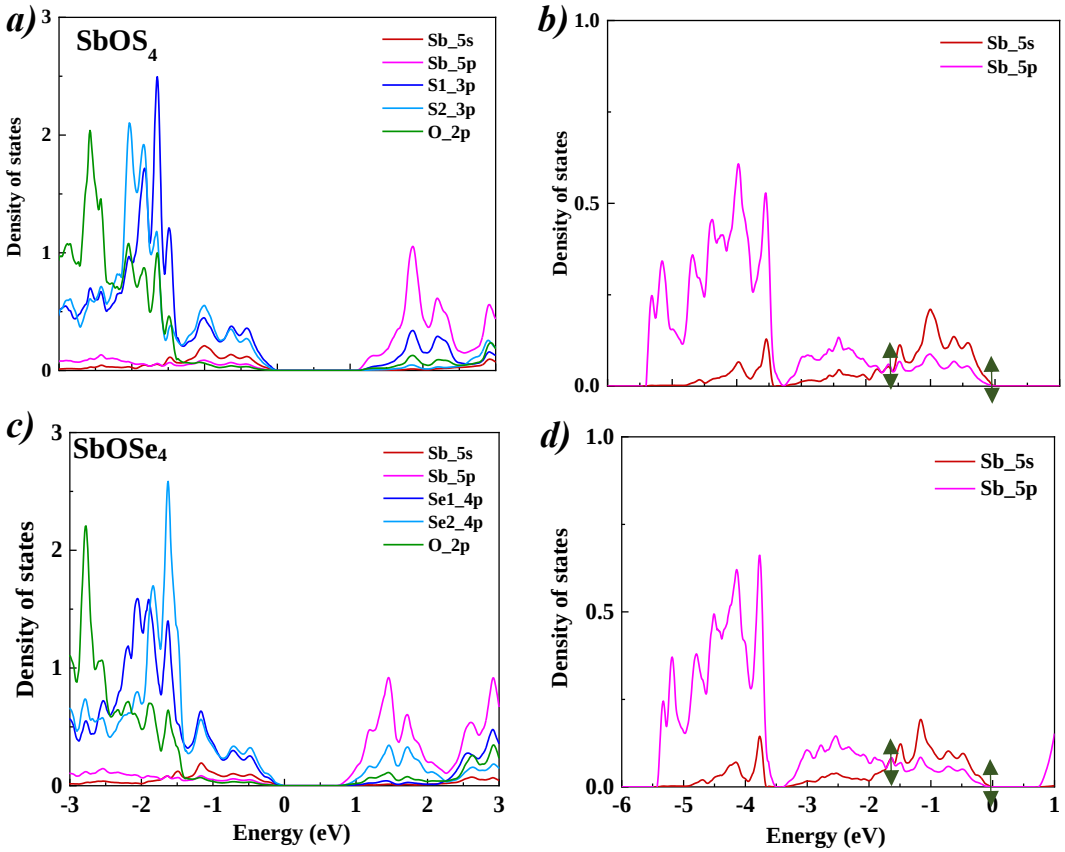

Figure 5.28 : (a) Partial density of states of SbS_4O entity. (b) PDOS of Sb-5*s* and Sb-5*p* in SbS_4O entity. (c) Partial density of states of $SbSe_4O$ entity. (d) PDOS of Sb-5*s* and Sb-5*p* in $SbSe_4O$ entity.

Table 5.12. Integrated PDOS from a specified energy level to the Fermi level and the calculated stereochemical activity factor for the SbS_4O and $SbSe_4O$ entity.

	SbS_4O entity	**$SbSe_4O$ entity**
I (Sb-s)	1.4	1.3
I (Sb-p)	2.33	2.39
R_{SCA}	0.60	0.54

As mentioned previously, DFT calculations were also carried out for the lower symmetry model ($P2_1/c$) of both phases and gave very similar results, which emphasizes the negligible difference between these two structural models. Particularly, the directions found for the high charge carriers' mobilities in the $C2/m$ model ($\Gamma \rightarrow V_2$ and $\Gamma \rightarrow A$ directions for the electrons and holes, respectively) are consistent with the ones found for the $P2_1/c$ model ($\Gamma \rightarrow Z$ and $\Gamma \rightarrow B$ directions for the electrons and the holes, respectively). The resulting plots for the conducted calculations in $P2_1/c$ model with the charge carriers' effective masses can be found in **Appendix 3, Section 3.4**.

5.2.5.2. Crystal Orbital Hamiltonian Population (COHP)

The Crystal Orbital Hamiltonian Population (COHP) calculation gives access to projected contributions of specific bonds with the dispersion but also an integral value representing the nature (bonding/antibonding) and strength of the bond on average. These calculations were done using the POSCAR file, with the atom's positions and numbers listed in the $P1$ symmetry. The integral I-COHP obtained for some bonds (Sb-S for instance), seem to have an evolution mostly depending on the distance with similar average distances in both compounds. On the other hand, the dispersion of the p-COHP allows a better comparative study (**Figure 5.29**). In the case of the $Sr_2Sb_2S_3O_2$ phase, the Sb-S antibonding states (that relate to the Sb $5s^2$ lone pair, as defined by the revised model[66,65]) extend from the Fermi level much deeper into the valence band, compared with $Sr_6Cd_2Sb_6S_{10}O_7$.[7] It is equivalent to greater curvature of bands used to determine the m_h^* and give explanation for the lower m_h^* in $Sr_2Sb_2S_3O_2$.

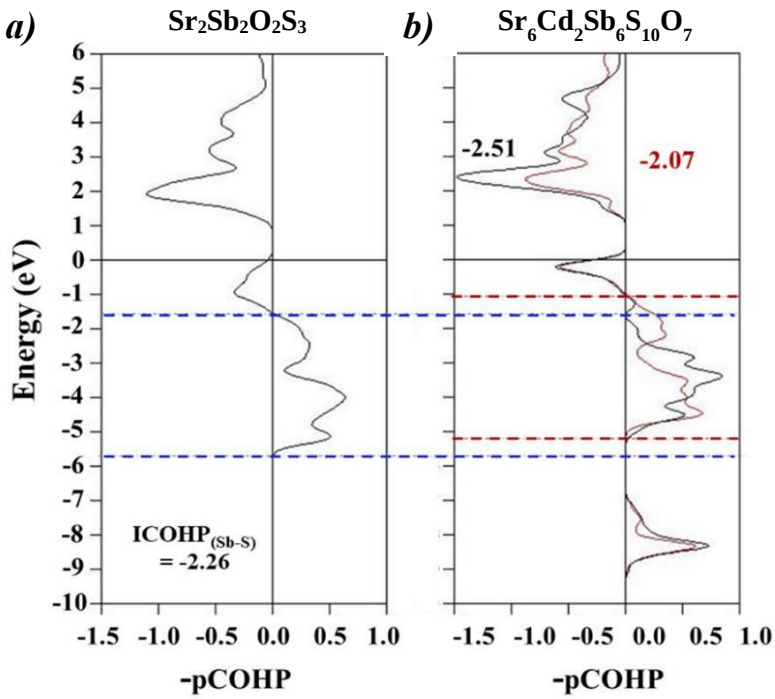

Figure 5.29 : (a) Projected COHP (p-COHP) for $Sr_2Sb_2O_2S_3$ phase on one of the "border" Sb-S bond (Sb23-S45), and (b) p-COHP for the phase $Sr_6Cd_2Sb_6S_{10}O_7$ on the Sb-S bond located at two opposite borders of the 1D unit (Sb5-S47 in red and Sb1-S35 in black). Dashed blue and red lines represent the extend of the Sb-S antibonding states in the valence band and of the lower bonding states.

5.3. Discussion

5.3.1. Structural characteristics

Some antimony Sb^{3+} oxychalcogenides exhibit a key feature in their structure which is the presence of a one-dimensional (1D) chains of edge-linked $SbOS_4$ square-based pyramids. For instance, we showed that $Sr_2O_2Sb_2S_3$ oxysulfide adopts a similar crystal structure to its previously reported oxyselenide analogue $Sr_2O_2Sb_2Se_3$;[20] where the $SbOS_4$ units form double chains of ${}^1_\infty[Sb(1)OS_3]^{3-}$ and ${}^1_\infty[Sb(2)OS_2]^{3-}$ extending along the *b* direction. These chains could be defined as a 1D building block unit within the structure separated by the Sr^{2+} ionic cations. On the other hand, $Sr_6Cd_2Sb_6Q_{10}O_7$ (Q = S, Se) phases,[7,54,2] contain similar 1D block formed by double-chains of ${}^1_\infty[Sb_2OS_{3.5}]^{-3}$ that consist of $[Sb(2)OS_4]^{7-}$ units edge-linked with $[Sb(1)S_5]^{7-}$ tetragonal pyramids, but it's not alone in the structure. In these more complex structures, the 1D block is

linked with another polyhedra CdS_4 through its corners, resulting $^{2}_{\infty}[CdSb_2OS_5]^{4-}$ layers, which in their turn are separated by the isolated $^{1}_{\infty}[SbO_{2.5}]^{2-}$ pseudo-chains (**Figure 5.30**).

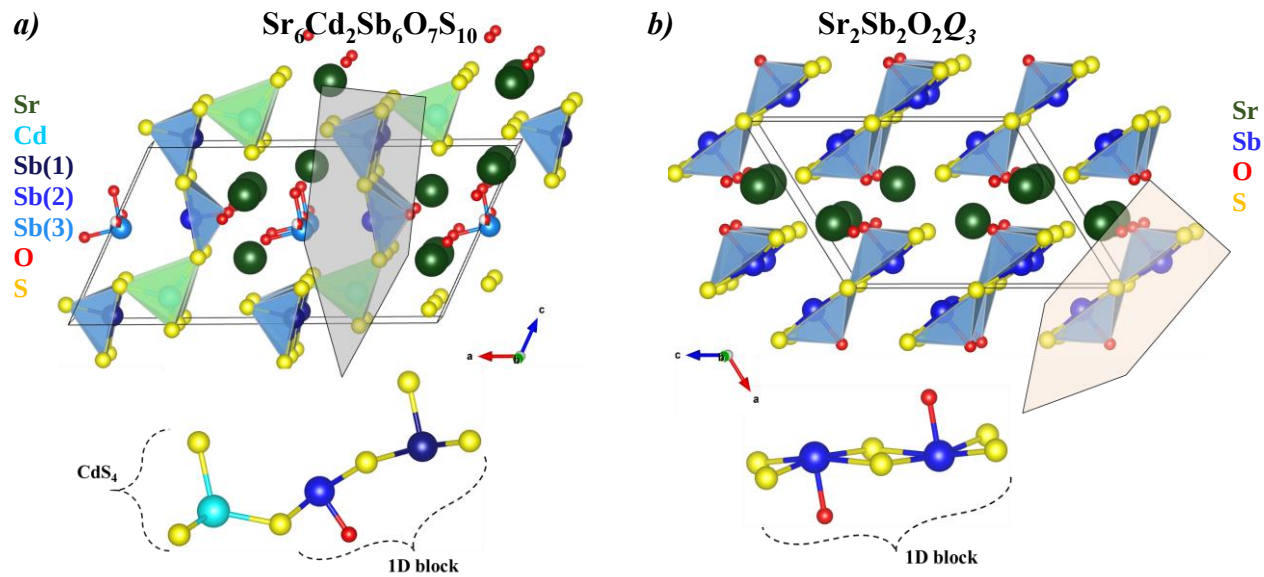

Figure 5.30 : Representation of $Sr_2Sb_2O_2Q_3$ and $Sr_6Cd_2Sb_6Q_{10}O_7$ (Q = S, Se), emphasizing the different building blocks within the structures.

5.3.2. Band gap magnitude and nature

Another common feature between those phases is the reduced optical band gaps in the case of the oxyselenides compared to the oxysulfides (**Table 5.13**). The presence of S 3*p*/Se 4*p* states hybridizing with the Sb 5*s* orbitals on top of the VB in these phases increased the valence band maximum, which decreased the band gap, compared to oxides. In addition, the presence of Se 4*p* states that contribute largely to the conduction band, with a Sb 5*p* -Se 4*p* orbitals hybridization at low energy level (higher covalency for the selenide) compared to the oxysulfide analogues (Sb 5*p* - S 3*p* hybridize at higher energy levels) (**Figure 5.26**). This result can be the origin of having lower conduction band minimum for the oxyselenide phases thus, further reduced band gaps, which is consistent with the diffuse reflectance measurements. As we are discussing the band gaps for these materials, other than the characteristic of the band gap magnitude these phases share, they don't exhibit the same band gap nature. Our electronic band calculations revealed that $Sr_2Sb_2O_2Q_3$

(Q = S, Se) phases have a direct band gap, whilst reports on $Sr_6Cd_2Sb_6Q_{10}O_7$ (Q = S, Se) phases confirmed their indirect band gap.[1,2]

Table 5.13. Optical Band gaps of $Sr_2O_2Sb_2Q_3$ and $Sr_6Cd_2Sb_6Q_{10}O_7$ (Q = S, Se)

Compound	Band gap (eV)	Compound	Band gap (eV)
$Sr_2O_2Sb_2S_3$	2.44	$Sr_6Cd_2Sb_6S_{10}O_7$	1.89
$Sr_2O_2Sb_2Se_3$	1.72	$Sr_6Cd_2Sb_6Se_{10}O_7$	1.55

5.3.3. Features contributing to the enhanced transport properties

One of the most interesting results we obtained in this study is the very low effective masses for both the electrons and holes, indication of a very promising transport properties for the $Sr_2O_2Sb_2Q_3$ (Q = S, Se) phases; therefore, further investigations were conducted in order to understand the origin of having this interesting characteristic, which is rare among this type of materials. In this part the focus is on comparing $Sr_2O_2Sb_2Q_3$ oxychalcogenides with $Sr_6Cd_2Sb_6S_{10}O_7$ oxysulfide.

5.3.3.1. Origin of high electron mobility

To start with the electrons, all three antimony oxychalcogenides show low effective masses (m_e^* = 0.160, 0.188 and 0.218 m_0 for $Sr_2O_2Sb_2Se_3$, $Sr_2O_2Sb_2S_3$ and $Sr_6Cd_2Sb_6S_{10}O_7$,[7] respectively). In this case, the interest is in the conduction band minimum which are formed by the Sb 5*p* and S 3*p*/Se 4*p* overlapping (in addition to the Cd orbitals for $Sr_6Cd_2Sb_6S_{10}O_7$ as we saw previously from the density of states and the fat bands; CdS is intensively studied as n-type semiconductor[67,68,69,70]). This overlap resulted in the highly dispersed conduction band we saw for the three phases, thus the comparably good electrons mobility.

5.3.3.2. Origin of high hole mobility

Regarding the holes transport, $Sr_2O_2Sb_2Q_3$ phases revealed low effective masses which was not the case for $Sr_6Cd_2Sb_6S_{10}O_7$ (m_h^* = 0.303, 0.435 and 6.5 m_0 for $Sr_2O_2Sb_2Se_3$, $Sr_2O_2Sb_2S_3$ and $Sr_6Cd_2Sb_6S_{10}O_7$,[7] respectively); this is quite striking and interesting to investigate. So, by looking at the VBM, in both cases it consisted of the Sb 5*s* and S/Se *np* states. With no difference in the VBM, except for the relative energies of the contributing orbitals, we looked for other reasons to

explain this observed difference. For instance, in $Sr_6Cd_2Sb_6S_{10}O_7$ all the sulfide anions at the border of the 1D unit are corner shared with Cd^{2+} cations which can weaken the Sb-S bonds, therefore a decreased VBM curvature; while in $Sr_2Sb_2O_2Q_3$, they are weakly interacting with ionic Sr^{2+}, an advantage for an increased band curvature.

As previously discussed, the presence of lone pairs electrons can have a huge influence on the physical properties of the material. According to the revised lone pair, the degree of its stereoactivity is determined by the filled antibonding interactions between Sb 5*s* and S/Se *np* states and/or O 2*p* states in the VBM.[65,66] Comparing the two $Sr_2O_2Sb_2Q_3$ phases, the Sb^{3+} $5s^2$ lone pair exhibited an increased stereochemical activity in the oxysulfide (0.68) compared to the oxyselenide (0.54), which resulted in a slightly higher distortion of the $SbOQ_4$ units within the 1D building block of the oxysulfide compared to the oxyselenide (S – Sb – S angles ~171°, compared with ~174° Se – Sb – Se angles). At the same time, and judging by the arrangement of the Sb containing units in $Sr_2O_2Sb_2Q_3$, the lone pairs are separated by only ~4 Å along the direction close to the orientation of both electron pairs (Γ → A). This leads to the exceptionally low m_h* values for $Sr_2O_2Sb_2Se_3$ (**Figure 5.31b)**. As for $Sr_6Cd_2Sb_6S_{10}O_7$, the lone pairs in SbS_5 and $SbOS_4$ units (contributing most to the valence band) are well separated (**Figure 5.31a**). In addition, the presence of the SbO_3 polyhedra in $Sr_6Cd_2Sb_6S_{10}O_7$ (most polar), with very ionic Sb-O bonds contributes to a decrease in the band curvature; a possible explanation for the poorer hole properties in this material, as discussed previously in **Chapter 4**.

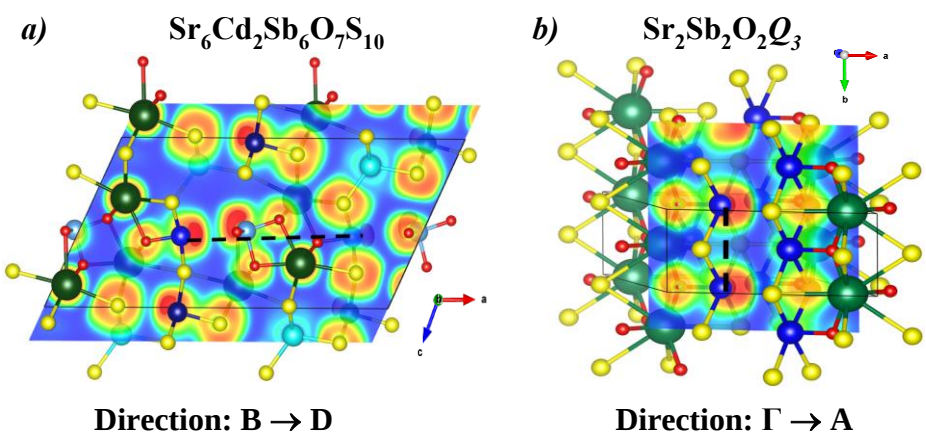

Figure 5.31 : Orbital overlap due to the distance between Sb $5s^2$ pairs in (a) $Sr_6Cd_2Sb_6O_7S_{10}$ and (b) $Sr_2Sb_2O_2S_3$.

Recently, Ha *et al* [71] reported the impact of the orbital overlap direction on the curvature of the conduction band, influencing then the charge carriers' transport properties. This study was done on Sn^{2+} oxides, their calculations revealed the importance of having a Sn – O – Sn angles close to 180° for a higher hybridization, which can lead to greater band dispersion resulting in lower holes effective masses. A deviation from this value can reduce this overlap and be unfavourable for the transport properties. Our structural investigations supported this hypothesis (**Figure 5.32**), where we noticed that the Sb – *Q* – Sb angles are ~180° in the centrosymmetric $Sr_2O_2Sb_2Q_3$ phases whilst in the case of the noncentrosymmetric $Sr_6Cd_2Sb_6S_{10}O_7$ these angles are curved and equal to ~168°, which could decrease the orbital overlap and bandwidth; another explanation for the different holes effective masses observed between these phases.

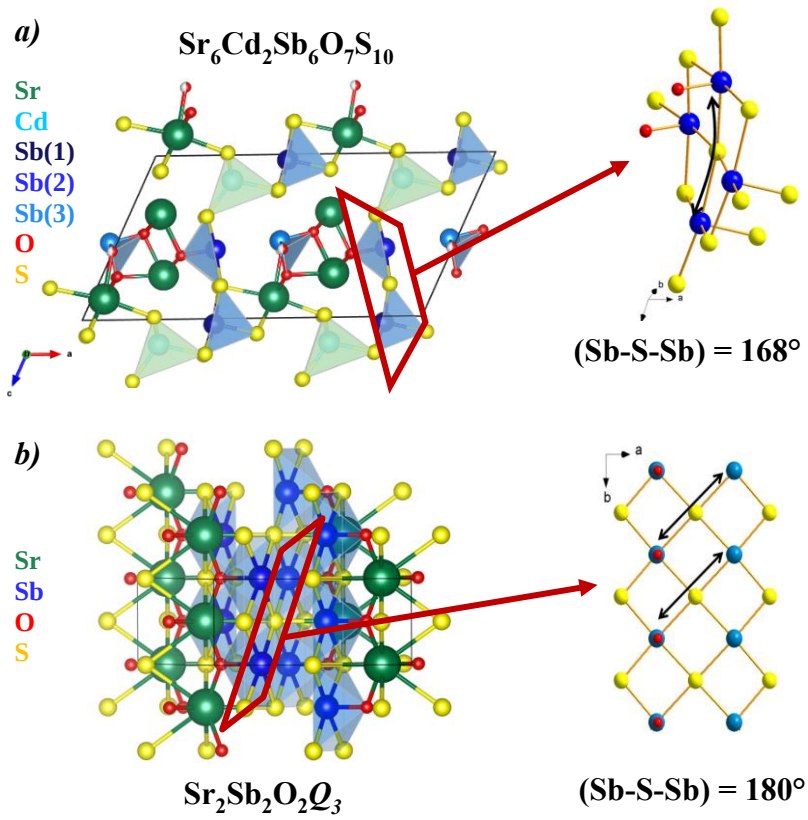

Figure 5.32 : Representation of the structure of $Sr_6Cd_2Sb_6O_7S_{10}$ and $Sr_2Sb_2O_2Q_3$ phases, respectively; with emphasis on the curvature due to deviation of the Sb-S-Sb angles.

5.3.4. Factors affecting the photocurrent response

Another importing result we observed is the capacity of the $Sr_2Sb_2O_2Q_3$ (Q = S, Se) phases to exhibit a photoelectric and photocatalytic activity under solar and UV irradiation, with or without an external bias voltage (**Figure 5.16**, **5.17** and **5.20**). These characteristics are rarely observed with this type of materials and are an indication of their promising ability for photocatalysis in visible light. Trying to relate this property to the structural aspects of these phases, we know that $Sr_2Sb_2O_2Q_3$ contain polar coordination environments around the antimony, which can be the origin of having a photoactivity at 0 V. In fact, having this intrinsic polarity can prompt the separation of the charge carriers without applying an external electric field. This theory was previously reported, where it was found that introducing polar units, with a local electric field, could enhance the electron-hole separation in the photocatalyst[72,73,74] by facilitating the transfer of the photo-generated pairs to different active sites,[75] resulting in a better photoactivity.[76] Other than $Na_3VO_2B_6O_{11}$ polar oxide,[77] we investigated this aspect in the previous chapter for $Sr_6Cd_2Sb_6O_7Q_{10}$ (Q = S, Se) polar oxysulfide.[7,2,1]

The final result to discuss, is the different peak shapes for the photocurrent responses observed for $Sr_2Sb_2O_2S_3$ and $Sr_2Sb_2O_2Se_3$ (**Figure 5.16** and **5.17**). As we mentioned before, having spikey peak shape, in the case of the oxyselenide, suggests the fast separation of the charge carriers upon illumination (fast kinetics); whilst the oxysulfide has slower kinetics (no spikey peak). This can be due to the slightly lower values of effective masses obtained for both the holes and the electrons in the oxyselenide compared to the sulfide, which we have attributed to the higher dispersion of the bands with the presence of the more covalent selenide. For the sake of comparison, looking at **Chapter 4**, $Sr_6Cd_2Sb_6O_7S_{10}$ exhibited similar behaviour although the less covalent sulfide is present. With the presence of three different coordination environment for the antimony SbS_5, $SbOS_4$ and SbO_3, we assigned the existence of the most polar entity SbO_3 within the structure to be the origin of having these anisotropic effects, including the fast electron-hole separation we observed. $Sr_6Cd_2Sb_6O_7Se_{10}$, on the other hand, did not show the same photocurrent response; in addition to its complex structure (which can impact the transport properties, as discussed previously), this can relate to the slightly lower dipoles $[SbOSe_4]^{7-}$ 15 D > $[SbSe_5]^{7-}$ 11.9 D[2] compared to the oxysulfide ($[SbOS_4]^{7-}$ 15.5 D > $[SbS_5]^{7-}$ 12.7 D).[1]

5.4. Conclusion

$Sr_2Sb_2O_2Q_3$ (Q = S, Se) oxychalcogenides are promising candidates for photocatalytic water-splitting under UV and solar irradiation. Our study highlights some key structural characteristics that contributed to this activity and which are necessary for enhanced physical properties, in particular the presence of a stereochemically active lone pair (Sb $5s^2$) and a mixed-anion environment (O:S/Se).

First, our optical measurements demonstrated the influence of the chalcogenide nature on tuning the magnitude of the band gaps (**Figure 5.11**), where the slightly lower electronegativity of the selenide compared to the sulfide can further increase the valence band minimum, resulting in a greater decrease in the band gaps. This can be systematic for designing materials with band gaps that can suit the solar spectrum.

Our DFT calculations, revealed the low effective masses for the electrons and holes in both phases. In the structural context, we attributed this result the presence of the isolated 1D unit (chains of edge-linked $SbOQ_n$ square-based pyramids) in these phases compared with $Sr_6Cd_2Sb_6O_7Q_{10}$ (Q = S, Se) phases that has it linked with the cadmium-based chains, which we suggest minimized the hole mobility. We saw the influence of this structural feature directly on the orbitals overlapping, and on the stereochemical activity of the lone pair; both crucial for having an optimized curvature of the bands. Besides, the exceptionally low hole effective mass for $Sr_2Sb_2O_2Se_3$ can also be attributed to the presence of the highly covalent selenide ion (Sb 5*s* – Se 4*p* hybridization), which resulted higher VBM dispersity. Although the literature states the role of these CdQ units as charge reservoirs, in our case we noticed that their presence could play a structural role that can lead to poorer electronic properties, specifically for the holes.

Both $Sr_2Sb_2O_2Q_3$ (Q = S, Se) materials gave photocurrent responses under solar irradiation with no external bias voltage applied, highlighting the importance of intrinsic polarization within the structure. More efficient electron-hole separation and migration was observed for $Sr_2Sb_2O_2Se_3$ explained by the lower effective masses calculated in the case of the oxyselenide, due to the higher band's dispersion with the presence of the highly covalent selenide ion.

In addition to the photocurrent results, these two phases showed photocatalytic activity, degrading the rhodamine B under solar light and UV irradiation. Whilst their activity was

comparable under UV irradiation (1.79×10^{-2} and 2.28×10^{-2} min^{-1} for S and Se, respectively), $Sr_2Sb_2O_2Se_3$ exhibited better kinetics under solar light (6.45×10^{-3} min^{-1}) unlike the oxysulfide (4.78×10^{-4} min^{-1}), which can be related to the fact of the difficult dispersion for $Sr_2Sb_2O_2S_3$ in aqueous solution. This demonstrates the ability of these phases in photodegradation. With additional work to optimize the applied protocol and the synthetic method, this outcome can be further improved. Simultaneously, another ongoing challenge is to reduce the photodegradation of these phases.

Our study on the $Sr_2Sb_2O_2Q_3$ (Q = S, Se) allowed us to demonstrate numerous aspects, that can be of use in designing new materials with interesting transport properties for efficient photocatalytic applications. Although Sb^{3+} oxychalcogenides are understudied for photocatalytic and photocurrent applications, our investigation proves their promising potential as a result of their tunable band gap, stereochemically active $5s^2$ electron pair and the resulting high electron and hole mobilities.

REFERENCES

(1) Wang, R.; Liang, F.; Wang, F.; Guo, Y.; Zhang, X.; Xiao, Y.; Bu, K.; Lin, Z.; Yao, J.; Zhai, T. Sr6Cd2Sb6O7S10: Strong SHG Response Activated by Highly Polarizable Sb/O/S Groups. *Angewandte Chemie International Edition* **2019**, *58* (24), 8078–8081.

(2) Wang, R.; Wang, F.; Zhang, X.; Feng, X.; Zhao, C.; Bu, K.; Zhang, Z.; Zhai, T.; Huang, F. Improved Polarization in the Sr6Cd2Sb6O7Se10 Oxyselenide through Design of Lateral Sublattices for Efficient Photoelectric Conversion. *Angewandte Chemie* **2022**.

(3) Vonrüti, N. Ferroelectricity and Metastability in (Mixed-Anion) Perovskite Oxides for Improved Solar Water Splitting, 2019.

(4) Clarke, S. J.; Adamson, P.; Herkelrath, S. J.; Rutt, O. J.; Parker, D. R.; Pitcher, M. J.; Smura, C. F. Structures, Physical Properties, and Chemistry of Layered Oxychalcogenides and Oxypnictides. *Inorganic chemistry* **2008**, *47* (19), 8473–8486.

(5) Ueda, K.; Hiramatsu, H.; Hirano, M.; Kamiya, T.; Hosono, H. Wide-Gap Layered Oxychalcogenide Semiconductors: Materials, Electronic Structures and Optoelectronic Properties. *Thin Solid Films* **2006**, *496* (1), 8–15.

(6) Vonrüti, N.; Aschauer, U. Band-Gap Engineering in AB (O x S 1− x) 3 Perovskite Oxysulfides: A Route to Strongly Polar Materials for Photocatalytic Water Splitting. *Journal of Materials Chemistry A* **2019**, *7* (26), 15741–15748.

(7) Al Bacha, S.; Saitzek, S.; McCabe, E. E.; Kabbour, H. Photocatalytic and Photocurrent Responses to Visible Light of the Lone-Pair-Based Oxysulfide Sr6Cd2Sb6S10O7. *Inorganic Chemistry* **2022**, *61* (46), 18611–18621.

(8) Medvedeva, J. E. Magnetically Mediated Transparent Conductors: In 2 O 3 Doped with Mo. *Physical review letters* **2006**, *97* (8), 086401.

(9) Van Hest, M.; Dabney, M. S.; Perkins, J. D.; Ginley, D. S.; Taylor, M. P. Titanium-Doped Indium Oxide: A High-Mobility Transparent Conductor. *Applied Physics Letters* **2005**, *87* (3), 032111.

(10) Hautier, G.; Miglio, A.; Ceder, G.; Rignanese, G.-M.; Gonze, X. Identification and Design Principles of Low Hole Effective Mass P-Type Transparent Conducting Oxides. *Nature communications* **2013**, *4* (1), 1–7.

(11) Medvedeva, J. E.; Hettiarachchi, C. L. Tuning the Properties of Complex Transparent Conducting Oxides: Role of Crystal Symmetry, Chemical Composition, and Carrier Generation. *Physical Review B* **2010**, *81* (12), 125116.

(12) Minami, T. Transparent and Conductive Multicomponent Oxide Films Prepared by Magnetron Sputtering. *Journal of Vacuum Science & Technology A: Vacuum, Surfaces, and Films* **1999**, *17* (4), 1765–1772.

(13) Kamiya, T.; Hosono, H. Material Characteristics and Applications of Transparent Amorphous Oxide Semiconductors. *NPG Asia Materials* **2010**, *2* (1), 15–22.

(14) Fortunato, E.; Barquinha, P.; Martins, R. Oxide Semiconductor Thin-film Transistors: A Review of Recent Advances. *Advanced materials* **2012**, *24* (22), 2945–2986.

(15) Kawazoe, H.; Yanagi, H.; Ueda, K.; Hosono, H. Transparent P-Type Conducting Oxides: Design and Fabrication of Pn Heterojunctions. *Mrs Bulletin* **2000**, *25* (8), 28–36.

(16) Walsh, A.; Watson, G. W. Influence of the Anion on Lone Pair Formation in Sn (II) Monochalcogenides: A DFT Study. *The Journal of Physical Chemistry B* **2005**, *109* (40), 18868–18875.

(17) Kawazoe, H.; Yasukawa, M.; Hyodo, H.; Kurita, M.; Yanagi, H.; Hosono, H. P-Type Electrical Conduction in Transparent Thin Films of CuAlO2. *Nature* **1997**, *389* (6654), 939–942.

(18) Kim, T.; Yoo, B.; Youn, Y.; Lee, M.; Song, A.; Chung, K.-B.; Han, S.; Jeong, J. K. Material Design of New P-Type Tin Oxyselenide Semiconductor through Valence Band Engineering and Its Device Application. *ACS applied materials & interfaces* **2019**, *11* (43), 40214–40221.

(19) Arai, T.; Iimura, S.; Kim, J.; Toda, Y.; Ueda, S.; Hosono, H. Chemical Design and Example of Transparent Bipolar Semiconductors. *Journal of the American Chemical Society* **2017**, *139* (47), 17175–17180.

(20) Panella, J. R.; Chamorro, J.; McQueen, T. M. Synthesis and Structure of Three New Oxychalcogenides: A2O2Bi2Se3 (A= Sr, Ba) and Sr2O2Sb2Se3. *Chemistry of Materials* **2016**, *28* (3), 890–895.

(21) Melot, B. C.; Tackett, R.; O'Brien, J.; Hector, A. L.; Lawes, G.; Seshadri, R.; Ramirez, A. P. Large Low-Temperature Specific Heat in Pyrochlore Bi 2 Ti 2 O 7. *Physical Review B* **2009**, *79* (22), 224111.

(22) Petříček, V.; Dušek, M.; Palatinus, L. Crystallographic Computing System JANA2006: General Features. *Zeitschrift für Kristallographie-Crystalline Materials* **2014**, *229* (5), 345–352.

(23) Lee, A. Charge Flipping for Routine Structure Solution. *Journal of Applied Crystallography* **2013**, *46* (5), 1306–1315.

(24) Palatinus, L.; Chapuis, G. SUPERFLIP–a Computer Program for the Solution of Crystal Structures by Charge Flipping in Arbitrary Dimensions. *Journal of Applied Crystallography* **2007**, *40* (4), 786–790.

(25) Rodriguez-Carvajal, J. Fullprof: A Program for Rietveld Refinement and Profile Matching Analysis of Complex Powder Diffraction Patterns. *Laboratoire Léon Brillouin (CEA-CNRS)* **1991**.

(26) Dollase, W. A. Correction of Intensities for Preferred Orientation in Powder Diffractometry: Application of the March Model. *Journal of Applied Crystallography* **1986**, *19* (4), 267–272.

(27) Stokes, H. T.; Hatch, D. M.; Campbell, B. J.; Tanner, D. E. ISODISPLACE: A Web-based Tool for Exploring Structural Distortions. *Journal of Applied Crystallography* **2006**, *39* (4), 607–614.

(28) Kubelka, P.; Munk, F. A Contribution to the Optics of Pigments. *Z. Tech. Phys* **1931**, *12* (593), 193.

(29) Tauc, J.; Grigorovici, R.; Vancu, A. Optical Properties and Electronic Structure of Amorphous Germanium. *physica status solidi (b)* **1966**, *15* (2), 627–637.

(30) Jiang, S.; Liu, Y.; Xu, J. Rare Earth Oxynitrides: Promising Visible-Light-Driven Photocatalysts for Water Splitting. *Materials Advances* **2021**, *2* (4), 1190–1203.

(31) Siritanaratkul, B.; Maeda, K.; Hisatomi, T.; Domen, K. Synthesis and Photocatalytic Activity of Perovskite Niobium Oxynitrides with Wide Visible-light Absorption Bands. *ChemSusChem* **2011**, *4* (1), 74–78.

(32) Lei, S.; Cheng, D.; Gao, X.; Fei, L.; Lu, W.; Zhou, J.; Xiao, Y.; Cheng, B.; Wang, Y.; Huang, H. A New Low-Temperature Solution Route to Aurivillius-Type Layered Oxyfluoride Perovskites Bi2MO5F (M= Nb, Ta) as Photocatalysts. *Applied Catalysis B: Environmental* **2017**, *205*, 112–120.

(33) Butler, M.; Ginley, D. Prediction of Flatband Potentials at Semiconductor-electrolyte Interfaces from Atomic Electronegativities. *Journal of the Electrochemical Society* **1978**, *125* (2), 228.

(34) Xu, Y.; Schoonen, M. A. The Absolute Energy Positions of Conduction and Valence Bands of Selected Semiconducting Minerals. *American Mineralogist* **2000**, *85* (3–4), 543–556.

(35) BaQais, A.; Curutchet, A.; Ziani, A.; Ait Ahsaine, H.; Sautet, P.; Takanabe, K.; Le Bahers, T. Bismuth Silver Oxysulfide for Photoconversion Applications: Structural and Optoelectronic Properties. *Chemistry of Materials* **2017**, *29* (20), 8679–8689.

(36) Shaikh, S. K.; Inamdar, S. I.; Ganbavle, V. V.; Rajpure, K. Y. Chemical Bath Deposited ZnO Thin Film Based UV Photoconductive Detector. *Journal of Alloys and Compounds* **2016**, *664*, 242–249.

(37) Zhao, Q.; Wang, W.; Carrascoso-Plana, F.; Jie, W.; Wang, T.; Castellanos-Gomez, A.; Frisenda, R. The Role of Traps in the Photocurrent Generation Mechanism in Thin InSe Photodetectors. *Materials Horizons* **2020**, *7* (1), 252–262.

(38) Inamdar, S.; Ganbavle, V.; Shaikh, S.; Rajpure, K. Effect of the Buffer Layer on the Metal–Semiconductor–Metal UV Photodetector Based on Al-doped and Undoped ZnO Thin Films with Different Device Structures. *physica status solidi (a)* **2015**, *212* (8), 1704–1712.

(39) Parkinson, B.; Turner, J.; Peter, L.; Lewis, N.; Sivula, K.; Domen, K.; Bard, A. J.; Fiechter, S.; Collazo, R.; Hannappel, T. *Photoelectrochemical Water Splitting: Materials, Processes and Architectures*; Royal Society of Chemistry, 2013.

(40) Peter, L. M. Energetics and Kinetics of Light-Driven Oxygen Evolution at Semiconductor Electrodes: The Example of Hematite. *Journal of Solid State Electrochemistry* **2013**, *17*, 315–326.

(41) Shi, Y.-F.; Li, X.-F.; Zhang, Y.-X.; Lin, H.; Ma, Z.; Wu, L.-M.; Wu, X.-T.; Zhu, Q.-L. [(Ba19Cl4)(Ga6Si12O42S8)]: A Two-Dimensional Wide-Band-Gap Layered Oxysulfide with Mixed-Anion Chemical Bonding and Photocurrent Response. *Inorganic chemistry* **2019**, *58* (10), 6588–6592.

(42) Ogisu, K.; Ishikawa, A.; Shimodaira, Y.; Takata, T.; Kobayashi, H.; Domen, K. Electronic Band Structures and Photochemical Properties of La− Ga-Based Oxysulfides. *The Journal of Physical Chemistry C* **2008**, *112* (31), 11978–11984.

(43) Leroy, S.; Blach, J.-F.; Huvé, M.; Léger, B.; Kania, N.; Henninot, J.-F.; Ponchel, A.; Saitzek, S. Photocatalytic and Sonophotocatalytic Degradation of Rhodamine B by Nano-Sized La2Ti2O7 Oxides Synthesized with Sol-Gel Method. *Journal of Photochemistry and Photobiology A: Chemistry* **2020**, *401*, 112767. https://doi.org/10.1016/j.jphotochem.2020.112767.

(44) Bott, A. W. Electrochemistry of Semiconductors. *Current Separations* **1998**, *17*, 87–92.

(45) Matsumoto, Y.; Omae, M.; Watanabe, I.; Sato, E. Photoelectrochemical Properties of the Zn-Ti-Fe Spinel Oxides. *Journal of the Electrochemical Society* **1986**, *133* (4), 711.

(46) Kalanur, S. S. Structural, Optical, Band Edge and Enhanced Photoelectrochemical Water Splitting Properties of Tin-Doped WO3. *Catalysts* **2019**, *9* (5), 456.

(47) Lin, L.; Lin, J. M.; Wu, J. H.; Hao, S. C.; Lan, Z. Photovoltage Enhancement of Dye Sensitised Solar Cells by Using ZnO Modified TiO2 Electrode. *null* **2010**, *14* (5), 370–374. https://doi.org/10.1179/143307510X12820854748791.

(48) Ohtani, B. Photocatalysis by Inorganic Solid Materials: Revisiting Its Definition, Concepts, and Experimental Procedures. *Advances in Inorganic Chemistry* **2011**, *63*, 395–430.

(49) Luo, Y.; Qiao, L.; Wang, H.; Lan, S.; Shen, Y.; Lin, Y.; Nan, C. Bismuth Oxysulfide and Its Polymer Nanocomposites for Efficient Purification. *Materials* **2018**, *11* (3), 447.

(50) Momma, K. *Visualization for Electronic and Structural Analysis*; 2019.

(51) Perdew, J. P.; Burke, K.; Ernzerhof, M. Generalized Gradient Approximation Made Simple. *Physical review letters* **1996**, *77* (18), 3865.

(52) Ishikawa, A.; Takata, T.; Kondo, J. N.; Hara, M.; Kobayashi, H.; Domen, K. Oxysulfide Sm2Ti2S2O5 as a Stable Photocatalyst for Water Oxidation and Reduction under Visible Light Irradiation (Λ≤ 650 Nm). *Journal of the American Chemical Society* **2002**, *124* (45), 13547–13553.

(53) Ishikawa, A.; Takata, T.; Matsumura, T.; Kondo, J. N.; Hara, M.; Kobayashi, H.; Domen, K. Oxysulfides Ln2Ti2S2O5 as Stable Photocatalysts for Water Oxidation and Reduction under Visible-Light Irradiation. *J. Phys. Chem. B* **2004**, *108* (8), 2637–2642. https://doi.org/10.1021/jp036890x.

(54) Wang, R.; Liang, F.; Wang, F.; Guo, Y.; Zhang, X.; Xiao, Y.; Bu, K.; Lin, Z.; Yao, J.; Zhai, T. Sr6Cd2Sb6O7S10: Strong SHG Response Activated by Highly Polarizable Sb/O/S Groups. *Angewandte Chemie* **2019**, *131* (24), 8162–8165.

(55) Allen, J. P.; Carey, J. J.; Walsh, A.; Scanlon, D. O.; Watson, G. W. Electronic Structures of Antimony Oxides. *The Journal of Physical Chemistry C* **2013**, *117* (28), 14759–14769.

(56) Wang, X.; Li, Z.; Kavanagh, S. R.; Ganose, A. M.; Walsh, A. Lone Pair Driven Anisotropy in Antimony Chalcogenide Semiconductors. *arXiv preprint arXiv:2109.08117* **2021**.

(57) Wang, V.; Xu, N.; Liu, J.-C.; Tang, G.; Geng, W.-T. VASPKIT: A User-Friendly Interface Facilitating High-Throughput Computing and Analysis Using VASP Code. *Computer Physics Communications* **2021**, *267*, 108033.

(58) Gamon, J.; Giaume, D.; Wallez, G.; Labégorre, J.-B.; Lebedev, O.; Al Rahal Al Orabi, R.; Haller, S.; Le Mercier, T.; Guilmeau, E.; Maignan, A. Substituting Copper with Silver in the BiMOCh Layered Compounds (M= Cu or Ag; Ch= S, Se, or Te): Crystal, Electronic Structure, and Optoelectronic Properties. *Chemistry of Materials* **2018**, *30* (2), 549–558.

(59) Hiramatsu, H.; Ueda, K.; Ohta, H.; Hirano, M.; Kikuchi, M.; Yanagi, H.; Kamiya, T.; Hosono, H. Heavy Hole Doping of Epitaxial Thin Films of a Wide Gap P-Type Semiconductor, LaCuOSe, and Analysis of the Effective Mass. *Applied physics letters* **2007**, *91* (1), 012104.

(60) Wang, X.; Li, Z.; Kavanagh, S. R.; Ganose, A. M.; Walsh, A. Lone Pair Driven Anisotropy in Antimony Chalcogenide Semiconductors. *Physical Chemistry Chemical Physics* **2022**, *24* (12), 7195–7202.

(61) Mohn, C. E.; Stølen, S. Influence of the Stereochemically Active Bismuth Lone Pair Structure on Ferroelectricity and Photocalytic Activity of Aurivillius Phase Bi 2 WO 6. *Physical Review B* **2011**, *83* (1), 014103.

(62) Hu, C.; Zhang, B.; Lei, B.-H.; Pan, S.; Yang, Z. Advantageous Units in Antimony Sulfides: Exploration and Design of Infrared Nonlinear Optical Materials. *ACS applied materials & interfaces* **2018**, *10* (31), 26413–26421.

(63) Hu, C.; Mutailipu, M.; Wang, Y.; Guo, F.; Yang, Z.; Pan, S. The Activity of Lone Pair Contributing to SHG Response in Bismuth Borates: A Combination Investigation from Experiment and DFT Calculation. *Physical Chemistry Chemical Physics* **2017**, *19* (37), 25270–25276.

(64) Yin, R.; Hu, C.; Lei, B.-H.; Pan, S.; Yang, Z. Lone Pair Effects on Ternary Infrared Nonlinear Optical Materials. *Physical Chemistry Chemical Physics* **2019**, *21* (9), 5142–5147.

(65) Payne, D. J.; Egdell, R. G.; Walsh, A.; Watson, G. W.; Guo, J.; Glans, P.-A.; Learmonth, T.; Smith, K. E. Electronic Origins of Structural Distortions in Post-Transition Metal Oxides: Experimental and Theoretical Evidence for a Revision of the Lone Pair Model. *Physical review letters* **2006**, *96* (15), 157403.

(66) Walsh, A.; Payne, D. J.; Egdell, R. G.; Watson, G. W. Stereochemistry of Post-Transition Metal Oxides: Revision of the Classical Lone Pair Model. *Chemical Society Reviews* **2011**, *40* (9), 4455–4463.

(67) Li, Q. H.; Gao, T.; Wang, T. H. Optoelectronic Characteristics of Single CdS Nanobelts. *Applied Physics Letters* **2005**, *86* (19), 193109.

(68) Gao, T.; Li, Q. H.; Wang, T. H. CdS Nanobelts as Photoconductors. *Applied Physics Letters* **2005**, *86* (17), 173105.

(69) Dong, L.; Jiao, J.; Coulter, M.; Love, L. Catalytic Growth of CdS Nanobelts and Nanowires on Tungsten Substrates. *Chemical Physics Letters* **2003**, *376* (5–6), 653–658.

(70) Gao, T.; Wang, T. Catalyst-Assisted Vapor− Liquid− Solid Growth of Single-Crystal Cds Nanobelts and Their Luminescence Properties. *The Journal of Physical Chemistry B* **2004**, *108* (52), 20045–20049.

(71) Ha, V.-A.; Ricci, F.; Rignanese, G.-M.; Hautier, G. Structural Design Principles for Low Hole Effective Mass S-Orbital-Based p-Type Oxides. *Journal of Materials Chemistry C* **2017**, *5* (23), 5772–5779.

(72) Dong, X.-D.; Zhang, Y.-M.; Zhao, Z.-Y. Role of the Polar Electric Field in Bismuth Oxyhalides for Photocatalytic Water Splitting. *Inorganic Chemistry* **2021**, *60* (12), 8461–8474.

(73) Lou, Z.; Wang, P.; Huang, B.; Dai, Y.; Qin, X.; Zhang, X.; Wang, Z.; Liu, Y. Enhancing Charge Separation in Photocatalysts with Internal Polar Electric Fields. *ChemPhotoChem* **2017**, *1* (5), 136–147.

(74) Dong, X.-D.; Yao, G.-Y.; Liu, Q.-L.; Zhao, Q.-M.; Zhao, Z.-Y. Spontaneous Polarization Effect and Photocatalytic Activity of Layered Compound of BiOIO3. *Inorganic Chemistry* **2019**, *58* (22), 15344–15353.

(75) Chen, F.; Huang, H.; Guo, L.; Zhang, Y.; Ma, T. The Role of Polarization in Photocatalysis. *Angewandte Chemie International Edition* **2019**, *58* (30), 10061–10073.

(76) Guo, Y.; Shi, W.; Zhu, Y. Internal Electric Field Engineering for Steering Photogenerated Charge Separation and Enhancing Photoactivity. *EcoMat* **2019**, *1* (1), e12007.

(77) Chen, J.; Zhai, Y.; Yu, Y.; Luo, J.; Fan, X. Spatial Separation of Photo-Induced Charge Carriers in a Na3VO2B6O11 Polar Material and Its Enhanced Photocatalytic Activity. *Applied Surface Science* **2021**, *556*, 149809.

Appendix 3

3.1. Comparison of related structures for $Sr_2Sb_2O_2S_3$

3.1.1. *C*2 model

In addition to the reported structure of $P2_1/c$ symmetry, other distortions form as $C2/m$ model were explored using ISODISTORT.[1] A polar model of $C2$ symmetry can be obtained using Γ_1^- irrep, which allows polar displacements of atoms along [010] to break the mirror plane in $C2/m$. We didn't see any improvement in the fit using this model (**Figure 3.1** and **Tables 3.1-3.2**).

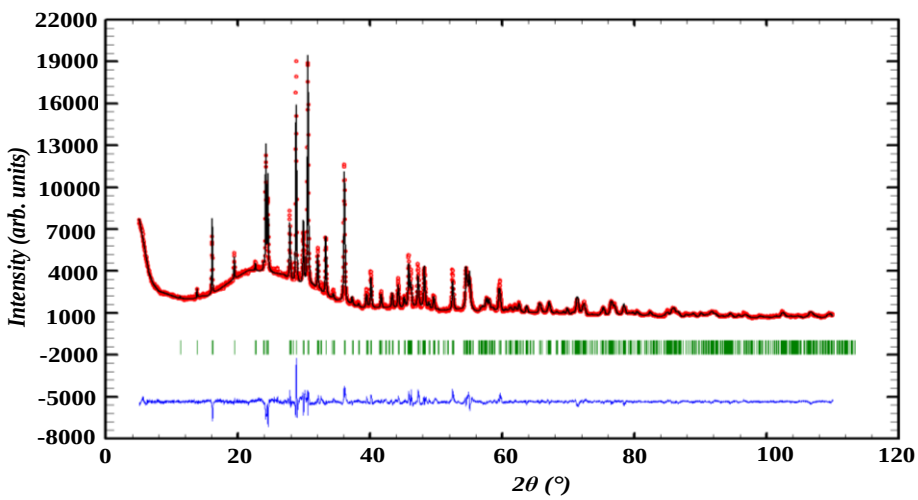

Figure 3.1 : Powder XRD Rietveld refinement profile of $Sr_2Sb_2O_2S_3$ in the $C2$ space group: the experimental (red) and the calculated (black) patterns are superimposed; the difference curve is represented in blue and Bragg positions in green. A March-Dollase function was used to model preferred orientation along the <010> direction.

Table 3.1. Refinement details from Rietveld refinement of $Sr_2Sb_2O_2S_3$ using room temperature XRPD data in space group $C2$; cell parameters are a = 13.0409(3) Å, b = 3.9543(1) Å, c = 9.3131(2) Å, β = 122.517(1) °, V = 404.97(1) Å^3, R_p = 4.81 %, R_{wp} = 6.38 %, R_{exp} = 2.38, R_f = 4.30, χ^2 = 7.18.

Atom	Wyckoff site	*X*	*y*	*Z*	U_{iso} (Å^2)
Sr1	*4c*	0.0942(3)	0.017(6)	0.3856(4)	0.0001(1)
Sb1	*4c*	0.7059(3)	0.050(6)	0.1444(4)	0.0001(1)
S1	*4c*	0.3790(6)	-0.018(8)	0.309(1)	0.0001(1)
S2	*2a*	0	0	0	0.0001(1)
O1	*4c*	0.677(1)	-0.017(9)	0.345(2)	0.0001(1)

Table 3.2. Bond distances (Å) for $Sr_2Sb_2O_2S_3$ following the Rietveld refinement in the space group *C*2.

Atoms 1,2	$d_{1,2}$ (Å)	Atoms 1,2	$d_{1,2}$ (Å)
Sr1-O1	2.68(1)	Sb1-S2	2.88(1)
Sr1-S1	3.24(2)	S1-S1	3.247(8)
Sr1-S2	3.109(3)	S1-O1	3.45(3)
Sb1-O1	2.11(2)	S2-O1	3.36(2)
Sb1-S1	2.58(2)	O1-O1	3.16(3)

3.1.2. *Cm* model

We also investigated the lower symmetry *Cm* model, derives from the *C*2/*m* model by using the Γ_2^- irrep to add ten additional parameters corresponding to the displacements of atoms within the *ac* plane. Again, did not give an improved fit compared with the *C*2/*m* model (**Figure 3.2** and **Tables 3.3-3.4**).

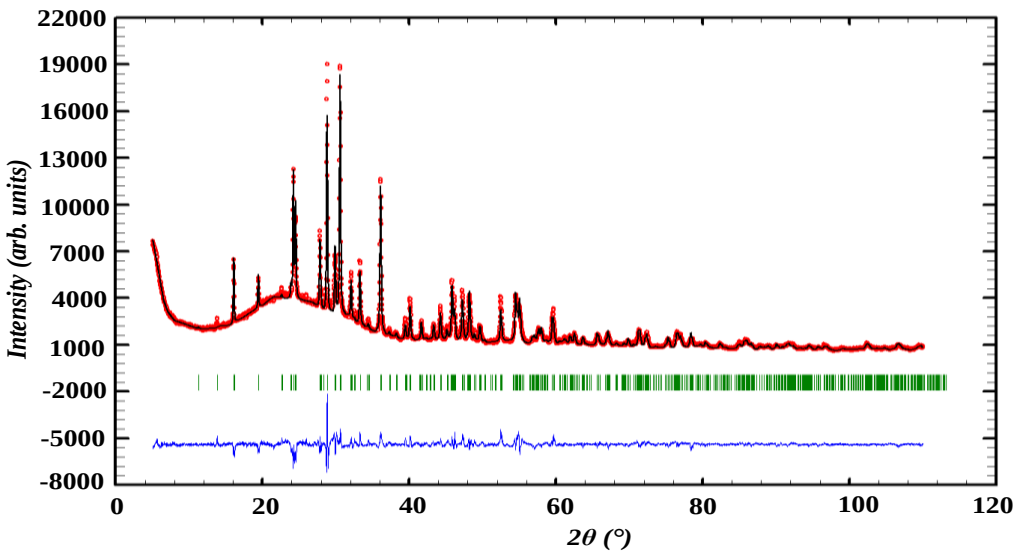

Figure 3.2 : Powder XRD Rietveld refinement profiles of $Sr_2Sb_2O_2S_3$ in the *Cm* space group: the experimental (red) and the calculated (black) patterns are superimposed; the difference curve is represented in blue and Bragg positions in green. A March-Dollase function was used to model preferred orientation along the <010> direction.

Table 3.3. Refinement details from Rietveld refinement of $Sr_2Sb_2O_2S_3$ using room temperature XRPD data in space group *Cm*; cell parameters are a = 13.0410(3) Å, b = 3.9544(1) Å, c = 9.3135(2) Å, β = 122.518(1) °, V = 405.00(2) Å^3, R_p = 5.15 %, R_{wp} = 6.83 %, R_{exp} = 2.38, R_f = 10.2, χ^2 = 7.23.

Atom	Wyckoff site	*x*	*y*	*z*	U_{iso} (Å^2)
Sr1	*2a*	0.0941(7)	0	0.3834(9)	0.0033(4)
Sr2	*2a*	-0.0973	0	0.6114	0.0033(4)
Sb1	*2a*	0.706(1)	0	0.134(1)	0.0033(4)
Sb2	*2a*	0.294(1)	0	0.846(1)	0.0033(4)
S1	*2a*	0.380(2)	0	0.279(3)	0.0033(4)
S2	*2a*	0.617(2)	0	0.662(3)	0.0033(4)
S3	*2a*	0.029(1)	0	-0.007(3)	0.0033(4)
O1	*2a*	0.700(4)	0	0.370(5)	0.0033(4)
O2	*2a*	0.073(3)	0	0.595(5)	0.0033(4)

Table 3.4. Bond distances (Å) for $Sr_2Sb_2O_2S_3$ following the Rietveld refinement in the space group *Cm*.

Atoms 1,2	$d_{1,2}$ (Å)	Atoms 1,2	$d_{1,2}$ (Å)	Atoms 1,2	$d_{1,2}$ (Å)
Sr1-O1	2.45(3) ×2	Sb1-S1	2.76(1) ×2	Sr2-S2	3.24(2) ×2
Sr1-O2	2.13(5)	Sb1-S3	2.77(1) ×2	S1-S2	3.23(2)
Sr1-S1	3.12(2) ×2	Sb2-O2	2.55(3)	S1-O2	3.31(2) ×2
Sr1-S2	3.31(2) ×2	Sb2-S2	2.81(1) ×2	O1-S2	3.43(6)
Sr1-S3	3.26(2)	Sb2-S3	3.27(1) ×2	S2-O2	2.0510(9) ×2
Sr2-O1	2.38(3)	Sb1-O1	2.24(5)		
Sr2-O2	2.31(4)	Sr2-S3	3.01(2)		

3.2. $Sr_2Sb_2O_2S_3$ phase transition comparison

Table 3.5 gathers the main structural and morphological characteristics, such as the color, synthetic temperature, unit cell parameters, EDX and SEM analysis and Pawley refinement for the titled orange oxysulfide powder and the red colored powder upon temperature increase.

Table 3.5. Structural information for $Sr_2Sb_2O_2S_3$ powder before (orange) and after phase transition (red).

	$Sr_2Sb_2O_2S_3$	$Sr_xSb_yO_zS_u$
Powder color	Orange 	Red 
Synthesis T°C	700 °C	800 °C
Unit cell parameters	a =13.0475 Å b = 3.9559 Å c = 9.3143 Å β = 122.498 °	a = 12.6542 Å b = 17.3486 Å c = 11.0075 Å β = 92.405 °
EDX ratio (%)	Sb: 28.9 Sr: 28.1 S: 43.0	Sb: 29.9 Sr: 29.81 S: 40.29
SEM	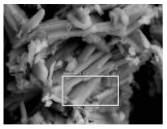	
Pawley refinement	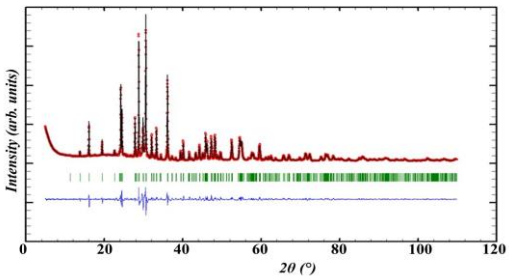	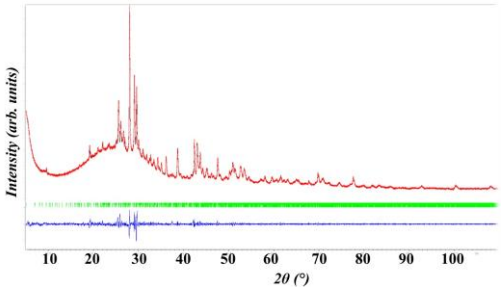

3.3. Photocatalytic activity of $Sr_2Sb_2O_2S_3$

Photocatalytic measurements for $Sr_2Sb_2O_2S_3$ are presented in this section. The test was performed under UV (254 nm, 40 W) and solar (100 mW cm^{-2}) irradiations on a solution consisting of 200 mL of Rhodamine B (5 $\times 10^{-6}$ mol dm^{-3}) and 100 mg of the photocatalyst powder ($Sr_2Sb_2O_2Q_3$ (Q = S, Se)). In this case the solution was stirred for 30 min in the dark to ensure an appropriate adsorption/desorption equilibrium without prior treatment in a sonicator for 20 mins.

Under UV irradiation, photocatalysis of Rhodamine B by $Sr_2Sb_2S_3O_2$ gave a 100 % degradation in 60 mins, based on the transparency that we saw in the last intake (**Figure 3.3a**). However, in the first 30 mins of the experiment no degradation occurred. The photocatalytic kinetics at the solid-liquid interface were described using the Langmuir-Hinshelwood model (LH),[2] taking an order 1 for the photodegradation reaction and plotting Ln(C_0/C) *vs.* time to determine the apparent speed constant (k_{app}) in **Figure 3.3b**. The plot showed a latency time of 30 min at the start of the reaction, then a linear evolution occurred with an apparent speed constant of 6.6×10^{-2} min^{-1}, indicating good kinetic performance of $Sr_2Sb_2O_2S_3$.

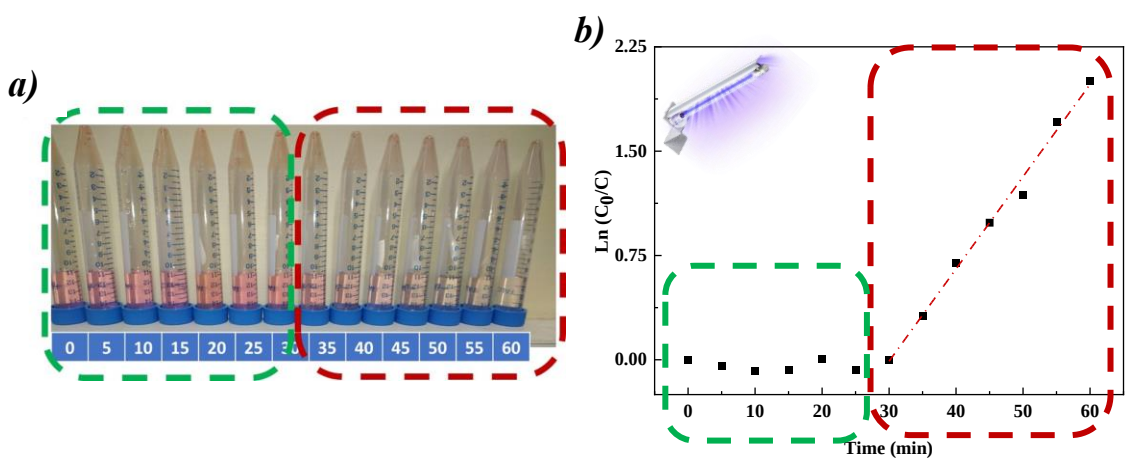

Figure 3.3 : (a) Langmuir-Hinshelwood kinetic plot for the degradation of Rhodamine B on $Sr_2Sb_2O_2S_3$ under UV (254 nm, 40 W) irradiation. (b) Samples taken at regular intervals for absorption observation.

Unlike UV irradiation, photocatalysis under solar irradiation in **Figure 3.4** did not show promising results. It is clear from **Figure 3.4a** that a minimal degradation occurred (judging from the fade discoloration of Rhodamine B), indication of the lack of photocatalytic activity efficiency.

This was also confirmed by the kinetics of the reaction in **Figure 3.4b**, where no clear of the curve in function of time can be detected.

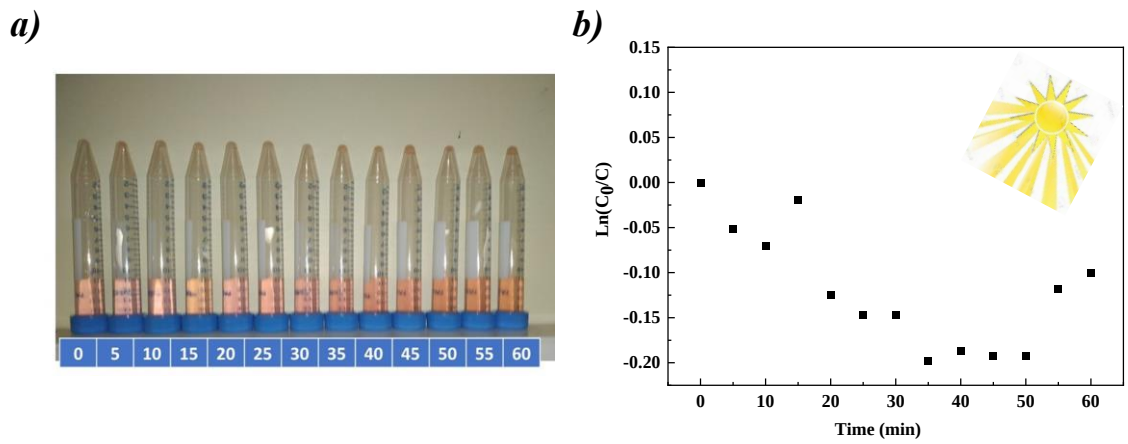

Figure 3.4 : (a) Langmuir-Hinshelwood kinetic plot for the degradation of Rhodamine B on $Sr_2Sb_2O_2S_3$ under Solar (100 mW.cm^{-2}) irradiation. (b) Samples taken at regular intervals for absorption observation.

The problem of the 30 mins latency time before the reaction occurred was due to the difficulty of the title phase to disperse in the solution, which is why we adopted the protocol described in the **Chapter 5**, **section 5.2.4.** where 20 minutes sonication was added to the protocol in order to break up agglomerates and give the best photocatalytic efficiency.

3.4. DFT calculations for $Sr_2Sb_2O_2Q_3$ (Q = S, Se) in the $P2_1/c$ model

The DFT calculations were also done using the $P2_1/c$ model. **Table 3.6** gives the charge carriers' effective masses and **Figure 3.5** represents the computed electronic band structure, density of states and fat bands corresponding to $S_{r2}Sb_2O_2S_3$ (**Figure 3.5a**, **3.5b** and **3.5c**) and $Sr_2Sb_2O_2Se_3$ (**Figure 3.5d**, **3.5e** and **3.5f**).

Table 3.6. Calculated electron (m_e^*) and hole (m_h^*) effective mass, m_0 being the free electron mass for $Sr_2Sb_2O_2Q_3$ for $P2_1/c$ model.

Directions	$Sr_2Sb_2O_2S_3$		$Sr_2Sb_2O_2Se_3$	
	m_e/m_0	m_h/m_0	m_e/m_0	m_h/m_0
$\Gamma \rightarrow A$	1.958(8)	0.718(4)	1.393(1)	0.447(7)
$\Gamma \rightarrow B$	0.651(8)	0.276(2)	0.428(3)	0.190(2)
$\Gamma \rightarrow Z$	0.191(6)	0.848(7)	0.163(2)	0.525(2)
$\Gamma \rightarrow Y_2$	1.681(2)	1.482(2)	1.656(2)	1.013(1)

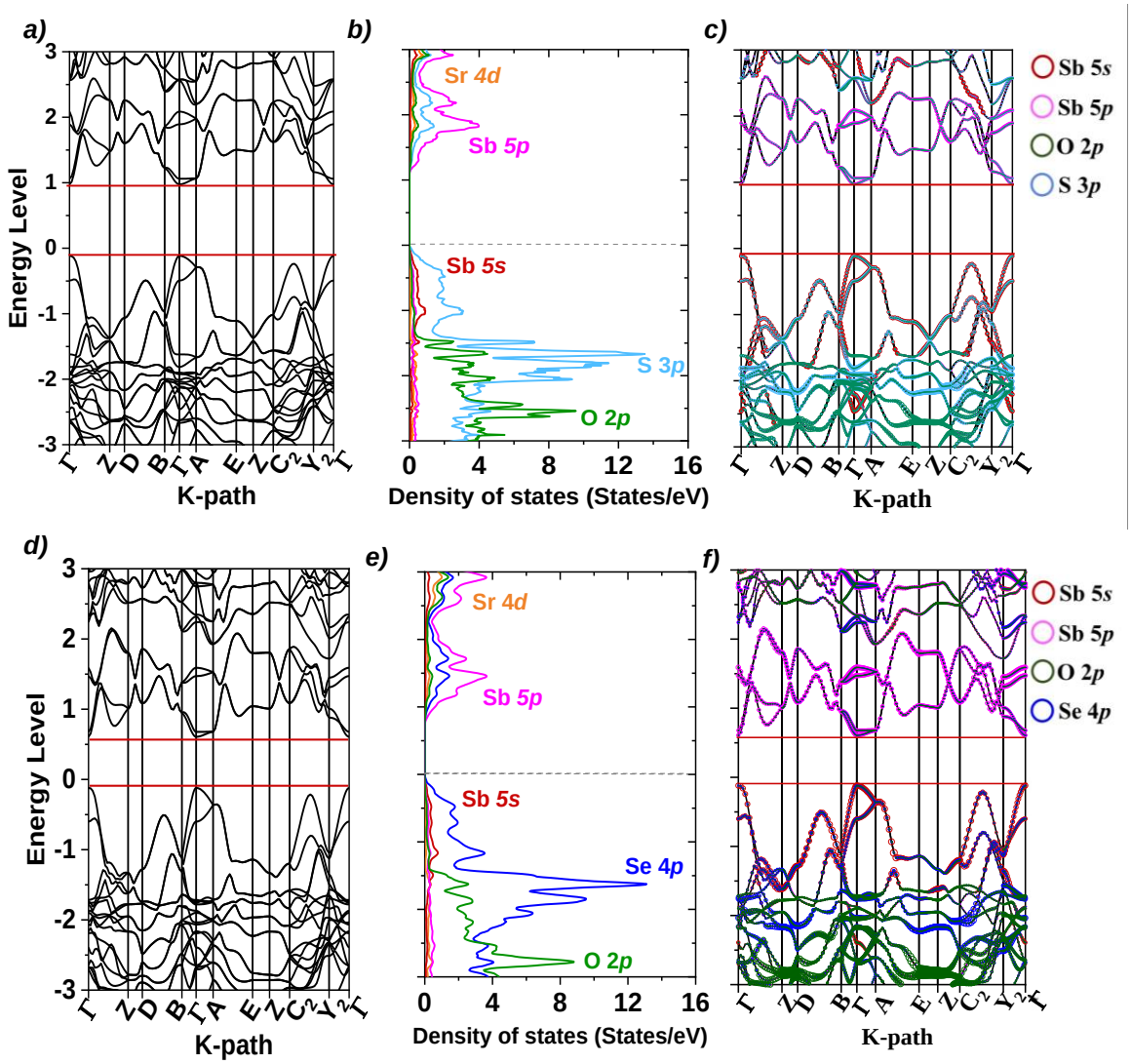

Figure 3.5 : (a) and (d) Electronic band structure, (b) and (e) Projected DOS is shown for the Sr 3*d*, Sb 5*s*, Sb 5*p*, S 3*p*/ Se 4*p* and O 2*p* states. The Fermi level is set to 0, (c) and (f) Fat bands showing the Sb 5*s*, Sb 5*p*, O 2*p* and S 3*p* states, calculated in the $P2_1/c$ model for $Sr_2Sb_2O_2S_3$ and $Sr_2Sb_2O_2Se_3$, respectively.

REFERENCES

(1) Stokes, H. T.; Hatch, D. M.; Campbell, B. J.; Tanner, D. E. ISODISPLACE: A Web-based Tool for Exploring Structural Distortions. *Journal of Applied Crystallography* **2006**, *39* (4), 607–614.

(2) Ohtani, B. Photocatalysis by Inorganic Solid Materials: Revisiting Its Definition, Concepts, and Experimental Procedures. *Advances in Inorganic Chemistry* **2011**, *63*, 395–430.

General Conclusion & Perspectives

This thesis focuses on investigating oxychalcogenide materials as potential candidates for water-splitting photocatalysis under visible light. In order to understand their structure-properties relationship and evaluate their applicative potential, their structural analysis, photoelectrochemical measurements, photocatalytic activity and electronic structure analysis were studied. Thus, the aim of this work was to investigate proposed design features for oxysulfide photocatalysts such as the optimized bandgap through anionic manipulation (oxygen/chalcogenide ratio), the connectivity, the cation choice and the polarity.

Several oxychalcogenide materials were synthesized and characterized before photoelectrochemical measurements were performed. The experimental work was combined with density functional theory calculations to give further insight into the materials properties. The studies were carried out around three family of oxychalcogenides: iron-based oxychalcogenides $La_2O_2Fe_2OQ_2$ and $CaFeOQ$ (Q = S, Se), oxysulfide $Sr_6Cd_2Sb_6O_7S_{10}$ and $Sr_2Sb_2O_2Q_3$ (Q = S, Se) oxychalcogenides.

Chapter 1 described some key features of oxychalcogenide photocatalysts, such as the structural connectivity (layers, fragments); the cation choice (lone pair cations, transition metals); the band structure properties (regarding different orbitals contribution) and the polarity (having polar units or polar structures) for enhanced transport properties. This informed our research and identified proposed design features we would explore to understand their influence on the photocatalytic activity. **Chapter 2**, briefly described the basis of the experimental and computational methods that were used.

In **Chapter 3**, the photocatalytic (and related) properties of four iron-based oxychalcogenides $La_2O_2Fe_2OQ_2$ and $CaFeOQ$ (Q = S, Se) were presented. This initial work highlighted the importance of choosing materials with appropriate band gaps: $La_2O_2Fe_2OQ_2$ phases (with small bandgaps due to strong Fe hybridization in the Fe_2O layers) were not photoactive, whilst $CaFeOQ$ oxychalcogenides were suitable photocathode materials under visible light, due to their wider bandgaps. Photocurrent measurements revealed the good activity of these materials under solar irradiation and a wide range of wavelengths (450 – 627 nm). The photocurrent response of CaFeOSe (**Figure 3.8**) revealed a very efficient electron-hole separation and migration. This effective e^-/h^+ separation may reflect the polarity of the structure, of $Cmc2_1$ symmetry composed of polar $FeSe_2O_2$ units. Comparison with the non-polar polymorph of CaFeOSe[1], composed of the

same polar $FeSe_2O_2$ units, would allow the influence of the polarity of the structure (compared with the presence of polar units) to be investigated. Unfortunately attempts to synthesise this non-polar polymorph were unsuccessful. Future work to prepare this, and other non-polar phases, would be needed to explore this aspect of polarity further. The probable oxidation of iron in CaFeOS during photocurrent measurements highlights a significant drawback of this class of materials for photocatalysis. This suggested the need to focus next on oxychalcogenide systems containing more redox-stable cations.

Chapter 4 focuses on the oxysulfide $Sr_6Cd_2Sb_6O_7S_{10}$. Although it showed better stability than CaFeOS in photocurrent and photocatalytic measurements, a lot of work was needed to improve the electrolyte system and reduce sample degradation, and further work to optimize the electrolyte is still needed. This highlights the chemical challenges of these materials for photocatalysis. Further work to optimize film deposition and operating conditions are underway. $Sr_6Cd_2Sb_6O_7S_{10}$ showed a promising photocurrent response under irradiation with visible light, and results of DFT calculations explain this activity. The optimal band gap in $Sr_6Cd_2Sb_6O_7S_{10}$ results largely from the $Sb(1)S_5$ and $Sb(2)S_4O$ units, which contribute to the top of the valence band (**Figures 4.18**, **4.19**), illustrating the role of the softer chalcogenide anions in reducing the bandgap.

The photocurrent response of $Sr_6Cd_2Sb_6O_7S_{10}$ (**Figure 4.8**) is typical of a material with very efficient electron-hole separation and migration which could be due to the polar structure and/or the presence of polar Sb units. This is supported by DFT calculations which indicate different mobility for electrons and holes, and very mobile electrons (with an effective mass below 0.5 m_0) within the layers. This results from effective overlap of Sb 5*p* and anion states in the conduction band. On the other hand, hole mobility was poor and so its relevant to consider the Sb 5*s* – S 3*p* states which make up the top of the valence band. Of the three Sb environments, the stereochemical activity of the Sb^{3+} lone pair (and the polarity of the unit) increases with increasing oxide coordination: $Sb(1)S_5 < Sb(2)OS_4 < Sb(3)O_3$ (see COHP calculations presented in **Figure 4.19**). We thus identify the $Sb(3)O_3$ entity as the most polar Sb site, contributing the most to the polar nature and enhancing electron-hole separation, whilst $Sb(1)S_5$ entities contribute most to the DOS at the VBM. This study demonstrates the importance of lone pair cations and anion-coordination in designing photocatalytic (and likely photovoltaic) materials.

Finally, **Chapter 5** explores the potential of $Sr_2Sb_2O_2Q_3$ (Q = S, Se) oxychalcogenides for photocatalytic activity. This study gives further insight into the activity of Sb^{3+} oxychalcogenides and allows a comparison with $Sr_6Cd_2Sb_6O_7S_{10}$. Wang *et al*[2] suggest that the photocatalytic (and related) properties of $Sr_6Cd_2Sb_6O_7Q_{10}$ are due in part to the presence of semiconducting CdQ units, and comparison with $Sr_2Sb_2O_2Q_3$ allows this to be tested. Overall, the photocurrent and photocatalytic activities of $Sr_2Sb_2O_2Q_3$ (Q = S, Se) suggest that CdQ units do not enhance this behaviour. $Sr_2Sb_2O_2S_3$ showed a photocurrent response under visible light (although with slower e^-/h^+ separation than $Sr_6Cd_2Sb_6O_7S_{10}$, **Figure 5.17a** and **Figure 4.8**) but with better photocatalytic activity under sunlight than the Cd-containing phase (with a rate constant K_{app} higher for $Sr_2Sb_2O_2S_3$ compared with $Sr_6Cd_2Sb_6O_7S_{10}$); $Sr_2Sb_2O_2Se_3$ showed very fast e^-/h^+ separation (**Figure 5.16c)** which was not observed for $Sr_6Cd_2Sb_6O_7Se_{10}$[2].

Both $Sr_2Sb_2O_2Q_3$ (Q = S, Se) oxychalcogenides have very low effective masses for electrons and holes within the layers (**Table 5.11**), which is explained by the effective orbital overlap and close-to-ideal Sb – Q – Sb bond angles. The increased covalency of the selenide, giving wider bands (**Figure 5.26**) has particularly good electron mobility, reflecting increased Sb – Se hybridization towards the bottom of the conduction band.

Both $Sr_2Sb_2O_2S_3$ and $Sr_2Sb_2O_2Se_3$ adopt the same non-polar structure, containing polar Sb units, with larger dipoles across the Sb sites in the oxysulfide (**Section 5.3.4**). It's striking that the photocurrent responses (**Figure 5.16**) indicate quite different e^-/h^+ separation rates for these analogous materials. This suggests that factors other than polarity may be more important and further work is needed to investigate this.

The overall results presented in this manuscript show the potential of oxychalcogenides for water splitting photocatalysis under visible light. Our first aim was to investigate the role of the anion in tuning the band gap. Increasing the chalcogenide coordination tended to decrease the band gap (particularly evidence when comparing the contribution of the different Sb units to the top of the valence band). However, the $La_2O_2Fe_2OQ_2$ materials highlight the need for caution: the Fe_2O connectivity already gives fairly wide bands in these materials and so the band edge positions are not compatible with water redox reactions. A further complexity is the hybridization of the anion p orbitals with cation ns^2 orbitals (if appropriate): the ratio of O:Q anions has a dramatic role in

tuning the states on the top of the valence band, not only tuning the bandgap but also influencing hole mobilities.

Our work also illustrates factors relating to cation-choice: the role of "lone pair" ns^2 cations (Sb^{3+} discussed here, potentially also Bi^{3+}, Sn^{2+} cations) can also give oxychalcogenides with electronic structures suggesting promising photocatalytic activity. Further research into lone pair oxychalcogenide systems is likely to be fruitful. On the other hand, the risk of sample decomposition is evident from our study of CaFeOS, suggesting that care should be taken to avoid easily-oxidized transition metal cations. Therefore, further work to optimize the electrolyte is required in order to ensure a convenient one that works with this type of material. In addition, the morphology (crystallinity, specific area…) are still to be investigated as they can have a significant role on these measurements.

We had also set out to investigate the role of polarity (both of the overall crystal structure and of the polar units). Our work has not yet allowed us to clearly distinguish between these roles. Our hope of comparing the polar and non-polar polymorphs of CaFeOSe would have given insight to this question. Our measurements on $Sr_2Sb_2O_2Q_3$ (Q = S, Se), which are isostructural, are intriguing: only the Se analogue (with lower dipoles than the sulfide) shows the spikey peak in photocurrent measurements indicating fast e^-/h^+ separation. This suggests that polarity may not play as large a role as anticipated and further investigations are needed to explore this.

The work described in this thesis combines both experimental studies (synthesis and structural characterization, as well as property measurements) and electronic structure calculations. This combined approach has given a much deeper understanding than a more narrow study would have allowed. For example, the importance of the connectivity of the active cation (e.g. the close-to 180° Sb – Q – Sb angles in the materials studied in **chapters 4** and **5**) are key to their low electron effective masses. This has also been highlighted for Sn-containing materials[3] and is a design strategy to take forward.

REFERENCES

(1) Cassidy, S. J.; Batuk, M.; Batuk, D.; Hadermann, J.; Woodruff, D. N.; Thompson, A. L.; Clarke, S. J. Complex Microstructure and Magnetism in Polymorphic CaFeSeO. *Inorganic Chemistry* **2016**, *55* (20), 10714–10726.

(2) Wang, R.; Wang, F.; Zhang, X.; Feng, X.; Zhao, C.; Bu, K.; Zhang, Z.; Zhai, T.; Huang, F. Improved Polarization in the Sr6Cd2Sb6O7Se10 Oxyselenide through Design of Lateral Sublattices for Efficient Photoelectric Conversion. *Angewandte Chemie* **2022**.

(3) Ha, V.-A.; Ricci, F.; Rignanese, G.-M.; Hautier, G. Structural Design Principles for Low Hole Effective Mass S-Orbital-Based p-Type Oxides. *Journal of Materials Chemistry C* **2017**, *5* (23), 5772–5779.